# Palaeoflood chronology of blocked-valley lakes in eastern South Africa

**Jamie Callum Wood**

A thesis submitted to the University of Gloucestershire in accordance with the requirements of the degree of Doctor of Philosophy in the School of Natural and Social Sciences

January 2020

Word Count: 50,582

# Abstract

Relatively few studies have examined blocked-valley lakes as potential palaeoenvironmental archives and until now radiometric chronologies for these geomorphic features have been limited to $^{210}$Pb and radiocarbon dating. With a particular focus on chronicling palaeoflood events, this study aimed to evaluate quartz optically stimulated luminescence dating (OSL) as a technique for dating of clastic sediment within blocked-valley lake deposits upon the Mfolozi catchment, eastern South Africa. A flood chronology was produced for sediments collected from a blocked-valley lake basin on the southern margin of the Mfolozi floodplain, using a combination of OSL, $^{14}$C AMS dating and Bayesian modelling. This was complemented by OSL flood chronologies produced for an avulsion channel and a crevasse splay situated on the central and northern areas of the floodplain respectively.

The suitability of OSL for dating blocked-valley lake deposits was dependent on the mode of $D_e$ acquisition. Ages calculated for multi-grain aliquots of fine silt tended to overestimate age owing to partial bleaching, whilst adoption of single-grain OSL enabled $D_e$ modelling and calculation of appropriate ages. The Mfolozi flood chronologies extended to a maximum of c. 7.2 ka and displayed close relation to regional climatic observations. During phases of climatic warming flood frequency appeared to increase, whilst for climatic cooling flood occurrences decreased until ceasing at lowstands, such as the mid-Holocene neoglacial and Little Ice Age (LIA).

Further to the work upon blocked-valley lake sediments, this study investigated the Hydrofluoric acid (HF) etching of quartz grains within the 180-250 µm fraction and the impact of varying treated sample mass and etching time upon naturally-dosed single-grain $D_e$ distributions. Adoption of strict rejection criteria highlighted sample-dependent systematic changes in overdispersion (OD) with increased HF treatment time whilst $D_e$ distribution appeared to normalise when treated sample mass was reduced. No variations in central $D_e$ values were detected across each of the treatment scenarios and it is suggested that the α-component either has a negligible impact upon central $D_e$ or can not be effectively removed using HF.

I declare that the work in this thesis was carried out in accordance with the regulations of the University of Gloucestershire and is original except where indicated by specific reference in the text. No part of the thesis has been submitted as part of any other academic award. The thesis has not been presented to any other education institution in the United Kingdom or overseas. Any views expressed in the thesis are those of the author and in no way represent those of the University.

Signed…….. Date: **10th January 2020**

doi: 10.46289/9JL99YR8

# Acknowledgements

I initially started this research on a studentship in the School of Natural and Social Sciences, University of Gloucestershire. I will always be grateful for the financial support from the University which enabled me to complete this work. Further funding to support fieldwork costs was obtained through the Dudley Stamp Memorial Award (Royal Geographical Society with IBG) and from research grants awarded by the British Society for Geomorphology (BSG) and the Quaternary Research Association (QRA). Fieldwork would not have been possible without this support.

I would like to thank all of my supervisors. Professor Phil Toms for introducing me to luminescence dating, providing lab training, sharing his knowledge and ideas, giving me the opportunity to work in a subject area that I love and for all his time and support in what has been a challenging 2019. Dr Michael Grenfell for his insights, introducing me to the study area and for his great help with fieldwork. Professor Frank Chambers for his insights and contributions in our supervisor team meetings.

Thank you to everyone that helped in South Africa during and after fieldwork. Professor Fred Ellery and Professor Marc Humphries provided coring equipment and were a great help in the field. The Umfolozi Sugar Mill provided access to the floodplain and the directors gave us the opportunity to discuss past flooding on the Mfolozi catchment. Salona Reddy and Dr Jemma Finch for their ongoing pollen and charcoal analysis of the South Lake sequence. Thanks also to Michael's parents who gave us a place to stay in Durban following the completion of fieldwork.

Finally, I would like to thank all my family and close friends for their amazing support throughout this study. My partner (and soon to be wife) Kirsty has stood by me throughout this journey and I couldn't have done it without her love and support. Our son Rory arrived at the perfect time and has brought so much joy into our lives, his smiles and laughter has helped us all get through a tough year. I am gutted that I didn't finish this in time for my Mum to see, but I am eternally grateful for everything she did for me and I will always treasure the memories that she left with us.

# Table of Contents

# List of Figures

# List of Tables

# Abbreviations and Symbology

| | |
|---|---|
| AMS | Accelerator Mass Spectrometry |
| CAM | Central Age Model (Galbraith *et al.,* 1999) |
| CW-OSL | Continuous Wave Optically Stimulated Luminescence |
| $D_\gamma$ | Gamma Dose Rate |
| $D_0$ | Saturation Dose |
| $D_{cos}$ | Cosmic Dose Rate |
| $D_e$ | Equivalent Dose |
| $D_r$ | Dose Rate |
| DRC | Dose-Response Curve |
| $D_\alpha$ | Alpha Dose Rate |
| $D_\beta$ | Beta Dose Rate |
| ENSO | El Niño-Southern Oscillation |
| FMM | Finite Mixture Model (Galbraith & Green, 1990) |
| Gy | Gray – SI unit of ionising radiation |
| $H_2O_2$ | Hydrogen Peroxide |
| HCl | Hydrochloric Acid |
| HF | Hydrofluoric Acid |
| HRGS | High-Resolution Gamma Spectrometry |
| ICP-MS | Inductively Coupled Plasma Mass Spectrometry |
| IR | Infrared |
| IRSL | Infrared Stimulated Luminescence |
| ITCZ | Intertropical Convergence Zone |
| ka | kiloannum (1 ka = 1000 years) |
| LIA | Little Ice Age |
| LOI | Loss-On-Ignition |
| MAM | Minimum Age Model (Galbraith *et al.,* 1999) |
| MWP | Medieval Warm Period |
| OD<br>$\sigma_{OD}$ | Overdispersion |
| OSL | Optically Stimulated Luminescence |
| PDFs | Probability Density Functions |

| | |
|---|---|
| QBO | Quasi-Biennial Oscillation |
| SAR | Single-aliquot regenerative-dose protocol |
| SEM | Scanning Electron Microscopy |
| SRZ | Summer Rainfall Zone |
| SST | Sea Surface Temperature |
| TL | Thermoluminescence |
| WRZ | Winter Rainfall Zone |
| XRF | X-Ray Fluorescence |
| YRZ | Year-Round Rainfall Zone |

# Chapter 1: Introduction

## 1.1. Research Context

Recent trends indicate that globally, an increasing number of ecosystems, people and economic assets are being exposed to climate-related hazards (IPCC, 2014). Of these hazards, flood and meteorological events are the most common; from 2005 to 2016 they combined to cause an average of *c.*17000 fatalities and financial losses of *c .*US$75 billion worldwide each year (Munich RE, 2017). Although ongoing mitigation and improvements in forecasting have helped to reduce vulnerability to such events (e.g. Jongman *et al.,* 2015), there remains a concern that total annual losses could rise through the coupling of climatic change and hazard exposure. With extreme precipitation and flood events experiencing a phase of intensification (Donat *et al.,* 2013; Mousavi *et al.,* 2011; Webster *et al.,* 2005), there is great value and interest in exploring the nature and frequency of past events.

When assessing global trends in extreme events, difficulties can arise from regional differences in both the spatial and temporal coverage of historical records. A coverage gradient is particularly noticeable between low- and high-income countries. For flood events alone, relatively few of those that occurred in low-income countries were reported to global hazard databases prior to the mid-1990s, largely as a result of poor data access and acquisition (Tanoue *et al.,* 2016). To disentangle the magnitude of natural and human-induced climate change and to determine whether the most extreme contemporary climatic events can be attributed to human-induced greenhouse gas emissions (Fischer & Knutti, 2015), it is necessary to obtain more complete long-term records of extreme climatic events.

Existing research has highlighted the potential of sedimentary deposits to document the frequency of extreme flood and meteorological events beyond the span of instrumental and historical records (Bøe *et al.,* 2006; Corella *et al.,* 2014; Madsen *et al.,* 2009). Wetland and lacustrine basins are amongst some

of the more useful depositional settings owing to their sensitivity to environmental change (Adrian *et al.,* 2009; Ouyang *et al.,* 2014) and ability to continuously accumulate sediment and biota from their surroundings. The preservation of stratigraphy within basin environments can enable researchers to identify the distinct changes in sedimentology associated with extreme events and, by utilising the numerous available proxies, reconstruct the environmental conditions before and after these episodes. The use of these basins as environmental archives could be the key to extending existing records of extreme climatic events, as has been demonstrated for flood events (McGlue *et al.,* 2012; Santisteban *et al.,* 2019) and hurricanes (e.g. Madsen *et al.,* 2009; McCloskey & Liu, 2012).

Whilst acting as potential environmental archives, wetlands also provide a diverse range of ecosystem services that benefit both the natural and human environment. However, increasing pressures from human activity, hydrological adjustments and climatic change have resulted in major losses (*c.* 50%) in world wetland area (Zedler & Kercher, 2005). From a climatic perspective one of the more concerning issues surrounding wetland degradation is the regulation of atmospheric gases. Wetlands, particularly those supporting peat formation, are able to sequester large volumes of carbon and can act as carbon sinks (Erwin, 2009). World storage rates of carbon in peatlands alone equates to 370 million tonnes of carbon dioxide ($CO_2$) per annum (Strack, 2008), a large proportion of which is retained in tropical/subtropical areas (Mitsch *et al.,* 2013). Continued losses of these carbon sinks risks a higher atmospheric concentration of $CO_2$. Wetland research focusing on extreme climatic event frequency has the opportunity to also explore the reaction of wetlands to environmental change, this could help to improve management practices and rehabilitation of wetland environments.

The highlighted issues of limited historical flood records and wetland degradation are particularly relevant to eastern South Africa, with the KwaZulu-Natal coast alone experiencing an 11% reduction in wetland area over 16 years (1992-2008 – Grundling *et al.,* 2013) and the South African instrumental climate records featuring missing data and the underreporting of high precipitation events (Kruger, 2006). Examination of wetland basins in this

region could aid with fulfilling and extending existing records of extreme climatic events and identifying the environmental pressures causing wetland degradation. A form of wetland which is underrepresented in wetland environmental research is blocked-valley lakes, these geomorphic features form in tributary valleys following impoundment by aggrading rivers upon the main river trunk. Existing work in KwaZulu-Natal has highlighted the potential of these basins to record flood events as clastic units within sediment sequences (Grenfell *et al.,* 2010), thus providing the opportunity for future studies to simultaneously assess wetland development and chronicle palaeoflood events.

Existing radiometric chronologies for blocked-valley lakes are currently limited to $^{210}$Pb and radiocarbon dating (Grenfell et al., 2010; Finlayson & Kenyon, 2006). Both techniques have limited applications as $^{210}$Pb ages can not be guaranteed for samples older than 100 years (Jia *et al.,* 2018) whilst radiocarbon dating requires the presence of organic material and actually isolates an age for when respiration ceases, not an age for deposition. This research focuses on the development of optically stimulated luminescence (OSL) dating of blocked-valley lake deposits for the first time, using sediments from the Mfolozi floodplain, eastern South Africa. This alternative dating technique benefits from being able to directly date inorganic sediments and produce ages for actual deposition as the OSL signal is reset by sunlight.

Existing work on blocked-valley lake sedimentology upon the Mfolozi catchment, eastern South Africa, has highlighted the presence of alternating clastic and organic sediments within profiles. These sequences are believed to represent an intermittent pattern of large flood events that have impacted the catchment since the onset of sedimentation *c.* 4000 years ago (Grenfell *et al*., 2010). Eastern South Africa is affected by large storm events that erode and disperse large volumes of sediment across the regions floodplains. This was demonstrated by Tropical Storm Domoina in 1984, which left around 90 km$^2$ of the Mfolozi floodplain flats covered in clastic sediment (Kovàcs *et al*., 1985). This dispersed sediment forms the interlaminated clastic layers recorded within the blocked-valley lake profiles, thus providing a marker for Domoina-scale flood events. The OSL dating within this research targets these

markers and seeks to chronicle the large palaeoflood events that have impacted the Mfolozi catchment.

## 1.2. Blocked-Valley Lakes

Blocked-valley lakes are unique wetland environments that form when a main river channel aggrades at a higher rate relative to a tributary, forming natural levees, which then impound the tributary valley (Figure 1.2.1; Grenfell et al., 2010; Finlayson & Kenyon, 2006). Following disconnection from a main river channel, blocked-valley lake basins can begin to fill with alluvium and occasionally form biologically diverse swamps (Blake & Ollier, 1971). The input of sediment and biological matter into these basins initiates the formation of environmental archives, with changes in biota and sediment source being recorded within sediment profiles. Preservation of stratigraphy and biological matter within these profiles could enable blocked-valley lakes to act as proxies for environmental change.

Early work by Blake and Ollier (1971) upon the Fly and Strickland River catchments, Papua New Guinea, highlighted the presence and characteristics of blocked-valley lakes using aerial imagery. Their work noted that blocked-valley lakes present across catchments in their study area had the distinctive shape of 'drowned valleys' and would feature semi-permanent, sinuous tie-channels that connected basins to the main river trunk. The formation of blocked-valley lakes upon the Fly-Strickland catchments was attributed to rapid aggradation of the main river trunk and the inability of tributaries to match alluviation rates, owing to their relatively low flow and sediment yields. Further blocked-valley lake research from the same catchments (Parker *et al.,* 2008; Day *et al.,* 2008) and from the Amazon basin (Neller *et al.,* 1992) has suggested that fluvial response to Pleistocene-Holocene sea level rise was the initial trigger for increased floodplain aggradation and the blocking of tributary valleys. An important point to take from Blake and Ollier (1971) is that natural levees are not required to form blocked-valley lakes, as the Fly-Strickland alluvial plains feature laterally active meandering channels that do not suit natural levee formation.

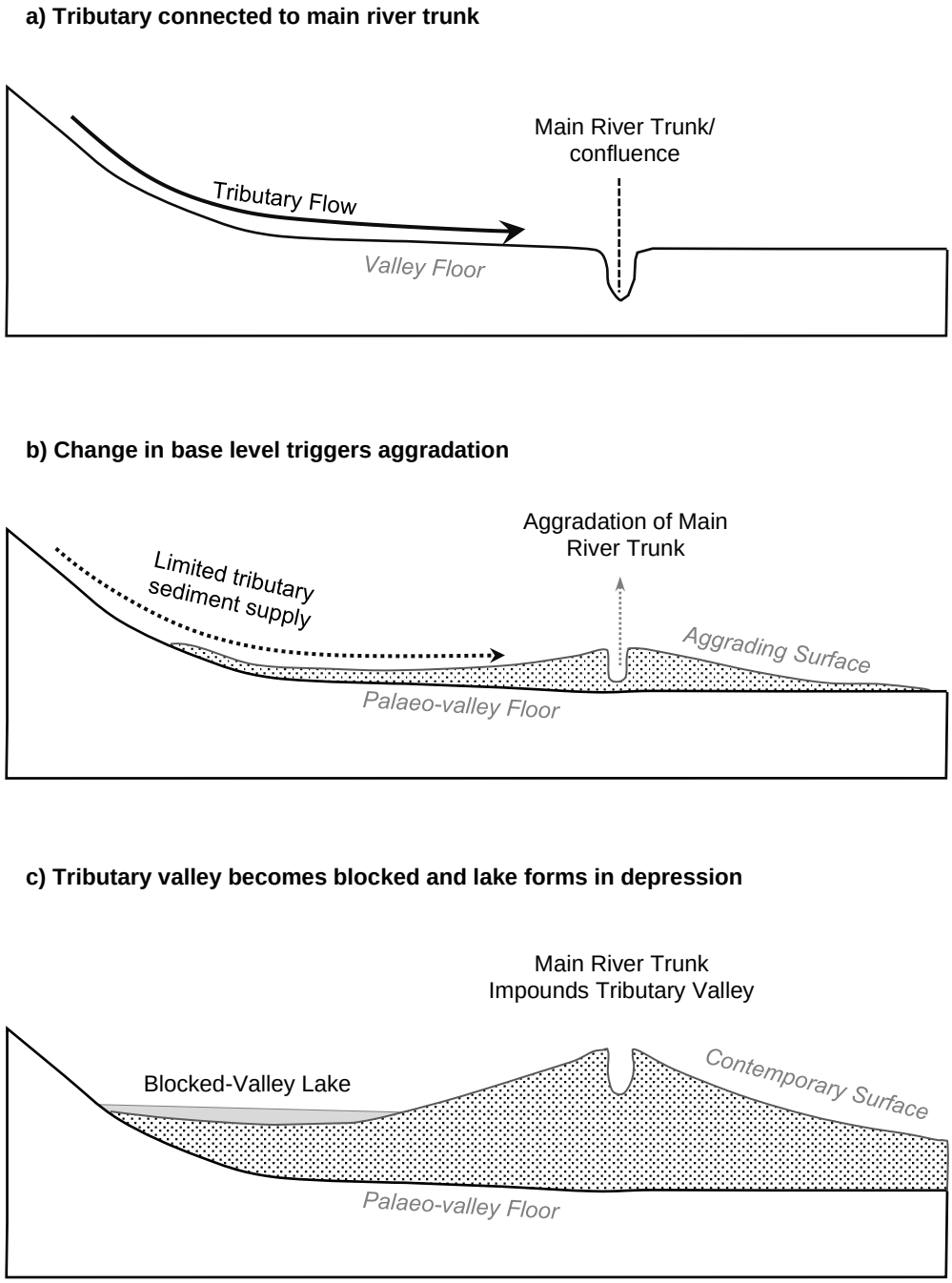


**Figure 1.2.1:** A schematic of trunk-dominated valley impoundment and blocked-valley lake formation. a) Tributary valley connected to the main river trunk, b) A change in base level (e.g. through sea level rise) triggers aggradation across the catchment but the tributary is unable to keep pace with the main river trunk owing to a limited sediment supply, c) the main river trunk impounds the tributary valley and forms a blocked-valley lake. (Valley profile adapted from: Grenfell *et al.,* 2010).

Following formation, blocked-valley lake basins can accumulate sediment via multiple pathways, one of which is through tie-channels. Tie-channels enable bi-directional flow between the main river trunk and blocked-valley basins and have been identified as key features for maintaining the ecological health of basins (Rowland *et al.,* 2009). When a main river trunk has a stage that is above the level of a blocked-valley lake basin, flow through tie-channels in the direction of the basin occurs, depositing water and sediment into the basin (Rowland & Dietrich, 2006). The influx of sediment into blocked-valley lakes during these high-stage phases creates localised deltaic features at the point where tie-channels enter the basins (Blake & Ollier, 1971). It is these deltas arising from tie-channel exchange that produce a datable record for past sediment loading within the main river trunk (e.g. Rowland *et al.,* 2005). When the main river trunk is at/or returns to a low stage level the flow through tie-channels reverses in direction. During periods of drought the shallow nature of blocked-valley lakes enables them to dry out (Swales *et al.,* 1999), which can lead to tie-channels becoming temporarily abandoned by drainage water and clogged by vegetation.

Tie-channel exchange systems have a relatively more complex sedimentary history owing to the interactions between the tributary valley and main river trunk, more relevant to this research is the overbank sedimentation of blocked-valley lake basins. During wet seasons or periods of flooding, main river trunks can overtop their banks, dispersing sediment-laden water into tributary valleys. Grenfell *et al*., (2010) were the first to explore blocked-valley lake sedimentology in South Africa, focusing on Lake Futululu, a basin upon the Mfolozi catchment. They found that Lake Futululu supported peat formation with organic units being preserved throughout sediment profiles. In addition to this they discovered interlaminated clastic lenses that fined with increasing distance from the main river trunk. Grenfell *et al.* (2010) attributed the preserved clastic lenses to overbank sedimentation that occurred during large floods. The recovery of peat formation within Lake Futululu following flood events and the continued preservation of clastic flood deposits, highlights a potential opportunity for blocked-valley lakes to act as archives for palaeoflood events. Although the work upon Lake Futululu determined a relative age of

flood deposits, through the interpolation of a radiocarbon date-derived age-depth model, an attempt has not been made to directly date the flood units. This thesis examines the potential of optical dating for chronicling clastic flood units preserved in blocked-valley lake profiles for the first time, extending current records of large flood events and providing a comprehensive time-frame for blocked-valley lake and wetland development upon the Mfolozi floodplain.

## 1.3. Optically Stimulated Luminescence Dating

### *1.3.1. Principles*

The use of optical dating upon sediment was first proposed by Huntley *et al.* (1985), who adopted similar concepts to those underlying thermoluminescence (TL) dating to utilise the ability of mineral grains to act as dosimeters. When buried, mineral grains accumulate a time-dependant luminescence signal that continues to grow until a mineral's lattice becomes saturated or is exposed to an external stimuli (primarily heat or light – Figure 1.3.1.). Optically stimulated luminescence (OSL) dating evaluates the light-sensitive signal of mineral grains (predominantly quartz and feldspar) to assess when sediment was last exposed to daylight and to estimate a depositional age. The stimulation and resetting of the OSL signal is termed 'bleaching', within the natural environment optical bleaching of sediment typically occurs through exposure to sunlight during erosion.

The OSL signal produced by a mineral grain arises from the excitation of electrons trapped within defects of its crystalline lattice. The 'free' electrons that can be absorbed by mineral grains are created by ionising radiation, which detaches electrons from parent nuclei within sedimentary deposits. Upon optical stimulation, electrons trapped within a mineral diffuse around the crystal lattice with a proportion recombining with optically-sensitive luminescence centres. The dissipation of energy in the recombination process in part results in the emission of photons. This luminescence is proportional to the number of electrons stored within its lattice (Aitken, 1998), which in turn relates to the amount of energy received through exposure to ionising radiation and enabling

minerals to act as dosimeters. Use of this signal as a chronometer requires an assessment of the rate of dose absorption.

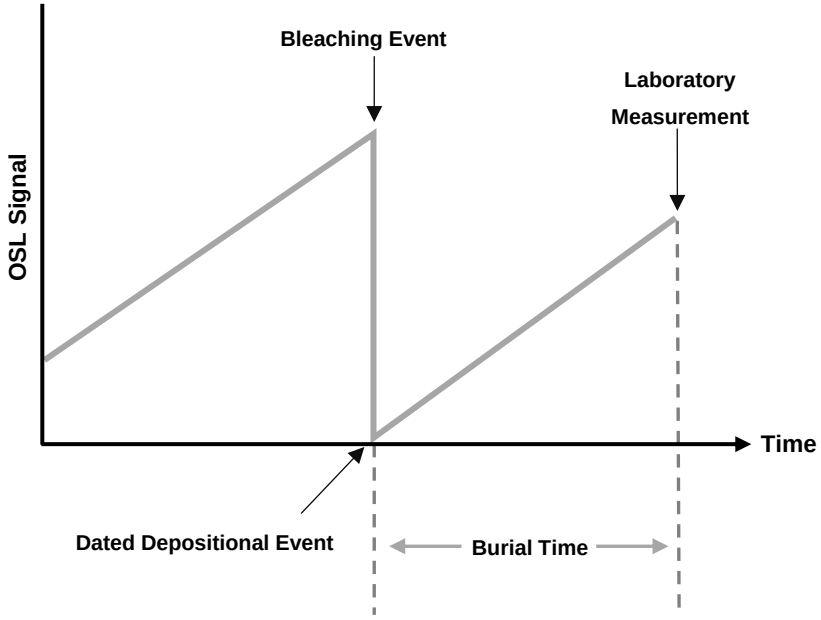


**Figure 1.3.1:** Graphic representation of OSL signal growth following a bleaching event (After: Aitken, 1998).

In OSL dating these parameters are the equivalent dose ($D_e$) and dose rate ($D_r$). $D_e$ can be defined as the laboratory beta or gamma dose required to produce an OSL signal of equal intensity to the natural signal. As such, providing accurate measurement, the $D_e$ should be identical to the natural dose absorbed by minerals during burial (Guérin et al., 2017). The rate of growth of the $D_e$ is controlled by the levels of ionising radiation emitted within and passing through a sediment body. Typically, the largest proportion of the radiation arises from radioactive elements within sediments, whilst a small contribution originates from cosmic rays. Four sources of radiation need to be considered for $D_r$ calculation; α ($D_\alpha$), β ($D_\beta$), γ ($D_\gamma$) and cosmic ($D_{cos}$).

$D_e$ and $D_r$ are both required for age calculation and luminescence ages are derived thus:

$$\text{Age (ka)} = \frac{\text{Equivalent Dose (Gy)}}{\text{Dose Rate (Gy ka}^{-1}\text{)}} = \frac{D_e}{D_r}$$

$D_e$ values are reported in units of Grays (Gy), where 1 Gy = 1 J $kg^{-1}$ of absorbed radiation. The $D_r$ is reported as Gy per unit of time, typically per 1000 years (i.e. Gy $ka^{-1}$).

To obtain $D_e$ the natural OSL signal of mineral grains is artificially stimulated and measured. Following this mineral grains are given a series of artificial known doses (typically β) for which the resultant OSL signals are assessed and used to produce dose response curves. The natural OSL signal can then be compared to the dose response curve and a value for $D_e$ produced via interpolation.

The $D_r$ is formed of two main contributors, cosmic and lithogenic. The cosmic contribution varies with altitude, latitude and overburden depth-density. When quantified, each of these variables can be combined to mathematically deduce the overall $D_{cos}$ following guidance from Prescott & Hutton (1994). The lithogenic contribution arises from radioactive elements within sediments, with three naturally-occurring radioelements contributing to overall $D_r$; potassium (K), thorium (Th) and uranium (U). Potassium-40 ($^{40}K$) is the radioactive isotope of K that contributes to $D_r$ whilst radiation from Th and U are provided by chains of elements headed by the parent isotopes; thorium-232 ($^{232}Th$), uranium-235 ($^{235}U$) and uranium-238 ($^{238}U$). To calculate the relative contribution of each radioelement to $D_r$, the concentrations of $^{40}K$ and radioisotopes within the Th and U decay chains are quantified (e.g. through high-resolution gamma spectrometry) and mathematically converted to overall radioactivity. This is discussed in greater detail in chapter 3.

### *1.3.2. Mineral Selection*

Although both quartz and feldspar can be used within OSL dating, their physical characteristics differ significantly and require careful consideration when adopting the technique for natural deposits. First, it is important to consider the depositional environment and the bleaching nature of quartz and feldspar minerals. Within optical dating, samples are artificially bleached during $D_e$ measurement using either blue-green or infrared light sources, owing to the optical sensitivities of quartz and feldspar respectively. It has been observed that the blue-green OSL signal from quartz bleaches at a faster rate than the infrared stimulated luminescence (IRSL) signal from feldspar grains (Godfrey-Smith *et al.,* 1988; Murray *et al.,* 2012). In environments where sunlight exposure is relatively brief or of insufficient intensity (e.g. turbid flood water), the luminescence signal stored by mineral grains may not be fully reset, resulting in a residual luminescence signal post-burial. This process of partial bleaching and presence of a residual signal can result in $D_e$ values higher than that dose absorbed during burial and thus overestimation of burial age. For active geomorphic environments it may therefore be preferable to adopt quartz minerals owing to their relatively fast OSL bleaching rate.

Quartz has often been the preferred mineral for optical dating as the IRSL signal within feldspars has been found to deteriorate with storage time. This phenomenon, known as anomalous fading, is the athermal loss of a luminescence signal and is believed to be caused by the quantum mechanical tunnelling of electrons within a mineral lattice (Spooner, 1994; Huntley & Lian, 2008). The presence of anomalous fading significantly complicates the use of feldspars, as $D_e$ estimates require correction to account for signal deterioration. Fading rates have to be obtained under laboratory conditions, producing further uncertainty as to whether laboratory-derived fading rates are representative of the fading experienced within sedimentary deposits over geological time (Thomsen *et al.,* 2008). Recently the use of feldspars has gained favour owing to the development of measurement protocols that focus on the isolation and measurement of non-fading signals (e.g. MET-pIRIR - Li & Li, 2011). However, these protocols are not always suited to dating younger

deposits owing to slow bleaching rates and resulting overestimation of burial dose (Buylaert *et al.,* 2012).

When deciding between quartz and feldspar it is also appropriate to consider an approximate age of the sedimentary event that is to be dated. Although both minerals can generally be used to date Late Pleistocene and Holocene deposits, beyond this quartz and feldspar have very different capabilities owing to contrasting dose saturation levels ($D_0$). The OSL signal which is conventionally used for the optical dating of quartz (blue/green stimulation - fast component) typically saturates between 150-250 Gy (Roberts *et al.,* 2015). Accepting that dose rates vary spatially and thus maximum age limits will depend on location, typically the upper age is limited to 100-200 ka (Buylaert *et al.,* 2012). However, for some samples it may be possible to obtain representative quartz $D_e$ values for higher doses, providing that the $D_e$ is less than twice the saturation dose ($2D_o$ – Wintle & Murray, 2006). Feldspar minerals saturate at much higher doses. Studies adopting measurement protocols that target the IRSL signals least affected by anomalous fading, suggest that $D_0$ values between 300-750 Gy are obtainable (Li & Li, 2011; Li *et al.,* 2013). Although dependent upon the accompanying $D_r$, this suggests that the upper limit of feldspar optical dating could extend through the Middle Pleistocene and latter parts of the Early Pleistocene. If a sample was expected to yield an optical age exceeding 100 ka, it may be preferable to target feldspars to avoid encountering a saturating signal.

In this study, the reasons for focusing on quartz OSL are two-fold:

1. Clastic laminations preserved within blocked-valley lakes are formed of fluvially-derived sediment and partial bleaching is likely to feature. Selection of the mineral with the fastest beaching rate maximises the chance of measuring a fully or at least the most well-bleached signal.
2. Blocked-valley lakes upon the Mfolozi formed around 4 ka, suggesting optical ages will fall well within the saturation limit of quartz.

### *1.3.3. Application of Quartz OSL to Water-Lain Deposits*

Very few early studies explored the application of quartz OSL to fluvial sediments owing to the presumption that water-lain mineral grains receive insufficient sunlight to fully reset the OSL signal prior to deposition. Some of the first quartz OSL research upon water-lain sediments was published by Murray *et al.* (1995), who examined $D_e$ values from a suite of 'modern' samples, including material from river channels, over-bank deposits and beach dunes. They found that in comparison to the other deposits, single-aliquot $D_e$ values from channel samples were much higher than anticipated and displayed a greater degree of dispersion. This was attributed to the inclusion of a small proportion of grains that had been poorly bleached. Although the work of Murray *et al.* (1995) highlighted issues of $D_e$ overestimation and increased scatter within fluvial samples, thus confirming the presence of partial bleaching, the study also highlighted the presence of a well-bleached component within some waterlain samples indicating OSL could be suited to some fluvial settings. Further evidence of the potential suitability of OSL for dating water-lain deposits came from modern fluvial sediments of the Loire River, France. Stokes *et al.* (2001) observed a systematic decrease in the residual OSL signal stored by quartz samples with increasing distance from the Loire River source, suggesting that water-lain quartz may become fully bleached, particularly if sediment has been transported over large distances (> 300 km).

Improvements in instrumentation (e.g. Markey *et al.,* 1997) have enabled routine $D_e$ measurement of large quantities of quartz aliquots, prompting OSL to be tested upon a variety of water-lain deposits. The development of single-grain stimulation units (Duller *et al.,* 1999a; Duller *et al.,* 1999b) has also enabled researchers to observe inter-grain variations in $D_e$. Further to the advances in technology, the development and refining of the single-aliquot regenerative-dose protocol (SAR) (Murray & Wintle, 2000; Murray & Wintle, 2003) has significantly improved quartz $D_e$ assessment. The SAR protocol corrects for sensitivity changes that can be induced within quartz by the cycles of irradiation and heating required to interpolate $D_e$ values, enhancing the reliability of burial dose assessment.

Despite the advances in both technology and measurement protocols, partial bleaching remains a common issue for water-lain sediments. Numerous approaches have been taken to assess the characteristics of partial bleaching in order to isolate representative burial doses, these can be classified into 'Signal Analysis' methods and 'Distribution' methods (Bailey 2003).

Signal analysis can be adopted for single-aliquot $D_e$ estimates and utilises the varying depletion rates of the OSL signal components (fast, medium and slow) outlined by Bailey *et al.* (1997). A common diagnostic for detecting partial bleaching from SAR derived $D_e$ estimates is to observe changes in $D_e$ with increased stimulation time (i.e. $D_e(t)$ plot; Bailey, 2003), where heterogeneous bleaching is indicated by higher $D_e$ values with increased stimulation time. However, the form of $D_e(t)$ plots are also dependant on the relative sizes of the pre- and post-burial doses and the fast and medium OSL components (Bailey, 2003), it is therefore not always possible to identify partial bleaching through signal analysis.

Distribution methods interpret the characteristics of $D_e$ distributions, exploring the shape, scatter and identification of dose populations. A number of statistical models (e.g. Galbraith *et al.,* 1999; Roberts *et al.,* 2000; Guerin *et al.,* 2017; Fuchs & Lang, 2001), which are explored in greater detail in Chapter 4, have been developed to isolate representative burial doses, particularly in instances when $D_e$ distributions are non-Gaussian and where mean values are likely to be misleading (Rodnight *et al.,* 2006). Each of the developed models are suited to different $D_e$ distributions and statistical parameters. Bailey & Arnold (2006) propose a decision tree to select the appropriate model. However, recent work from Thomsen *et al.* (2016) noted this decision tree led to age underestimates of greater than 40% for samples with independent age control and reaffirmed that $D_e$ modelling requires careful consideration.

Further caution should be taken, particularly when analysing single-grains, as other extrinsic factors such as micro-dosimetry (Olley *et al.,* 1997; Mayya *et al.,* 2006) and pedoturbation (Bateman *et al.,* 2003) have the potential to influence $D_e$ distributions and could lead to misinterpretation of measured doses. Single-grain distributions often display higher variability between $D_e$

values in comparison to multiple grain aliquots, largely as a result of the averaging that occurs when more than one grain contributes to the observed OSL signal (Duller, 2008). Typically users of single-grain OSL draw upon the overdispersion parameter ($\sigma$ - i.e. the observed variability which is outside of that expected for a Gaussian distribution) to help determine whether samples were fully bleached upon deposition, where samples with $\sigma$<20% are generally considered to have been well-bleached (Olley *et al.,* 2004). For fluvial/water-lain samples it is suggested that single-grain OSL is only necessary for sediments younger than 1 ka (Jain *et al.,* 2004). Jain *et al.* (2004) made this recommendation as most of their OSL ages that were >1 ka displayed consistency with independent age controls, with residual doses having a lesser impact upon modelled $D_e$ values for older samples. Murray & Olley (2002) on the other hand indicate that only fluvial samples which are <20 ka would require single-grain analysis, as their observations indicated that samples >20 ka displayed no systematic effects of partial bleaching. These observations should be accepted with caution and selection of single- or multiple-grain aliquots should be made on a sample-by-sample basis. This is reiterated by Arnold *et al.* (2007) who replicated single- and multi -grain age estimates for fluvial sediment from Colorado. They found that only 50% of samples produced statistically similar results, with a majority of multi-grain aliquots overestimating the dose obtained through single-grain measurements. With the passage of time dose distributions become a function of small-scale variations in dose rate, but for relatively young deposits pre-burial partial bleaching and post-burial reworking need to be considered. Single-grain $D_e$ distribution analysis often provides the best means of capturing the burial dose.

The sediment of focus in this research comprises material collected from blocked-valley lake basins and flood deposits from the central floodplain, with flood units of known age (<100 years) coming from the central floodplain. Examples of the application of OSL to similar sediments and environments includes work by Rowland *et al.* (2005), who examined sedimentation and advancement rates in oxbow lake tie-channels across three alluvial river systems; the Mississippi, Fly River and Yukon River. These young sediments (<1000 years), dated using a combination of single-aliquot and single-grain

quartz OSL, were able to discriminate between units that were deposited <40 years apart and, for the Mississippi catchment, OSL ages closely matched historical sources. Despite evidence of partial bleaching within OSL samples, Rowland *et al.* (2005) were able to calculate accretion rates and attribute tie-channel advancement rates to variations in sediment load of the main river channel.

Madsen *et al.* (2009) produced a hurricane chronology for landfalls occurring in Massachusetts, USA, adopting quartz OSL to directly date storm deposits. Spanning *c.* 600 years their OSL chronology closely matched historical records and was also relatively consistent with pollen and $^{137}Cs$ profiles that were analysed throughout core samples. However, in one instance it was noted that quartz OSL overestimated age, despite the application of a minimum age model. In this case the sample displayed some evidence of incomplete resetting of the OSL signal on deposition, including a wide and skewed distribution. This is particularly likely for flood units harboured by blocked-valley lakes as these units are created by overbank deposition from the main river channel. Overbank deposits are prone to partial bleaching and have been shown to significantly overestimate age (Li *et al.,* 2014).

Further work upon storm driven sedimentation has indicated that quartz OSL can successfully be applied to high-energy deposition, even in situations where incomplete bleaching is certain. Cunningham *et al.* (2011) conducted multi-grain OSL dating upon storm surge sediment preserved amongst coastal dune deposits in the Netherlands. Given the nature of storm surge sediment and the likelihood of limited light exposure, Cunningham *et al.* (2011) opted to adopt early background subtraction, thus reducing the contribution of the quartz OSL slow component to negligible levels (Cunningham & Wallinga, 2010). By isolating the fast component during $D_e$ analysis, resultant OSL ages matched written accounts of storm surge events that had occurred in 1775 and 1776. Dates of the storm surge sediment were complimented by stratigraphically consistent OSL ages from surrounding aeolian sediments.

Existing research from similar environments and deposits, indicate that quartz OSL has the potential to be successful upon the Mfolozi catchment. The ability

of the technique to directly date clastic flood deposits has a significant advantage over interpretation of AMS radiocarbon dates as external calibration is not required. Given the young, water-lain nature of the Mfolozi sediments, it appears likely that partial bleaching could influence age estimates produced in this study. The adoption of single-grain OSL in this research will help to quantify overdispersion and attempt to identify representative burial doses.

### 1.4. Research Aim and Objectives

The preservation of sedimentology within blocked-valley lake basins upon the Mfolozi catchment, provides a unique opportunity to examine these basins as potential palaeoflood archives. With a particular focus on palaeoflood events, this thesis aims to evaluate OSL as a technique for dating of clastic sediment within blocked-valley lake deposits upon the Mfolozi catchment. To achieve this aim the following objectives are addressed:

1) Collect core samples from blocked-valley lake and modern flood deposits across Mfolozi floodplain
2) Model dose rates throughout core lengths effectively, such that variations in moisture, density and radioactivity are incorporated.
3) Investigate sample pre-treatments to produce a robust methodology for quartz OSL dating of blocked-valley environments.
4) Assess the reliability of quartz single-grain OSL age estimates with assistance from the available modern analogues.
5) Construct an OSL-based Bayesian age model, verifying its suitability using independent radiocarbon dating age estimates.
6) Assess the suitability of quartz OSL dating for use upon blocked-valley lake deposits.

The objectives presented above provide a general structure for the subsequent chapters within this thesis. Whilst providing an overview and justification for the selected sampling locations, Chapter 2 provides a review of the literature surrounding the atmospheric processes, contemporary flood patterns and the palaeoenvironmental change that has been experienced both on a catchment

and regional scale. Chapter 3 provides an outline of methods used within this research, particular focus is paid to the modelling of $D_r$ values throughout core lengths owing to their complex sedimentology. Chapter 4 explores the origins of inter-grain $D_e$ distribution and isolates a suitable hydrofluoric acid treatment for quartz undergoing single-grain $D_e$ analysis. The results obtained from optically dating the Mfolozi sediments are presented in Chapter 5, including age estimates obtained from modern analogues to assess presence and range of residual signals. Chapter 6 explores Bayesian modelling and uses it to couple radiocarbon and OSL dates, subsequently the constructed models are used to assess the overall agreement of the chronologies based on relative stratigraphic position. Chapter 7 provides a synthesis of the chronologies obtained from each sampling site and explores the implications for the luminescence dating community. Finally, Chapter 8 provides the concluding points to this research.

# Chapter 2: The Mfolozi Catchment

## 2.1. Regional Setting

The Mfolozi floodplain is situated on the eastern coast of KwaZulu-Natal, eastern South Africa (Inset - Figure 2.1.1). The floodplain hosts two alluvial rivers; the Mfolozi and the Msunduze that, during normal flow conditions (i.e. very low - Grenfell & Ellery, 2009), pass eastwards over the northern and southern margins of the floodplain respectively. The Mfolozi River catchment drains an area of *c.* 11,068 km$^2$ (Grenfell & Ellery, 2009) while the Msunduze drains a much smaller area of *c.* 559 km$^2$ (Lindsay et al., 1996). Prior to reaching the coast the two rivers meet at a confluence on the eastern margin of the floodplain and, on occasion, share an estuary with Lake St Lucia (Figure 2.1.1).

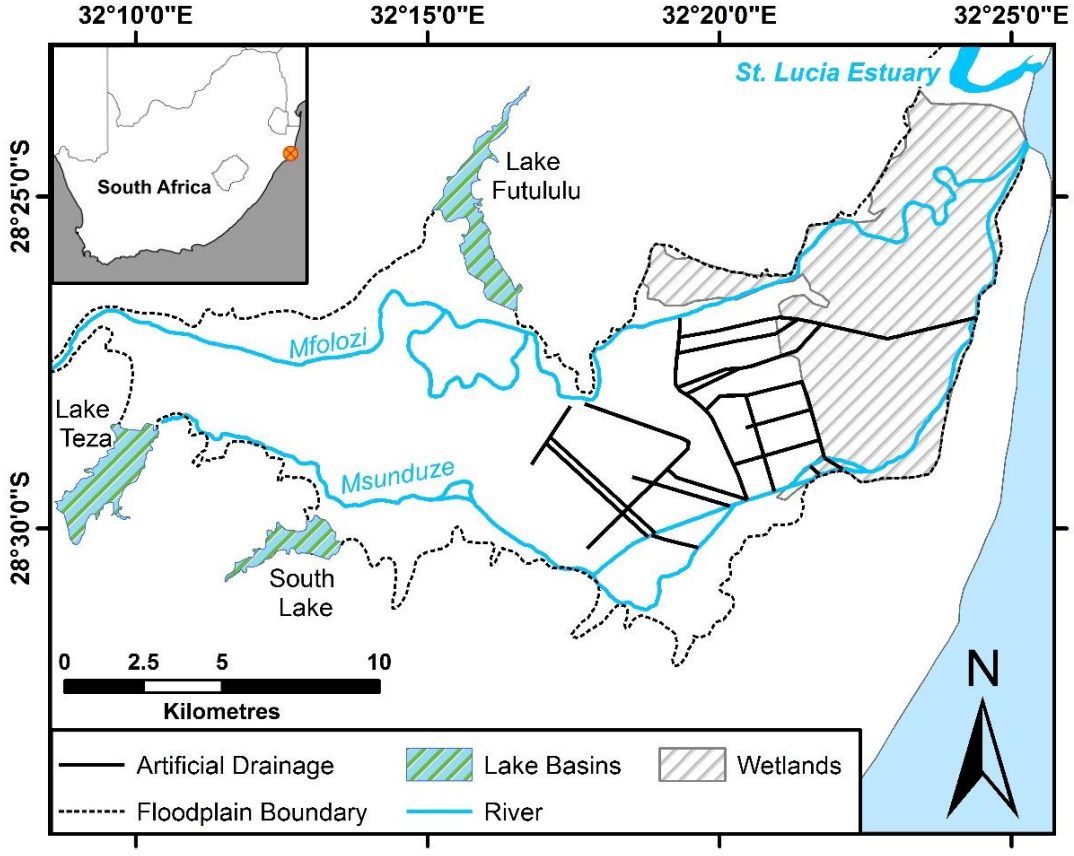


**Figure 2.1.1:** The Mfolozi floodplain (current wetland extent and artificial drain locations adapted from: Grenfell *et al.*, 2009)

The relatively flat floodplain occupied by the Mfolozi and Msunduzi (Figure 2.1.2) is very wide, spanning over 10 km across some central regions. This is significantly different to the upper reaches of the Mfolozi River, which is constrained by deep narrow valleys. This contrast owes itself to variations in underlying bedrock, the Mfolozi floodplain covers a geology featuring Zululand Group silt- and sandstone bedrock overlain by unconsolidated aeolian deposits that is less resistant and more susceptible to weathering than the basalt geology that features upstream. Both the floodplain and upstream valleys of the Mfolozi were formed during an erosional phase that followed a eustatic low-stand at 18 ka (Grenfell *et al*., 2009; Ramsay & Cooper, 2002; Ramsay, 1995), with the less resistant basal material in the lower reaches of the Mfolozi enabling the creation of a wide floodplain.

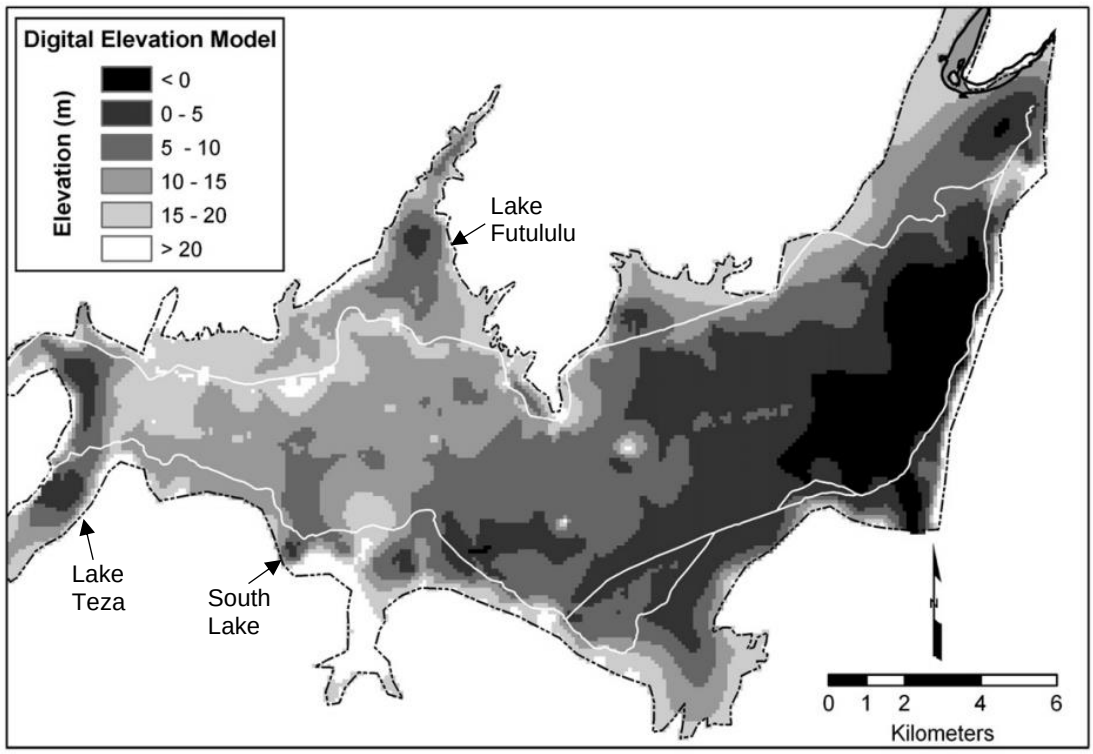


**Figure 2.1.2:** Digital elevation model of the Mfolozi floodplain (from: Grenfell *et al.,* 2009)

A large proportion (65%) of the Mfolozi floodplain is used for sugar cane cultivation, which currently produces around 0.81 million tonnes of this crop in a typical growing season (Umfolozi Sugar Mill, 2016). Drainage work by sugar cane producers, for land reclamation and more recently for flood mitigation measures, has been ongoing since the 1930s. Although a large proportion of the flats are heavily managed for cultivation, some areas of natural wetland still remain within the margins of the floodplain. This includes Lake Futululu, which was subject to the first blocked-valley lake study upon the catchment (Grenfell et al., 2010). Work by Grenfell *et al.* (2009) highlights the progressive drainage of the natural wetland upon the Mfolozi floodplain since 1937. By the 1980s over half of the natural wetland upon the floodplain had been lost (Taylor *et al.,* 1995), largely as a result of the human activity. The natural wetland that remains on the floodplain is restricted to marginal lakes and the eastern-most portion of the floodplain flats (Figure 2.1.1).

## 2.2. Contemporary Climate of Eastern South Africa

### *2.2.1. Overview*

Two distinct climatic regions exist in South Africa, the Winter Rainfall Zone (WRZ) and Summer Rainfall Zone (SRZ). These zones are defined as having >66% of their annual precipitation falling within the respective austral seasons. A third, less distinct climatic regime is described by Chase and Meadows (2007); the Year-Round Rainfall Zone (YRZ), which acts a transition from the temperate conditions of the WRZ to the subtropical SRZ. Regions within the YRZ can receive large quantities of precipitation throughout the seasons.

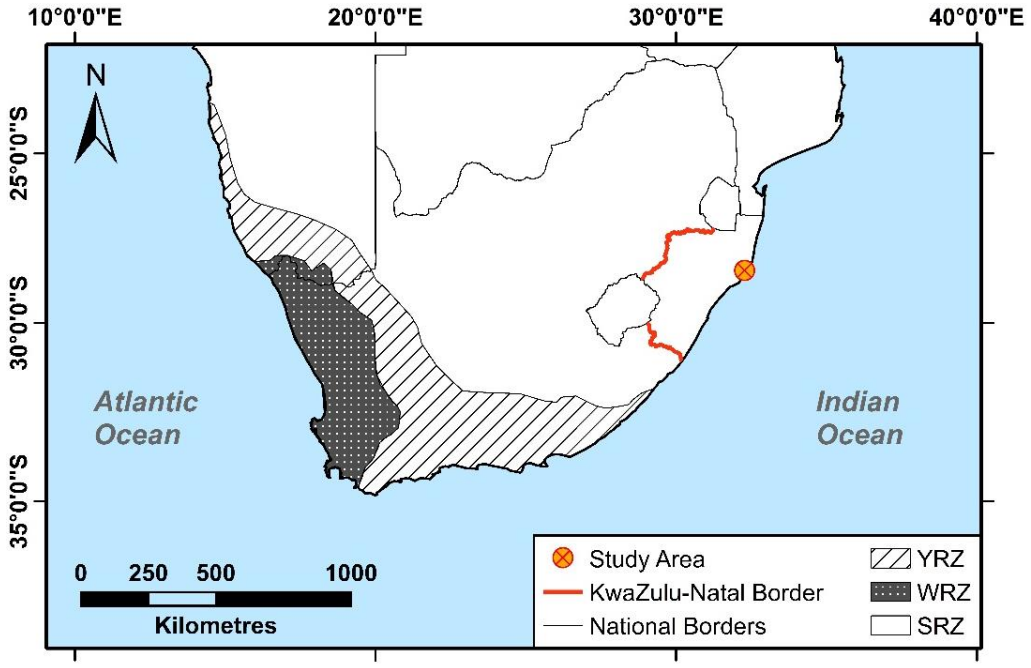


**Figure 2.2.1:** Climatic regions of Southern Africa; Winter (WRZ), Summer (SRZ) and Year-Round (YRZ) rainfall zones (Adapted from: Chase & Meadows, 2007)

The seasonal gradient between the climatic zones is largely attributed to the latitudinal positioning of South Africa and the interplay between atmospheric cells and the Intertropical Convergence Zone (ITCZ). The landmass is situated beneath a high pressure atmospheric belt which circles the earth at ~30°S (Tyson & Preston-Whyte, 2000). This subtropical ridge is formed of numerous anticyclonic high pressure cells created by descending masses of

cool air from meridional (Hadley and Ferrel cell) circulation. Anticyclonic cells influencing the South African climate include the South Atlantic Anticyclone, South Indian Anticyclone and Continental High (Figure 2.2.2).

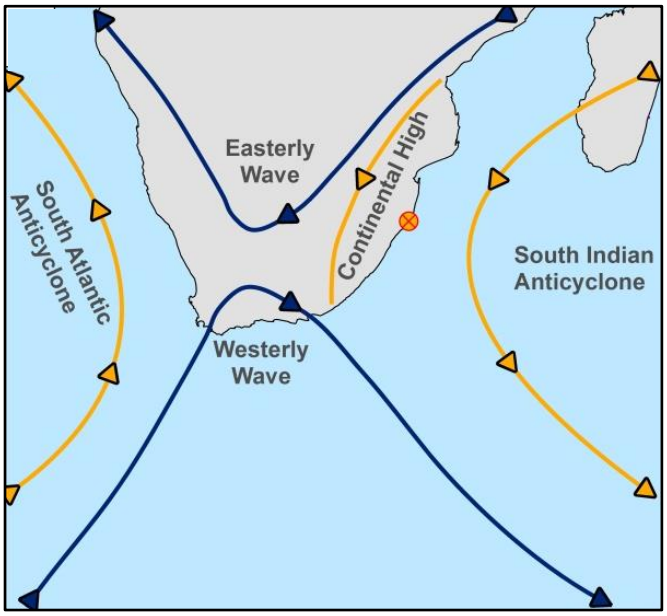


**Figure 2.2.2:** Meridional atmospheric circulation influencing the South African climate (Adapted from: Tyson & Preston-Whyte, 2000)

As with most eastern regions of South Africa, the Mfolozi floodplain is situated in the subtropical SRZ and receives a majority (80%) of annual precipitation (645-1090 mm) during the austral summer (Reason & Mulenga, 1999; Grenfell et al., 2009). The summer rainfall experienced by the Mfolozi catchment and SRZ, is typically associated with easterly waves (east-west airflow) and tropical systems derived from the Indian Ocean (Stager *et al.,* 2013). Rainfall induced by the easterlies occurs more frequently during the austral summer owing to the southerly migration of the ITCZ. Over the African continent and the Indian Ocean basin the ITCZ can reach its southern-most position of 8°S (Schneider *et al.,* 2014). This migration forces the South Indian Anticyclone and easterly waves to a more southerly position, enabling the easterlies to transport moisture laden air from the Indian Ocean over the eastern regions of South Africa, thus producing the summer rainfall. The opposite effect is seen in the WRZ, however, rainfall

regimes are instead associated with westerly airflow and Atlantic-derived weather fronts.

To fully appreciate the climate dynamics of South Africa's SRZ it is also important to consider zonal circulation and modulation of the effects of the El Niño-Southern Oscillation (ENSO). In general, the impact of ENSO cycles upon the SRZ is observed as reduced rainfall and drought during warm, El Niño phases and enhanced rainfall during cool, La Niña phases (Nicholson, 1997; MacKellar *et al.,* 2014). The ocean-atmosphere exchange of moisture and heat during ENSO cycles influences Walker Circulation. Over southern Africa a slowing of this zonal circulation occurs during El Niño events. This causes cloud convergence and rainfall to shift offshore, thus producing the associated drought conditions. However, this pattern is not always consistent (e.g. 1997/98 El Niño; Fauchereau *et al.,* 2009) and, although not fully understood, it is believed the impacts of ENSO related changes are modulated by a Quasi-Biennial Oscillation (QBO) of stratospheric winds (Tyson & Preston-Whyte, 2000). The QBO is observed as having an easterly and westerly phase, with El Niño related variability being stronger during the westerly phases. Nicholson (2001) suggests that sea surface temperatures (SST) off the coast of South Africa require specific patterns in order for ENSO-induced rainfall changes to occur, this typically occurring in every 3 of 4 ENSO events.

### *2.2.2. Extreme Rainfall and Flood Events*

Despite the normal low flow conditions of the Mfolozi catchment, during extreme rainfall events vast changes in both flow and geomorphology occur across the catchment (See Figure 2.2.3). As this research examines palaeoflood deposits preserved across the Mfolozi, it is appropriate to highlight the synoptic systems associated with the heaviest precipitation and flooding upon the catchment and across KwaZulu-Natal.

Although rainfall associated with easterly airflow in the SRZ can last for a number of days, it is not necessarily conducive to flooding. There are two particular synoptic systems which have been associated with heavy rainfall

and flash-flooding for this region of South Africa, namely cut-off lows and tropical storms. Created in the westerlies, cut-off lows are unstable cold-cored systems which slope west with increasing altitude (Tyson & Preston-Whyte, 2000). The nature of cut-off lows is such that they produce a large amount of vertical uplift, promoting deep convection that can sustain heavy rainfall for a number of days (Singleton & Reason, 2007).

For many coastal regions of KwaZulu-Natal, a cut-off low system in September 1987 caused some of the worst flooding on record (Kovacs, 1988). The system sustained rainfall for 5 days over KwaZulu-Natal with some areas receiving 800 mm of rain, a considerable amount in comparison to the regional annual average of 1000 mm (Badenhorst *et al.,* 1989). Unfortunately, as was found by Grenfell *et al.* (2009), there is no 1987 post-flood aerial imagery for the Mfolozi catchment so it is difficult to examine the physical changes resulting from this extreme cut-off low system. Around 380 lives were lost as a result of flood-related incidents (Bell, 1994). It should be noted that not all cut-off lows produce such devastating effects. Of the average 11 systems per annum, only one in five cause flooding (Singleton & Reason, 2007).

Tropical storms are currently a less frequent problem for the eastern regions of KwaZulu-Natal. Although an average of 12 tropical storms per year form in the South-West Indian Ocean (Mavume *et al.,* 2009), relatively few pass into the Mozambique Channel and reach the South African coastline. Those that do have the potential to maintain heavy rainfall for a substantial amount of time owing to the latent heat energy fuelling the systems (Tyson & Preston-Whyte, 2000). Despite the relatively low frequency of tropical storms impacting eastern South Africa, they remain a concern as recent trends indicate that storm intensification is occurring across the Indian Ocean basin (Webster *et al.,* 2005) and an increasing number of storms are tracking to the south of Madagascar (Fitchett & Grab, 2014). The coupling of these two factors could result in a higher frequency of intense tropical storms making landfall over South Africa.

.

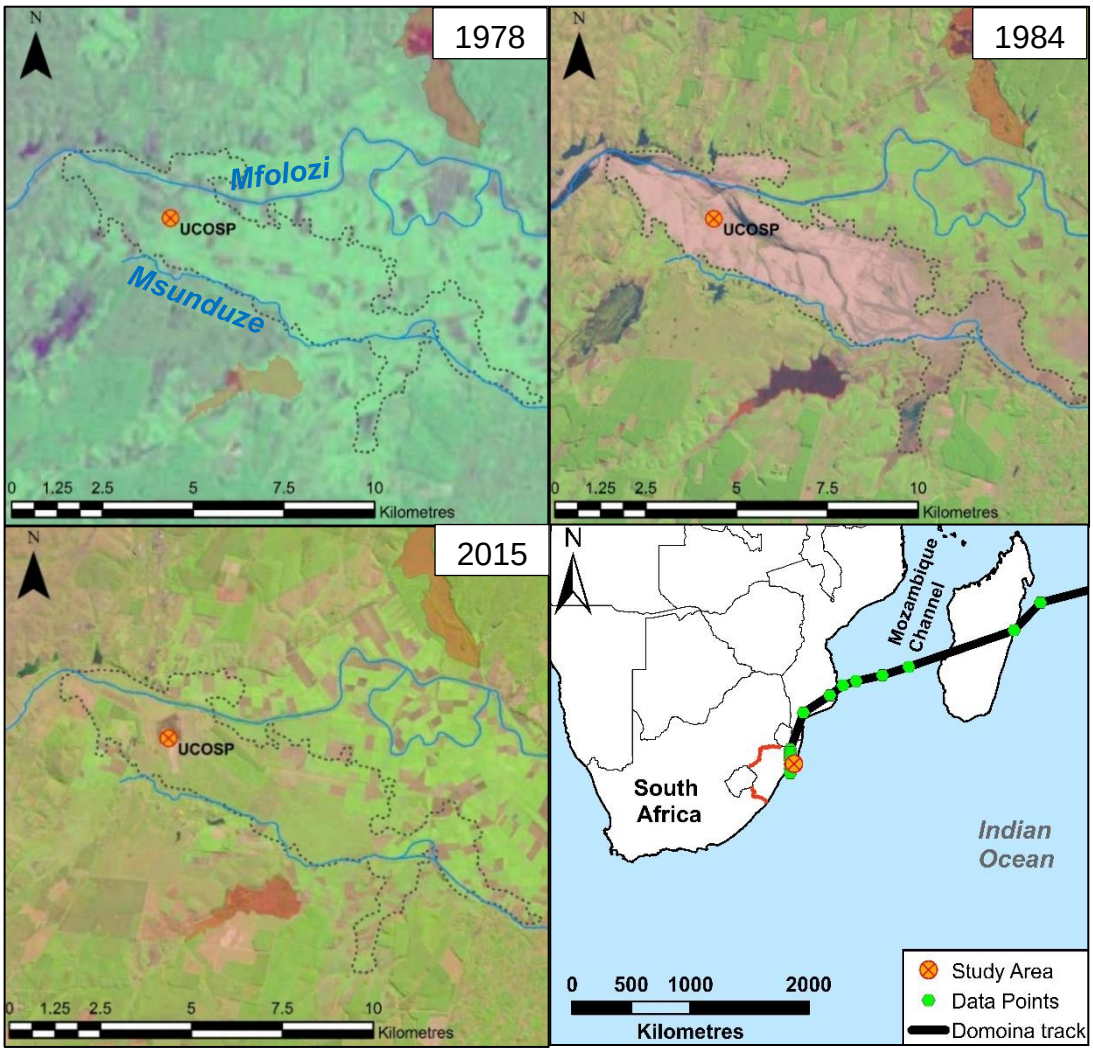


**Figure 2.2.3:** Tropical Storm Domoina track (lower right) and Landsat satellite imagery of Mfolozi floodplain. Pre-, post-Domoina and contemporary imagery provided. Contemporary watercourse for Msunduze and Mfolozi highlighted. (Storm Track Data: The Weather Company, 2017. Satellite Imagery Courtesy of the U.S. Geological Society, 1978, 1984 and 2015)

Of the recent tropical storms to impact eastern South Africa, Tropical Storm Domoina in January 1984 was the most devastating. Being one of the relatively few storms to pass into the Mozambique Channel (Figure 2.2.3), Domoina made landfall over Mozambique and continued to track south over the KwaZulu-Natal coastline. Domoina maintained five days of heavy rainfall over the South African coastline with total rainfall exceeding 900 mm near the

Mfolozi catchment (Kovacs *et al.,* 1985). North of that catchment, conditions were more extreme than the cut-off low system which was to follow in 1987. Flooding affected *c.*10,000 people across Southern Africa, and in in South Africa alone damages exceeded R100 million (South African Rand) and more than 200 lives were lost (Kovacs *et al.,* 1985).

Pre- and post-Domoina satellite imagery of the Mfolozi catchment (Figure 2.2.3) provides some indication of the vast geomorphological changes that occurred upon the catchment. The high flow of the Mfolozi (16000 $m^3$ $s^{-1}$) mobilised large volumes of clastic sediment which, upon deposition, covered *c.*90 $km^2$ of the Mfolozi flats (Kovacs, 1985). One of the most striking changes, as displayed in Figure 2.2.3, is the occurrence of a mass avulsion and the diversion of the Mfolozi towards the southern margins of the floodplain into the Msunduze. The contemporary image reveals that the Mfolozi recovers and reverts back to its normal course, suggesting that deposits upon this avulsion channel could record large flood events that impact the catchment.

Although not attributed to the larger flood events, thunderstorms are an important synoptic feature and produce a large proportion of the precipitation received by coastal regions of Kwa-Zulu Natal. The storms display a distinct diurnal pattern with late evening rainfall peaks observed in the region. The storms and their patterns are created by offshore winds originating from the Drakensberg Mountain plain (Tyson & Preston-Whyte, 2000)

## 2.3. Historical Trends

### *2.3.1. Regional Observations*

Many studies have explored historic rainfall patterns in South Africa in order to understand and isolate the drivers behind rainfall variability. Amongst the first to publish upon this area was Tyson *et al.* (1975), who analysed rainfall data from 157 stations across South Africa with some records spanning from 1880 to 1972. Their statistical analysis highlighted three distinct cycles in rainfall patterns occurring over timescales of; 16-20, 10-12 and 3-4 years, with eastern South Africa displaying distinct cyclical peaks at 16-20 and 3-4

years. Since this early work the former two cycles have been refined and attributed to an 18.6 luni-solar cycle and a 10-11 year solar cycle (Currie, 1993). The occurrence of the less distinct 3-4 year cycle initially suggested by Tyson *et al.* (1975), varies in subsequent studies with the presence of 2.3, 3.5-5 and 4-7 year cycles being proposed in subsequent work (Jury, 1996; Malherbe *et al.,* 2016). These shorter cycles are less pronounced in eastern South African rainfall patterns than the ~18 year cycle and have been linked to forcing by the ENSO and QBO.

Within rainfall records the ~18 year cycle typically manifests as alternating 9 year spells of above and below average rainfall (Table 2.3.1). In the SRZ it has been found that extreme rainfall events (both floods and droughts) tend to occur in association with El Niño events during a spell of below average rainfall or, when a La Niña occurs during a spell of above average rainfall (Kruger, 1999), complicating the general pattern highlighted earlier in this chapter. Observation of extreme rainfall events over two 30 year periods (1931-60 & 1961-90) has suggested that large areas of the SRZ could be experiencing a >10% intensification of 10-year high rainfall events (Mason *et al.,* 1999).

**Table 2.3.1:** Observed wet and dry periods between 1905 and 1990 over South Africa (after: Tyson & Preston-Whyte, 2000).

| Wet Years | Dry Years |
|---|---|
| | 1905/06 to 1915/16 |
| 1916/17 to 1924/25 | 1925/26 to 1932/33 |
| 1933/34 to 1943/44 | 1944/45 to 1952/53 |
| 1953/54 to 1961/62 | 1962/63 to 1970/71 |
| 1971/72 to 1980/81 | 1981/82 to 1989/90 |

Existing analysis of historical rainfall data suggests that there has been little change in precipitation across South Africa for the past 100 years (Kruger, 2006). This is partially true for KwaZulu-Natal, which displays a long term trend of stability for precipitation totals, however, the total number of rain days appears to have decreased for coastal areas and increased inland (MacKellar *et al.,* 2014). There also appears to have been shifts in seasonality, with significant decreases in autumn rainfall being observed in the Drakensberg area of KwaZulu-Natal (Nel, 2009).

Although historical rainfall records provide an indication of long-term cyclical changes, they are not necessarily the most useful records for identifying extreme events. The 1984 tropical storm and 1987 cut-off low for example, occurred during a dry phase of the ~18 year cycle (Tabe 2.3.1). As a whole, records of actual flooding across KwaZulu-Natal appear relatively fragmented, with the best temporal range for the region occurring in Durban and Pietermaritzburg (with the exception of the Mfolozi records) that are *c.* 230 and 255 km southwest of the study area, respectively (Figure 2.3.1).

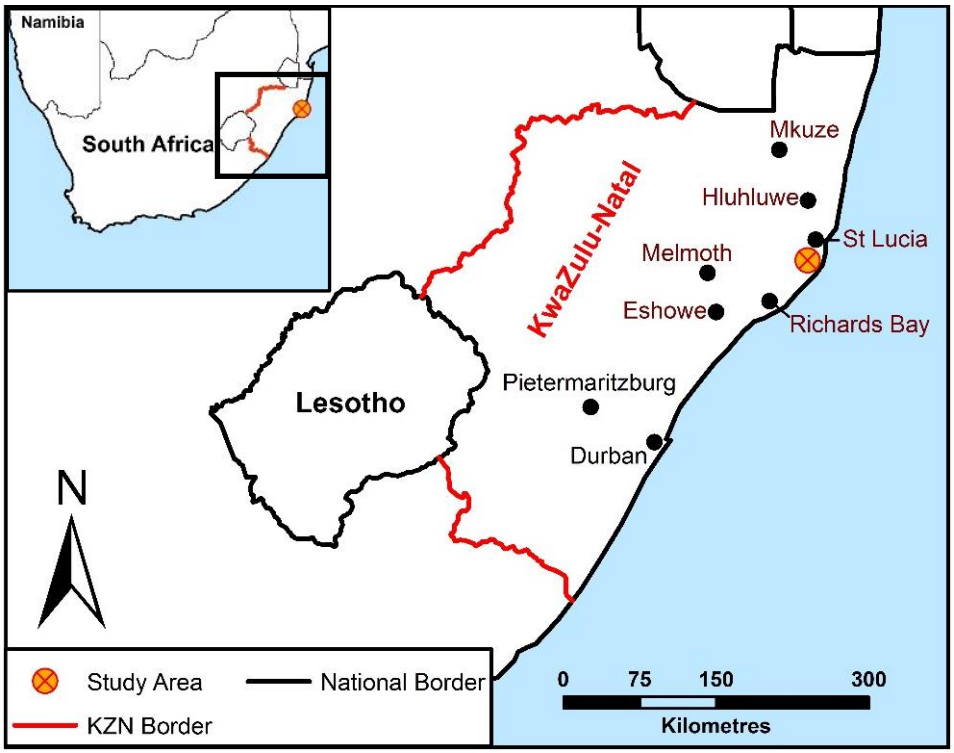


**Figure 2.3.1:** Flood record locations (Data Source: South African Weather Service, pers.comm)

Records of flood occurrence were obtained from the South African Weather Service (SAWS, pers. comm.) for the named areas in Figure 2.3.1. The data for Durban and Pietermaritzburg display the best temporal range, both of which display a significant increase in reported flood events in recent decades (Figure 2.3.2). This suggests that either flooding has become more prominent or the dataset is incomplete and does not provide a continuous record of flooding. The data also indicate that Durban is either; a) susceptible to a large amount of localised flooding or, b) more proficient at recording flood events, as the frequency of recorded floods exceeds that for KwaZulu-Natal in all decades except the present.

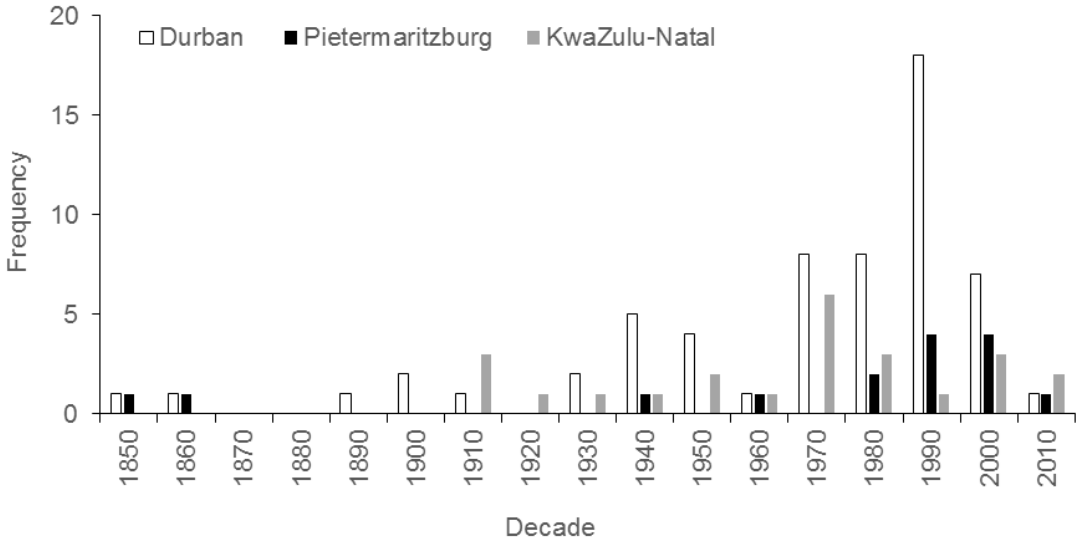


**Figure 2.3.2:** Recorded flood frequency for Durban, Pietermaritzburg and the KwaZulu-Natal region.

Although the data used for Figure 2.3.2 does not provide the opportunity to assess regional variations in flood frequency, some of the recorded events may prove useful when determining the extent of the flooding highlighted by the more complete Mfolozi records. As such, flood records from Durban, Pietermaritzburg and KwaZulu-Natal that detail fatalities, damage to property and associated storm events, have been isolated in Table 2.3.2. For this process records from Mpumalanga (region bordering the northwest of KwaZulu-Natal) were also included as events associated with tropical storms were more consistently recorded.

**Table 2.3.2:** Flood event years with associated damages, fatalities or storms (*Date (Storm Name)).*

| Durban | Pietermaritzburg | KwaZulu-Natal | Mpumalanga |
|---|---|---|---|
| 1917 | 1947 | 1918 | 1958 |
| 1947 | 1987 | 1925 | *1960 (Brigitte)* |
| 1959 | 1995 | 1937 | *1966 (Claude)* |
| 1976 | 1999 | *1972 (Euginie)* | *1972 (Euginie)* |
| *1980 (Kolia)* | 2005 | *1976 (Danae)* | *1976 (Danae)* |
| 1988 | 2009 | *1977 (Emilie)* | *1977 (Emilie)* |
| 1997 | | *1984 (Domoina)* | *1984 (Domoina)* |
| 1999 | | *1984 (Imboa)* | 1985 |
| 2003 | | 2008 | 1996 |
| 2008 | | | *2000 (Eline)* |
| 2011 | | | 2000 |
| | | | 2012 |

From Table 2.3.2 it appears that flooding associated with tropical storms occurs simultaneously across both KwaZulu-Natal and Mpumalanga. However, floods associated with other processes display great temporal variations. A period of intense frequent flooding appears to have impacted eastern South Africa between 1972 and 1984. This is most likely to have been driven by the presence of a strong SST dipole between the Mozambique Channel and Central Indian Ocean, forcing heavy rainfall from 1975 to 1984 (Neumann *et al.,* 2010). The greater distance of Pietermaritzburg to the coast, could be an underlying factor as to why it has fewer floods and why fewer appear to correspond with the other observed areas. It is also interesting to note that the 1987 cut-off low is not highlighted in the SAWS flood data, further highlighting the issue of record fragmentation for this region of South Africa.

Most climate-related historical records for eastern regions of South Africa appear to be restricted to the 20$^{th}$ and 21$^{st}$ centuries. In other climate-related studies some authors have attempted to use ship records in order to reconstruct palaeoclimatic changes (e.g. Jones & Salmon, 2005). Given the

Dutch and British colonial past of South Africa, the potential of ship records was briefly explored. The CLIWOC (2007) database provides access to digitised global ship observations recorded between 1750 and 1854. The full extent of the database is described by Garcia-Herrera *et al.* (2005), but weather conditions are provided within the database, including observations of gusts, rainfall, hail and thunderstorms.

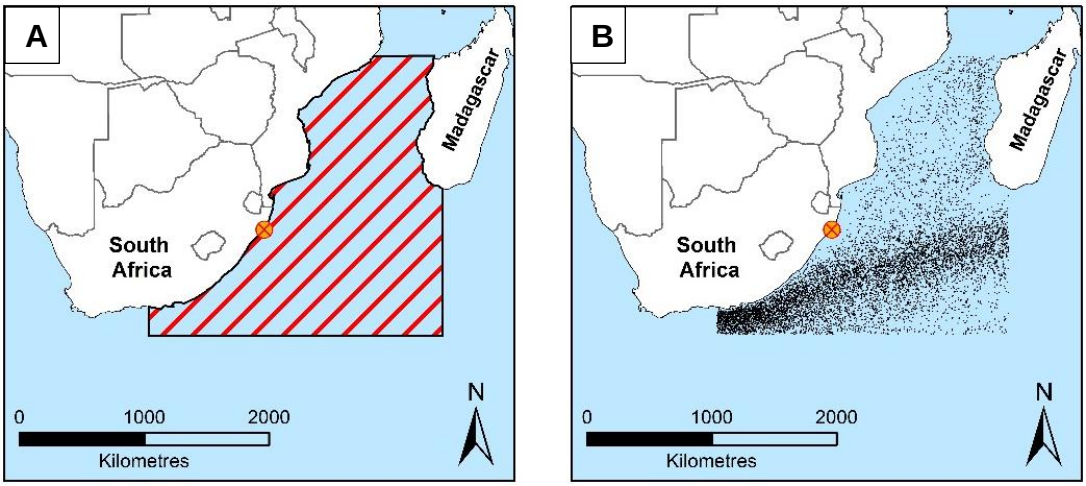


**Figure 2.3.3:** CLIWOC filtered data: A) Selected area, B) Isolated ship records.

For the purpose of this research an area off the eastern coast of South Africa was selected (Figure 2.3.3A) in the anticipation that ocean-derived storm systems influencing the coastline could be captured. A total of 8241 records were observed within the highlighted area (Figure 2.3.3B), which were further refined to records observing gusts (449), rainfall (1080), hail (20) and thunderstorms (450). Although this database provides a large volume of observations, as there are no historical records from the mainland it would be very speculative to associate any young age estimates from the Mfolozi sediments with any of the CLIWOC observations, especially given the typical errors associated with OSL and that the spatial distribution of observations is driven by shipping routes.

*2.3.2. Catchment and Adjacent Areas*

Rainfall data from regional stations was also obtained from SAWS (pers. comm.). The most complete records from the area came from stations located within 100 km of the Mfolozi floodplain. The selected stations; Kwambonambi, Mpila and Mahlabatini all include data from 1970 to 2014 with no observed gaps. Although other rainfall stations were available within close proximity to the Mfolozi floodplain, all had missing data for monthly rainfall averages and only had coverage spanning back to 1980.

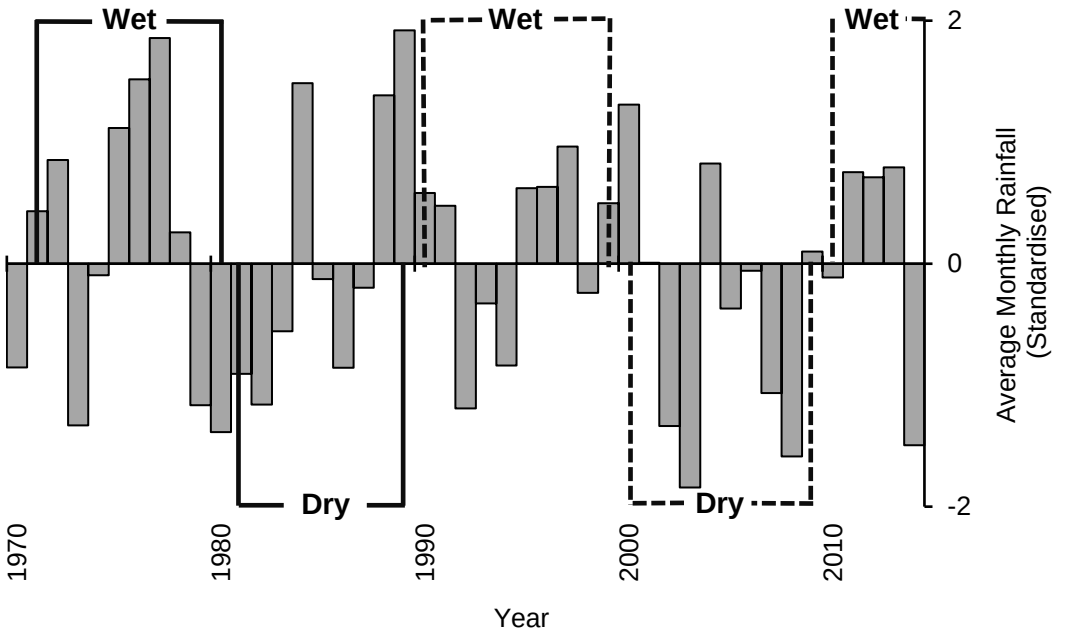


**Figure: 2.3.4:** Standardised average monthly rainfall for winter (October-March). Rainfall stations include: Kwambonambi, Mpila and Mahlabatini (Source: SAWS, pers. comm.). Wet and dry spells (solid lines) adapted from Tyson & Preston-Whyte (2000) – dashed lines represent projected spells.

Winter rainfall from the selected stations closely match the wet and dry spells observed over South Africa (Figure 2.3.4). Although there are anomalies within each of the spells, the total number of wet or dry years outnumber each other in the respective seasons. As observed in the previous section, the dry spell spanning 1981/82 to 1989/90 displays significant anomalies. This includes the 1984 regional rainfall peak, which could be associated with

the occurrence of Tropical Storm Domoina. As with the regional trends, the data used for Figure 2.3.4 does not display any significant changes in overall rainfall for the selected time interval.

To identify any events that had potentially been missed by the regional SAWS data, flood records from locations closer to the Mfolozi floodplain (displayed in Figure 2.3.1) were explored. Floods with associated damages, fatalities and tropical storms were isolated and are provided in Table 2.3.3. Unlike the regional data the 1987 cut-off low, which was one of the most devastating events to impact the region, was recorded in St Lucia.

**Table 2.3.3:** Flood events with associated; damages, fatalities or storms (Source: SAWS, pers. comm.).

| Year | Area | Reported Damages? | Reported Fatalities? | Associated Storm |
|---|---|---|---|---|
| 1940 | Eshowe | No | Yes | N/A |
| 1956 | Eshowe | No | Yes | N/A |
| 1985 | Hluhluwe | Yes | No | N/A |
| 1987 | St Lucia | Yes | Yes | Cut-Off Low |
| 1993 | Hluhluwe | Yes | Yes | N/A |
| 1997 | Richards Bay | No | No | Tropical Cyclone Gretelle |
| 1998 | Hluhluwe | No | Yes | N/A |
| 2000 | Mkuze | Yes | No | N/A |

Flood records for both the region and areas adjacent to the Mfolozi catchment appear to display a significant increase in reported flooding, particularly since the 1970s. However, it is difficult to decipher whether this is a function of better monitoring/reporting or an actual trend. Fortunately the presence of the sugar cane plantation upon the Mfolozi floodplain means that flooding of the Mfolozi River has been monitored since 1911 and a continuous record is available (Figure 2.3.5).

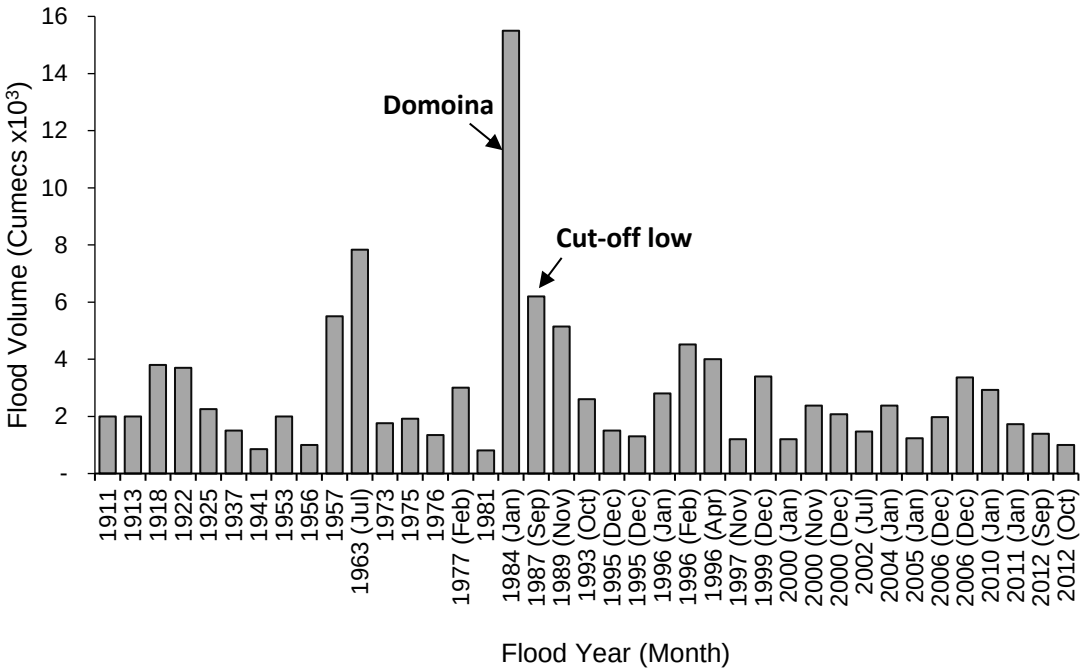


**Figure 2.3.5:** Flood occurrence and volume upon the Mfolozi floodplain 1911-2013 (Data courtesy of: The Umfolozi Sugar Mill, pers.com)

The Mfolozi flood records (Figure 2.3.5) highlight the significance of the 1984 flooding associated with Tropical Storm Domoina, with total flood water volume almost double that of the next largest event (1963). Three large flood events in 1957, 1963 and 1984 coincided with increased tropical cyclone activity off the coast of eastern South Africa (Umfolozi Sugar Mill, pers. comm.). Between 1911 and 1969 the floodplain experienced between one and three floods per-decade. This increased to four and then eight flood events for 1970-1989 and 1990-2009, respectively. This suggests that the trend of increased flood frequency in recent decades, exhibited by other regional records, could be representative.

## 2.4. Holocene Environmental Change

Existing work from two marginal lakes upon the Mfolozi (Futululu and Teza) indicate that lacustrine basin-derived chronologies will span the Holocene (Neumann *et al.,* 2010). For blocked valley lakes this is likely to be restricted

to the latter half of this epoch (Grenfell *et al.,* 2010). As such, the environmental change for the whole of the Holocene is discussed. Although the volume of palaeoenvironmental research is increasing for eastern South Africa, some aspects of environmental change remain poorly understood, particularly through the mid- to late-Holocene (e.g. Humphries *et al.,* 2016). Discussion of Holocene environmental change will therefore draw upon key studies both from within and outside of this region (Figure 2.4.1).

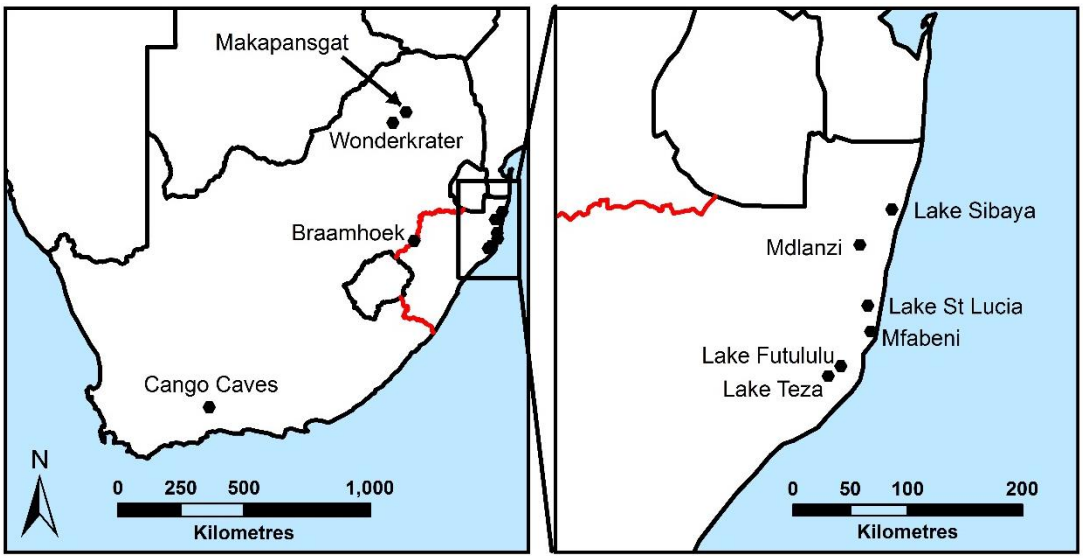


**Figure 2.4.1:** Location of key study sites

*2.4.1. South Africa*

For many South African palaeoenvironmental studies, speleothem records remain a primary proxy for inter-comparison. Isotope analysis of speleothems enables the reconstruction of past temperatures through observation of Oxygen-18 fluctuations ($\delta^{18}O$), whilst past vegetation changes can also be inferred through exploring fluctuations in Carbon-13 ($\delta^{13}C$). Typically, samples from speleothems are chronicled using a combination of Uranium-series dating and Carbon isotope analysis. Talma & Vogel (1992) conducted some of the initial work in South Africa upon speleothems collected from Cango Caves in the Western Cape Province. The samples collected from this site extended to 30 ka, however, stalagmite growth ceased between 13.8 and

5 ka, providing no coverage of the first half of the Holocene. Temperature reconstruction from the Cango Cave speleothems revealed relatively little variation throughout the mid- to late-Holocene, with temperatures not surpassing +1 or -2°C (Figure 2.4.2). However, significant increases in $\delta^{13}C$ occurred after 5 ka and have been attributed to a higher localised coverage of $C_4$ grasses (Talma & Vogel, 1992). As $C_4$ grasses are typically suited to high radiation and warm growing seasons, increases in $\delta^{13}C$ can be indicative of changes in temperature, moisture and rainfall seasonality (Holmgren *et al.,* 2003). Given that the Holocene temperature curve from the Cango Cave site displayed little variation, Talma & Vogel (1992) attributed the $\delta^{13}C$ increase to a shift in seasonality producing a winter rainfall regime.

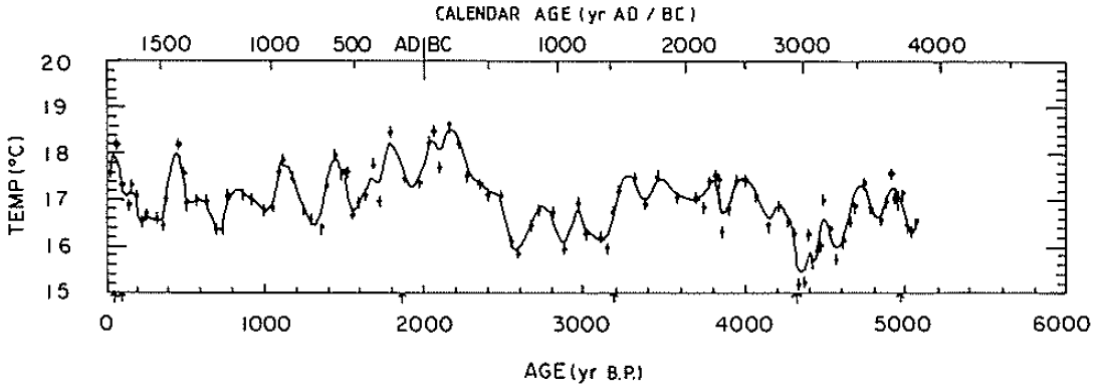


**Figure 2.4.2:** Reconstructed temperatures for the mid- to late-Holocene, derived from Cango Cave speleothems (From: Talma & Vogel, 1992)

Although the Cango Cave speleothems highlight the significant temperature difference between present day and the Last Glacial Maximum, where temperatures were 5-7°C cooler (Talma & Vogel, 1992), environmental reconstruction for the Holocene is somewhat restricted owing to the coarse sampling resolution and incomplete record. Subsequent work by Holmgren *et al.* (2003) upon speleothems from the Makapansgat valley, Limpopo province, provides a record that extends from the present day to 25 ka and incorporates a large proportion of the Holocene. Generation of the Makapansgat speleothem record was staggered (Repinski *et al.,* 1999;

Holmgren *et al.,* 1999; Lee-Thorp *et al.,* 2001; Holmgren, 2003) and utilised three different stalagmites (T5, T7 & T8).

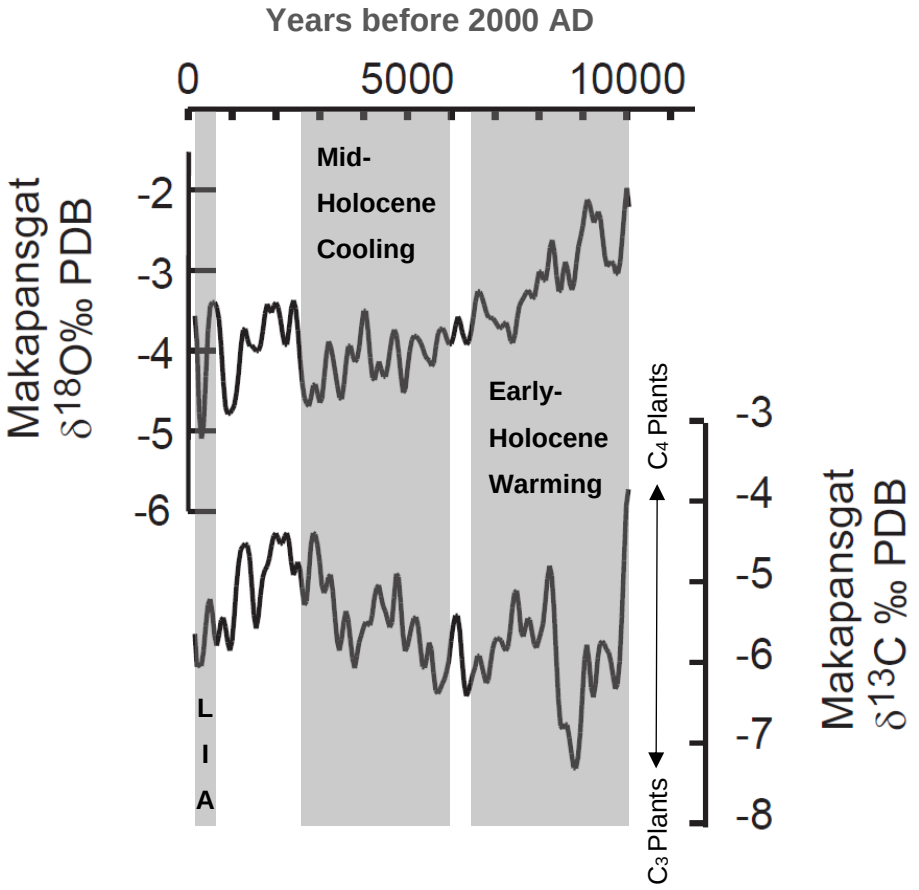


**Figure 2.4.3:** Holocene $\delta^{18}O$ and $\delta^{13}C$ levels derived from the Makapansgat T8 speleothem – LIA represents the Little Ice Age (From: Holmgren *et al.,* 2003)

The most recent work upon the T8 stalagmite provides the most comprehensive coverage of the Holocene (present day to 10.2 ka), providing a ~9-year resolution record that closely agrees with $\delta^{18}O$ patterns observed in the Taylor Dome Antarctic ice-cores (Steig *et al.,* 2000). Holmgren *et al.* (2003) observed a number of significant Holocene climatic phases, the first of these occurred from 10.2 to 6 ka, an 'Early-Holocene Warming'. Despite the overall decreasing trend, here $^{18}O$ levels were much higher than the present day (Figure 2.4.3) indicating warmer conditions. The sharp decrease in $\delta^{13}C$

within this phase suggests a decrease in $C_4$ grasses and in combination with low observed organic contents, the climate was interpreted as being relatively arid. Although not highlighted within Figure 2.4.3, between 6 and 8 ka a peak in warm temperatures, described as the Holocene Altithermal, has been observed across Southern Africa. The effects of this high-stand are variable between localities (Partridge *et al.,* 1999) and are discussed further in Section 2.4.2.

Between 6 and 2.5 ka a gradual mid-Holocene cooling is observed within the T8 speleothem, with $\delta^{13}C$ indicating significant increase in grasses between 3 and 2.5 ka (Holmgren *et al.,* 2003). Following this, warm phases were observed between 2.5 to 1 ka and 1000 to 1300 AD, the latter of which is associated with the medieval warming period (MWP). One of the sharpest Holocene declines observed in both $\delta^{18}O$ and $\delta^{13}C$ is centred upon 1700 AD and is associated with the Little Ice Age (LIA). From the isotopic analysis, it is estimated that during the MWP the regional climate was over 3°C warmer than the present day, whilst during the LIA it is believed to have been around 1°C cooler (Tyson *et al.,* 2000). In areas of western KwaZulu-Natal these abrupt late-Holocene climate swings have been associated with destabilisation of land surfaces and the onset of an erosional phase (Lyons *et al.,* 2013). With the exception of the LIA and MWP, Holmgren *et al.* (2003) suggests that a general pattern of cooling was observed following 1 ka.

A large proportion of the findings from the Makapansgat speleothems are discussed in conjunction with palynological sequences from the Wonderkrater thermal spring sediments, also situated in the Limpopo Province. Initial work from Wonderkrater highlighted the preservation of pollen within continuous peat sequences spanning to *c.* 35 ka (Scott, 1982). Based on the pollen assemblages found in the initial study, Scott & Thackeray (1987) provide an overview of the climatic interpretations, relative to the present day. For the Pleistocene-Holocene transition they observe a wetter and much cooler climate (5 to 6°C) until 9.5 ka where cool conditions prevailed but a much drier climate was experienced, marked by a reduction in montane forested areas. These initial two phases are not comparable with the Makapansgat speleothem records owing to their hiatus between 10.2 and

12.7 ka. From 9.5 ka to 6 ka Scott & Thackeray (1987) note a warm climate with savannah pollen assemblages indicating a drier environment, this broadly corresponding to the early-Holocene warming proposed by Holmgren *et al.* (2003). Between 6 and 4 ka a similar climate to the present is observed and is followed by cooler, wetter conditions until 2 ka, indicated by upland bushveld plant species occupying the area. From 2 ka to the present, conditions are described as remaining relatively stable, with the potential of a slightly wetter period between 1 and 2 ka. More recently, Scott *et al.* (2003) have revisited the pollen assemblages from Wonderkrater and have constructed temperature and moisture indices for the site. Although these do not follow the same pattern as the speleothem records precisely, they display similar trends and draw common inferences. However, Scott *et al.* (2003) also note that the most recent sediments from this site were sampled at a much lower resolution, so interpretations for the past 2 ka should be accepted tentatively.

Although climatic trends and abrupt changes can be observed within speleothem and pollen records, there can be significant regional differences in the effects of Holocene climatic shifts. The Younger Dryas which is observed in the Northern Hemisphere at the Pleistocene-Holocene boundary, offers further complexity as speleothem offer no data for this period and pollen records from across the interior of South Africa display inconsistencies between moisture and temperature indices (Scott *et al.,* 1995). It is therefore necessary to focus discussion of Holocene climatic change upon KwaZulu-Natal to examine the likely conditions experienced by the Mfolozi floodplain.

### *2.4.2. Regional Observations*

A large proportion of the palaeoenvironmental reconstructions for coastal regions of KwaZulu-Natal utilise wetland and lacustrine basins. In cases where authors have continuous proxy data, particularly for pollen sequences, climatic phases are often isolated and discussed independently. For consistency, Holocene phases similar to those highlighted by work upon Lake Teza (Neumann *et al.,* 2010), a marginal lake upon the western side of

the Mfolozi-Msunduze floodplain, have been adopted for discussion here. Phases include the Early Holocene (11-6.8 ka), Mid-Holocene (6.8-3.6 ka) and Late Holocene (3.6 ka - present). As the Lake Teza record only extends to 10.2 ka an additional phase spanning the Pleistocene-Holocene transition (17.5-11 ka), as observed in the neighbouring Mfabeni wetland (Finch & Hill, 2008), has been incorporated.

Prior to discussing the observed Holocene changes it is beneficial to highlight the availability of a SST curve for the Mozambique Channel (Figure 2.4.4) produced by Bard *et al.* (1997). The alkenone marine record (core MD79257) spans from the present day to 45 ka and is used in some of the subsequent studies to draw climatic inferences. With sea-level change acting as an important driver of blocked-valley lake formation upon the Mfolozi floodplain (Grenfell *et al.,* 2010), it is also important to note the availability of sea-level curves for the region. Ramsay (1995) produced an initial curve covering a majority of the Holocene (Figure 2.4.5), which was subsequently extended into the Pleistocene by Ramsay & Cooper (2002).

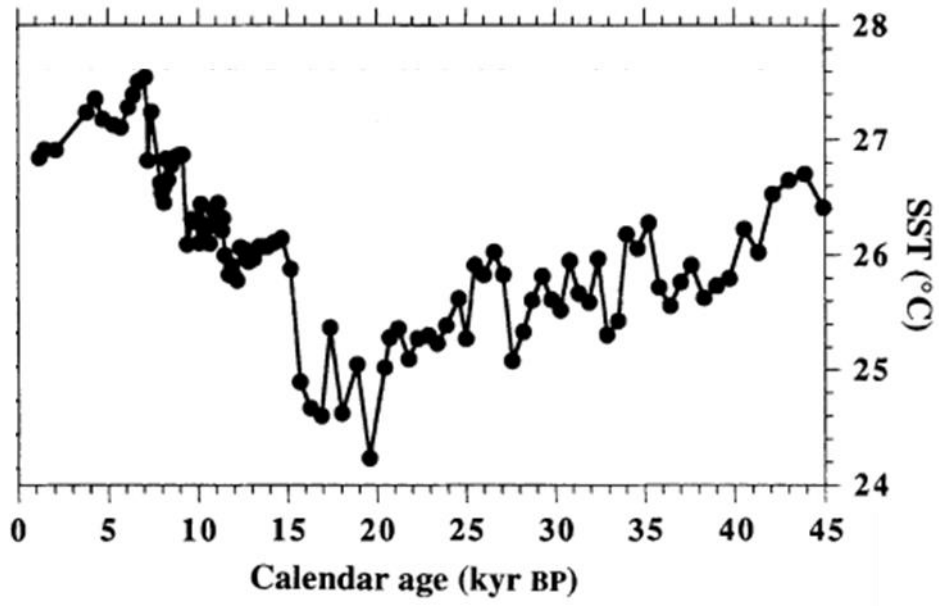


**Figure 2.4.4:** Mozambique Channel sea surface temperature curve derived from the alkenone marine record of core MD79257 (Source: Bard *et al.* 1997)

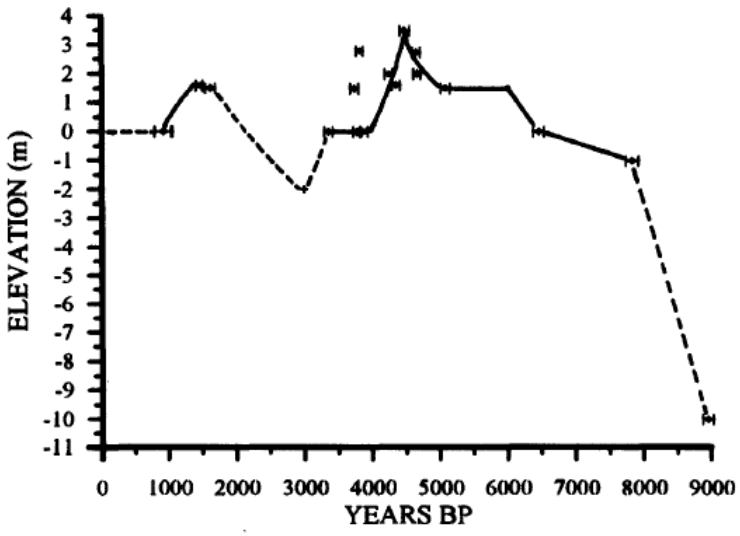


**Figure 2.4.5:** Sea-level curve for Coastal South Africa, derived from beach rocks and $^{14}C$ ages (from: Ramsay, 1995)

*Pleistocene-Holocene transition (17.5-11 ka)*

The Pleistocene-Holocene transition pre-dates existing basin work upon the Mfolozi floodplain. However, the inter-dune Mfabeni wetland on the margins of the neighbouring Lake St Lucia, had been accumulating peat since 44-47 ka owing to a period of coastal dune stability and higher groundwater levels (Porat & Botha, 2008). Baker *et al.* (2014) observed a cool, dry climate for the Mfabeni wetland until 14.3-10.8 ka, where a period of increased precipitation and waterlogging is indicated by a significant increase in total organic carbon. Within the same wetland Finch & Hill (2008) note a cool dry climate with the dominance of grass (*Poaceae*) throughout this period and also point to an increase in moisture at the Holocene boundary with the establishment of tree stands (*Podocarpus*). A consistent pattern is observed inland at the Braamhoek wetland, located at the KwaZulu-Natal/Free State border. Charcoal within sequences suggests a high number of fires between 15-13.5 ka, which then reduces significantly after this period (Norström *et al.,* 2009). Coupled with the dominance of *Poaceae* and little evidence of *Podocarpus* within pollen sequences, the changes at Braamhoek also suggest a cool, dry climate that became relatively moist.

SST in the Mozambique Channel record a significant increase of *c.* 1.5°C between 17 and 14 ka, which is followed by a steady decrease (*c.* 0.4°C)

towards the initiation of the Holocene (Figure 2.4.4). The relatively warm SST towards the end of this period coincides with the moist conditions observed in KwaZulu-Natal. Sea-level rose throughout this period with changes of >35 m proposed (Ramsay & Cooper, 2002).

*Early Holocene (11-6.8 ka)*

Throughout the Early Holocene sea levels continued to rise until reaching the Holocene high-stand at *c.* 6.5 ka. This acted as an important phase for the Mfolozi floodplain as a rise in base level initiated a shift from fluvial incision to a period of deposition upon the floodplain (Grenfell *et al.,* 2010). The lake Teza record starts at 10.2 ka and is characterised by fluvial sediments until 7.2 ka where accumulation rates indicate a shift towards a lacustrine environment (Neumann *et al.,* 2010). Pollen analysis upon the Teza sequence indicates relatively warm temperatures and wet conditions between 10.2 and 8 ka, with seasonal grassland and palm tree (*Phoenix*) stands dominating the area. From 8-7 ka a progressively arid environment is interpreted at Teza, with *Poaceae* dominating and a loss of tree stands. At Mfabeni Finch & Hall (2008) suggest cool and wet conditions were experienced at 11 ka with *Podocarpus* forests expanding rapidly. Subsequently they note a shift towards a warm and moist climate, indicated by continued forest coverage and the dominance of 'swampy' vegetation (*Cyperaceae*) between 8 and 6 ka, a period representing the Holocene Altithermal. An additional feature at Mfabeni is the presence of an abrupt cooling event at 7 ka where carbon accumulation displays a significant disturbance (Baker *et al.,* 2014). In western KwaZulu-Natal the Braamhoek wetlands observe an increase in wetland species (e.g. *Phragmites*) between 10.6 and 9.7 ka, marking a cool and wet environment (Norström et al., 2009). Following this, increased fire activity and loss of wetland species suggests warm and dry conditions with localised desiccation, however, at 8 ka a cool/wet event is observed.

SST for the early-Holocene also display a general pattern of warming. It is interesting to note that a deviation from this trend can be seen and is centred

between 8 and 7 ka (Figure 2.4.4), corresponding to the observations of a cool event at Braamhoek and Mfabeni.

*Mid-Holocene (6.8-3.6 ka)*

Throughout the mid-Holocene sea-levels remained high and influenced many of the coastal basins with higher water tables being recorded. Lake Teza for example records a high abundance of species associated with mangrove and swamp forest vegetation. From 6.8 ka Teza observed a loss of grassland coverage and an increase in tree pollen (*Phoenix & Podocarpus*) which indicates a shift towards warm and wet conditions, with *Phoenix* pollen peaking at 5.5 ka (Neumann *et al.,* 2010) at the tail-end of the Holocene Altithermal. A similar warm mid-Holocene phase is represented at Lake Sibaya, northern KwaZulu-Natal (Neumann *et al.,* 2008). The appearance of freshwater mollusc species at Lake Teza from 4.7 ka coincides with a lowering of sea-level to an elevation similar to the present day along the eastern coast of South Africa (Figure 2.4.5), indicating reduced influence of tidal patterns upon the catchment. Following this retreat, Lake Futululu became fully impounded by the aggrading Mfolozi River at around 4 ka, producing an environment suitable for *Cyperus papyrus* and peat formation (Grenfell *et al.,* 2010).

From 6 ka the Mfabeni wetland highlights a significant decline in *Podocarpus* abundance and a return of grassland species (Finch & Hill, 2008), indicating a cooling and dry phase for the region. Baker *et al*. (2014) infer a higher presence of sedges up until 6 ka and suggest the occurrence of a short-lived wet period prior to a cooling event centred on 5.3 ka, indicated by a significant trough in total organic carbon. A more recent study from the Mfabeni wetland indicates an increased phase of aeolian activity between 6 and 4 ka (Humphries *et al.,* 2016a), further supporting the occurrence of a cool event in this region. Similarly the Braamhoek wetlands observe conditions attributable to a cool and dry climatic phase between 7.5 and 2.5 ka, with high fire frequencies and low organic accumulation rates (Norström et al., 2009).

SST in the Mozambique Channel for this period (Figure 2.4.4) records a peak between 7 and 6.5 ka. This is followed by a cooling phase between 6.5 and 5 ka, corresponding to the cooling events observed across some wetlands. SST display another smaller peak at *c.* 4 ka which is followed by a period of cooling until 1 ka (Figure 2.4.4).

*Late Holocene (3.6 ka - present)*

For the initial part of this phase (3.6-2 ka) Lake Teza records a rapid decline in *Podocarpus* abundance and a recovery of grasslands suggesting a savannah-like arid environment. This corresponds to a globally-recognised neoglacial event from 3.5-2.5 ka (Mayewski *et al.,* 2004). A similar phase of drying occurs at 0.7 ka and is indicated by significant vegetation changes. The surrounding area experiences desiccation with swamp and tree species displaying significant decline. Although this dry phase coincides with the LIA Neumann *et al.* (2010) highlight that climatic events are difficult to interpret for this period owing to increased human activity in the region from the Iron Age onwards. Despite this, observations of LIA desiccation coincides with a period of reduced rainfall signalled in a dendroclimatological record from the KwaZulu-Natal midlands (Vogel *et al.,* 2001), reaffirming the Teza record.

Upon the same floodplain the occurrence of a neoglacial period is also highlighted within the Lake Futululu basin. Desiccation of the peat environment and the occurrence of a large fire is indicated by a charcoal layer preserved amongst peat deposits which dates to 2.06 ka (Grenfell *et al.,* 2010). Although there is a slight lag, this still associates with the dry conditions during this period. The sequence examined by Grenfell *et al.* (2010) at Lake Futululu is predominantly formed of peat, however, some clastic layers that are attributed to flood events are recorded at 1700, 1470, 700, 550 and 180 years BP. The authors were unable to attribute the increased flood frequency to climatic change or influences of the main river channel.

At the Mfabeni wetland, the dominance of wetland sedge species and increase in organic carbon within the sequence marks a return to warm,

moist conditions until 3 ka. There are discrepancies after 3 ka between the two studies at Mfabeni. Finch and Hill (2008) noted an increase in savannah grassland pollen and infer a regionally cooler climate from 3 ka until the present, with anthropogenic practices (since 5 ka) leading to the reduction of observed *Podocarpus* pollen in their profile. However, Baker *et al.* (2014) provide a less straightforward scenario and suggest an overall warm/moist trend from 3 ka to the present, with the exception of an abrupt cooling/drying event at 1.4 ka. Recent work on the adjacent Lake St Lucia highlights a significant ENSO-related desiccation event between 1.7 and 1.1 ka (Humphries *et al.,* 2017), which could correspond to the cooling/drying event suggested by Baker *et al.* (2014). Further support for this proposal comes from the Braamhoek wetland, where the dominance of wetland vegetation and presence of grasses indicate warm humid conditions for this phase, with an increase in organic accumulation rate following 1.5 ka (Norström et al., 2009).

*Overview*

For a majority of the climatic/pollen zones, there appears to be a general consistency across the reconstructed environmental records. In some cases there appears to be some lag between the climatic signals, as displayed by the mid-Holocene warming phase at Lake Teza that appears to have occurred at the end of the Holocene Altithermal. However, some slight temporal discrepancies would be expected between localities. The regional observations appear to tie-in with the general pattern highlighted by speleothem records. However, the observed localised changes incorporate more subtle climatic swings (e.g. 7.1, 5.3 and 1.4 ka cooling events) which may not be detected outside of the region. As with upper units of the discussed profiles, the younger wetlands of the coastal KwaZulu-Natal, including the Mdlanzi swamp (Turner & Plater, 2004) and Lake Sibaya (Neumann *et al.,* 2008) provide sequences whose climatic signals are difficult to unpick, predominantly because of human disturbance. This problem appears to have occurred at the Mfabeni site with two contrasting scenarios for the period spanning 3 ka to the present day.

## 2.5. Sampling Strategy

Fieldwork was conducted in July 2014, during which three different sampling sites (Futululu, UCOSP and South Lake) were established across the Mfolozi floodplain (Figure 2.5.1).

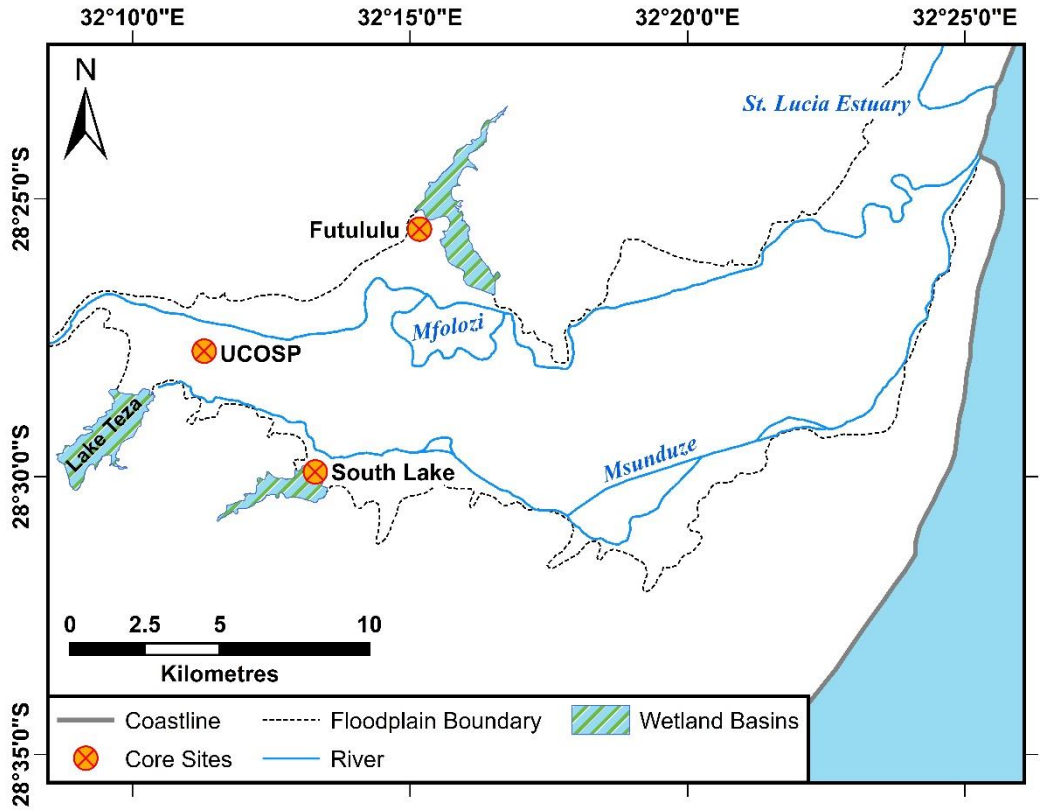


**Figure 2.5.1:** Core site locations upon the Mfolozi floodplain

### *2.5.1. South Lake*

The South Lake core site (S 28° 29' 55.3", E 32° 13' 17.7") is situated within a blocked-valley lake wetland on the southern margin of the Mfolozi floodplain. Test gouge core samples from the basin highlighted the presence of both organic ("peaty") and clastic units within the upper 1-2 meters of the basin's profile. This potentially represented a similar flood-driven sedimentology to that ascribed to Lake Futululu by Grenfell *et al.* (2010). The South Lake site was chosen to produce the age estimates for the blocked-valley lake palaeoflood chronology in this study. Evaluation of OSL for use in this environment focussed predominantly on age estimates from this site, owing to the inaccessibility of other blocked-valley lake basins across the

catchment during fieldwork. A vibracoring system and aluminium core tubes (76 mm diameter) were used to collect core samples for OSL analysis (Figure 2.5.2). A coring depth of 5.68 m below the contemporary land surface was achieved.

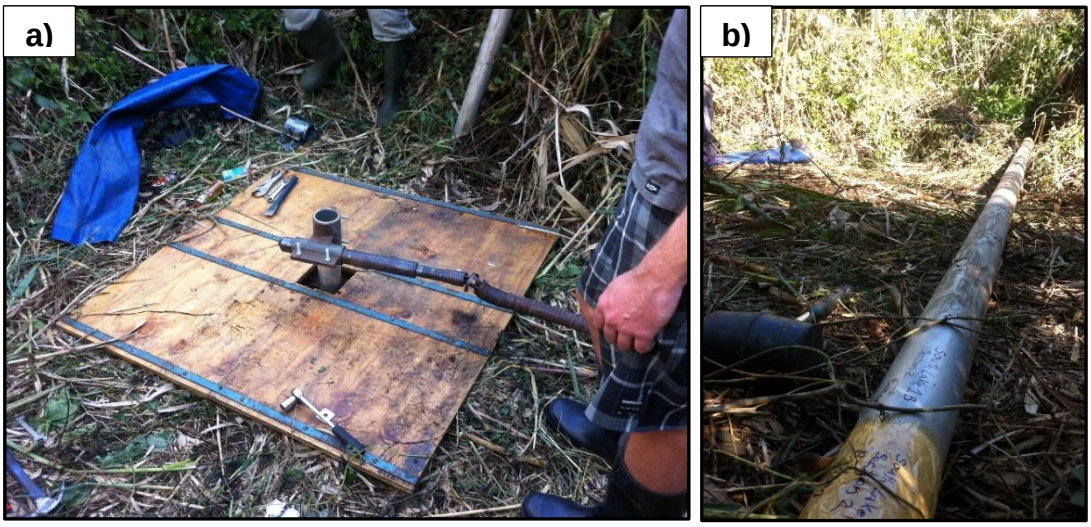


**Figure 2.5.2: a)** Aluminium core tubing with vibracorer attached, **b)** retrieved South Lake core sample

*2.5.2. UCOSP*

The centrally located UCOSP site (S 28° 27’ 44.9”, E 32° 11’ 17.6”) featured an exposed section (Figure 2.5.3), comprised of sediments from three large flood events which were recorded by the Umfolozi Sugar Mill (pers.comm; 2015). The flood events associated with the sedimentary units occurred in 1925, 1963 and 1984, with the most recent being from Tropical Cyclone Domoina. The presence of sediments of known age enables this site to act as a modern analogue, from which the likely resolution of OSL palaeoflood chronologies can be assessed. The UCOSP site also provides chronostratigraphic comparisons with the South Lake site, which would help to verify the accuracy of age models and to distinguish between localised and floodplain-scale flooding. The location of the UCOSP site is also highlighted earlier in this chapter in Figure 2.2.3. It can be seen that the site is positioned directly upon flood units created by the avulsion of the Mfolozi River.

Samples from the UCOSP site were collected from the vertical section in short aluminium core tubes. A vibracore sample was also collected at the base of the section. The basal core collected material from a depth of 4.8 to 9.1 m below the contemporary land surface.

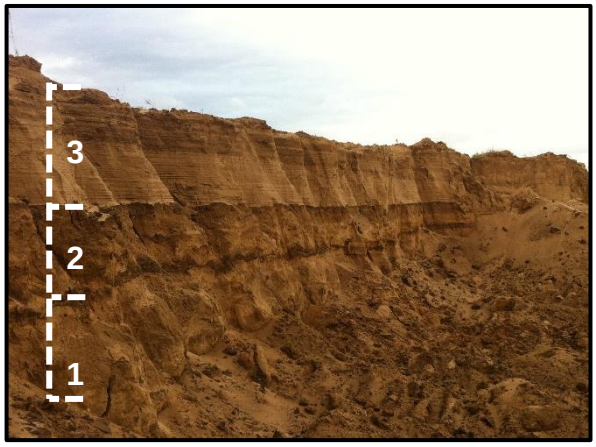


**Figure 2.5.3:** Three recent flood deposits (1925 - unit 1, 1963 – unit 2 and 1984 – unit 3) recorded by the UCOSP section. Depth of section: 2.2 m.

*2.5.3. Futululu*

The final sampling site was situated on the northern reaches of the floodplain upon the margin of Lake Futululu (S 28° 25’ 33.1”, E 32° 15’ 10.4”). The coring site sat upon a crevasse splay feature which had protruded into the Futululu basin. Aerial photographs indicate that this feature had been present since 1937. The crevasse splay is believed to have been created by breaches of the Mfolozi River levee following large flood events. The Futululu site was selected to provide a chronostratigraphic comparison for the blocked-valley lake palaeoflood chronology, enabling the consistency of OSL dating across the floodplain to be evaluated. Samples for OSL analysis were collected at this site using a Cobra corer and plastic sleeves (48 mm diameter). Material was collected from the contemporary land surface to a depth of 4 m.

## 2.6. Composition of Core Samples and OSL Sampling

To preserve the natural luminescence signal within the collected material, core lengths were opened under subdued red lighting conditions provided by Encapsulite RB-10 filters. As it was not possible to visually assess the stratigraphy of core lengths, small samples (1.25 $cm^3$) were collected at 1 cm intervals and transferred to normal lighting conditions for loss-on-ignition (LOI) and sediment logging. LOI provides a good estimate of organic content and was used to pinpoint the clastic palaeoflood units (i.e. organic poor). The combination of LOI and sediment logging reproduced the stratigraphy preserved within core lengths and provided an indication of each site's sedimentology, aiding selection of luminescence sampling locations.

During sampling it was noted that all cores contained many regions of clay-rich material; a relatively low ignition temperature (430°C) was therefore selected to avoid overestimation of organic content through the dewatering of clays. Ignition temperatures of 430°C have been shown to produce representative estimates of the total organic carbon (TOC) present within a sample (Davies, 1974; Schulte & Hopkins, 1996). A standard LOI procedure, as outlined in Wood (2015), was used to assess organic content. Retrieved core samples underwent compaction during sampling (with exception of the UCOSP samples), sample depths in this section represent distance into core samples, not depths below the contemporary ground surface

### *2.6.1. South Lake*

The South Lake site displays a relatively complex sedimentology (Figure 2.6.1a) and for ease of discussion its profile has been split into four units. With the exception of the A horizon, the uppermost unit (4) of the site is characterised predominantly by silts and clays and it remains organic-poor throughout. On occasion the matrix supports fine sands, however, at these locations silts and clays remain the dominant material. One distinct change in sedimentology is notable at 0.4-0.5 m depth, where a fine/medium sand bed is preserved.

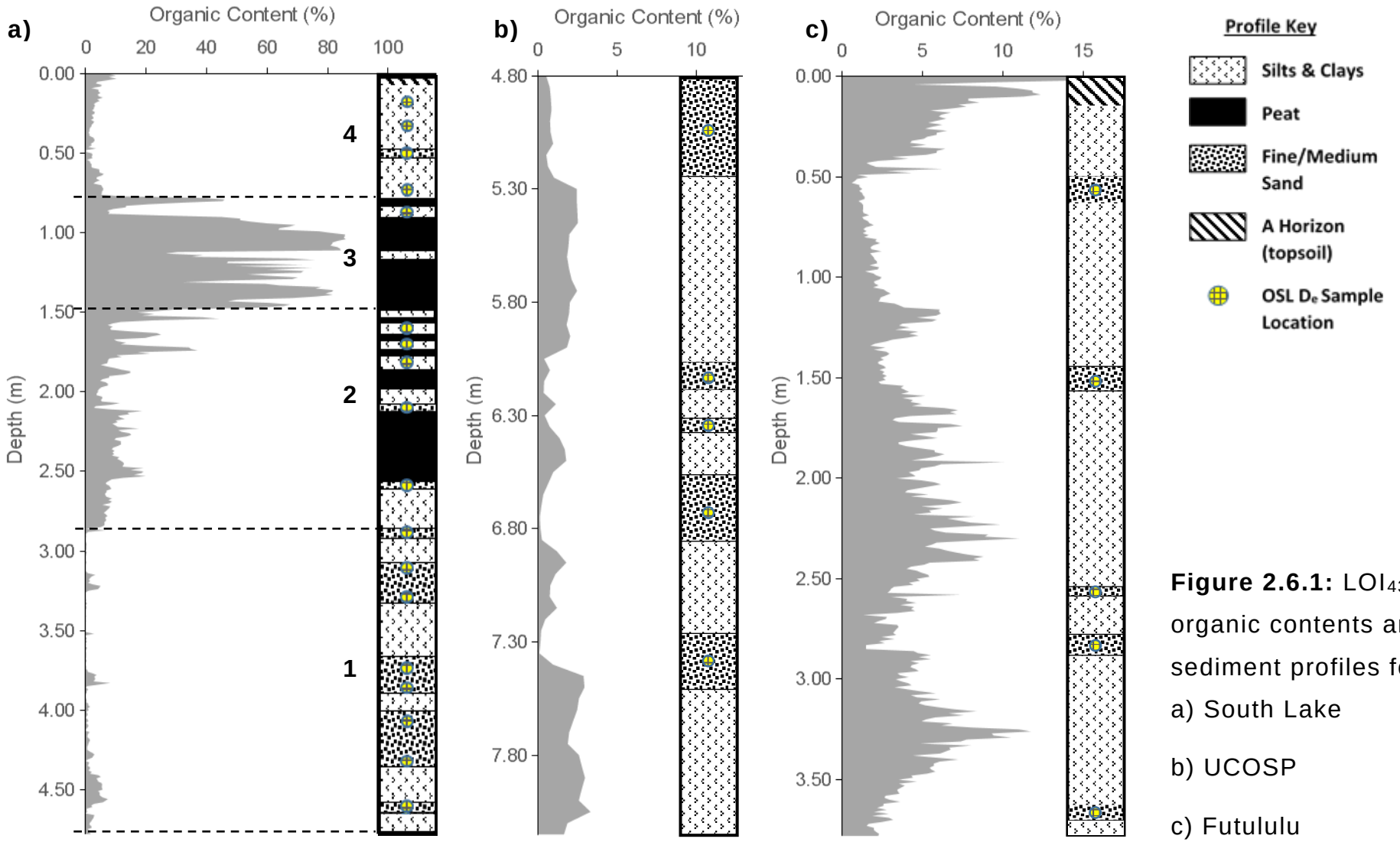


**Figure 2.6.1:** $LOI_{430}$ organic contents and sediment profiles for:
a) South Lake
b) UCOSP
c) Futululu

Unit 3 of the profile is organic rich, containing peat and well-preserved leaf and root litter (Figure 2.6.2). Within this section there are some distinct fluctuations in organic content (e.g. at 1.14 m). These are created by clastic bands preserved amongst the peat units. The clastic bands are formed of silts and clays.

Organic content may indicate that unit 2 is comprised of very different sediment to that in unit 3. However, it was noted that a similar pattern of peat and fine clastic interlamination remained. The difference in estimated organic content may have been created by a combination of more humified organics and a low ignition temperature, as humified organics tend to combust between 530 and 540°C (Boyle, 2004). Although the clastic beds within the unit are dominated by silts and clays, some fine/medium sands are incorporated within their matrix. A bed formed solely of fine/medium sands is preserved at 2.10 m.

**Figure 2.6.2**: Leaf and root litter preserver within peat units, sample taken from 1 m depth. Scale provided in Inches (upper) and cm (lower).

The lowermost unit (1) of the South Lake profile observes a transition to a clastic rich sequence, which alternates between fine/medium sand and clay rich beds. Fine/Medium sand beds occupy the majority of this part of the

profile. It is noted that some coarse sands are incorporated within the fine/medium sand beds, but again this represents a very small proportion of the matrix.

### *2.6.2. UCOSP*

The UCOSP core lengths are organic-poor and are formed almost entirely from clastic units (Figure 2.6.1b). The stratigraphy of the core lengths display a similar pattern to what can be observed in the exposed section at the site (Figure 2.5.3); that is the alternation of fine/medium sands (lighter in colour) to silt and clay beds that harbour a little organic matter (darker colour). As with the South Lake cores, some sands are incorporated within the silt and clay beds, but these also represent a small proportion of the matrix. From the basal profile it is evident that there are five distinct sand beds interspersed by the finer material; these sand beds represent Mfolozi flood/avulsion deposits.

### *2.6.3. Futululu*

The Futululu core lengths are also organic-poor and are comprised predominantly of fine silts and clays. These beds contained some organics but the overall content rarely exceeds 10% after the A-Horizon (Figure 2.6.1c). Five fine/medium sand units are preserved within core samples. The most recent of these deposits (*c.* 0.60 m) contains material that is noticeably coarser than the sand units preserved at greater depths. This could be an indication of high energy processes at the time of deposition or variations in sediment source. Similar to the avulsion deposits at the UCOSP site, the coarse sand units are interpreted as flood driven sedimentation, with the Mfolozi overtopping levees and distributing more material across the Futululu crevasse splay feature.

# Chapter 3: Optically Stimulated Luminescence Dating of Quartz

## 3.1. The Equivalent Dose

As outlined in Chapter 1, luminescence dating evaluates two values in order to produce age estimates, the equivalent dose ($D_e$) and dose rate ($D_r$). For quartz OSL dating the $D_e$ can be defined as the laboratory beta or gamma dose required to produce an OSL signal of equal intensity to the natural signal. As such, providing accurate measurement, the $D_e$ should be identical to the natural dose absorbed by quartz minerals during burial (Guérin *et al.,* 2017).

The process from which a quartz luminescence signal arises can be explained using an energy-level diagram (Figure 3.1.1). Exposure to ionising radiation (Figure 3.1.1a) separates electrons from parent nuclei within the quartz crystalline lattice, resulting in the transfer of negatively-charged electrons from the valence band to the conduction band. This loss of negative charge from the valence band creates positively charged 'holes'. Whilst the crystalline lattice remains in a non-excited state, defects within the mineral lattice of quartz grains act as 'traps' and can store 'free' charge (L & T – Figure 3.1.1b). Positively-charged traps (T) are able to store electrons whilst negatively-charged traps (L) can capture holes and act as recombination centres (Preusser *et al.,* 2009). Stimulation of quartz grains with the appropriate wavelength of light, or temperature (Figure 3.1.1c), evicts trapped electrons which diffuse around the quartz crystal until reaching a recombination centre. The recombination process is considered instantaneous and only those electrons which recombine with luminescence centres will emit photons (Aitken, 1998).

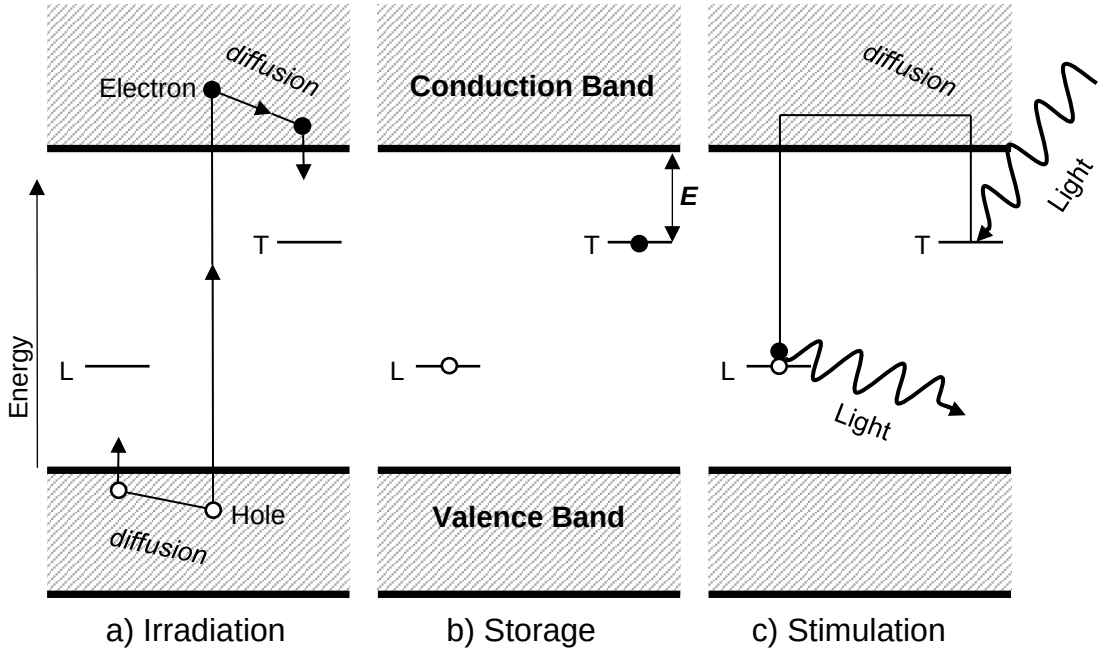


**Figure 3.1.1:** An energy-level diagram of the OSL process for the; a) irradiation, b) storage and c) stimulation of quartz trapped charge (Adapted from: Aitken, 1985).

An important value to observe in Figure 3.1.1b is the depth (***E***) of trap 'T' below the conduction band, this determines both the lifetime of electron storage within a trap and the energy that is required to evict electrons. Quartz produces TL emissions from traps of various depths (e.g. Bailey 2001); however, the OSL signal from which $D_e$ is calculated originates from a readily bleachable trap occurring at a depth of ~1.66 ± 0.03 eV below the conduction band (Murray & Wintle, 1999). Existing work confirms that the quartz OSL signal shares a trap with a TL peak at 325ºC; for example, Wintle & Murray (1997) observed the removal of the quartz 325ºC through green light exposure, whilst Wintle & Murray (1998) highlighted the reduction of the quartz OSL signal to <1% of initial values following a ramped TL stimulation from 280ºC to 330ºC. Both the OSL and TL signal from the 325ºC TL peak are considered thermally stable and at ambient temperatures have predicted lifetimes of $110 \times 10^6$ and $30 \times 10^6$ years respectively (Wintle & Murray, 2000; Wintle, 1975), far exceeding the typical OSL dating range for sedimentary quartz.

The quartz OSL signal is most effectively bleached by shorter wavelengths of the visible spectrum (Singarayer *et al.,* 2005), however, the emission spectra produced by quartz upon optical stimulation is also of a short wavelength, centred around 365 nm (near-ultraviolet – Huntley *et al.,* 1991). Careful consideration of stimulation source and filter combination is therefore required during $D_e$ assessment to ensure the natural signal can be effectively separated from the stimulation source; this is discussed further in section 3.1.3. Laboratory optical stimulation (bleaching) of quartz aliquots produces OSL signals that are observed as decay curves, similar to that shown in Figure 3.1.2. The intensity of the initial OSL signal will tend to be higher for aliquots (of similar sensitivity) that have absorbed a larger burial dose.

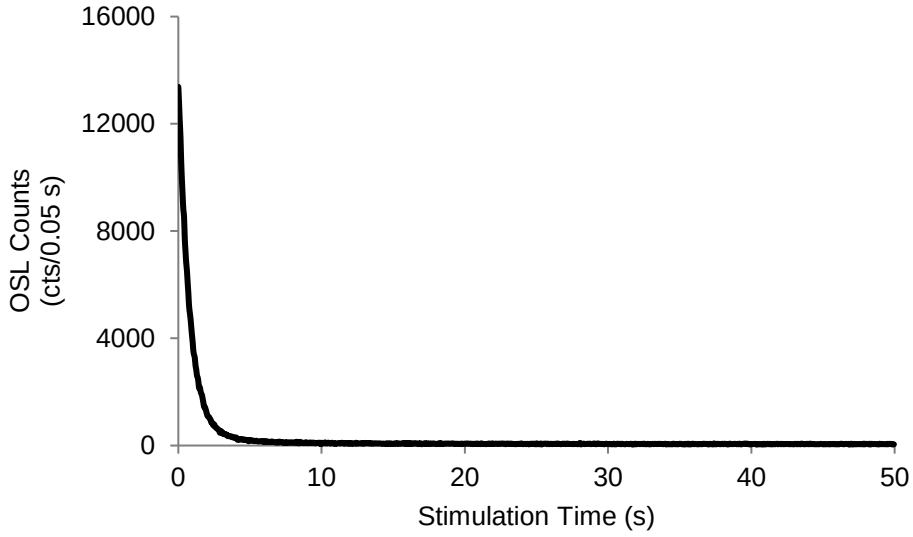


**Figure 3.1.2:** An example OSL decay curve for a multiple-grain quartz aliquot

### *3.1.1. Coarse Grain $D_e$ Preparation*

The overall aim of both coarse- and fine-grain $D_e$ preparation is to isolate a pure quartz residue from samples. Other minerals, such as feldspar, exhibit different luminescence characteristics and inclusion within measurement can hamper the accuracy of $D_e$ estimates. Coarse grain preparation is conducted upon samples that contain a fine-sand fraction (63-250 µm) and procedures have remained relatively standardised since the inception of OSL dating. All

of the $D_e$ preparation stages outlined here were conducted under subdued red lighting conditions in order to preserve the UV-sensitive luminescence properties of quartz samples.

#### *3.1.1.1 $D_e$ Sampling & Moisture Content Assessment*

$D_e$ samples were collected from preserved clastic units within core sequences. Prior to extracting sediment from core lengths for dating, the outer surfaces of cores were removed to eliminate the risk of contamination induced by the coring process. For samples taken in-section (UCOSP), the material at each end of sampling tubes was discarded and the unexposed inner material was retained for $D_e$ preparation. Samples were oven dried at 40ºC to avoid thermally-assisted bleaching of the OSL signal. To ensure that the moisture content from LOI analysis was representative, the moisture content of samples for OSL dating was also assessed through weight loss, where:

**Eqn. 3.1**

$$Moisture\ Content\ (\%) = \frac{Wet\ Mass\ (g) - \ Dry\ Mass\ (g)}{Wet\ Mass\ (g)}\ X\ 100$$

Many samples from both the South Lake and Futululu site comprised large volumes of clay. Following assessment of moisture content, clay-rich samples where soaked overnight in a 2% sodium hexametaphosphate ($(NaPO_3)_6$) solution to disaggregate the fine material. Samples were then placed in an ultrasonic bath for two minutes and rinsed at least five times with distilled water, centrifuging at 300 rpm for two minutes between rinses to flocculate the clay fraction and to retain the silt and sand fractions. The remainder of the $D_e$ samples (>5 μm) were dried prior to the next stage of preparation.

*3.1.1.2 Removal of Carbonates & Organics*

Dry samples were treated with 10% Hydrochloric acid (HCl) overnight to remove any carbonates and were given a ramped Hydrogen Peroxide ($H_2O_2$) treatment, similar to that adopted by Mauz *et al.* (2002), to remove all organic material. Samples were submersed overnight in 10% $H_2O_2$, after which the concentration of additional $H_2O_2$ was ramped to a maximum of 20% until oxidisation was complete and the material no longer reacted with further addition of $H_2O_2$.

Given the high organic content at many depths within the South Lake core, the removal of organics formed an important stage of preparation. As the $H_2O_2$ reaction with organics is exothermic, it is essential to minimise the ferocity of the reaction in order to avoid thermally-assisted depletion of the datable OSL signal in quartz. Prior to treating OSL samples, material from a hyper-organic unit of the South Lake core was used to investigate the most appropriate ramped $H_2O_2$ treatment. Four different $H_2O_2$ treatment conditions were examined for 15 g of dried organic material; 10, 15, 20% and a ramped treatment as described above. Table 3.1.1 outlines the maximum temperature reached for each treatment, although the ramped treatment did produce some thermal output, it did not exceed 50°C and accelerated the decomposition of organics in comparison to a concentration of 10%. Hence, the lighting conditions and heat produced during the ramped $H_2O_2$ pre-treatment are not considered to produce thermally assisted bleaching.

**Table 3.1.1:** Temperatures reached for four hydrogen peroxide treatments of 15 g of dry material from the South Lake Core. (*treatment preceded by 10% overnight)

| Treatment | Initial Temperature (°C) | Peak Temperature (°C) |
|---|---|---|
| 10% | 22 | 25 |
| 15% | 22 | 72 |
| 20% | 19 | 96 |
| 10-20% Ramped* | 19 | 48 |

*3.1.1.3 Grain Fraction & Mineral Isolation*

The effective dose absorbed by quartz grains varies with grain size and it is necessary to isolate discrete grain fractions to deliver precise laboratory doses for $D_e$ analysis. Samples were subsequently dry sieved to isolate the following grain fractions: 90-125, 125-180 and 180-250 µm. For samples undergoing single-grain analysis only the 125-180 and 180-250 µm grain fractions were taken forward for analysis. Standard single-grain discs for $D_e$ analysis contain 100 holes 300 µm in diameter; by using the largest grain fraction (i.e. 180-250 µm) the likelihood of having more than one grain in each of the holes and pseudo-single-grain $D_e$ values is significantly reduced. Specialist single-grain discs containing 200 µm holes were obtained for the analysis of grains in the 125-180 µm fraction.

Following sieving, quartz grains (2.65 g $cm^{-3}$) were isolated using sodium polytungstate density separations removing feldspars (<2.62 $g.cm^{-3}$) and heavy minerals (>2.68 $g.cm^{-3}$).

*3.1.1.4 Removal of the α-component*

There are four components, external to quartz, contributing to the $D_r$ value; alpha (α), beta (β), gamma ($\gamma$) and cosmic. The alpha activity within sediment is localised (*c.* 25 µm – Aitken, 1998) and is unable to completely pass through sand-sized quartz grains, penetrating only the outer *c.* 10 µm. To simplify the OSL age equation it is a standard procedure to treat quartz with concentrated Hydrofluoric acid (HF) to etch the outer α-irradiated rind of grains, eradicating the α-component from age calculation. An additional benefit of the HF treatment is that it digests feldspars, dissolving any residual low-density minerals which were unsuccessfully removed by density separation.

Early work suggested that the α-component for 90-120 µm quartz grains is reduced to negligible levels (2.5-5%) following a 40 minute HF treatment (Bell & Zimmerman, 1978). However, etching is not isotropic across the surface of grains and etching rates can vary significantly between samples (Porat et al., 2015). Although existing work has examined the changes in the physical

appearance of grains following acid treatment and the impact of HF treatment upon multi-grain $D_e$ values (Goedicke, 1984), little attention has been paid to required treatment for the 180-250 μm grain fraction and the impact of varying HF treatment upon naturally-dosed single-grain $D_e$ distributions. Chapter 4 examines the impact of various HF treatments upon single-grain $D_e$ distributions in order to isolate a suitable treatment for quartz grains within the 180-250 μm fraction.

As a result of the investigation outlined in Chapter 4, for the single-grain quartz samples from the Mfolozi floodplain 5 g of quartz was treated for 60 minutes in 100 ml of concentrated HF (40%), whilst for samples in the 90-125 and 125-180 μm fractions 5 g of material was etched for 40 minutes. Samples were agitated during treatment using an electromagnetic stirrer and were neutralised following etching. To remove acid soluble fluorides samples were then submersed in 10% HCl and rinsed with distilled water.

#### *3.1.1.5 Sample Mounting*

Samples for multi-grain measurement were mounted upon 9.7 mm aluminium discs using Viscasil oil, applied to the central 8 mm. Discs were upturned onto the prepared quartz. Loose grains were removed by gently tapping the discs, leaving a monolayer of grains across the oiled surface. For each sample (including those for single-grain analysis), one multi-grain aliquot was prepared to provide an indication of signal intensity and an approximation of the size of the dose. A further 18 multi-grain aliquots were produced for dose recovery tests, providing three aliquots for each preheat temperature.

$D_e$ analysis for samples finer than 125-180 μm was conducted at the multi-grain level, using 48 aliquots. Samples with a 125-180 or 180-250 μm fraction underwent single-grain $D_e$ analysis. With the aid of a low-powered microscope, individual grains of quartz were mounted upon aluminium discs 9.7 mm in diameter containing a 10x10 matrix of either 200 or 300 μm holes (depending on the grain fraction). Grains were moved into each position with tweezers and a fine brush. A visual check was conducted on each disc prior to measurement to ensure that each position only contained one grain.

### *3.1.2. Fine Grain $D_e$ Preparation*

The fine-grain procedure follows that of the coarse grain procedure up to section 3.1.1.3, excluding density separation. Following dry sieving, the fine-silt fraction (5-15 µm) for each sample was isolated using acetone sedimentation. From Stokes law, material <15 µm remains in suspension within a 10 cm column of acetone after 2 minutes 20 seconds, whilst the >5 µm fraction would settle after 21 minutes. The isolated <15 µm fraction was submersed for two weeks in 35% Fluorosilicic acid ($H_2SiF_6$) to remove all material but quartz (Jackson *et al.,* 1976; Berger *et al.,* 1980). Following neutralisation, samples were submersed in 10% HCl to remove acid soluble fluorides and rinsed using distilled water. The 21 minute acetone sedimentation was adopted on the remaining material to remove any grains <5 µm, including those partially digested (Rees-Jones, 1995). Saturated with silica, $H_2SiF_6$ digests feldspars but leaves the fine silt quartz in tact.

Isolated fine silt was mounted upon 9.7 mm aluminium discs using a sedimentation chamber and a 1.5 $mg.ml^{-1}$ quartz/acetone solution. 1 ml of the solution was deposited in each disc chamber and was left for two days for the acetone to evaporate, leaving each disc with a covering of *c.* 1.0 mg fine-grained quartz. Whilst the number of aliquots used for initial assessment and dose recovery tests remained the same as that for coarse grain measurements (1 and 24 aliquots, respectively), $D_e$ values for fine grain aliquots were based on fewer (12) aliquots owing to the enhanced precision of mean $D_e$ values arising from the larger number of grains per aliquot relative to coarse grain measurements.

### *3.1.3. Instrumentation*

All $D_e$ measurements were conducted on a Risø TL-DA-15 TL/OSL reader (Bøtter-Jensen *et al.,* 2000) with an updated DA-20 controller. Multi-grain stimulation was provided by an array of blue diodes delivering a peak wavelength of 470 nm, whilst infrared (IR) diodes provided a peak wavelength of 875 nm for detecting feldspar contamination. Single-grain stimulation was delivered by a 532 nm solid state green laser, capable of XY

scanning and focused to illuminate a 20 μm surface of each grain position (Duller *et al.,* 1999). The stimulated signal from quartz grains was detected using an EMI 9235QA photomultiplier tube fronted with 7.5 mm of Hoya U-340 filters to eradicate wavelengths produced by the stimulation sources.

Aliquot irradiation was conducted using a 1.48 GBq $^{90}$Sr/$^{90}$Y β source, calibration was initially conducted by Phillip Toms at the multi- and single-grain level using sensitised quartz, irradiated against the 'Hotspot 800' $^{60}$Co γ source at the National Physical Laboratory, UK. In the present study source calibration was verified for the 180-250 μm fraction using the Risø γ-irradiated 4.81 Gy calibration quartz detailed by Hansen *et al.* (2015). The calibration check was to ensure that the 'old' style, plaque source continued to deliver a homogenous β field across single-grain discs. Calibration was conducted using a single-aliquot regenerative-dose protocol (see 3.1.4), using a 260ºC preheat and 220ºC cut heat upon 600 grains of calibration material. Grains were rejected if recycling ratios fell outside 10% (i.e. 1.00 ± 0.10), post-IR/OSL depletion ratios fell outside of 10% and signal recuperation was >5%. Grains were also rejected if their observed OSL signal was less than 3σ above background levels. In total 325 grains were accepted for calibration, providing at least three values for most positions. Despite the anticipated overdispersion of ~10% (Hansen *et al.,* 2015), a total 85.5% of grains fell within two standard deviations (2σ) of the central dose with an overdispersion of 10.61% and no systematic variation was observed in the β dose delivered to each grain position (Figure 3.1.3a).

Source dose rate for samples measured after calibration was calculated using Equation 3.2:

**Eqn. 3.2**

$$D_{r(t)} = D_{r(0)}\, e^{-\lambda t/\tau_{\frac{1}{2}}}$$

Where; $D_{r(t)}$ = present dose rate, $D_{r(0)}$ = dose rate at calibration, λ = 0.693 (decay constant), t = time elapsed since calibration and $\tau_{½}$ = $^{90}$Sr/$^{90}$Y half-life (28.79 years – Chu *et al.,* 1999).

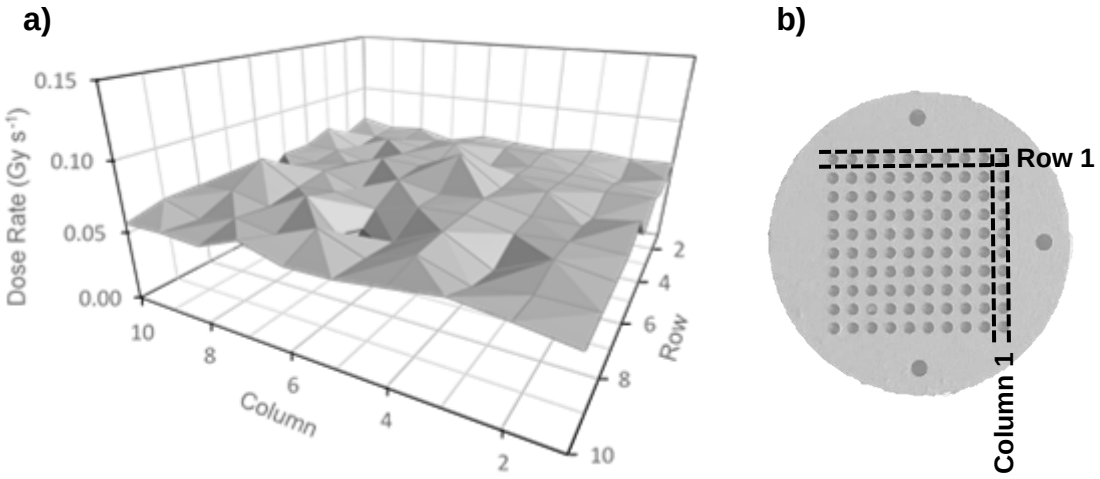


**Figure 3.1.3:** a) Source dose rate observed across single-grain discs using 4.81 Gy Risø calibration quartz (Batch 108); b) Relative positions single-grain disc rows and columns

*3.1.4. Single-Aliquot Regenerative-Dose Protocol (SAR)*

Since its development by Murray & Wintle (2000), the single-aliquot regenerative-dose (SAR) protocol has been successfully used to estimate $D_e$ values for quartz originating from a diverse range of geomorphic settings. Based upon an earlier protocol put foward by Murray & Roberts (1998), SAR accounts for sensitivity-changes induced by the repeated heating and irradiation of aliquots during measurement. Such changes can be observed as variability in OSL emissions per unit of dose. Sensitivity correction is achieved by administering a fixed test dose during each measurement cycle and normalising the regenerative signal ($L_x$) against the signal induced by the test dose ($T_x$). Following measurement of the natural signal ($L_n$) and first test dose, samples examined using the SAR protocol are given an incremental series of laboratory regenerative doses to produce sensitivity-corrected ($L_x/T_x$) dose-response curves (DRC). Interpolation of the natural signal ($L_n/T_x$) upon the constructed DRC can then be used to obtain an estimate of $D_e$ (Figure 3.1.4).

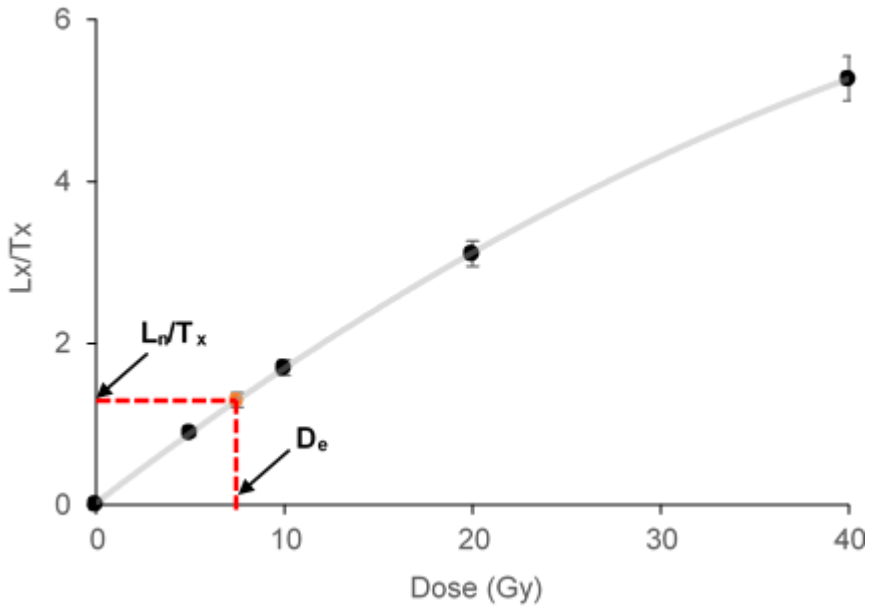


**Figure 3.1.4:** An example Dose Response Curve (DRC) with the inclusion of the interpolated $D_e$ from $L_n/T_x$

Although numerous methods of interpolation are available for $D_e$ acquisition (e.g. Duller, 2007), this research acknowledges that each component of the quartz OSL follow first-order kinetics, producing a single saturating exponential (Singarayer & Bailey, 2003). Therefore for samples in this study either an exponential or an exponential plus linear function was used for DRC fitting. An exponential plus linear fitting can be expressed as follows:

**Eqn. 3.3**

$$Y = D_{max}\left(1 - e^{-\frac{D}{D_0}}\right) + c$$

Where: $Y = L_x/T_x$, $D_{max}$ = saturation level, D = laboratory dose, $D_0$ = dose at which the onset of saturation occurs and c = linear offset (removed for exponential fitting).

Revisions to the original SAR protocol were suggested by Murray & Wintle (2003). This included the requirement for a dose recovery test prior to $D_e$ assessment and the inclusion of an elevated temperature OSL bleach following each SAR cycle to minimise recuperation of the OSL signal (Table

3.1.2 – Step 7). Aliquots or grains displaying significant recuperation (>5%) following a repeated zero-dose in the SAR protocol are typically eliminated from $D_e$ evaluation to avoid underestimation. During SAR, samples are preheated prior to OSL measurement to remove thermally unstable components which could compromise accurate $D_e$ acquisition. The optimum preheat for quartz aliquots is sample-dependent and the dose recovery test ensures the correct preheat is used. During the dose recovery test, aliquots are first bleached at low temperature to avoid sensitisation and are subsequently given a known artificial dose similar in magnitude to the anticipated natural dose. The known dose is then recovered using a SAR protocol with different preheat temperatures being adopted for each aliquot. The preheat temperature which produces a given to measured dose ratio closest to unity is typically selected for SAR $D_e$ assessment.

Further internal checks of the suitability of the SAR protocol for a given sample include the measurement of repeated dose points to produce recycling ratios. If SAR and sensitivity correction is performing well the recycling ratio of a given dose would be expected to fall within errors of unity (i.e. 1.0). However, given the inclusion of systematic error, Murray & Wintle (2000) suggest ratios within 10% of unity (i.e. 0.90-1.10) are acceptable. The SAR protocol adopted for samples in this study included both a low and high dose recycled point for each aliquot/grain to assess measurement reproducibility across the dose range.

A potential source of error within SAR OSL measurement is feldspar contamination. Feldspars experience anomalous fading during burial time (Wintle, 1973) and inclusion with quartz OSL measurement can result in significant underestimation of $D_e$. Although sample preparation should ensure complete removal of feldspar grains, this mineral can exist as inclusions that are incorporated into the mineral lattice of quartz grains. An OSL-IR depletion ratio can be used in conjunction with SAR to identify such contamination (Duller, 2003). The OSL signal produced by feldspars deteriorates when stimulated by IR diodes at room temperature whilst the OSL signal of quartz does not. Inclusion of an additional recycled point with a room temperature IR stimulation prior to OSL measurement produces a post-IR OSL signal.

Should the recycled dose show significant OSL signal deterioration through a poor recycling ratio, feldspar contamination is almost certain.

For samples in this study a test multi-grain aliquot was initially used to assess signal intensity and to select a suitable artificial dose for dose recovery tests using $L_x/T_x$. Dose recovery tests were then conducted upon 18 multi-grain aliquots for each sample. Six preheat temperatures between 180 and 280°C (3 aliquots per preheat) were examined. Single- and multi-grain aliquots were examined using the SAR protocol outlined in Table 3.1.2, using the appropriate preheat temperatures informed by dose recovery tests. Cut heat temperatures of 180°C were used for preheats ≤220°C whilst 220°C cut heats were used for preheat temperatures ≥240°C. Five regenerative doses were used for each sample along with a fixed test dose of 5 Gy. Each sample measurement included a zero dose measurement, repeated low and high dose measurements and an OSL IR depletion test. All OSL measurements were conducted at 125ºC to avoid accumulation of signal within the 110ºC TL peak (Wintle & Murray 1998).

**Table 3.1.2:** Adopted SAR protocol for $D_e$ acquisition (Step 1 omitted for natural signal during first cycle; note differences in single- (SG) and multi-grain (MG) stimulation time)

| Step | Treatment | Observation |
|---|---|---|
| 1 | Give Regenerative β Dose | - |
| 2 | Preheat (180-280°C) for 10 s | - |
| 3 | OSL at 125°C for 1 or 50 s (SG/MG) | $L_n$ or $L_x$ |
| 4 | Give Test Dose (5 Gy) | - |
| 5 | Cut Heat (<Preheat °C) | - |
| 6 | OSL at 125°C for 1 or 50 s (SG/MG) | $T_x$ |
| 7 | OSL at 280°C for 50 s | - |
| 8 | Return to step 1 | - |

The SAR protocol is suited to OSL signals dominated by the fast component (Wintle & Murray, 2003), since it is stable on geological timescales and rapidly bleached (Cunningham & Wallinga, 2010). Although it is not possible to isolate the fast from the medium and slow components of the quartz signal using continuous wave stimulation (CW-OSL), it is possible to mathematically screen multi-grain aliquot decay curves using the 'fast ratio' (Durcan & Duller, 2011) to determine whether a CW-OSL decay curve is dominated by the fast or other components. It is suggested that the fast ratio is applied to both the natural and regenerated signals of aliquots and should surpass a threshold of 20 if an aliquot is considered to be dominated by the fast component.

To isolate the fast-dominated signal in quartz OSL, only the initial part of the decay curve is used for signal integration as *c.* 80% of it comprises of the fast component (Wintle & Murray, 2006). For samples in this research (including calibration), the initial 0.03 and 0.25 seconds were used for signal integration for single- and multi-grain measurements respectively. Background measurement noise was subtracted using the final 0.3 seconds of stimulation for single-grain measurements and 10 seconds for multi-grain aliquots.

### *3.1.5. Intrinsic Sources of $D_e$ Uncertainty*

Intrinsic sources of uncertainty typically arise from machine and analytical error and should be correctly accounted for when producing $D_e$ estimates, particularly when assessing natural dose distributions. They differ from extrinsic factors (e.g. partial bleaching & pedoturbation), which are explored in Chapter 4.

Early work exploring the reproducibility of Risø luminescence readers estimated that error arising from instrumental uncertainty was *c.*1-2% for multi-grain measurements (Armitage *et al.,* 2000) and *c.* 3.5% for single-grain measurements (Truscott *et al.,* 2000). More recent assessment of single-grain measurements indicates that technological improvements have reduced such errors (e.g. Jacobs *et al.,* 2006). Given the likelihood of inter-laboratory variations in reproducibility and the significant changes observed when altering signal integration limits (Thomsen *et al.,* 2005), it is important

to assess each instrument's uncertainty using the same parameters as those for $D_e$ assessment.

The reproducibility of the Risø luminescence reader used in this study was assessed for both single- and multi-grain measurements using a similar approach to Thomsen *et al* (2005). From the sensitised quartz provided with the Risø calibration material (see 3.1.3), 29 single-grains and six 8 mm multi-grain aliquots were assessed using 10 cycles of the SAR protocol outlined in Table 3.1.2. Sensitised quartz grains/aliquots were given repeated regeneration doses of 10 Gy with preheat and cut heat temperatures set at 260 and 220ºC respectively. Machine reproducibility was calculated using $L_x/T_x$ measurements to ensure no discrepancies were caused by any unexpected sensitivity changes.

The observed variability, indicated by the relative standard deviation ($\sigma_{rel}$), of $L_x/T_x$ measurements was inclusive of the errors arising from counting statistics. To isolate machine reproducibility, counting statistic errors were first calculated using the equation suggested by Galbraith (2002):

**Eqn. 3.4**

$$RSE = \frac{\sqrt{Y_0 + \bar{Y}/k}}{Y_0 - \bar{Y}}$$

Where: $Y_0$ = integrated OSL signal counts, $\bar{Y}$ = integrated background counts and k = scaling factor to account for the different number of channels used for signal and background integration.

Subtraction, in quadrature, of counting statistic errors from $\sigma_{rel}$ provided an estimate of the measurement uncertainty for $L_x/T_x$. However, given that $L_x/T_x$ is based upon two measurements, values were divided by $\sqrt{2}$ to produce the expected error for each OSL measurement (Jacobs *et al.,* 2006). A summary of the observations for both single- and multi-grain reproducibility assessment is provided in Appendix A (Table A.1/A.2). Overall, the average reproducibility for each single-grain measurement was calculated to be 2.7% ($L_x/T_x$ = 3.8%), whilst for multi-grain aliquots it was 0.7% ($L_x/T_x$ = 1.0%).

These are very similar to the values published by other laboratories, however, for multi-grain studies it is suggested that a systematic error of *c.* 1.5% should be applied to each $D_e$ value (Duller, 2016). This was adopted as a precaution for all multi-grain measurements in this study, to incorporate any further measurement uncertainties not observed upon the sensitised quartz.

Further uncertainty in $D_e$ is attributed to the construction of DRC and fitting errors post-measurement. Such errors vary between aliquots/grains depending on the suitability of the fitted curve. For SAR-derived data the average deviation of regenerative dose points away from fitted DRC can be calculated as suggested by Duller (2007 – (Eqn.7)):

**Eqn. 3.5**

$$Average\ Deviation = \frac{\sum_1^n (Predicted\ Dose - Actual\ Dose)^2}{n}$$

Where: n = number of regenerative dose points. For samples in this study measurement and curve fitting errors were combined in quadrature using 'Analyst' (v4.31.9 – Duller, 2016). Resultant $D_e$ estimates and associated uncertainties were subject to the inclusion of a further 3.5% β-source calibration error when converting units of dose from seconds to Gray, owing to errors associated with calculating the absorbed γ-dose for calibration material (P.Toms, pers.comm., Hansen *et al.,* 2015).

### 3.2. The Dose Rate

The rate of growth of the $D_e$ is controlled by the levels of ionising radiation emitted within and passing through a sediment body. Typically, the largest proportion of the radiation arises from radioactive elements within sediments, whilst a small contribution originates from cosmic rays. Four sources of radiation need to be considered for $D_r$ calculation; α ($D_\alpha$), β ($D_\beta$), γ ($D_\gamma$) and cosmic ($D_{cos}$).

It is suggested that quartz OSL samples are collected from a *c.* 300 mm field of homogenous material to simplify the calculation of $D_r$ (Aitken, 1998).

However, assessment of the composition of the South Lake core lengths (see 2.6.1) highlighted a complex stratigraphy that incorporates many different materials. The variable composition is accompanied by differing densities, particularly when shifting between organic and clastic units. The majority of samples do not sit within homogenous units 300 mm in thickness. Therefore careful modelling is required to ensure an accurate assessment of $D_r$.

### *3.2.1. Cosmic Dose Contribution*

The $D_{cos}$ forms a relatively small proportion of the overall $D_r$ and only acts as a significant contributor when over 1 km in altitude (Aitken, 1998). $D_{cos}$ comprises a 'soft' and 'hard' component. The former penetrates only the upper *c.* 167 g.cm$^{-2}$ of sedimentary deposits (Barbouti & Rastin, 1983; Durcan *et al.,* 2015) and can be ignored for samples collected beyond such depths. The 'hard' component is predominantly composed of muons, whose contribution to the overall $D_r$ varies with altitude, latitude and overburden depth-density.

For a sample collected at sea-level at a geomagnetic latitude of 55°, Barbouti & Rastin (1983) calculate the contribution from the cosmic component using:

**Eqn. 3.6**

$$D_{cos}(Gy\ ka^{-1}) = \frac{6072}{((x+11.6)^{1.68}+75)(x+212)}(\exp(-Bx)$$

Where: x = depth in hg.cm$^{-2}$ (100 g cm$^{-2}$) and B = 5.50 x 10$^{-4}$. For samples collected from other locations it is possible to correct $D_{cos}$ for differences in altitude, geomagnetic latitude and longitude using the step-by-step process suggested in the Appendix of Prescott & Hutton (1994). This process was followed for all samples in this study, including $D_{cos}$ correction for temporal geomagnetic field changes.

Calculation of $D_{cos}$ following the steps outlined by Prescott & Hutton (1994) produces a value with *c.* 5% uncertainty. However, core samples collected

from the South Lake site underwent significant compaction (*c.* 15%), with 5.68 m of cored material being compressed into 4.78 m. Addition, in quadrature, of the uncertainties associated with $D_{cos}$ calculation and core depth produced an overall error of 16%, which was used for all South Lake $D_{cos}$ estimates. For the Fututulu and UCOSP sites compaction was not as extreme owing to the clastic nature of deposits and a 10% error was included for $D_{cos}$ estimates.

Given the silt/sand dominated matrix of deposits from the Fututulu and UCOSP sites, a similar approach to Armitage *et al.* (2007) was taken, whereby the overburden density was assumed to be 1.86 $g.cm^{-3}$. For the South Lake site, overburden density was reconstructed (see 3.2.5) and the average modelled dry and saturated density values were used for calculation of $D_{cos}$. The standard error of mean density estimates were included within error calculations.

### *3.2.2. Lithogenic $D_r$ Contributors*

Unlike some mineral grains used in luminescence dating, such as K-feldspars and Zircons, quartz generally comprises limited quantities of radionuclides (Th and U) and thus has a negligible internal $D_r$ (Jacobs *et al.,* 2008) which can be omitted from age calculation. But in some instances (e.g. Murray *et al.,* 2007) a minimal internal $D_r$ of 0.06 Gy $ka^{-1}$ is applied. Assessment of $D_r$ for sand-sized quartz is further simplified by the HF treatment (see 3.1.1.4) as it removes the alpha-irradiated rind of grains, requiring only the external contributions from $D_\beta$, $D_\gamma$ and $D_{cos}$ (3.2.1) to be considered.

$D_\alpha$, $D_\beta$ and $D_\gamma$ are all localised, with contributions coming from c. 0.03, 3 and 300 mm radial fields, respectively, in the surrounding sediment. Three naturally-occurring radioelements contribute to the overall $D_r$; potassium (K), thorium (Th) and uranium (U). Potassium-40 ($^{40}K$) is the radioactive isotope of K that contributes to $D_r$ whilst radiation from Th and U are provided by chains of elements headed by the parent isotopes; thorium-232 ($^{232}Th$), uranium-235 ($^{235}U$) and uranium-238 ($^{238}U$). The radioactive decay chains

headed by the latter three nuclides comprise numerous daughter isotopes (Appendix G - Aitken, 1985). $^{40}$K produces both β and γ emissions whilst the decay chains of $^{232}$Th, $^{235}$U and $^{238}$U also produce α emissions.

For thorium and uranium decay chains that are in equilibrium, the production rate of daughter isotopes is equivalent to the rate of radioactive decay of their parent isotope. Therefore, when a radiation field is a closed system assessment of $D_r$ is simplified as the activity of daughter isotopes should be equivalent to that of the parents'.

In some instances, the thorium and uranium series can experience disequilibrium through the preferential removal of individual isotopes. Olley *et al.* (1996) examined the impact of disequilibria upon dose rates of fluvial samples, identifying three potential causes of disequilibrium; diffusion of radon (Rn) isotopes, alpha particle recoil and solution/precipitation reactions. From their study they concluded that disequilibrium in the $^{232}$Th decay chain is unlikely to have a significant impact upon $D_r$ estimates for older samples, owing to the relatively short half-lives of daughter isotopes (e.g. Radium-228 ($^{228}$Ra) = 5.75 years). However, for the $^{238}$U decay chain they suggest that disequilibrium has the potential to persist for a significant amount of time owing to longer half-lives of isotopes (e.g. 1600 years in the case of $^{226}$Ra). A particular concern for $D_r$ estimation and the $^{238}$U decay chain is disequilibrium created by $^{226}$Ra removal, as it and subsequent daughter isotopes account for 75% of the overall $^{238}$U dose (Olley *et al.,* 1996). A typical diagnostic for assessing disequilibrium in the uranium chain is to assess the $^{238}$U/$^{226}$Ra ratio, ensuring this ratio falls within 0.5 of unity. Given the waterlain nature of sediments in this study and the potential post-depositional mobility of isotopes from the $^{232}$Th and $^{238}$U chains, close attention is paid to identification of disequilibria.

### *3.2.3. High-Resolution Gamma Spectrometry*

Numerous techniques are available to quantify the concentrations of K, Th and U for $D_r$ determination. Examples of those commonly adopted for *ex situ* analysis include thick source alpha counting (Zöller & Pernicka, 1989), beta

counting (Bøtter-Jensen & Mejdahl, 1988), inductively-coupled plasma mass spectrometry (ICP-MS – Bailey *et al.,* 2003) and high-resolution gamma spectrometry (Murray *et al.*, 1987). Where possible, it is advisable that OSL ages incorporate *in situ* measurement of the gamma spectrum to identify any discrepancies in the $\gamma$-field which may not be detected in sub-samples taken for *ex situ* analysis. This typically involves the use of a multi-channel sodium iodide (NaI) field gamma spectrometer (Mercier & Falguéres, 2007), which takes direct measurements of the $\gamma$-spectrum from where a $D_e$ sample has been taken. Although this has the benefit of identifying discrepancies in the $\gamma$-field, as with other techniques, the assumption is that radionuclide concentrations have not significantly varied since deposition. Unfortunately *in situ* gamma spectrometry was not available during fieldwork, however, this would only have been beneficial for those samples collected in-section (UCOSP site) as the diameter of the gamma spectrometer was larger than the borehole created by the coring equipment.

High-resolution gamma spectrometry (HRGS) was adopted for all samples. Although the technique is unable to directly assess the α-decay of the parent isotopes $^{232}$Th and $^{238}$U, there are sufficient gamma-emitting daughter isotopes which enable accurate estimation of the overall radionuclide content and detection of U disequilibrium. Additionally, the technique can produce stand-alone estimates of the required radionuclide concentrations, whilst some other techniques have to be used in unison, such as alpha- and beta-counting owing to the lack of an α-emission created by the radioactive decay of $^{40}$K (*cf.* Bailey *et al.,* 2001).

HRGS of radionuclide concentrations for OSL dosimetry is typically conducted using low-background germanium (Ge) spectrometers. These are able to detect the relatively low levels of gamma activity experienced by natural sediments. Spectrometers are calibrated to continuously count gamma emissions for a set time-period for a given mass of material presented in a set geometry. Distinct gamma energies are detected and are used to identify isotopes and quantify their activity. Initially, radioactivity is quantified in Becquerels per kilogram (Bq $kg^{-1}$). These quantities can then be

converted into relative proportions (ppm or %) of radioactive isotopes and converted into $D_\alpha$, $D_\beta$ and $D_\gamma$ emissions.

### *3.2.3.1 Sample Preparation*

For the South Lake Site, each $D_e$ sample was accompanied by 13 samples for HRGS; one at each $D_e$ sampling point and a further six taken from above and below at 5 cm intervals to assess the $\gamma$-field for $D_\gamma$ modelling (see 3.2.4). Duplicate samples were not taken where HRGS samples overlapped throughout the core lengths. For the Futululu and UCOSP sites, only one sample for HRGS was used per $D_e$ sample owing to minimal variation in the sediment matrix surrounding each of the sampled units and in the $\gamma$ activity observed between each of the samples.

Samples for HRGS were oven-dried and homogenised into a fine powder using a TEMA disc mill. Depending upon the availability of material, either 30 or 50 g of homogenised material was subsequently sealed in 150 cc Azlon polystyrene pots with polyethylene lids. Prior to measurement, samples were stored for at least three weeks for radon retention, satisfying the storage time of five $^{222}$Rn half-lives (3.8 days) used by Murray *et al.* (1987).

### *3.2.3.2 Instrumentation & Measurement*

Samples were measured for 24 hours using an Ortec GEM-S high purity Ge coaxial detector, calibrated by Phillip Toms (University of Gloucestershire) using certified CANMET and SARM-3 reference materials. The detector is cooled with liquid nitrogen and is housed in lead shielding to minimise background radiation. The detector housing also consists of a copper (Cu) buffer which minimises $^{210}$Pb contamination from the shielding itself and also assists with attenuation of low energy bremsstrahlung created by the Pb shielding (Bonczyk, 2013). The isotopes calibrated for this detector and their relevant characteristics are shown in Table 3.2.1.

**Table 3.2.1:** Gamma peak energies of the calibrated isotopes for the High-Resolution Ge Gamma Spectrometer at the University of Gloucestershire

| Parent Isotope | Observed Isotope | γ Peak Energy (keV) |
|---|---|---|
| **$^{40}$K** | Potassium-40 ($^{40}$K) | 1460.8 |
| **$^{232}$Th** | Actinium-228 ($^{228}$Ac) | 968.9 |
| | Actinium-228 ($^{228}$Ac) | 911.1 |
| | Thallium-208 ($^{208}$Tl) | 583.1 |
| | Actinium-228 ($^{228}$Ac) | 338.4 |
| | Lead-212 ($^{212}$Pb) | 238.6 |
| **$^{238}$U** | Bismuth-214 ($^{214}$Bi) | 609.3 |
| | Lead-214 ($^{214}$Pb) | 351.9 |
| | Lead-214 ($^{214}$Pb) | 295.2 |
| | Radium-226 ($^{226}$Ra) | 186.0 |
| | Thorium-234 ($^{234}$Th) | 63.3 |
| | Lead-210 ($^{210}$Pb) | 46.5 |

Given the use of the $^{238}$U/$^{226}$Ra to assist with determination of disequilibrium in the $^{238}$U chain, it is important to note that the γ peak emission at 186.0 keV is also formed of a strong emission from $^{235}$U. To separate the contribution of the two isotopes from this peak it is possible to use the method suggested by Murray *et al.* (1987), whereby the $^{234}$Th emission (63.3 keV) is used for quantification of $^{238}$U and a $^{235}$U/$^{238}$U ratio of 0.04605 is assumed for samples in equilibrium.

As no direct measurement is available for the quantification of the parent isotopes in the $^{232}$Th and $^{238}$U decay chains, equilibrium was initially assumed and the average activity of daughter isotopes was used. For the $^{232}$Th chain, averages were derived from $^{228}$Ac (at 338.4 & 911.1 keV), $^{212}$Pb (at 238.6 keV) and $^{208}$Tl (at 583.1 keV). Whilst, for the $^{238}$U chain, average activity was calculated using $^{214}$Bi (at 609.3 keV) and $^{214}$Pb (at 295.2 & 351.9 keV). An example γ spectrum and the relevant peaks is provided in Figure 3.2.1.

Nuclides not used to calculate average activity were retained for identification of disequilibria, ensuring the relative activities were within errors of unity. By assessing the present-day activity of daughter isotopes and confirming secular equilibrium, the maximum potential temporal shift in $D_r$ equates to *c.* 2% for a 75 ka timeframe, as opposed to an *c.* 8% shift for those $D_r$ estimates generated by direct quantification of parent isotopes (Olley *et al.,* 1997).

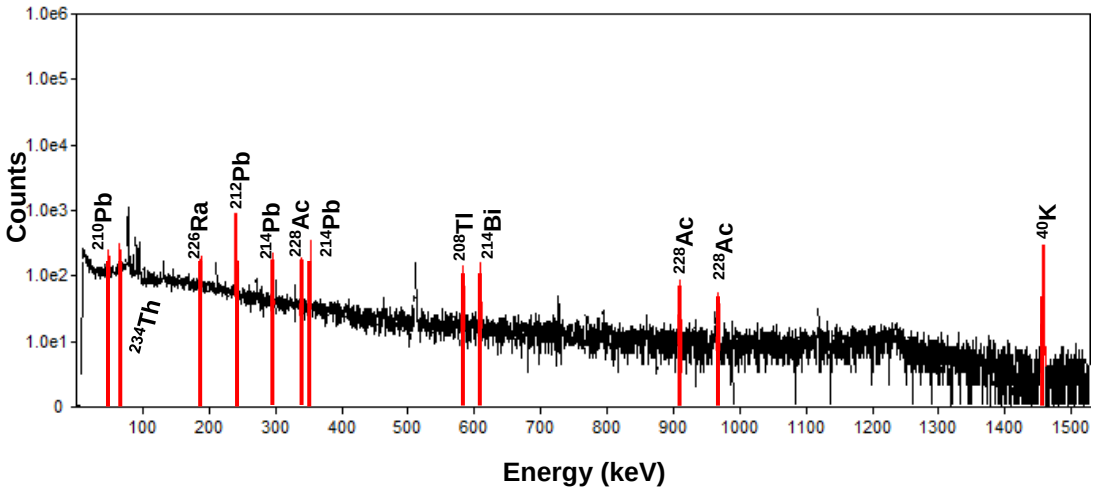


**Figure 3.2.1:** γ spectrum obtained from a 24 hour HRGS measurement of GL14001 with calibrated peaks identified.

*3.2.4. Conversion of Radioactivity to Absorbed Dose*

Estimated concentrations of K (%), Th (ppm) and U (ppm) from HRGS were converted to α (5-15 µm fraction only), β and γ $D_r$ using conversion factors and associated errors provided by Liritzis *et al.* (2013). The attenuation of $D_\beta$, as forced by grain size, was calculated using factors determined by Mejdahl (1979), values of which were corrected to account for HF etching of quartz grains (Brennan, 2003). Moisture attenuation was calculated using the values obtained for present day moisture content and factors provided by Zimmerman (1971). For the 5-15 µm fraction only, an alpha-efficiency value (a-value) of 0.038 ± 0.002 (Rees-Jones, 1995) was adopted to account for the elevated ionising potential of α particles.

Contributions of α and β (plus γ for UCOSP and Futululu) towards the overall $D_r$ were based upon radionuclide concentrations derived from material collected within 5 cm of $D_e$ samples, where an infinite matrix dose was assumed. For all $D_e$ sampling locations the organic content was <20% and a similar approach to Madsen et al. (2009) was taken, whereby separate consideration of organic and moisture content attenuation, using the methods outlined by Divigalpitiya (1982), was deemed unnecessary. The γ-field for the South Lake core was more complex, particularly given that for some samples that field incorporated sediments with organic contents >40%. However, given that samples for HRGS were not ashed and that $D_\gamma$ modelling accounts for density variations within the sediment matrix, further incorporation of organic stopping powers could overcompensate for γ attenuation and result in an underestimation of $D_r$. It was therefore decided not to incorporate a further correction for organic attenuation and calculate South Lake $D_\gamma$ values based upon 5 cm interval HRGS measurements and density variations.

### *3.2.5. South Lake $D_\gamma$ Modelling*

The dosimetric properties in OSL dating require consideration of the density of the material to be dated and its surrounds. When modelling $D_\gamma$, variable densities need to be considered as existing calculations on γ gradients are based on an assumed value of 2 $g.cm^{-3}$ (Aitken, 1985). It is possible to scale these γ gradients, providing that the density of the units to be modelled are known. Given the lacustrine nature of South Lake deposits, it was deemed suitable to calculate both the dry and saturated density of material to assist with the γ profiling of core lengths.

Initially the dry density of core samples was assessed at 5 cm intervals. This was achieved using a 5 ml syringe and 2-3 g of core material. The dry core material was compacted into the syringe, enabling the density of the material to be calculated from the sample mass and compacted volume. The saturated density of the material was then calculated using a similar procedure to that highlighted by Nelson & Rittenour (2015). Dry samples were transferred to 15 ml centrifuge tubes and distilled water added to fill

pore spaces. To achieve packing of the sediment, samples were centrifuged at 1600 RPM for 10 minutes. Excess water was drained after centrifuging and the saturated density calculated (using the packed sample mass and volume). Both dry and saturated assessments were completed three times for each sampling location

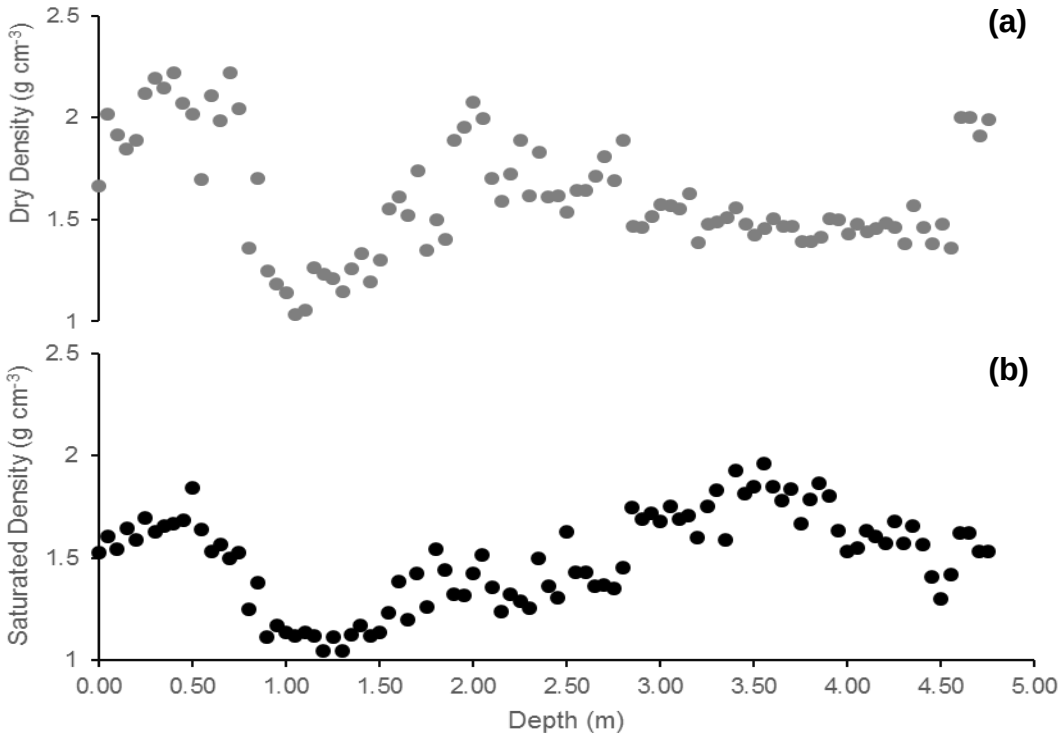


**Figure 3.2.2:** Dry (a) and saturated (b) density assessment of South Lake core lengths

Density assessment displayed significant variations throughout the South Lake core lengths (Figure 3.2.2). Although a large proportion of the core lengths were situated below the present water table and considered saturated, existing work upon the Mfolozi catchment has highlighted the occurrence of drought and desiccation of blocked-valley lake sediments in the Mid- to Late-Holocene (Grenfell *et al.,* 2010). It was therefore decided to calculate mean density and standard error using the six density measurements (dry and saturated) at each 5 cm interval, given the unknown fluctuations in moisture availability. These density values were also adopted for the calculation of the cosmic dose contribution (see 3.2.1). It is acknowledged that the adopted sample mass for density assessment was

~10% of that suggested by Nelson & Rittenour (2015), however, sample mass had to be preserved for $D_e$ and $D_r$ analysis.

Each South Lake $D_e$ sample was accompanied by 13 gamma spectrometry measurements for the assessment of $D_\gamma$. Dry $D_\gamma$ values were initially calculated, corrections were then applied through the modelling process to account for moisture content attenuation and variable densities. Guidance is taken from Aitken (1985 - Appendix H) for calculating inter-layer $\gamma$ contributions.

### *3.2.5.1 Worked Example: GL15015*

As modelling of $D_\gamma$ is relatively complex, a worked example using sample GL15015 (see Figure 2.6.1. for location: 45-50 cm) is provided here. Most of this modelling procedure uses Løvborg's fractional $\gamma$ dose table (p. 290, in Aitken, 1985) to calculate the contributions of $D_\gamma$ from each radioactive unit. For the calculations $f(z)$ represents the density-corrected distance into a radioactive unit and values correspond to the distances provided within the fractional $\gamma$ dose table. Calculations for $D_\gamma$ are based on attenuation factors for the 180-250 µm quartz fraction of GL15015. The sample has a $D_\beta$ and $D_{cos}$ of 1.24±0.25 and 0.19±0.03 Gy.ka$^{-1}$ respectively.

**Table 3.2.2:** Summary of GL15015 dosimetry data for $\gamma$ modelling

| Distance from $D_e$ unit border (cm) | Moisture content (%) | Density (g cm$^{-3}$) | Dry $D_\gamma$ (Gy ka$^{-1}$) |
|---|---|---|---|
| + 30 | 28 | 1.74 ± 0.07 | 1.11 ± 0.04 |
| + 25 | 27 | 1.74 ± 0.07 | 1.10 ± 0.05 |
| + 20 | 22 | 1.91 ± 0.11 | 1.06 ± 0.04 |
| + 15 | 23 | 1.91 ± 0.14 | 1.11 ± 0.05 |
| + 10 | 22 | 1.90 ± 0.11 | 1.07 ± 0.04 |
| + 5 | 21 | 1.95 ± 0.13 | 1.03 ± 0.05 |
| 0 ($D_e$) | 17 | 1.88 ± 0.09 | 1.05 ± 0.05 |
| - 5 | 21 | 1.93 ± 0.09 | 1.06 ± 0.05 |
| - 10 | 24 | 1.67 ± 0.20 | 1.20 ± 0.05 |
| - 15 | 28 | 1.81 ± 0.13 | 1.25 ± 0.05 |
| - 20 | 30 | 1.77 ± 0.10 | 1.30 ± 0.05 |
| - 25 | 33 | 1.86 ± 0.17 | 1.30 ± 0.05 |
| - 30 | 52 | 1.78 ± 0.12 | 0.78 ± 0.04 |

To identify regions of radioactive homogeneity the dry $D_\gamma$ at the $D_e$ sampling location was first observed and neighbouring $D_\gamma$ estimates were considered to be of similar radioactivity if they were statistically indistinguishable. This process was extended 30 cm either side of the $D_e$ sample. The depth at which a significant change in $D_\gamma$ occurred was defined by $D_\gamma$ being statistically distinct from those $D_\gamma$ values measured from the immediately overlying and underlying 5 cm. Dosimetry data for GL15015 (Table 3.2.2) suggested that there were three distinct layers of Dγ; unit 1 (-5 to +30 cm), unit 2 (-10 to -25 cm) and unit 3 (-30 cm - Figure 3.2.3).

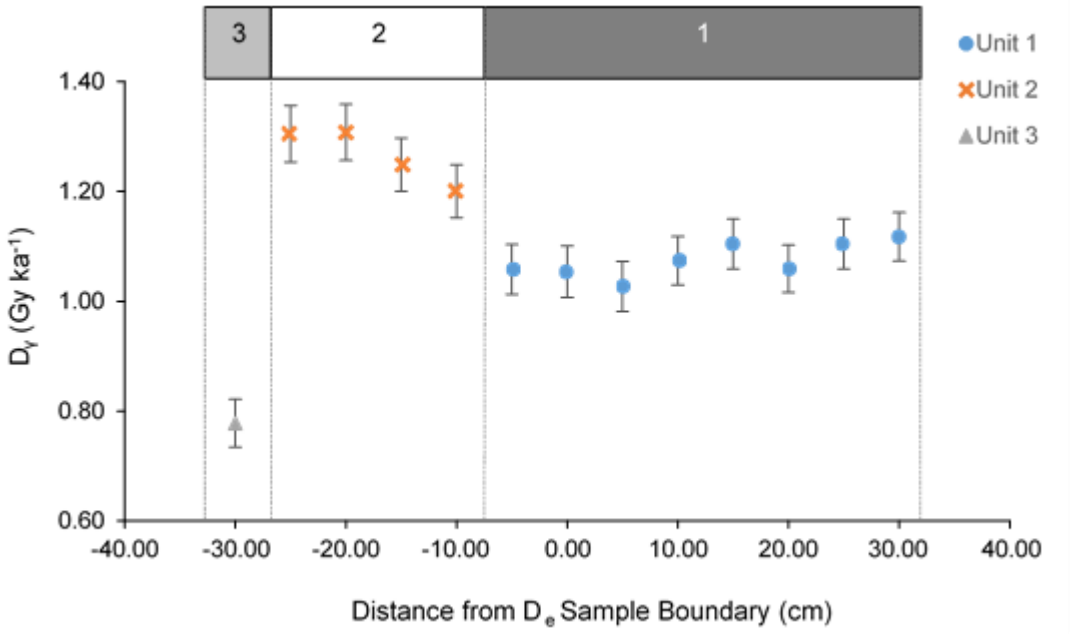


**Figure 3.2.3:** γ units identified for GL15015

The initial stage of modelling assesses the $D_\gamma$ absorbed at the $D_e$ location owing to the radioactivity in its immediate vicinity (i.e. Unit 1). To do this units 2 and 3 are considered inert (inactive) and the distance ($x$) of the $D_e$ sample to the boundary at unit 1 and 2 is scaled to the appropriate density ($\rho$), providing $z$. Scaling to z is achieved by multiplying $x$ by $2/\rho$, this is done incrementally every 5 cm to account for changes in density. It is important to note that the boundaries of radioactive units are considered to occur at the midpoint between the 5 cm interval HRGS and density samples. As such, an

additional 2.5 cm is incorporated within modelling calculations as the $D_r$ is calculated for the centre of each $D_e$ (5 cm wide) sampling point.

*Absorbed $D_\gamma$ from Unit 1:*

*Scaling x to z:* $z = x\left(\frac{2}{\rho}\right)$

*Values substituted* $z = \left(5 \times \frac{2}{1.93}\right) + \left(2.5 \times \frac{2}{1.88}\right) = 7.84$

*z Rounded to nearest tabular point in Aitken (1985, p.290)* = 8

*Fractional dose:* $f(z) = f(8) = 0.8487$

*Absorbed $D_\gamma$:* $= Unit\ 1\ Average\ D_\gamma \times 0.8487$

$= 1.0738 \times 0.8487 = 0.9113\ Gy.ka^{-1}$

The following stage calculates the absorbed dose from the units adjacent to the $D_e$ sample. Through laws of superposition it is possible to treat unit 1 as an inert medium and then use the function 1 - $f(z)$ to calculate the absorbed dose, where *z* becomes the distance into the inert (assumed) medium from the boundary. Note that scaling of z also becomes inverted through superposition.

*Absorbed $D_\gamma$ from Unit 2:*

*Scaling x to z:* $z = x\left(\frac{\rho}{2}\right)$

*Values substituted* $z = \left(5 \times \frac{1.93}{2}\right) + \left(2.5 \times \frac{1.88}{2}\right) = 7.175$

*z Rounded to nearest tabular point in Aitken (1985, p.290)* = 7

*Fractional dose:* $1 - f(z) = 1 - f(7) = 1 - 0.8292 = 0.1708$

*Absorbed $D_\gamma$:* $= Unit\ 2\ Average\ D_\gamma \times 0.1708$

$= 1.2625 \times 0.1708 = 0.2156\ Gy.ka^{-1}$

Absorbed dose from unit 3 uses a similar concept, however, units 1 and 2 are combined and treated as one inert unit.

*Absorbed $D_\gamma$ from Unit 3:*

*Scaling x to z:* $z = \left(5 \times \frac{1.86}{2}\right) + \left(5 \times \frac{1.77}{2}\right) + \left(5 \times \frac{1.81}{2}\right) + \left(5 \times \frac{1.67}{2}\right) + \left(5 \times \frac{1.93}{2}\right) + \left(2.5 \times \frac{1.88}{2}\right) = 24.95$

*z Rounded to nearest tabular point in Aitken (1985, p.290)* = 25

*Fractional dose:* $1 - f(z) = 1 - f(25) = 1 - 0.9772 = 0.0228$

*Absorbed $D_\gamma$* $= Unit\ 3\ D_\gamma \times 0.0228$

$= 0.78 \times 0.0228 = 0.0178\ Gy.ka^{-1}$

To complete the $\gamma$ modelling, attenuation owing to moisture content needs to be incorporated within calculations. For this, a running average of moisture content is calculated for each unit, which is inclusive of moisture content values for the radioactive unit and from the unit boundary to the $D_e$ sampling locations. This should account for the sharp fluctuations in moisture content displayed in the core lengths.

*Absorbed 'moist' $D_\gamma$ from Units 1-3:*

*Average moisture content: Unit 1 = 23%, Unit 2: 26% and Unit 3 = 29%*

*Moist $D_\gamma$:* $= \frac{D_\gamma\ (dry)}{1+1.14W}$

*Values Substituted:* $= \frac{0.9113}{1+(1.14 \times 0.23)} + \frac{0.2156}{1+(1.14 \times 0.26)} + \frac{0.0178}{1+(1.14 \times 0.29)}$

$= 0.9017\ Gy.ka^{-1}$

Once this has been completed for each unit the moist $D_\beta$ and $D_{cosmic}$ can be combined with the total modelled $D_\gamma$ values to produce the overall $D_r$.

*Total $D_r$:*

$$D_r = D_\beta + D_\gamma + D_{cos}$$

$$= 1.24 + 0.90 + 0.19 = 2.33 \pm 0.34\ Gy.ka^{-1}$$

This process is tested for each $D_e$ scenario. However, for $D_e$ samples lying within a homogenous radiation field gamma profiling was not required. Errors for $\gamma$ modelling were combined appropriately in quadrature, which included relatively large error margins for moisture content (20%) and core compaction (15%) to account for fluctuations during burial and potential variations induced by the coring process.

### *3.2.6. Sources of $D_r$ Uncertainty*

As with most sediments for optical dating, the $D_r$ values within this study have been determined from present-day radionuclide concentrations, moisture contents and sedimentology. The underlying assumption is that there have been minimal fluctuations in these variables during burial. However, the underlying caveats are recognised. Blocked-valley lakes upon the Mfolozi catchment experience flooding, desiccation and even fires (Grenfell *et al.,* 2010), making determination of overburden and moisture content particularly difficult for the South Lake site. Although linear models for sedimentation can be beneficial for $D_r$ calculation in some settings (e.g. Madsen *et al.,* 2005), given the potential sources of variability it was decided not to model sedimentation rates and overburden changes for South Lake, but instead widen the error margin for $D_{cos}$ (16%) and $D_\gamma$ modelling (15% for core compaction). A relatively large error of 20% was also applied to all moisture content values in an attempt to account for past fluctuations in the water table.

Further to the errors provided by Liritzis *et al.* (2013) for conversion of radionuclide concentration to absorbed dose, guidance was taken from Murray & Olley (2002) to account for other systematic errors impacting the evaluation of $D_r$. This included a 3% error for radionuclide estimates obtained by HRGS and a 2% error for attenuation factors. As with all other associated uncertainties, errors were combined in quadrature using either equation 3.7 or 3.8 for addition/subtraction or multiplication/division respectively.

**Eqn. 3.7**

$$\delta_{total} = \sqrt{(\delta a^2) + (\delta b^2) + \ldots}$$

**Eqn. 3.8**

$$\frac{\delta_{total}}{ab \ldots_{total}} = \sqrt{\left(\frac{\delta a}{a}\right)^2 + \left(\frac{\delta b}{b}\right)^2 + \ldots}$$

Where δ = the respective errors of each term.

## 3.3. Evaluating Reliability

### *3.3.1. Modern Analogue: Tropical Storm Domoina Sediments*

The blocked-valley lake environment provides challenging aspects for OSL dating, particularly given the complex sedimentology, relatively low $D_e$ values (those less than 20 Gy; *cf*. Murray & Olley *et al*., 2002) and waterlain origin of sediments. All of the sediments collected from the South Lake site are of unknown age making it difficult to assess the accuracy of age estimates and outline the utility of OSL flood chronologies.

Fortunately, the known-age deposits at the UCOSP site provide the opportunity to test the accuracy and precision of OSL dating Mfolozi flood sediments. As discussed in Chapter 2, the UCOSP section incorporates three different flood/avulsion units associated with storm events that have

occurred over the past century (1925, 1963 and 1984), the most recent of which was caused by Tropical Storm Domoina. Single-grain analysis of the known-age flood deposits not only provides the opportunity to determine the likelihood of OSL estimating the correct age, it enables this study to examine the characteristic $D_e$ distributions associated with flood sediments and isolate the best model for producing representative burial doses.

### *3.3.2. $^{14}C$ AMS Dating*

Given the availability of organic material within the South Lake cores, four samples of plant material were submitted to Beta Analytic for $^{14}C$ AMS (accelerator mass spectrometry) age determination, primarily to further ratify the developed OSL chronologies. AMS dating utilises the radioactive decay of $^{14}C$ as a time-dependant signal. Through respiration the $^{14}C$ of all organisms should be in equilibrium with atmospheric $^{14}C$ until they die, after which $^{14}C$ trapped within the organic matter will undergo radioactive decay. By examining the concentration of $^{14}C$ contained within organic material it is possible to compare concentrations to a standard (atmospheric concentration in 1950) and, following calibration, calculate the time that has elapsed since the associated organism ceased to interact with the atmosphere (respiring).

All $^{14}C$ samples in this study were collected from the hyper-organic depths of the South Lake core where isolation of minerogenics for OSL dating was not possible. There are several potential sources of error which require consideration when sampling lacustrine core material for $^{14}C$ AMS dating. To avoid anomalous ages created by sampling errors, guidance provided by Beta Analytic (2016) was followed to collect and prepare samples for shipping. All sample preparation was conducted on sheets of aluminium foil and powder free nitrile gloves were worn at all times to prevent body oils from contaminating samples. Organic sediments were initially extracted from core tubes as *c.* 2 cm (depth) slices of material, these were transferred in sealed containers to an air-controlled pollen laboratory for preparation to limit the potential of modern carbon being introduced. To prevent sediment which had been stratigraphically displaced by coring from being included within $^{14}C$

analysis, the outer material of each slice was removed and disregarded. Around 5 g of organic sediment remaining from each core slice was wrapped in tin foil and placed in zip-lock bags for shipping. Plant material was isolated during laboratory preparation undertaken by Beta Analytic.

Whilst every precaution was taken during sampling, errors induced by natural processes cannot always be avoided. The $^{14}C$ time-dependant signal represents the point at which respiration ceased within organisms not the point of deposition. If significant time elapsed between the death of an organism and deposition, a $^{14}C$ date would overestimate the age of a sedimentary unit. In some instances, plants can be intrusive and grow into older sediments (Beta Analytic, 2016), in this scenario the inclusion of younger material within $^{14}C$ samples would result in an underestimate of depositional age. Post-depositional reworking by physical or biological processes has the potential to create ages which are either too young or too old. Although the $^{14}C$ samples in this study were collected from sedimentary units which appeared undisturbed, it is not possible to speculate on the depositional history of the organic material analysed and $^{14}C$ ages are considered alongside stratigraphy and the South Lake OSL chronology.

All samples were calibrated using OxCal (Bronk Ramsey, 2009) and the SHCAL13 calibration curve (Hogg *et al.,* 2013). Table 3.2.3 provides an overview of the $^{14}C$ samples processed.

**Table 3.2.3:** $^{14}C$ AMS dates for plant material obtained from the South Lake cores. Ages reported for 68% (1σ) confidence intervals

| Sample | Beta Number | Depth (m) | Radiocarbon Age (BP-1950) | $\delta^{13}C$ (‰) | 1σ Calibrated Age (cal BP) | Age (ka) |
|---|---|---|---|---|---|---|
| SL_AMS_1 | 446039 | 1.20 | 1240 ± 30 | -24.8 | 1186 ± 55 | 1.19 ± 0.06 |
| SL_AMS_2 | 469558 | 0.90 | 1350 ± 30 | -23.4 | 1295 ± 46 | 1.30 ± 0.05 |
| SL_AMS_3A | 485916 | 1.72 | 1480 ± 30 | -28.1 | 1392 ± 23 | 1.39 ± 0.02 |
| SL_AMS_5 | 526302 | 2.71 | 4150 ± 30 | -22.1 | 4729 ± 135 | 4.73 ± 0.14 |

### *3.3.3. Bayesian Modelling*

The work discussed so far forms the basis for Bayesian modelling. Bayesian statistics provide a means to assess the probability of an event occurring based on given, related parameters. It is possible to combine absolute dating information in the form of OSL age estimates with relative information provided by stratigraphical relationships into a Bayesian model, quantifying the quality of the OSL age data set and refining the raw chronology of sedimentation (Rhodes *et al.,* 2003).

Bronk Ramsey (2009) developed the OxCal (v.4.2.) freeware program which is designed to, with the use of Bayesian statistics, assist the analysis of chronological information. The software has been successfully adopted within the radiocarbon dating field, both to calibrate ages and to compile a variety of chronological information (e.g. Hajdas *et al.,* 2006). It is also possible to use the program for Bayesian analysis of luminescence age estimates (e.g. Rhodes *et al.,* 2003).

All Bayesian models are derived from Bayes theorem;

**Eqn. 3.9**

$$p(Depth|OSL) \propto p(OSL|Depth)p(Depth)$$

Where: *p(Depth)* is the prior/ information about the explored parameters, *p(Depth|OSL)* is the likelihood for an OSL estimate at a given Depth and *p(OSL|Depth)* is the posterior probability of a Depth given an OSL age estimate (format adapted from Millard (2006) and Bronk Ramsey (2009)).

The theorem has been adjusted slightly so that it corresponds to the usage in this study. Two parameters are considered for the modelling of each sites' chronology; age estimates and depth. As each OSL age estimate has an associated depth, it is possible to substitute the required parameters into the theorem to estimate an age for a depth of unknown age. When constructing a

Bayesian model for chronological assessment, it is important to note that the errors associated with adjacent age estimates need to overlap in order for the modelling to work and to enhance the chronology (Rhodes *et al.,* 2003). When modelling in OxCal an agreement index is produced, both for the overall model and for individual ages. The overall agreement index enables the reliability of models to be assessed and can indicate whether Bayesian modelling is suitable for the provided parameters. Values for the overall agreement index are expressed in percent and it is recommended that these should not fall below 60% (Bronk Ramsey, 1995). Individual agreement values can be used to assess the suitability of individual samples relative to the created model. These individual agreement values can assist with highlighting problematic ages.

A large proportion of the core samples used in this study incorporated clastic material suitable for OSL, however, some regions of the cores had adjacent OSL age estimates whose errors did not overlap, resulting in some gaps in the chronologies. Where it was not possible to use OSL to fill gaps in the chronologies owing to the organic-rich nature of sediments, $^{14}C$ AMS dates were adopted. The radiocarbon time-dependent signal is independent of the OSL signal. Hence it was also used to verify the accuracy of the OSL-based chronologies and enhance the robustness of the Bayesian age models, particularly for the blocked-valley lake deposits. Bayesian modelling acts as a summarising aspect of this research as it enables all relevant chronostratigraphic information to be drawn together for interpretation of each sites' sedimentology. As such it is utilised in this study to evaluate the stratigraphic consistency of OSL dates and to produce a modelled chronology of sedimentation at each site.

.

# Chapter 4: Origins of Inter-Grain $D_e$ Dispersion

## 4.1. Adopting Quartz Single-Grain OSL

Since the initial development of single-grain stimulation units for $D_e$ measurement (Duller *et al.,* 1999), OSL dating of single quartz grains has been applied to sediments from a diverse range of depositional environments. For young fluvial sediments the development of single-grain OSL systems has been particularly important owing to the increased likelihood of incomplete resetting of the OSL signal and overestimation of burial $D_e$. Rittenour (2008) highlights several processes in fluvial environments which can influence the 'apparent' completeness of bleaching within sediments including the; attenuation of light through water columns, mode of sediment transport, inclusion of unbleached sediment from eroded surfaces and minimal light exposure during high discharge events. Burial doses obtained from multi-grain aliquots of sediments that have experienced such processes can produce significant overestimation of dose, predominantly as a result of averaging or through bright partially bleached grains dominating the OSL signal. Thus, to detect partial bleaching and to isolate a representative burial dose, it is advisable that the smallest aliquot size possible should be used for $D_e$ acquisition (Wallinga, 2002).

Given the water-lain nature of sediments from the Mfolozi catchment and prevalence of feldspar inclusions within UCOSP multi-grain test discs, for this research it was deemed most appropriate to isolate quartz for single-grain $D_e$ measurements where the presence of sufficient quantities of fine sand quartz allowed. Not only does the analysis at the inter-grain level enable the eradication of grains exhibiting feldspar characteristics (e.g. IR depletion), it also provides the opportunity to closely assess $D_e$ distributions and identify discrete grain populations which may not be obvious in multi-grain analysis. Although it was not possible to obtain sand from each sampling location at the South Lake site, recent research indicates that for sediments originating from deltaic and over-bank deposits, the latter of which is associated with

flood units within blocked-valley lake sequences (Grenfell *et al*., 2010), both the sand- and silt-sized quartz fractions are likely to be bleached to an equal extent upon deposition (Chamberlain & Wallinga, 2018). This suggests that it is suitable to integrate both fine- and single-grain OSL ages within the chronicled South Lake sequence and potentially draw inferences from the single-grain $D_e$ distributions about the likely bleaching nature of the adjacent fine-grain units.

When describing the distribution of single-grain $D_e$ values a key parameter which is often used in OSL dating is overdispersion. Overdispersion (OD) can be described as the observed variability for a set of values which is outside of that expected for a Gaussian distribution, for which *c.* 95% of values typically fall within two standard deviations (2σ) of the mean. In OSL dating it is widely accepted that there are numerous factors which can cause OD within $D_e$ distributions. However, well-bleached samples are typically expected to be up to 20% overdispersed (Olley *et al.,* 2004; Arnold & Roberts, 2009). This chapter provides an overview of the sources of OD discussed within the literature and the methods proposed for identification of representative burial doses. It then considers potential, additional source of OD - the impact of hydrofluoric acid (HF) treatments upon single-grain $D_e$ distributions of naturally-dosed quartz grains. The aim of that investigation is to isolate the most suitable HF treatment for 180-250 µm quartz grains undergoing single-grain $D_e$ analysis, with particular attention given to influences of this acid digestion on distribution and OD of $D_e$ estimates.

## 4.2. Sources of Inter-Grain $D_e$ Dispersion

### *4.2.1. Intrinsic Sources*

Whilst significant attention is given to the extrinsic sources of OD for sedimentary samples, existing work examining the OD of laboratory irradiated single quartz grains (both heated and unheated) indicates that there is an underlying intrinsic source of dispersion. Dose-recovery experiments upon single grains of laboratory β- and γ-irradiated quartz have

revealed OD values between 7% and 12% (Jacobs *et al.,* 2006; Thomsen *et al.,* 2007), with greater OD values commonly observed for samples irradiated with a $\gamma$-source. Further work using dose-recovery experiments has highlighted OD as dose-dependent with doses >50 Gy producing greater dispersion and unreliable results (Thomsen *et al.,* 2012). Such trends would be expected following observations by Duller (2012) whose work highlighted significant inter-grain variability in saturation doses ($D_0$), with $D_0$ values varying between 10 and 100 Gy for naturally dosed-quartz grains originating from a single sample. Given the existence of OD for samples which have been artificially bleached and given a known laboratory dose, all sedimentary deposits would be expected to have an underlying, similar OD (*c.* 5-10%) even in the absence of extrinsic influences upon natural $D_e$ distributions. Although saturation doses are sample-dependent, the OD values for the relatively young (Mid- to Late-Holocene) samples of focus in this research are unlikely to be influenced significantly by grains entering saturation.

### *4.2.2. Partial Bleaching*

For samples of fluvial or water-lain origin, significant OD of single-grain $D_e$ populations is commonly attributed to partial bleaching. Partial bleaching tends to occur where sediments have experienced minimal light exposure during transportation owing to attenuation of light through turbid water columns (Berger, 1990), rapid deposition (Gray & Mahan, 2015), variable sediment loads (Jain *et al.,* 2004) or transportation during the night (Rhodes, 2011). Duller (1994) identifies two 'types' (A & B) of partial bleaching; type A occurs where mineral grains are partially bleached to an equal extent thus, display relatively little scatter within $D_e$ distributions and retain similar residual doses. Not only is this type of partial bleaching difficult to detect, but it is unlikely to occur in the natural environment (Duller, 2008). It is more likely that grains experience 'type B' partial bleaching, receiving varying degrees of light exposure and producing scattered $D_e$ distributions (OD >20%) owing to variable residual doses.

It is essential that partial bleaching is identified to avoid age overestimation. At the multi-grain level it is possible to investigate the impact of increasing signal integration time upon the apparent $D_e$ value. By producing a $D_e(t)$ plot (Bailey 2003a; Bailey 2003b) partial bleaching can be inferred where an increase in $D_e$ with stimulation time is observed, with the increase in $D_e$ created by incomplete resetting of the medium- and slow-components of the quartz OSL signal. However, for single-grain CW-OSL the fast-dominated quartz signal is usually isolated and partial bleaching is instead identified by observing the distribution of $D_e$ estimates. For homogenously well-bleached samples which have remained stationary in a homogenous radiation field during burial, the distribution of single-grain $D_e$ values are expected to resemble a normal/Gaussian distribution (Figure 4.2.1a). Whilst for samples which have experienced partial bleaching, $D_e$ values typically produce asymmetric distributions which are positively skewed (Olley *et al.,* 1999; Figure 4.2.1b). The presence of a small fraction of grains which were bleached to a lesser extent upon deposition produce substantial OD and the long tail of skewed distributions.

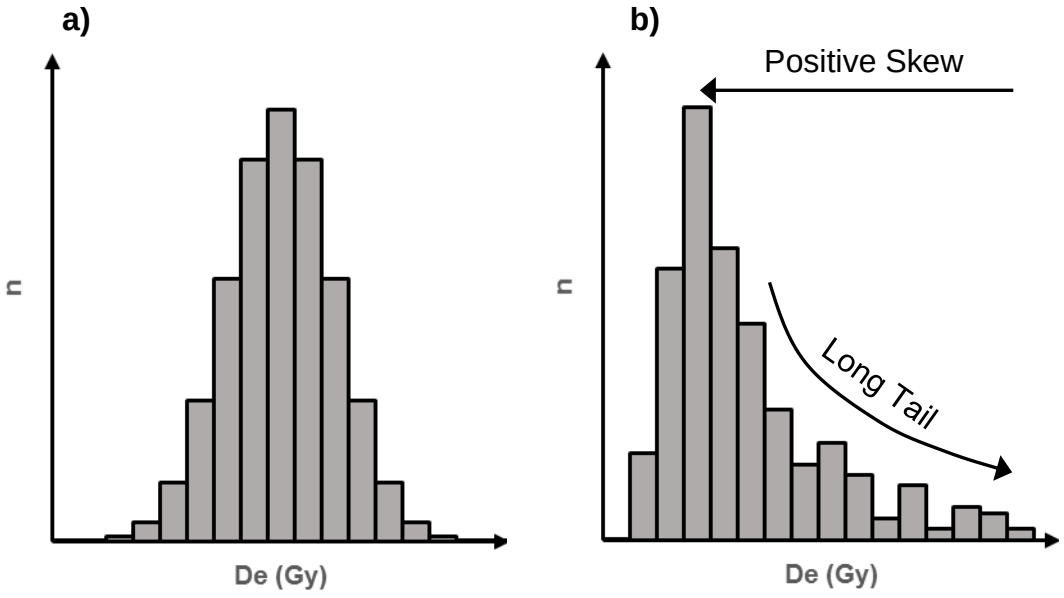


**Figure 4.2.1: a)** A distribution (normal) typically associated with a well-bleached sample **b)** A distribution (positively skewed) typically associated with a partially-bleached sample.

*4.2.3. Mircodosimetry*

Further OD in $D_e$ can arise through the presence of β-microdosimetry. $D_r$ calculation is typically based upon average radionuclide concentrations and the assumption of an infinite matrix dose. However, investigations into β-microdosimetry have shown that radioactive 'hotspots', usually attributed to the presence of $^{40}K$ containing feldspars, can create OD and in some scenarios produce $D_e$ distributions that mimic that of partially bleached samples (i.e. positively skewed – Nathan *et al.,* 2003). For sediments with K contents ranging between 0.1 and 4%, computer modelling indicates that heterogeneous β-microdosimetry can produce 18-46% of the OD for single-grain $D_e$ populations (Mayya *et al.,* 2006). Despite more recent modelling work by Guerin *et al.* (2012) producing slightly different magnitudes of OD created by β-microdosimetry, as with the work from Mayya *et al.* (2006), it was concluded that samples with higher dose rates and/or number of hotspots would experience lower OD in comparison to samples from a low dose/hotspot sediment matrix.

Although early investigations into β-microdosimetry focused primarily upon K-feldspar hotspots as the source of $D_r$ heterogeneity, Jankowski & Jacobs (2018) show that the presence of heavy minerals which contain Th and U can also create significant OD. Given the complexity of microdosimetry it is not currently possible to reduce the absolute uncertainty of age estimates, however, techniques are available for sedimentary deposits to confirm whether β-microdosimetry is likely to be a significant contributor to the observed OD within $D_e$ measurements. Bailiff *et al*. (2013) were able to combine scanning electron microscopy (SEM) with autoradiography to undertake elemental mapping of sediment to assess the spatial variation of $D_r$. Despite their work concluding that spatial variation in $D_r$ was not a contributing factor to OD in their samples, it was suggested that further research at a finer resolution (i.e. sub-millimetre) would be beneficial for the OSL dating community. Subsequently, Martin *et al.* (2015a) explored the potential of DosiVox (Martin *et al.,* 2015b), a β-dosimetry simulation software, for evaluating the distribution of $D_r$ from cave deposits. Following evaluation

of stratigraphy and dosimetry using X-ray fluorescence (XRF), autoradiography, ICP-MS and SEM, Martin *et al.,* (2015a) showed that, in addition to radioelement distribution, water content heterogeneity, compactness of grain-packing and chemical compositions also had significant effects upon β-dosimetry and resultant $D_e$ OD.

A key difference between the OD driven by partial bleaching and that created by microdosimetry is the influence of burial time. Whilst both processes can result in similar $D_e$ distributions, the effect of partial bleaching is believed to lessen with burial time (Rittenour, 2008) as residual doses become less statistically significant with growth in $D_e$. Whereas β-microdosimetry can persist throughout burial time and can amplify the observed spread in $D_e$ distributions, particularly in low $D_r$ environments where hotspots have greatest influence.

### *4.2.4. Pedoturbation*

For near-surface sediments, post-depositional reworking by physical or biological processes (pedoturbation) can have great implications upon observed $D_e$ distributions. Pedoturbation can cause grains to be displaced both vertically and laterally resulting in the inclusion of grains that are older, younger or have been exposed to a different $D_r$ during burial. Initial single-grain investigations into pedoturbation observed the presence of zero-dose grains throughout disturbed sediment profiles and $D_e$ distributions that appeared poorly sorted (overdispersed) and significantly skewed (Bateman *et al.,* 2003). Further work by Bateman *et al.* (2007a; 2007b) identified OD, $D_e$ skewness and trends in the proportion of zero-dose grains as suitable statistical parameters for examining the extent of bioturbation when OSL profiling a sedimentary sequence, particularly in cases where no independent age control is available (Bateman *et al.,* 2007b). Such work has noted that the proportion of zero-dose grains typically reduces with depth as strata become detached from surface processes. More recent work has identified the upper *c.* 50-60 cm of deposits as being the most susceptible to post-depositional mixing (Stockmann *et al.,* 2013; Gliganic *et al.,* 2016), the latter

of whom produced a conceptual model for mixing within aggradational deposits.

The model proposed by Gliganic *et al.* (2016) assumes temporal stability in mixing processes and solely on the downward mixing of grains. Whilst this does not incorporate the complexity of natural sediments, that is the bi-directional movement of grains, it does provide a basic appreciation of the relationships buried strata have with surface sediments. For aggradational environments it is proposed that there are three 'zones'; zone 1 (0-50 cm depth), zone 2 (50-60 cm) and zone 3 (>60 cm). Zones 1 and 2 are considered active mixing regions whilst the effects of mixing in zone 3 are thought to be negligible, as indicated by systematic change in minimum $D_e$, proportion of zero-dose grains and skewness with depth. By following a similar approach to Gliganic *et al.* (2016) it may be possible to identify the presence of disturbed sediments, however, significant difficulties remain in isolating representative burial doses for sediments significantly impacted by pedoturbation (e.g. Lombard *et al.,* 2010; Lomax *et al.,* 2011). Although statistical models exist to aid in distinguishing $D_e$ populations (see section 4.3), the correct burial doses are not always represented by the highest frequency of values within a given $D_e$ distribution (Rhodes *et al.,* 2010), complicating ratification of age estimates. In some scenarios post-depositional modelling may have occurred to such an extent that age calculation is not possible (Stockmann *et al.,* 2013), particularly where other contextual information is unavailable.

With regards the expected impact of pedoturbation upon $D_e$ distribution it is necessary to consider separate scenarios as to where grains could have migrated to/from. Bateman *et al.* (2003) provides some hypothetical scenarios and the anticipated $D_e$ distributions for sediments impacted by post-depositional mixing, these are summarised in Table 4.2.1.

**Table 4.2.1:** Impact of pedoturbation scenarios upon $D_e$ distribution (after: Bateman *et al.,* 2003).

| Scenario | Impact upon $D_e$ Distribution |
|---|---|
| Inclusion of older material | Positively skewed distribution – potentially bimodal |
| Inclusion of younger material | Negatively skewed distribution – potentially bimodal |
| Significant mixing | Wide range of $D_e$ values produced – no strong peak |
| Well-bleached and undisturbed | Strong narrow peak – with a small distribution |

Whilst the distributions highlighted in Table 4.2.1 are useful for assessing pedoturbation, careful consideration is required before concluding which process is responsible for any $D_e$ distribution. Particularly when using the example of a positively skewed dataset as this can be attributed to partial bleaching, microdosimetry and pedoturbation. If more than one extrinsic process is contributing to the observed $D_e$ dispersion it can be difficult to isolate the dominant driver of dispersion and subsequently the appropriate burial dose.

### *4.2.5. Preparation and Measurement Uncertainties*

Given the inter-sample variability in optimum preheat temperatures for quartz grains undergoing SAR measurements, one of the greatest undetectable uncertainties is the sensitivity change that grains experience during the first preheat of a measurement cycle. Although dose-recovery tests pinpoint a preheat temperature which best recovers an artificial dose, they do not account for any changes that occur to the natural signal following the first

exposure to elevated temperatures. It remains very difficult to speculate whether or not, and by what magnitude, the initial thermal treatment is likely to contribute to the OD of single-grain $D_e$ distributions.

During laboratory preparation quartz is isolated from sedimentary samples, this includes isolation of a specific grain size fraction to which the radioactive source used in measurement is calibrated. For natural samples it is unlikely that the distribution of grains will be evenly distributed across the selected fraction suggesting some calibration uncertainty will arise. Armitage & Bailey (2005) suggested that for multi-grain aliquots measured using a Risø TL-DA-15 reader the variation in source $D_r$ to sand-sized quartz is negligible. More recently, Hansen *et al.* (2018) calculated that for the 180-250 μm grain fraction a maximum variation in source $D_r$ of 5% could be expected to single grains of quartz, however, they highlight that in practice this is much lower given the distribution of grain sizes within a fraction.

A majority of the laboratory procedures used for quartz OSL preparation are non-destructive and the appropriate precautions are taken to ensure preservation of the UV-sensitive signal. However, one particular stage that physically alters the shape of quartz grains is the use of hydrofluoric acid. This acid treatment is adopted primarily to simplify calculation of $D_r$ as the α-irradiated rind of quartz grains is considered to be reduced to negligible levels. Although investigations into sources of single-grain OSL variability by Thomsen *et al.* (2005) found that HF etching had no impact upon $D_e$ variance for laboratory γ-irradiated material, little attention has been paid to the impact of HF treatment upon single-grain $D_e$ distributions for naturally-dosed samples. This is particularly important given that samples display variable resistance to HF and that treatments can significantly modify grain size distribution (Porat *et al.,* 2015; Duval *et al.,* 2018). This is explored further in section 4.4.

### 4.3. Identification of Burial Dose

Whilst standard statistical measures may be suitable to assess some $D_e$ distributions, the highlighted extrinsic forces upon OD can complicate

interpretation and make isolation of a representative burial dose difficult. Numerous modelling and statistical methods have been developed to assist with the deconvolution of $D_e$ distributions. Selection of the appropriate model can be dependant of the nature of deposition and conditions during burial. Whilst statistical models are able to isolate $D_e$ populations it is important to consider that calculated $D_r$ values are averages and selection of the inappropriate age model could result in age discrepancies.

### *4.3.1. Lowest 5%*

A relatively straightforward approach for young fluvial samples which exhibit partial bleaching is the 'lowest 5%' method, as adopted by Olley *et al.* (1998). Suggested for dating sediments deposited within the past 500 years, the mean is calculated from the 5% of aliquots producing the smallest $D_e$ values. Within their study Olley *et al.* (1998) observed asymmetric $D_e$ distributions for two 'modern' fluvial samples of known age (5 and 70 years) and by isolating the lowest 5% of values were able to produce $D_e$ estimates consistent with zero and correct OSL ages of 64±7 years for youngest and oldest sample respectively.

Although the lowest 5% method worked in the context of the above samples Bailey & Arnold (2006) note that in a majority of cases the lowest 5% method will underestimate the true burial dose. They also note that the use of the lowest 5% of values is effectively calibrated to the known age of the deposits dated by Olley *et al.* (1998) and suggests a different proportion of $D_e$ values may be suited to other scenarios therefore referring to the method instead as the 'lowest x%'.

### *4.3.2. Leading Edge*

Lepper *et al.* (2000) employed the hypothesis that the distribution of $D_e$ values are convolutions of dispersion arising from experimental error, sedimentary and depositional processes. Using fluvial and aeolian quartz from Oklahoma they demonstrate that by using regenerative doses to assess measurement uncertainty, deconvolution can be conducted upon measured

$D_e$ values to isolate a distribution with a sharp leading edge that is solely influenced by natural processes (Figure 4.3.1).

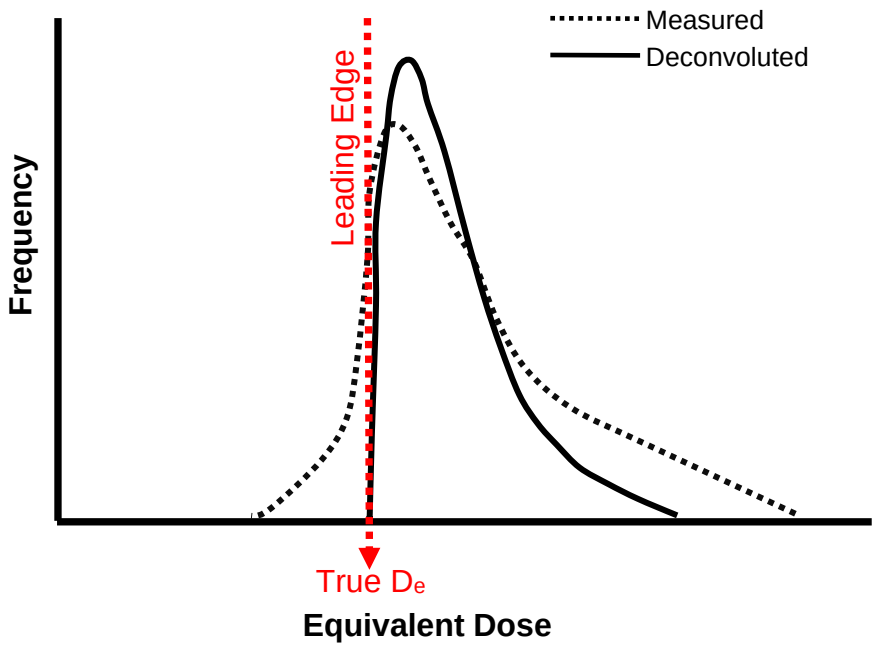


**Figure 4.3.1:** Schematic of deconvolution of a measured $D_e$ distribution (After: Lepper *et al.*, 2000)

Following deconvolution Lepper *et al.* (2000) suggest constructing a histogram using the median $D_e$ error to define bin width. From the distribution the 'true' $D_e$ is then calculated using equation 4.1, whilst slope and sharpness are used as confidence parameters (equation 4.2 and 4.3).

**Eqn. 4.1**

$$D_{e\ True}\ (Gy) = D_{e\ mode} + D_{e\ min} / 2 \pm D_{e\ mode} - D_{e\ min} / 2$$

**Eqn. 4.2**

$$Slope\ (Gy^{-1}) = n_{mode} - n_{min} / D_{e\ mode} - D_{e\ min}$$

**Eqn. 4.3**

$$Sharpness\ (Gy^{-2}) = slope / bin\ width$$

Where: $D_{e\ mode}$ = bin containing the highest frequency, $D_{e\ min}$ = minimum $D_e$ value, $n_{mode}$ = frequency in the highest occurring bin and $n_{min}$ = frequency in the lowest $D_e$ bin.

Subsequent work by Lepper & McKeever (2002) details a simplified approach to the leading edge technique which does not require deconvolution of a dataset. Following construction of a histogram using median $D_e$ error to define bin width, bin centre and bin frequency are transformed into x,y coordinates and the $D_e$ is calculated from the second derivative of a Gaussian equation fitted to the rising limb of the distribution. Further modifications to this leading edge approach were suggested by Woda & Fuchs (2008) who noted that the fitting parameter suggested by Lepper & McKeever (2002) had a relatively poor success rate, particularly when only a small number of aliquots were available. By fixing the centre of the Gaussian function to the modal bin and by fitting a two parameter function to data sets Woda & Fuchs (2008) suggest that an 80% improvement in successful fitting could be achieved.

The underlying assumption for leading edge methods is that the sharp edge should be present in heterogeneously bleached $D_e$ distributions as quartz grains cannot have their OSL signal reset to less than zero when exposed to sunlight. If partial bleaching were solely responsible for an observed skewed distribution then the leading edge technique would appear a logical choice for isolation of $D_e$ as it would select the grains which were fully bleached upon deposition. However, given the complexity of many natural sediments it is likely that more than one factor will contribute to the observed dispersion within a dataset and, in addition to relatively high associated errors (Olley *et al.,* 2004), it has been observed that leading edge techniques frequently underestimate $D_e$ (Bailey & Arnold, 2006).

### *4.3.3. Fuchs & Lang (2001)*

Within their study of fluvial quartz from Greece, Fuchs & Lang (2001) identified a large scatter in $D_e$ values which they attributed to heterogeneous bleaching. Given the limited amount of quartz available only 9-10 aliquots

could be produced for $D_e$ estimation and the resultant arithmetic means produced overestimates of $D_e$. To produce representative estimates it was suggested that dose recovery tests should be conducted on laboratory bleached/irradiated quartz to identify the variability (relative standard deviation) arising from measurement uncertainty. Using the relative standard deviation obtained in dose-recovery tests (4%), Fuchs & Lang (2001) ordered natural $D_e$ values in numerical order and selected the smallest two $D_e$ values calculating the arithmetic $D_e$ progressively, including 1 additional $D_e$ value for each iteration. Once the 4% variability was just exceeded they used the mean value for age calculation.

A similar approach was taken by Zhang *et al.* (2003), however, rather than conducting separate dose-recovery tests to assess measurement variability, the first regeneration point was treated as an unknown dose. In their study the sensitivity corrected natural signals ($L_n/T_x$) were ordered from smallest to largest and in the same manner as Fuchs & Lang (2001) the mean $D_e$ was calculated progressively until the relative standard deviation calculated from the first regenerative dose was achieved. In the case of Zhang *et al.* (2003), they believe this isolated the well-bleached proportion of aliquots. Both of these techniques were explored by Olley *et al.* (2004) upon single-grain distributions from Holocene marine sediments; they found that in both cases $D_e$ was substantially underestimated.

### *4.3.4. Common Age Model*

The precision of $D_e$ values obtained from both aliquots and single-grains is often highly variable and to establish a common mean it is suggested that each $D_e$ value should first be weighted by the inverse square of its standard error (Galbraith & Roberts, 2012). For many of the age (dose) models commonly adopted throughout the literature $D_e$ data sets are also log-transformed to natural logarithms (ln) prior to statistical analysis.

The common age model proposed by Galbraith *et al.* (1999) considers an 'ideal' sample, whereby grains have been fully bleached and received the same $D_r$ throughout burial. Such a sample would be expected to produce a

normal $D_e$ distribution with negligible OD and 95% of values that fall within two standard deviations of the mean. The common log palaeodose ($\delta$) and associated standard error (se($\delta$)) for such a sample can be calculated as follows:

**Eqn. 4.4**

$$\hat{\delta} = \frac{\sum_{i=1}^{n} w_i \hat{\delta}_i}{\sum_{i=1}^{n} w_i}$$

**Eqn. 4.5**

$$se(\hat{\delta}) = \left(\sum w_i\right)^{-\frac{1}{2}}$$

Where: $\hat{\delta}_i$ = the estimated log $D_e$ of grain $i$ with standard error $\sigma_{wi}$ and $w_i$ = $1/\sigma_{wi}$.

*4.3.5. Central Age Model*

In a majority of cases $D_e$ distributions will display some degree of OD, for which the common age model is not appropriate. The central age model (CAM) also proposed by Galbraith *et al.* (1999) is similar to the common age model but includes the additional unknown parameter 'σ' which represents the OD of a $D_e$ dataset. In some instances CAM is only used as a tool to provide an estimate of OD (e.g. Guerin *et al.,* 2017). Estimates of the central log palaeodose ($\delta$) and OD (σ) are calculated by simultaneously solving equation 4.4 and 4.6, with standard errors for each parameter calculated using equation 4.5 and 4.7 (note the change in weighting of $w_i$).

**Eqn. 4.6**

$$\sum_{i=1}^{n} {w_i}^2 (\widehat{\delta_i} - \delta)^2 = \sum_{i=1}^{n} w_i$$

**Eqn. 4.7**

$$se(\hat{\sigma}) = \left(2\sigma^2 \sum_{i=1}^{n} {w_i}^2\right)$$

Where: $w_i = 1/(\sigma^2 + {\sigma_{wi}}^2)$

*4.3.6. Minimum Age Model*

The common and central age models are suitable where a log-normal distribution exists. However, many fluvial samples include partially-bleached grains and produce truncated $D_e$ distributions. In such instances the central age model is likely to overestimate the true burial dose and the minimum age model (Galbraith *et al.,* 1999) may be more suited. The minimum age model (MAM) is comprised of four components; minimum log dose ($\gamma$), proportion of fully-bleached grains upon burial ($\rho$) plus $\mu$ and $\sigma$ which would correspond to the mean and standard deviation (respectively) of the log-$D_e$ distribution if it were non-truncated. However, given that MAM is typically used for heterogeneously bleached samples both $\mu$ and $\sigma$ are adjustable parameters within the model. In some cases it is not possible to fit all four components within the MAM so a three parameter model (MAM-3) is suggested where $\gamma = \mu$.

Galbraith *et al.* (1999) highlight that calculation of MAM and isolation of values for each parameter is complex and that assistance can be provided by statistical software. Recently the 'Luminescence' R package (Kreutzer *et al.,* 2012; Kreutzer *et al.,* 2018) has been developed which enables the analysis of many forms of luminescence data and the application of age models. For MAM the Luminescence package calculates and profiles the log-likelihood for each parameter selecting a suitable value for each unknown. Subsequently the minimum dose and standard error can be calculated. For this research age models were applied to $D_e$ datasets using the Luminescence package. An important consideration for the MAM model is that it selects a low-dose population and although this could isolate those values which were bleached

to the greatest extent upon deposition it could also isolate those which have experienced a low $D_r$ or have migrated from younger strata.

An interesting adaption to the MAM is proposed by Olley *et al.* (2006), using samples collected from grave-infill it was determined that, given the likelihood of complete bleaching upon deposition, sample collection had resulted in contamination of light-exposed material. It was determined that the population of grains with the highest $D_e$ values would best represent the true burial dose. To isolate the maximum dose Olley *et al.* (2006) multiplied logged $D_e$ values by -1, inverting the distribution. Subsequently the minimum age model was applied to the exponent of the inverted data, following transformation of the minimum dose an OSL age consistent with the estimated age of the deposits was produced. This application of the 'maximum age model' would potentially suit samples impacted by pedoturbation and the downward mixing of grains.

### *4.3.7. Finite Mixture Model*

The finite mixture model (FMM) was initially developed for fission track dating but has since been adopted for use upon OSL $D_e$ distributions (Galbraith & Green, 1990; Galbraith, 2005; Roberts *et al.,* 2000). The model is designed to identify and isolate discrete components that exist within a population that have potentially arisen from the physical mixing of sediment. The model considers a log distribution of values containing normally distributed components ($k$) which have a common standard deviation (σ), producing means ($\mu_1$, $\mu_2$,…$\mu_k$) and proportion of values within each component ($\pi_1$, $\pi_2$,…$\pi_k$). If $k$=1 the FMM becomes the CAM.

To apply the model a value for σ is set for all components; this represents the variance arising from measurement uncertainty and inter-grain variability. Using synthetic mixtures of laboratory-irradiated quartz Roberts *et al.* (2000) set σ to 0.11 and 0.20 (i.e. 11% & 20%) and found that the FMM was able to identify the correct doses in both scenarios. However, they also found that when σ = 0.2 the incorrect mixing proportion was calculated, highlighting the importance of selecting an appropriate value. Arnold & Roberts (2009)

suggest that users of the FMM may opt to use a value for σ which is of a similar magnitude to 0.1 given that this is the expected best case scenario for OD of a fully-bleached, undisturbed sample. In subsequent work Galbraith & Roberts (2012) suggest that, in the absence of an estimate of σ from the same material being dated, a better approach is to bracket the potential σ-values for a well-bleached sample. As an example they suggest calculating age models using σ=0.10 and σ=0.20 and selecting the most appropriate fit, this is also applicable for defining σ within the MAM model.

When using the FMM upon natural $D_e$ distributions the total number of components ($k$) within a population is often unknown and the most suitable parameters have to be determined iteratively. Two numerical indices are typically used to isolate the most appropriate number of components and/or σ -value for the FMM; the maximum log likelihood ($L_{max}$) and Bayes Information Criterion (BIC). When the fit of the FMM is improved by an additional component the value of $L_{max}$ is expected to increase significantly (≥2) and will continue to do so until a redundant component is added where an increase in $L_{max}$ will be minimal (Roberts *et al.,* 2000). The BIC value incorporates $L_{max}$ but reduces in value when an improvement in FMM fit is observed, whilst a rise indicates that additional components are unnecessary (Galbraith, 2005; Galbraith & Roberts, 2012). The FMM parameters producing the lowest BIC value/score typically indicates the optimum fitting. For samples in this research application of the FMM was also conducted in the 'Luminescence' R package and optimum fittings were informed by both $L_{max}$ and BIC values.

### *4.3.8. Model Selection and Suitability*

The age models incorporating the standard errors for individual $D_e$ estimates (4.3.4 onwards) are generally considered the more robust. However, selecting the most appropriate model for samples of unknown age can present a challenge. To select an appropriate age model based on statistical grounds the decision tree produced by Bailey & Arnold (2006) can be adopted. This decision process utilises the statistical parameters; skewness ($c$), kurtosis ($k$), OD (σ) and presence of negative $D_e$ values to determine

whether the Lowest 5%, CAM or MAM (3- and 4-paramter) is appropriate for a $D_e$ dataset. Whilst they state that in some scenarios no age model will be suitable, they suggest in a majority of cases (*c.* 85%) their decision tree process will identify the most appropriate model. More recent single-grain work from Thomsen *et al.* (2016) criticises the decision tree process as it was found that age model selection resulted in significant underestimation of $D_e$ for both natural and laboratory-irradiated quartz grains.

The $L_{max}$ and BIC values used for setting the parameters of the FMM can also be used to assess the suitability of the MAM and could be used to determine which, if any, model best suits a $D_e$ distribution. Given the sample-dependant nature of age-modelling numerous models are explored for each of the samples presented in this research. The statistical parameters used by Bailey & Arnold (2006) are also explored to examine the nature of $D_e$ datasets.

## 4.4. Hydrofluoric Acid Etching of Quartz Grains

### *4.4.1. Overview*

Prior to making quartz OSL $D_e$ measurements a number of preparation stages are required to refine collected material to a pure quartz state. These pre-treatments remain relatively standardised between luminescence laboratories, however, within the literature it is evident that there are some subtle inter-laboratory differences.

A particular focus here is the 40-48% HF treatment which combines to remove low-density minerals that might remain after density separation and chemically-etch the alpha (α) irradiated rind of sand-sized quartz grains. Within quartz luminescence dating (OSL and TL) it is assumed that the α affected regions of quartz grains within the 90-120 μm fraction, are reduced to negligible levels (2.5 - 5%) following a 40 minute HF acid treatment (Bell & Zimmerman, 1978). This enables simplification of age calculation as only the beta (β) and gamma ($\gamma$) components need to be considered for dose rate contribution.

When considering physical change, it is reported that a 40 minute HF treatment results in the outer ~10 μm of quartz grains being removed, for a sample with an average grain diameter of 137.5 μm (Hong, 1998). Despite the assumption that such a treatment will sufficiently reduce the α-component, it is well noted that the HF etching is not isotropic. Preferential etching will often occur across faults and fissures within the quartz lattice; such heterogeneous etching can result in residual α doses (Goedicke, 1984). To complicate matters further, samples display variable resistance to HF treatments and some quartz grains will etch more quickly than others (Aitken, 1985, p. 256). Mineralogically less mature samples in particular have been found to be less resistant and can lose their outer 30-50 μm during a 40 minute HF etch (Porat *et al*., 2015).

Little attention has been paid to the consistency of HF treatments across the fine/medium grain sand fractions. HF strength can vary (40-48%) and treatment times for applied OSL studies range from 30 minutes (e.g. Owen et al., 2002) to 80 minutes (e.g. Srivastava et al., 2001) for various grain fractions, highlighting a potential source of inter-grain $D_e$ variability. In addition, there is little mention of a suitable sample mass to HF ratio, Porat *et al.* (2015) being the exception (5 cc per gram of quartz), and it is likely that inter-laboratory variations occur. Furthermore, Duval *et al.* (2018) highlight a significant increase in quartz etch-depth when samples are continuously agitated for the adopted treatment time and suggest halving treatment time to accommodate this. Given the variation in HF treatment observed from the literature, there is a need to investigate and refine quartz HF treatment further.

A large proportion of existing research upon the HF etching of quartz grains focuses on physical change, either inferred through weight-loss or using SEM. Most investigations into the impact of treatment upon $D_e$ were conducted at the multi-grain level prior to the development of single-grain OSL measurement systems. Although these multi-grain studies provide a good indication of the impact upon average $D_e$ values, they cannot detect any inter-grain variations created by the HF treatment. Interpretation of single-grain $D_e$ distributions is already complex owing to the potential

combined influences of micro-dosimetry, partial bleaching, pedoturbation and variable inter-grain response to measurement protocols. Should HF treatment also impact distributions and OD values, it would need to be accommodated in the interpretation of single-grain OSL data.

Although Thomsen *et al.* (2005) concluded that acid etching has negligible impacts upon single-grain $D_e$ variance, their investigation solely used artificially-irradiated grains which were etched prior to dosing. To date, no single-grain investigations into the impact of variable HF treatments upon naturally-dosed quartz $D_e$ distributions has been undertaken. Here the impacts of varying HF to sample ratios and HF treatment time have been investigated at the single-grain level using the 180-250 µm quartz fraction. As typical single-grain measurement discs consist of 100 holes 300 µm in diameter, by selecting this grain fraction the likelihood of more than one grain being in each measurement position is significantly reduced. In addition to contributing to the existing knowledge on HF etching, this investigation will assist in producing a suitable methodology for the preparation of fine/medium sand palaeoflood deposits from the Mfolozi catchment.

### *4.4.2. Methods*

Three samples were used in this investigation; GL14023 a fluvial sample originating from the River Meuse in the Netherlands, GL15025 a basal sand unit from the South Lake site on the Mfolozi catchment and GL16180 an eolian dune sample from NSW, Australia. Samples were selected based upon previous SAR measurement performance, sedimentary origin and material availability. Sample selection also provided a geographical spread in origin.

Quartz grains were isolated using the standard coarse-grain procedures outlined in section 3.1.1, including dry sieving to isolate the 180-250 µm fraction, 10% HCl to remove carbonates, ramped $H_2O_2$ to remove organics and density separations at 2.62 and 2.68 g $cm^{-3}$ to isolate quartz-density minerals. Given the large sample mass, GL14023 was used to evaluate both the influence of HF time and HF to sample mass ratio. Samples GL15025

and GL16180 were used to extend the study of the influence of HF treatment time. All treatments were conducted under subdued red lighting conditions where (with the exception of the control/untreated sub-sample) 100 ml of 40% HF was poured onto quartz grains deposited on the base of polypropylene beakers. Continuous magnetic stirring was adopted to disperse the material during treatment. Following treatment, samples were neutralised with distilled water and were subsequently rinsed in 10% HCl to remove acid soluble fluorides. Contrary to the suggestion by Porat *et al.* (2015), samples were re-sieved using the same mesh sizes adopted for dry sieving so that confidence in single-grain beta source calibration could be retained. The matrix of treatments is shown in Table 4.4.1

**Table 4.4.1:** Summary of 100 ml HF treatments and remaining material

| Sample | Treated Mass (g) | Treatment Time (g) | Post- HF Mass (g) | Post-re-sieve Mass (g) |
|---|---|---|---|---|
| **GL14023** | 0 (Control) | 0 | - | - |
| | 2.46 | 60 | 1.054 | 0.408 |
| | 4.92 | 30 | 3.118 | 2.393 |
| | 4.92 | 60 | 3.276 | 2.378 |
| | 4.92 | 90 | 2.214 | 1.312 |
| | 9.84 | 60 | 7.051 | 5.775 |
| **GL15025** | 0 (Control) | 0 | - | - |
| | 5 | 30 | 3.103 | 2.007 |
| | 5 | 60 | 2.912 | 1.825 |
| | 5 | 90 | 2.677 | 1.654 |
| | 5 | 120 | 2.431 | 1.587 |
| **GL16180** | 0 (Control) | 0 | - | - |
| | 5 | 30 | 3.546 | 2.431 |
| | 5 | 60 | 3.421 | 2.097 |
| | 5 | 90 | 2.937 | 1.864 |
| | 5 | 120 | 2.544 | 1.643 |

Single-grain measurements were conducted using the SAR protocol and the same instrumentation highlighted in 3.1.3. Preheat temperatures of 240°C (GL15025) and 280°C (GL14023 & 16180) were selected using dose-recovery tests at the multi-grain level for the 60 minute HF treatment of each sample. A cut heat temperature of 220°C was adopted for all samples. To standardise measurement procedures, preheat temperatures were retained for each treatment scenario. Within single-grain analysis rejection criteria based upon SAR measurement performance and signal detectability are often adopted. Rejection criteria effectively filter the grains that produce little/no signal and perform poorly during measurement from analysis. For this investigation grains were rejected if their post-IR/OSL depletion ratio fell outside of 10% (i.e. 1.00 ± 0.10) and signal recuperation was >5%. Grains were also rejected if their observed OSL signal was less than 3σ above background levels. Recycling ratios were adjusted to produce two orders of precision; 'strict' rejection criteria where grains were rejected if mean recycling values fell outside of 10% and 'relaxed' criteria whereby grains were rejected if associated recycling errors did not overlap with 10% of unity. For example, a recycling ratio of 0.86±0.05 would be rejected by the more stringent criteria but accepted by the more relaxed.

**Figure 4.4.1:** Microscope set-up for grain image capture

In addition to examining the impacts upon $D_e$ distribution, image analysis was conducted upon quartz grains for each HF treatment. Images were collected using a low-powered microscope with a stage micrometre (Figure 4.4.1) and were analysed in ImageJ (Schneider *et al.,* 2012). To assess variability in grain size between treatments grains from the raw images (Figure 4.4.2a) were outlined and the background removed (Figure 4.4.2b). Both the perimeter and area (2D) were automatically calculated and used for inferring change in overall grain size. In some instances image processing was unable to successfully identify the 'true' edges of grains, in such cases these were removed from analysis (e.g. circled grain in Figure 4.4.2b).

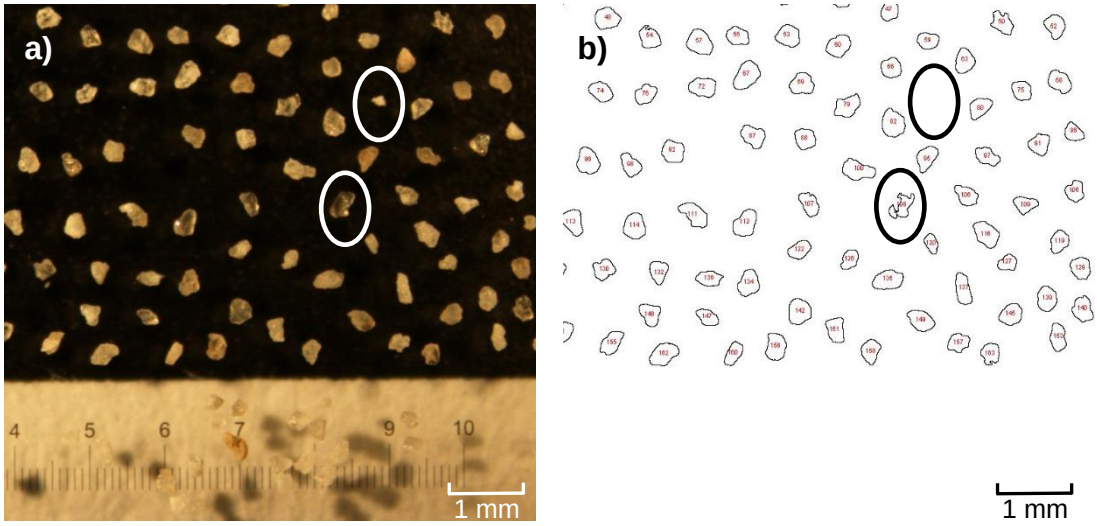


**Figure 4.4.2:** a) Raw image of GL15025 quartz grains following 90 minute HF etch; b) Processed image with outlined grains – circled grain edges unsuccessfully identified.

### *4.4.3. Results*

#### *4.4.3.1 Variation in Sample Mass Treated – Physical Change*

Investigation into the effects of varying sample mass treated with 100 ml of 40% hydrofluoric acid were conducted using sample GL14023. The treatment of 2.46 g of material displayed the greatest loss in mass and experienced a 57% and 83% loss pre- and post-re-sieve respectively (Figure 4.4.3). The relative loss in mass prior to re-sieving was greater for the 2.46 g scenario

than the loss experienced by the other treated masses following re-sieving. Treatment of 4.92 and 9.84 g of material displayed similar relative mass loss following a 60 minute treatment (28 & 33%). However, the difference in relative mass loss widened slightly following re-sieving, with the 4.92 g treatment scenario losing 52% of the overall mass and the 9.84 g scenario losing 41%. Relative mass loss appears to be greater when a smaller mass is treated with 100 ml of HF for the 60 minute duration. It is likely that the effectiveness of HF is reduced by the dissolution of more material when greater masses are treated.

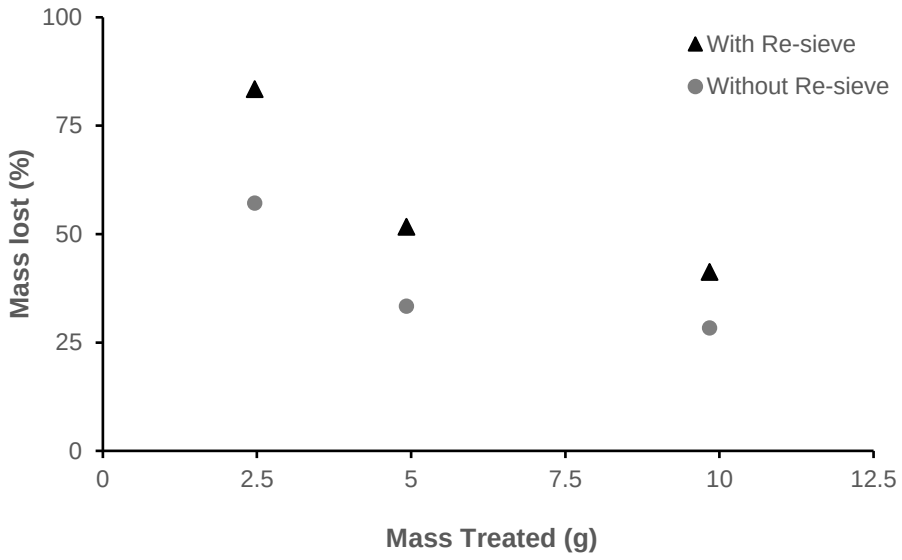


**Figure 4.4.3:** Mass lost following a 60 minute HF treatment of 2.46, 4.92 and 9.84 g of 180-250 µm quartz from GL14023 (with and without re-sieving)

Image analysis, conducted only on the re-sieved material, displayed no systematic change in the average perimeter or area of grains (Figure 4.4.4). All treatment scenarios displayed a reduction in average grain area and perimeter following HF treatment. For the 4.92 g treatment the average perimeter appears to be significantly lower than the treatments of 2.46 and 9.84 g of material, however, in actual terms this only represents *c.* 30 µm difference in average perimeter.

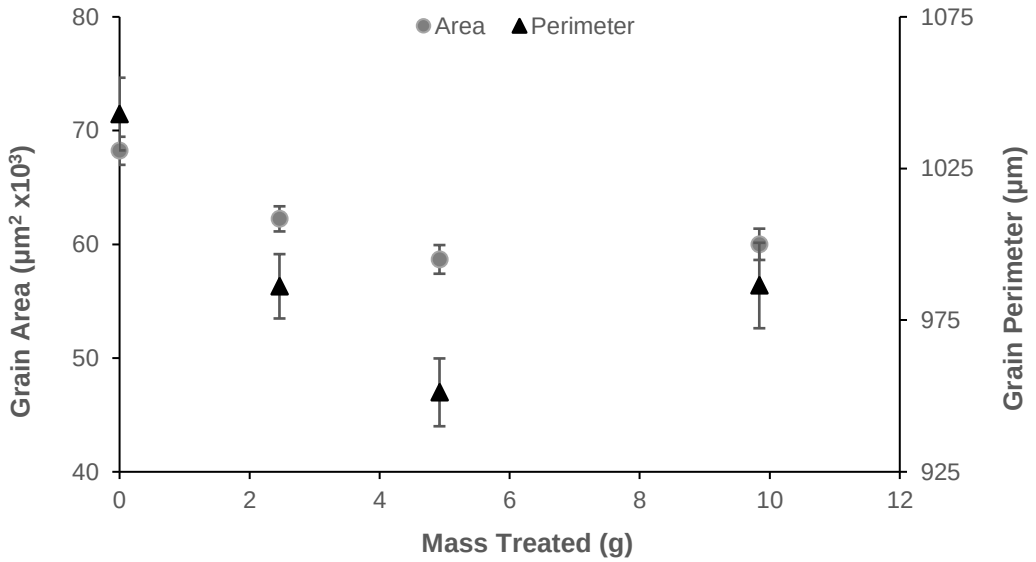


**Figure 4.4.4:** Average grain area and perimeter with standard errors following a 60 minute HF treatment (and re-sieve) of 2.46, 4.92 and 9.84 g of 180-250 µm quartz from GL14023 (Untreated fraction at 0 on x-axis).

*4.4.3.2 Variation in Sample Mass Treated – Impact upon $D_e$*

$D_e$ values obtained using both 'strict' and 'relaxed' rejection criteria are highlighted in Table 4.4.2 and 4.4.3 respectively. In both cases the proportion of grains that were accepted following HF treatment appears to increase with a reduction in sample mass treated. A similar pattern is exhibited in the proportion of grains which fall within 2σ of the median $D_e$ value with exception the of the control and 9.84 g values, which appear to be reversed when applying the relaxed rejection criteria.

For central measures of $D_e$ (i.e. median and CAM) all HF treatments produce $D_e$ values consistent with the untreated fraction for the 'relaxed' rejection criteria. With exception of median $D_e$ for the 9.84 g treatment, this is also the case when strict rejection criteria are applied. Minimum age modelling of each treatment also produces values consistent with the untreated fraction when the relaxed rejection criteria are adopted. However, when strict criteria are used the 4.92 g treatment produces a significantly elevated dose (8.05 ± 0.63 Gy) relative to the untreated fraction (6.43 ± 0.56 Gy).

**Table 4.4.2:** Summary of single-grain $D_e$ values for various masses of GL14023 treated with 100 ml of HF, strict rejection criteria adopted (errors reported with 1σ confidence)

| Mass Treated (g) | Treatment Time (mins) | Grains Measured | Grains Accepted (Number (%)) | Within 2σ (%) | $D_e$ values (Gy) | | | | | | |
|---|---|---|---|---|---|---|---|---|---|---|---|
| | | | | | Median | CAM | MAM | FMM *k** | $FMM_{min}$ | $FMM_{max}$ | $FMM_{maj}$ |
| N/A | 0 | 6000 | 24 (0.40) | 37.5 | 9.39 ± 0.57 | 8.87 ± 0.56 | 6.43 ± 0.56 | 2 | 6.72 ± 0.40 | 10.64 ± 0.55 | 10.64 ± 0.55 |
| 2.46 | 60 | 3900 | 38 (0.97) | 60.5 | 8.84 ± 0.44 | 8.77 ± 0.44 | 7.06 ± 0.45 | 2 | 6.61 ± 0.45 | 9.67 ± 0.43 | 9.67 ± 0.43 |
| 4.92 | 60 | 3900 | 27 (0.69) | 48.1 | 9.50 ± 0.49 | 9.43 ± 0.49 | 8.05 ± 0.63 | 2 | 8.42 ± 0.51 | 11.39 ± 0.83 | 8.42 ± 0.51 |
| 9.84 | 60 | 3900 | 24 (0.62) | 41.7 | 8.16 ± 0.48 | 8.15 ± 0.47 | 6.51 ± 0.53 | 2 | 6.66 ± 0.52 | 9.52 ± 0.63 | 9.52 ± 0.63 |



**Table 4.4.3:** Summary of single-grain $D_e$ values for various masses of GL14023 treated with 100 ml of HF, relaxed rejection criteria adopted (errors reported with 1σ confidence)

| Mass Treated (g) | Treatment Time (mins) | Grains Measured | Grains Accepted (Number (%)) | Within 2σ (%) | $D_e$ values (Gy) | | | | | | |
|---|---|---|---|---|---|---|---|---|---|---|---|
| | | | | | Median | CAM | MAM | FMM *k** | $FMM_{min}$ | $FMM_{max}$ | $FMM_{maj}$ |
| N/A | 0 | 6000 | 95 (1.58) | 53.7 | 9.58 ± 0.43 | 9.51 ± 0.42 | 6.89 ± 0.39 | 3 | 6.60 ± 0.54 | 12.55 ± 0.99 | 9.41 ± 0.97 |
| 2.46 | 60 | 3900 | 104 (2.67) | 59.6 | 9.31 ± 0.40 | 9.20 ± 0.40 | 7.15 ± 0.41 | 3 | 6.56 ± 0.39 | 12.34 ± 0.81 | 9.43 ± 0.46 |
| 4.92 | 60 | 3900 | 96 (2.46) | 58.3 | 9.50 ± 0.42 | 9.46 ± 0.40 | 7.48 ± 0.45 | 2 | 8.02 ± 0.40 | 11.32 ± 0.56 | 8.02 ± 0.40 |
| 9.84 | 60 | 3900 | 87 (2.23) | 50.6 | 9.04 ± 0.42 | 9.02 ± 0.42 | 6.39 ± 0.39 | 3 | 6.22 ± 0.37 | 11.66 ± 0.69 | 8.68 ± 0.61 |

Application of the FMM to each treatment produced similar values for most treatments. The treatment of 4.92 g of material again appears to display some discrepancies, where strict rejection criteria are applied the minimum dose component ($FMM_{min}$) is larger than that produced by the other treatment scenarios and the component containing the largest proportion of grains ($FMM_{maj}$) is noticeably smaller. Where relaxed rejection criteria are adopted one less component is identified for the 4.92 g treatment relative to the other scenarios, resulting in both the $FMM_{min}$ producing a higher $D_e$ and $FMM_{maj}$ producing a lower $D_e$ relative to the other treatments.

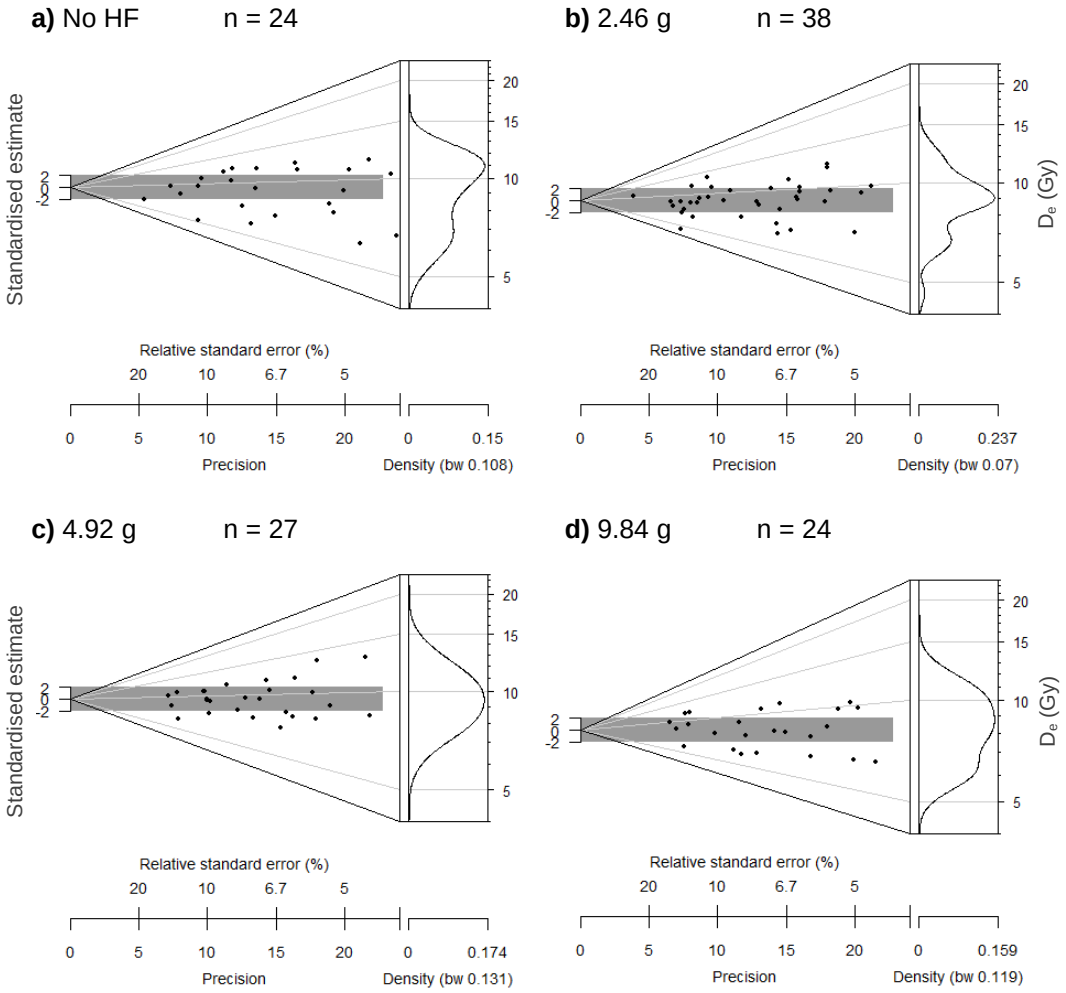


**Figure 4.4.5:** Abanico plots of single-grain $D_e$ values for variable masses (a: No HF, b: 2.46, c: 4.92 and d: 9.84 g) of GL14023 treated with 100 ml of HF, strict rejection criteria adopted. This and subsequent Abanico plots produced after Dietz *et al.* (2016) using the R coding of Dietze & Kreutzer (2018).

Visually the distribution of $D_e$ values obtained using the strict rejection criteria appears to vary significantly between treatments (Figure 4.4.5). Whilst the distributions of the untreated and 2.46 g scenario appear to be bimodal featuring one stronger high-dose peak, the treatment of 4.92 and 9.84 g of material resembles a relatively normal distribution. The distribution of the 9.84 g scenario appears to feature a minor population of $D_e$ values in the low-dose region, however, this is subtle in comparison to that displayed in Figure 4.4.5a and b.

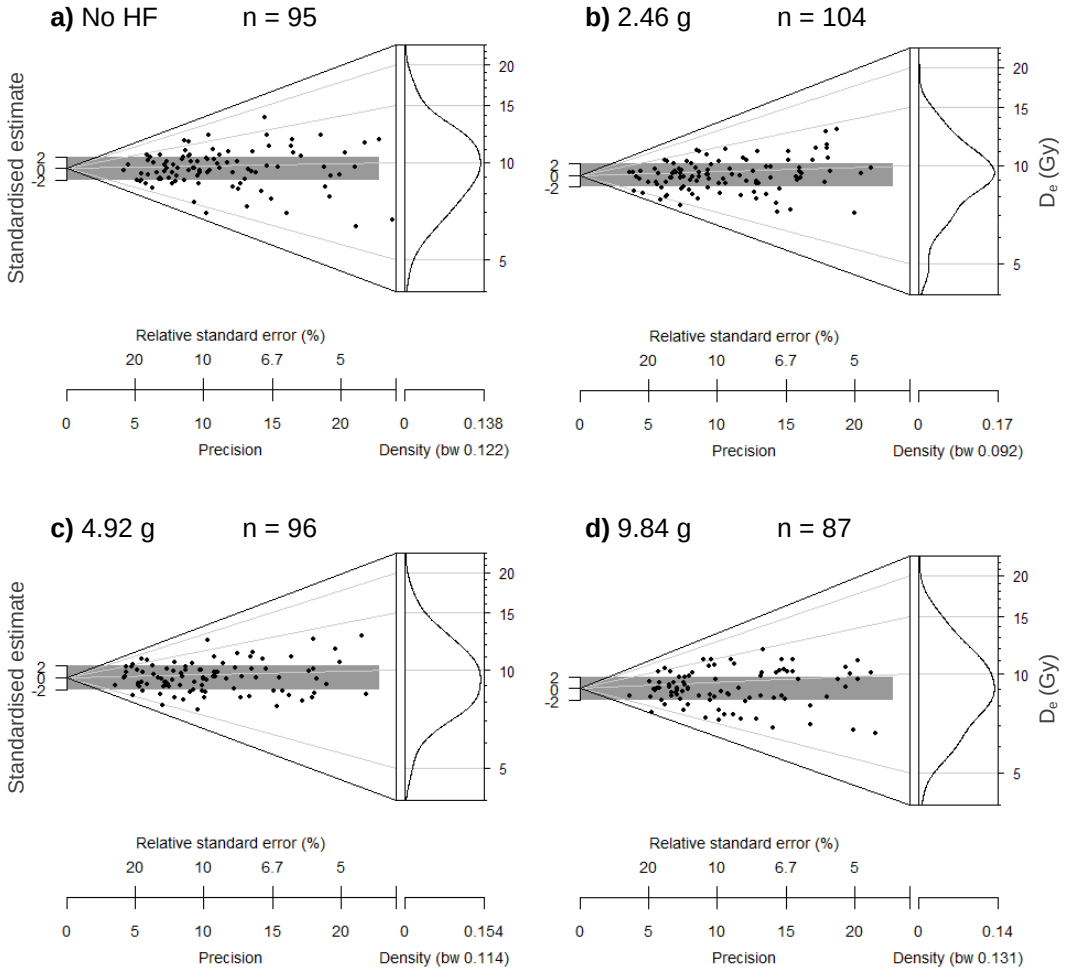


**Figure 4.4.6:** Abanico plots of single-grain $D_e$ values for variable masses (a: No HF, b: 2.46, c: 4.92 and d: 9.84 g) of GL14023 treated with 100 ml of HF, relaxed rejection criteria adopted.

For the relaxed rejection criteria each treatment scenario produces a distribution that is unimodal (Figure 4.4.6). In this instance the only treatment which visually replicates a similar distribution for the relaxed and strict rejection criteria is the 4.92 g treatment (4.4.5c & 4.4.6c). The kernel density estimate for each plot in Figure 4.4.6 peaks in a similar position for each treatment scenario, however, the distribution around each point appears to broaden with an increase in treated sample mass.

Shapiro-Wilk normality tests (Table 4.4.4) indicate $D_e$ values obtained using strict rejection criteria originate from a normally distributed population. The p-value systematically reduces and approaches the 95% confidence interval (i.e. 0.05) with an increase in sample mass treated with 100 ml of HF. For $D_e$ values obtained using relaxed rejection criteria, normality tests indicate that it is only the 2.46 g and no HF scenario which originate from a normal distribution. No obvious systematic trend can be observed in changes in the p-value. Accompanying Q-Q plots (Appendix B: Figure B1.1 & B1.2) mimic the results in Table 4.4.4, with smaller p-values manifesting as greater deviations from a straight line in Q-Q plots.

**Table 4.4.4:** Shapiro-Wilk normality test (95% confidence intervals) results for $D_e$ values obtained from each mass scenario using 'strict' and 'relaxed' rejection criteria.

| Mass Treated (g) | Strict Rejection Criteria | | | Relaxed Rejection Criteria | | |
|---|---|---|---|---|---|---|
| | W | p-value | Null-Hypothesis | W | p-value | Null-Hypothesis |
| **2.46** | 0.99 | 0.93 | Accepted | 0.99 | 0.50 | Accepted |
| **4.92** | 0.97 | 0.72 | Accepted | 0.97 | 0.02 | Rejected |
| **9.84** | 0.94 | 0.17 | Accepted | 0.97 | 0.04 | Rejected |
| **No HF** | 0.93 | 0.11 | Accepted | 0.97 | 0.06 | Accepted |

As the modelling and display of $D_e$ distributions are typically analysed on a logarithmic scale normality tests were also conducted upon logarithmically-transformed datasets. This appeared particularly important given the log-normal appearance of the distributions obtained using relaxed rejection criteria in Figure 4.4.6. With exception of the $D_e$ values obtained using relaxed rejection criteria for the treatment of 2.46 g of GL14023, Shapiro-Wilk normality tests upon the log-transformed datasets (Table 4.4.5) reveal that $D_e$ values are derived from log-normal distributions. No systematic change is evident with a change in treated mass.

**Table 4.4.5:** Shapiro-Wilk normality test (95% confidence intervals) results for log-transformed $D_e$ values obtained from each mass scenario using 'strict' and 'relaxed' rejection criteria.

| Mass Treated (g) | Strict Rejection Criteria | | | Relaxed Rejection Criteria | | |
|---|---|---|---|---|---|---|
| | W | p-value | Null-Hypothesis | W | p-value | Null-Hypothesis |
| **2.46** | 0.97 | 0.49 | Accepted | 0.97 | 0.04 | Rejected |
| **4.92** | 0.98 | 0.95 | Accepted | 0.99 | 0.92 | Accepted |
| **9.84** | 0.94 | 0.16 | Accepted | 0.99 | 0.58 | Accepted |
| **No HF** | 0.92 | 0.06 | Accepted | 0.99 | 0.82 | Accepted |

Overdispersion (OD), skewness (c) and kurtosis (k) were calculated for each treatment/mass scenario (Figure 4.4.7). A *c.* 25% OD was observed for the untreated fraction when using both strict and relaxed rejection criteria. When strict rejection criteria are adopted each mass treated with HF display a slight reduction in OD relative to the untreated scenario, with the treatment of 4.92 g displaying the lowest OD of 17.74%. The change in OD is less pronounced for relaxed rejection criteria and the treatment of 9.84 g of material produces an OD slightly larger than that calculated for the untreated fraction. No

systematic change can be observed in OD with a change in treated sample mass.

All fractions treated with HF display a positive skewness value for both strict and relaxed rejection criteria. No clear trend in skewness is visible from the data presented in Figure 4.4.7. However, it can be seen that the untreated fraction returns a slight negative skew when strict rejection criteria are applied and a strong positive skewness value when the relaxed criteria are adopted.

Each treatment scenario produces a similar value for kurtosis when relaxed rejection criteria are adopted, with values ranging between 2.63 and 3.33. When strict rejection criteria are adopted a reduction in sample mass appears to be accompanied by an increase in kurtosis. A kurtosis of 1.54 is observed for the untreated fraction which progressively increases to 2.77 for the treatment of 2.46 g of material. Linear regression of kurtosis values produced by the HF treated fractions using strict rejection criteria (Appendix B: Figure B1.3) confirm this negative linear trend, however, the significant errors associated with kurtosis are large and overlap for each treatment indicating this trend is not significant. Standard errors associated with kurtosis and skewness for strict rejection criteria appear large owing to the relatively small number of accepted $D_e$ values and method of calculation (Bailey & Arnold, 2006).

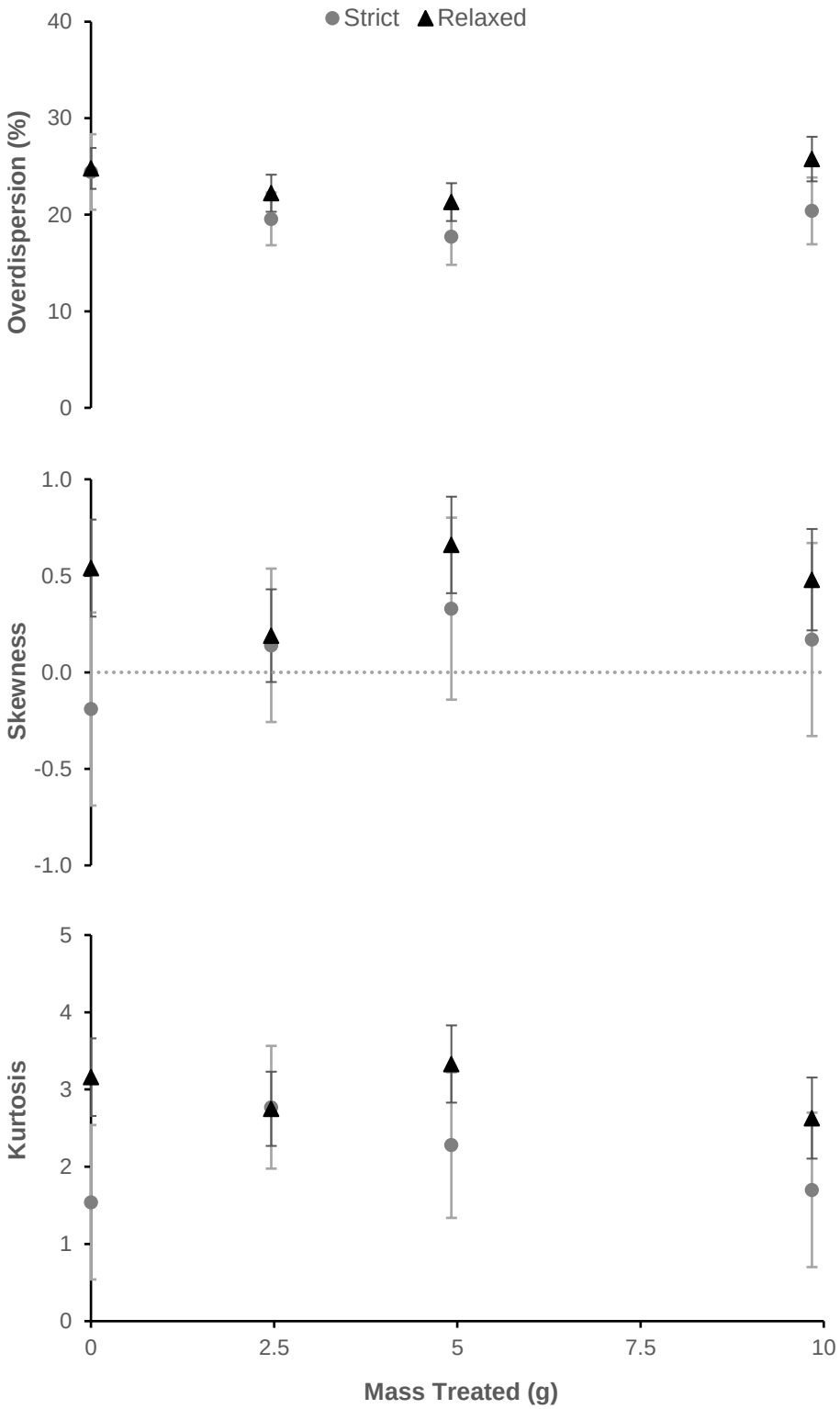


**Figure 4.4.7:** Overdispersion, Skewness and Kurtosis of $D_e$ estimates obtained using 'strict' and 'relaxed' rejection criteria for various masses of GL14023 treated with 100 ml of HF (Untreated fraction at 0 on x-axis). Skewness and Kurtosis errors calculated using guidance from Bailey & Arnold (2006).

*4.4.3.3 Variation in HF Treatment Time – Physical Change*

Four HF time scenarios were examined for each sample; 0, 30, 60 and 90 minute treatments, whilst material availability for GL15025 and GL16180 enabled a further treatment of 120 minutes to be explored. Following 30 and 60 minute HF treatments GL14023 displayed similar mass losses (Figure 4.4.8a) both before and after re-sieving. The 90 minute treatment displays a significant change with a 55% mass loss being observed prior to re-sieving and an overall loss of 73% post-re-sieve.

Despite experiencing slightly different magnitudes of mass loss following HF treatment, samples GL15025 and GL16180 display a similar systematic pattern of mass loss with increased HF treatment time. Linear regression of the percentage loss for fractions which had/had not been re-sieved display a well-fitted positive-trend line for each sample (Figure 4.4.8b and c). For sample GL15025 mass losses ranged from 38 to 51% for the fractions not re-sieved and 60 to 68% for re-sieved fractions, whilst for sample GL16180 the respective losses ranged from 29 to 49% and 51 to 67%.

Image analysis of the re-sieved fractions produced variable results for each of the three samples (Figure 4.4.9). For GL14023 each HF treated fraction displayed a *c.*9% and 15% reduction in average grain perimeter and area relative to the untreated fraction respectively. With the exception of the untreated material, minimal variation is displayed when HF treatment time is increased; this appears as a plateau in Figure 4.4.9a. GL15025 displays minimal change across each of the HF treatment times (Figure 4.4.9b). The greatest change relative to the control is the 90 minute treatment, but this only corresponds to a *c.* 4% and 6% reduction in average grain perimeter and area respectively. GL16180 displays minimal change after a 30 minute treatment but following a 60 minute treatment an increase in average grain perimeter (*c.* 8%) and area (*c.* 6%) is observed; this appears consistent with the 90 and 120 HF treatment times appearing as a plateau in Figure 4.4.9c.

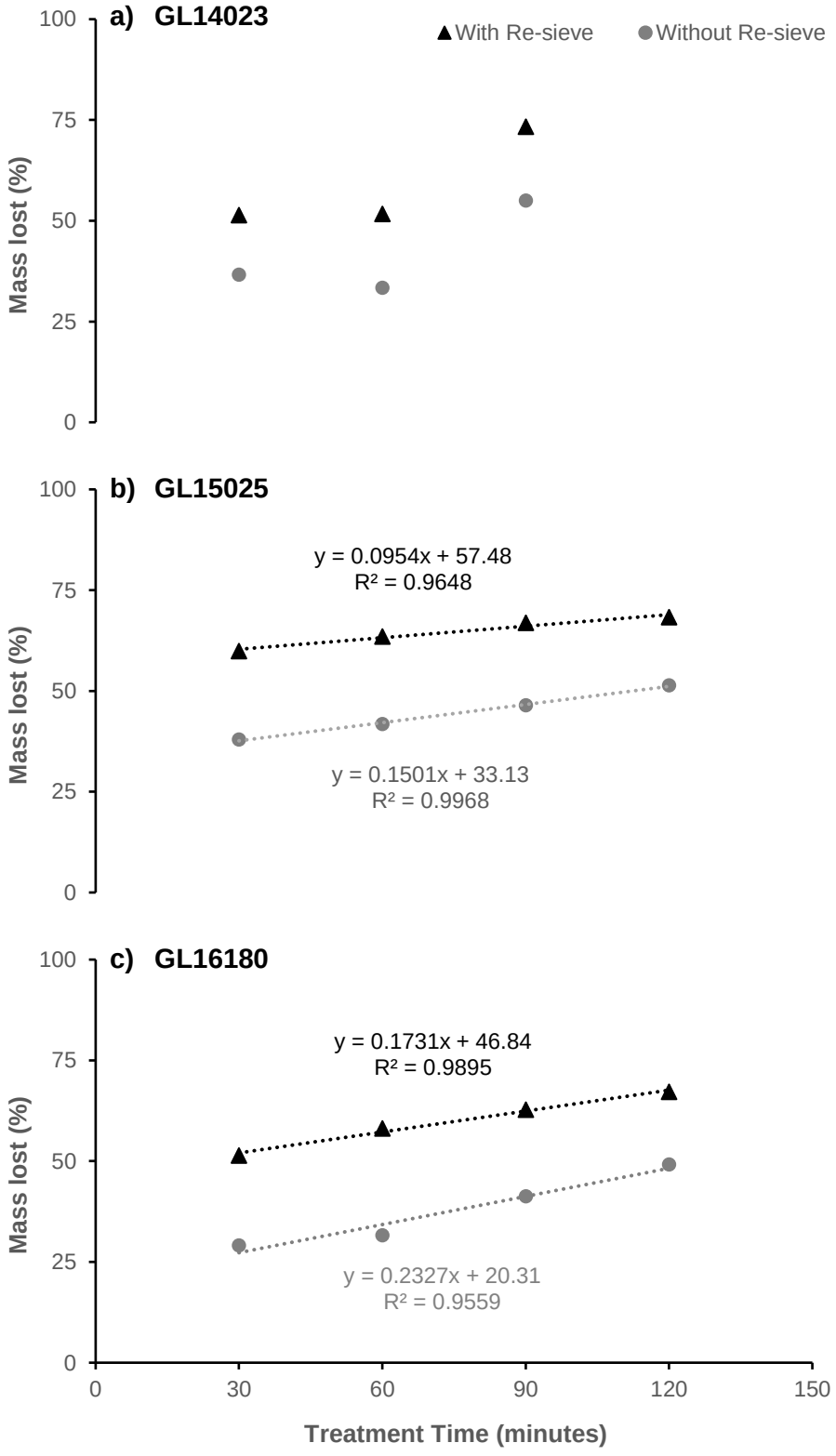


**Figure 4.4.8:** Mass lost following various HF treatment times of 180-250 µm quartz from GL14023 (a), GL15025 (b) and GL16180 (c - with and without re-sieving). Linear trend lines fitted to b and c.

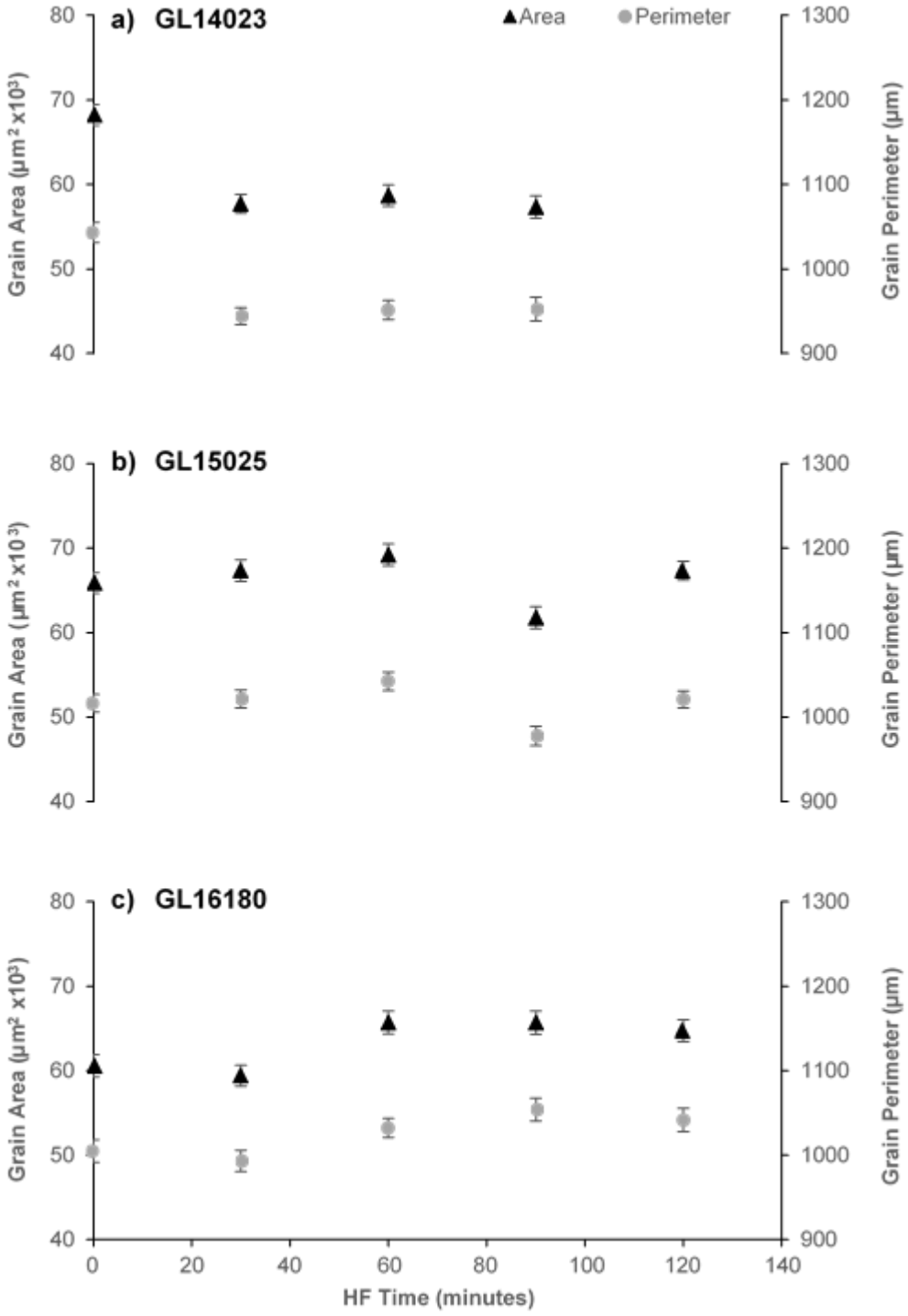


**Figure 4.4.9:** Average grain area and perimeter with standard errors following 0, 30, 60, 90 and 120 minute HF treatment (and re-sieve) of 180-250 µm quartz from GL14023 (4.92 g), GL15025 and GL16180 (both 5 g - Untreated fraction at 0 on x-axis).

#### *4.4.3.4 Variation in HF Treatment Time – Impact upon $D_e$*

$D_e$ values obtained for HF time investigations using both 'strict' and 'relaxed' rejection criteria are highlighted in Table 4.4.6 and 4.4.7 respectively. In both cases there appears to be no systematic change in the proportion of grains which are accepted with extension of HF treatment time, but in most instances the untreated fraction produced the lowest proportion of accepted $D_e$ values. Only sample GL14023 displays a systematic trend in the proportion of grains falling within 2σ of the median $D_e$, where strict rejection criteria are applied the proportion rises from 37.5% for the untreated fraction to 83.3% for the 90 minute HF treatment.

For all samples, central measures of $D_e$ (i.e. median and CAM) for each HF treatment scenario produce $D_e$ values consistent with the untreated fractions. This is also the case when MAM is applied to $D_e$ populations obtained using relaxed rejection criteria. However, MAM $D_e$ values obtained using strict criteria display some inter-sample variability. GL14023 displays an increase in minimum $D_e$ with increased HF treatment time and there is a 1.82 Gy difference in minimum dose between the untreated fraction and 90 minute HF. Only the 30 minute treatment of GL14023 produces a minimum $D_e$ consistent with that of the untreated fraction. Using the strict rejection criteria for GL15025 produces MAM estimates for all HF treated fractions which are consistent with the untreated fraction. As with GL14023 the 90 minute HF treatment also produces the largest minimum dose estimate, but this is still within errors of the untreated fraction. With exception of the 120 minute HF treatment, all MAM estimates for the HF treated fractions of GL16180 are consistent with the control when strict rejection criteria are applied.

The FMM is only applicable to three of the four treatment scenarios for GL14023. When strict rejection criteria are applied $FMM_{min}$ increases with HF time and neither the 30 or 60 minute treatment are consistent with the untreated fraction. $FMM_{max}$ also increases with HF time but estimates fall within errors of the untreated fraction. When relaxed rejection criteria are applied to GL14023 the untreated and 30 minute HF scenario both produce consistent estimates for $FMM_{min}$, $FMM_{max}$ and $FMM_{maj}$.

**Table 4.4.6:** Summary of single-grain $D_e$ values for fractions of GL14023, GL15025 and GL16180 treated with 100 ml of 40% HF for various submersion durations, strict rejection criteria adopted (errors reported with 1σ confidence)

| Sample | Mass Treated (g) | Treatment Time (mins) | Grains Measured | Grains Accepted (Number (%)) | Within 2σ (%) | $D_e$ values (Gy) | | | | | | |
|---|---|---|---|---|---|---|---|---|---|---|---|---|
| | | | | | | Median | CAM | MAM | FMM *k** | $FMM_{min}$ | $FMM_{max}$ | $FMM_{maj}$ |
| **GL14023** | N/A | 0 | 6000 | 24 (0.40) | 37.5 | 9.39 ± 0.57 | 8.87 ± 0.56 | 6.43 ± 0.56 | 2 | 6.72 ± 0.40 | 10.64 ± 0.55 | 10.64 ± 0.55 |
| | 4.92 | 30 | 7000 | 38 (0.54) | 46.2 | 9.66 ± 0.47 | 9.30 ± 0.47 | 7.38 ± 0.52 | 2 | 7.76 ± 0.40 | 11.16 ± 0.57 | 11.16 ± 0.57 |
| | 4.92 | 60 | 3900 | 27 (0.69) | 48.1 | 9.50 ± 0.49 | 9.43 ± 0.49 | 8.05 ± 0.63 | 2 | 8.42 ± 0.51 | 11.39 ± 0.83 | 8.42 ± 0.51 |
| | 4.92 | 90 | 7000 | 24 (0.34) | 83.3 | 9.08 ± 0.42 | 9.14 ± 0.44 | 8.25 ± 0.66 | - | - | - | - |
| **GL15025** | N/A | 0 | 1000 | 36 (3.60) | 47.2 | 10.50 ± 0.59 | 10.46 ± 0.57 | 7.83 ± 0.55 | 2 | 8.57 ± 0.47 | 12.62 ± 0.66 | 12.62 ± 0.66 |
| | 5 | 30 | 1000 | 72 (7.20) | 58.3 | 10.07 ± 0.48 | 10.22 ± 0.47 | 7.92 ± 0.53 | 3 | 9.76 ± 0.42 | 14.91 ± 1.33 | 9.76 ± 0.42 |
| | 5 | 60 | 1000 | 41 (4.10) | 51.2 | 9.93 ± 0.51 | 9.96 ± 0.48 | 8.06 ± 0.58 | 2 | 8.59 ± 0.64 | 11.44 ± 0.95 | 11.44 ± 0.95 |
| | 5 | 90 | 1000 | 56 (5.60) | 62.5 | 9.86 ± 0.46 | 10.12 ± 0.41 | 8.87 ± 0.60 | 2 | 9.38 ± 0.46 | 12.77 ± 1.11 | 9.38 ± 0.46 |
| | 5 | 120 | 1000 | 68 (6.80) | 61.8 | 9.66 ± 0.43 | 9.63 ± 0.43 | 7.71 ± 0.47 | 2 | 7.17 ± 0.53 | 10.46 ± 0.44 | 10.46 ± 0.44 |
| **GL16180** | N/A | 0 | 1800 | 21 (1.16) | 76.2 | 0.88 ± 0.06 | 0.86 ± 0.05 | 0.71 ± 0.08 | 2 | 0.79 ± 0.07 | 1.05 ± 0.21 | 0.79 ± 0.07 |
| | 5 | 30 | 1800 | 31 (1.72) | 83.9 | 0.83 ± 0.05 | 0.87 ± 0.05 | 0.68 ± 0.06 | - | - | - | - |
| | 5 | 60 | 1800 | 29 (1.61) | 72.4 | 0.76 ± 0.06 | 0.83 ± 0.06 | 0.79 ± 0.08 | - | - | - | - |
| | 5 | 90 | 1800 | 34 (1.89) | 55.9 | 0.81 ± 0.06 | 0.85 ± 0.06 | 0.64 ± 0.07 | 2 | 0.70 ± 0.09 | 1.16 ± 0.14 | 0.70 ± 0.09 |
| | 5 | 120 | 1800 | 31 (1.72) | 74.2 | 0.96 ± 0.07 | 0.96 ± 0.05 | 0.96 ± 0.05 | 2 | 0.83 ± 0.06 | 1.14 ± 0.11 | 0.83 ± 0.06 |

**Table 4.4.7:** Summary of single-grain $D_e$ values for fractions of GL14023, GL15025 and GL16180 treated with 100 ml of 40% HF for various submersion durations, relaxed rejection criteria adopted (errors reported with 1σ confidence)

| Sample | Mass Treated (g) | Treatment Time (mins) | Grains Measured | Grains Accepted (Number (%)) | Within 2σ (%) | $D_e$ values (Gy) | | | | | | |
|---|---|---|---|---|---|---|---|---|---|---|---|---|
| | | | | | | Median | CAM | MAM | FMM *k** | $FMM_{min}$ | $FMM_{max}$ | $FMM_{maj}$ |
| **GL14023** | N/A | 0 | 6000 | 95 (1.58) | 53.7 | 9.58 ± 0.43 | 9.51 ± 0.42 | 6.89 ± 0.39 | 3 | 6.60 ± 0.54 | 12.55 ± 0.99 | 9.41 ± 0.97 |
| | 5 | 30 | 7000 | 118 (1.69) | 60.2 | 9.30 ± 0.40 | 9.30 ± 0.40 | 6.92 ± 0.39 | - | - | - | - |
| | 5 | 60 | 3900 | 96 (2.46) | 58.3 | 9.50 ± 0.42 | 9.46 ± 0.40 | 7.48 ± 0.45 | 2 | 8.02 ± 0.40 | 11.32 ± 0.56 | 8.02 ± 0.40 |
| | 5 | 90 | 7000 | 100 (1.43) | 59.0 | 9.46 ± 0.43 | 9.66 ± 0.41 | 7.46 ± 0.44 | 3 | 6.69 ± 0.54 | 13.74 ± 0.92 | 9.43 ± 0.42 |
| **GL15025** | N/A | 0 | 1000 | 116 (11.60) | 64.7 | 10.37 ± 0.46 | 10.36 ± 0.46 | 8.12 ± 0.47 | 3 | 7.04 ± 0.62 | 13.21 ± 0.86 | 9.81 ± 0.57 |
| | 5 | 30 | 1000 | 221 (22.10) | 65.2 | 10.21 ± 0.42 | 10.36 ± 0.40 | 7.98 ± 0.41 | 3 | 9.38 ± 0.38 | 14.97 ± 0.86 | 9.38 ± 0.38 |
| | 5 | 60 | 1000 | 123 (12.30) | 61.8 | 9.43 ± 0.39 | 9.40 ± 0.39 | 7.35 ± 0.40 | 3 | 8.67 ± 0.56 | 11.36 ± 0.62 | 8.67 ± 0.56 |
| | 5 | 90 | 1000 | 169 (16.90) | 69.2 | 9.79 ± 0.39 | 9.83 ± 0.38 | 8.06 ± 0.43 | 2 | 8.88 ± 0.42 | 11.92 ± 0.76 | 8.88 ± 0.42 |
| | 5 | 120 | 1000 | 156 (15.60) | 69.9 | 9.69 ± 0.39 | 9.76 ± 0.39 | 7.82 ± 0.38 | 3 | 6.68 ± 0.45 | 10.01 ± 0.39 | 10.01 ± 0.39 |
| **GL16180** | N/A | 0 | 1800 | 59 (3.28) | 72.9 | 0.89 ± 0.04 | 0.91 ± 0.05 | 0.68 ± 0.06 | 2 | 0.76 ± 0.04 | 1.20 ± 0.09 | 0.76 ± 0.04 |
| | 5 | 30 | 1800 | 131 (7.28) | 78.6 | 0.91 ± 0.04 | 0.92 ± 0.04 | 0.73 ± 0.05 | - | - | - | - |
| | 5 | 60 | 1800 | 133 (7.39) | 80.5 | 0.82 ± 0.04 | 0.86 ± 0.04 | 0.75 ± 0.06 | 2 | 0.82 ± 0.03 | 1.27 ± 0.15 | 0.82 ± 0.03 |
| | 5 | 90 | 1800 | 154 (8.56) | 69.5 | 0.86 ± 0.04 | 0.86 ± 0.04 | 0.64 ± 0.05 | 3 | 0.72 ± 0.05 | 1.32 ± 0.11 | 0.93 ± 0.08 |
| | 5 | 120 | 1800 | 111 (6.17) | 80.2 | 0.84 ± 0.04 | 0.92 ± 0.04 | 0.74 ± 0.06 | 2 | 0.83 ± 0.04 | 1.19 ± 0.09 | 0.83 ± 0.04 |

No clear systematic trend is evident from FMM estimates for GL15025, however, for both strict and relaxed rejection criteria the 30 minute treatment produces the highest $D_e$ estimates for $FMM_{min}$ and $FMM_{max}$ whilst the 120 minute treatment produces the lowest estimates. The only scenario where each FMM component is consistent with that of the control is the 60 minute HF treatment but only when strict criteria are applied. For GL16180, where FMM is applicable, most identified doses are consistent with that of the untreated fraction. The only exception is for relaxed rejection criteria and the 90 minute treatment where the inclusion of an additional component results in a higher $FMM_{maj}$.

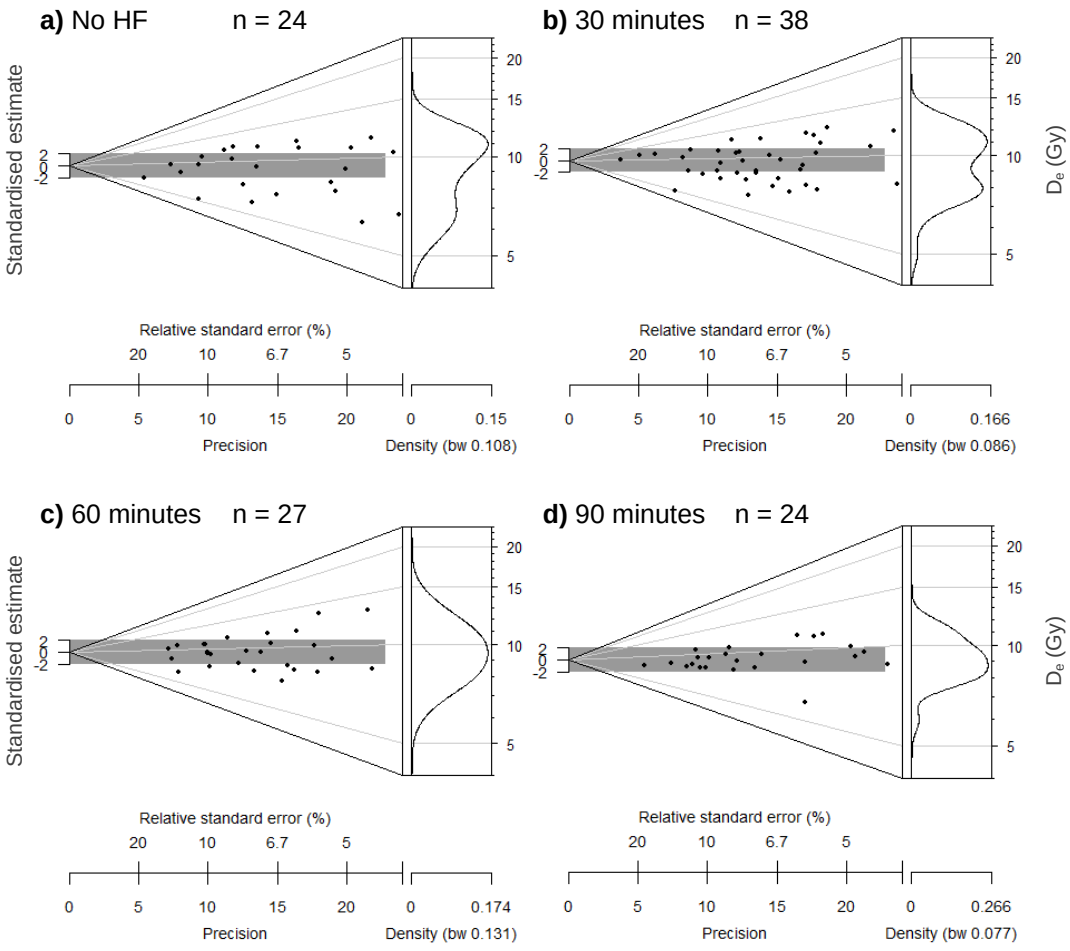


**Figure 4.4.10:** Abanico plots of single-grain $D_e$ values for 180-250 µm quartz from GL14023 treated with 100 ml of HF for; a) 0, b) 30, c) 60 and d) 90 minutes. Strict rejection criteria adopted.

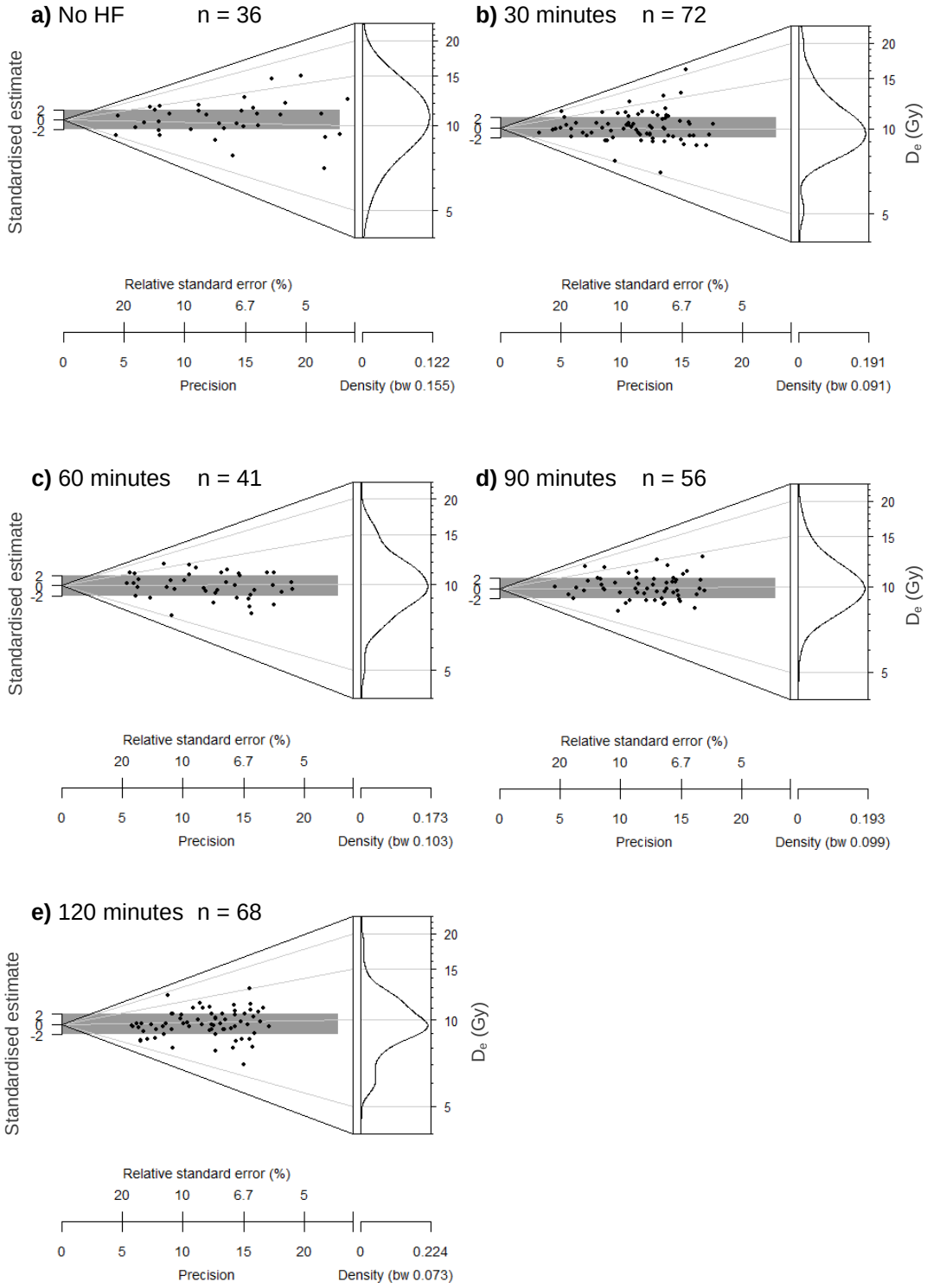


**Figure 4.4.11:** Abanico plots of single-grain $D_e$ values for 180-250 µm quartz from GL15025 treated with 100 ml of HF for; a) 0, b) 30, c) 60, d) 90 and e) 120 minutes. Strict rejection criteria adopted.

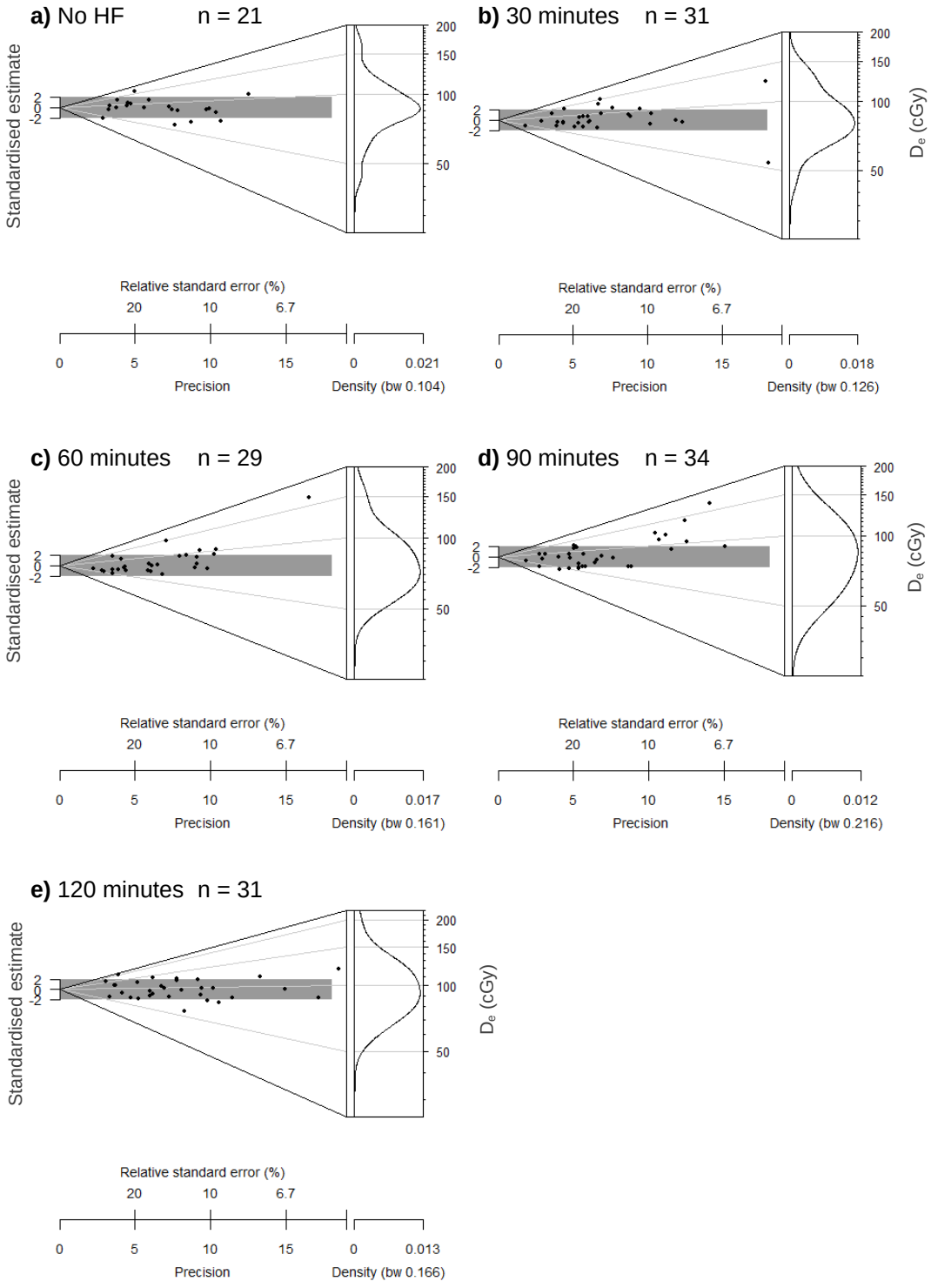


**Figure 4.4.12:** Abanico plots of single-grain $D_e$ values for 180-250 µm quartz from GL16180 treated with 100 ml of HF for; a) 0, b) 30, c) 60, d) 90 and e) 120 minutes. Strict rejection criteria adopted (Note: Change in scale to cGy (i.e. 0.01 Gy)).

Visually the distribution of $D_e$ values for GL14023 obtained using the strict rejection criteria (Figure 4.4.10) appears to alter significantly with increased HF treatment time. The untreated fraction (a) produces a negatively skewed $D_e$ distribution which is relatively broad. The spread in $D_e$ values appears to decrease with increased treatment time and following a 60 minute treatment the distribution appears normal. The 90 minute treatment produces the least dispersed plot with the greatest proportion of grains falling within 2σ of the median. For the relaxed rejection criteria all plots (Appendix B – Figure B2.1) produce similar unimodal distributions. It is only the 90 minute treatment that is slightly different and produces a plot that indicates that the data are more positively skewed.

For GL15025 each HF treatment scenario produces a unimodal distribution when both strict (Figure 4.4.11) and relaxed (Appendix B – Figure B2.2) rejection criteria are adopted. As with GL14023, the spread in $D_e$ estimates obtained using strict criteria appears to reduce with an increase of HF time up to 90 minutes, the treatment which also produces the highest proportion of $D_e$ values falling within 2σ. However, the additional 120 minute treatment explored for this sample produces a greater spread in $D_e$ values relative to the 90 minute treatment, owing primarily to the inclusion of a higher proportion of low-dose values. This reversal in data spread is also apparent when using the relaxed rejection criteria.

GL16180 appears to display the opposite pattern to those already discussed. When strict rejection criteria are adopted it is the untreated fraction which displays the least dispersion among $D_e$ estimates (Figure 4.4.12) and an increase in treatment time is accompanied by a broadening of $D_e$ distributions up to the 90 minute treatment, as marked by the broadening of KDE part of the Abanico plots. The 120 minute treatment for this sample also appears to display a reversal in dispersion, however, for this sample the 120 minute treatment is accompanied by a reduction in OD relative to the 90 minute treatment (Figure 4.4.13). When relaxed rejection criteria are used all treatment scenarios produce a unimodal distribution and visually the changes in distribution are less obvious (Appendix B – Figure B2.2).

Shapiro-Wilk normality tests upon each HF time scenario (Table 4.4.8) indicate that all $D_e$ values obtained using strict rejection criteria for sample GL14023 originate from a normal distribution. Q-Q plots associated with the strict criteria for this sample (Appendix B: Figure B2.4) display points which closely follow a straight line which is indicative of a normally distributed sample. Where relaxed rejection criteria are adopted, normality tests suggest that only $D_e$ values obtained from the untreated fraction originate from a normal distribution, associated Q-Q plots (Appendix B: Figure B2.5) appear to display greater deviation from normality with an increase in treatment time.

**Table 4.4.8:** Shapiro-Wilk normality test (95% confidence intervals) results for $D_e$ values obtained from each HF time using 'strict' and 'relaxed' rejection criteria.

| Treatment Time (mins) | Strict Rejection Criteria | | | Relaxed Rejection Criteria | | |
|---|---|---|---|---|---|---|
| | **W** | **p-value** | **Null-Hypothesis** | **W** | **p-value** | **Null-Hypothesis** |
| ***GL14023*** | | | | | | |
| **0** | 0.93 | 0.10 | Accepted | 0.97 | 0.06 | Accepted |
| **30** | 0.97 | 0.30 | Accepted | 0.96 | <0.01 | Rejected |
| **60** | 0.97 | 0.72 | Accepted | 0.97 | 0.02 | Rejected |
| **90** | 0.96 | 0.52 | Accepted | 0.92 | <0.01 | Rejected |
| ***GL15025*** | | | | | | |
| **0** | 0.99 | 0.94 | Accepted | 0.97 | 0.01 | Rejected |
| **30** | 0.90 | <0.01 | Rejected | 0.91 | <0.01 | Rejected |
| **60** | 0.97 | 0.26 | Accepted | 0.99 | 0.39 | Accepted |
| **90** | 0.94 | <0.01 | Rejected | 0.96 | <0.01 | Rejected |
| **120** | 0.95 | 0.01 | Rejected | 0.94 | <0.01 | Rejected |
| ***GL16180*** | | | | | | |
| **0** | 0.93 | 0.14 | Accepted | 0.94 | <0.01 | Rejected |
| **30** | 0.96 | 0.21 | Accepted | 0.96 | <0.01 | Rejected |
| **60** | 0.88 | <0.01 | Rejected | 0.82 | <0.01 | Rejected |
| **90** | 0.96 | 0.23 | Accepted | 0.95 | <0.01 | Rejected |
| **120** | 0.90 | <0.01 | Rejected | 0.86 | <0.01 | Rejected |

For samples GL15025 and GL16180 normality tests (Table 4.4.8) suggest that $D_e$ values for most treatment scenarios do not originate from a normal distribution and Q-Q plots (Appendix B – Figures: B2.6 to B2.9) indicate that a small number of values significantly deviate from the normality line. However, when $D_e$ distributions are log-transformed the Shapiro-Wilk test (Table 4.4.9) indicate that most treatments produce $D_e$ populations which are consistent with a log-normal distribution both for strict and relaxed rejection criteria. No clear systematic trend in normality test results is visible for natural or log-transformed datasets.

**Table 4.4.9:** Shapiro-Wilk normality test (95% confidence intervals) results for log-transformed $D_e$ values obtained from each HF time using 'strict' and 'relaxed' rejection criteria.

| Treatment Time (mins) | Strict Rejection Criteria | | | Relaxed Rejection Criteria | | |
|---|---|---|---|---|---|---|
| | **W** | **p-value** | **Null-Hypothesis** | **W** | **p-value** | **Null-Hypothesis** |
| ***GL14023*** | | | | | | |
| **0** | 0.92 | 0.06 | Accepted | 0.99 | 0.82 | Accepted |
| **30** | 0.97 | 0.30 | Accepted | 0.95 | <0.01 | Rejected |
| **60** | 0.98 | 0.95 | Accepted | 0.99 | 0.92 | Accepted |
| **90** | 0.95 | 0.33 | Accepted | 0.99 | 0.39 | Accepted |
| ***GL15025*** | | | | | | |
| **0** | 0.98 | 0.80 | Accepted | 0.99 | 0.45 | Accepted |
| **30** | 0.96 | 0.04 | Rejected | 0.99 | 0.03 | Rejected |
| **60** | 0.98 | 0.80 | Accepted | 0.99 | 0.53 | Accepted |
| **90** | 0.96 | <0.01 | Rejected | 0.99 | 0.97 | Accepted |
| **120** | 0.97 | 0.16 | Accepted | 0.98 | 0.07 | Accepted |
| ***GL16180*** | | | | | | |
| **0** | 0.97 | 0.67 | Accepted | 0.99 | 0.87 | Accepted |
| **30** | 0.98 | 0.86 | Accepted | 0.99 | 0.46 | Accepted |
| **60** | 0.96 | 0.25 | Accepted | 0.96 | <0.01 | Rejected |
| **90** | 0.99 | 0.91 | Accepted | 0.99 | 0.29 | Accepted |
| **120** | 0.98 | 0.72 | Accepted | 0.97 | 0.03 | Rejected |

$D_e$ estimates obtained using strict rejection criteria for sample GL14023 and GL15025 display a progressive reduction in OD with an increase in HF treatment time of up to 90 minutes (Figure 4.4.13) whilst the corresponding estimates for GL16180 display the opposite, increasing with longer etching periods. The 120 minute treatment for GL15025 and GL16180 appears to display a reversal in the observed trends. When the 120 minute data is omitted linear regression produces a well-fitted trend line for each of the samples (Appendix B – Figure B2.10). Estimates obtained using relaxed rejection criteria display little evidence of any systematic trend. For GL14023 each fraction treated with HF has a similar OD which is less than that of the untreated fraction. For GL15025 the relaxed rejection criteria produces a similar OD for most scenarios, with the smallest value being produced by the 90 minute treatment. With the exception of the 90 minute treatment of GL16180 which produces an elevated OD, each HF treated fraction produces a similar OD which is less than the control.

The skewness (Figure 4.4.14) of $D_e$ distributions obtained for each sample display little variation between each of the HF treatment times, both for estimates obtained using strict and relaxed rejection criteria.

For GL14023, $D_e$ estimates obtained using strict rejection criteria appear to display an increase in kurtosis (Figure 4.4.15) with increased HF submersion time, however this change is minimal (<1) and all associated errors overlap. When relaxed rejection criteria are adopted only the 90 minute treatment produces a significantly greater value than that of the other treatments. The kurtosis of $D_e$ distributions obtained for GL15025 and GL16180 appear to show some variability, but only $D_e$ values obtained using relaxed rejection criteria for sample GL16180 appear to produce a systematic pattern; this is similar to that observed for OD.

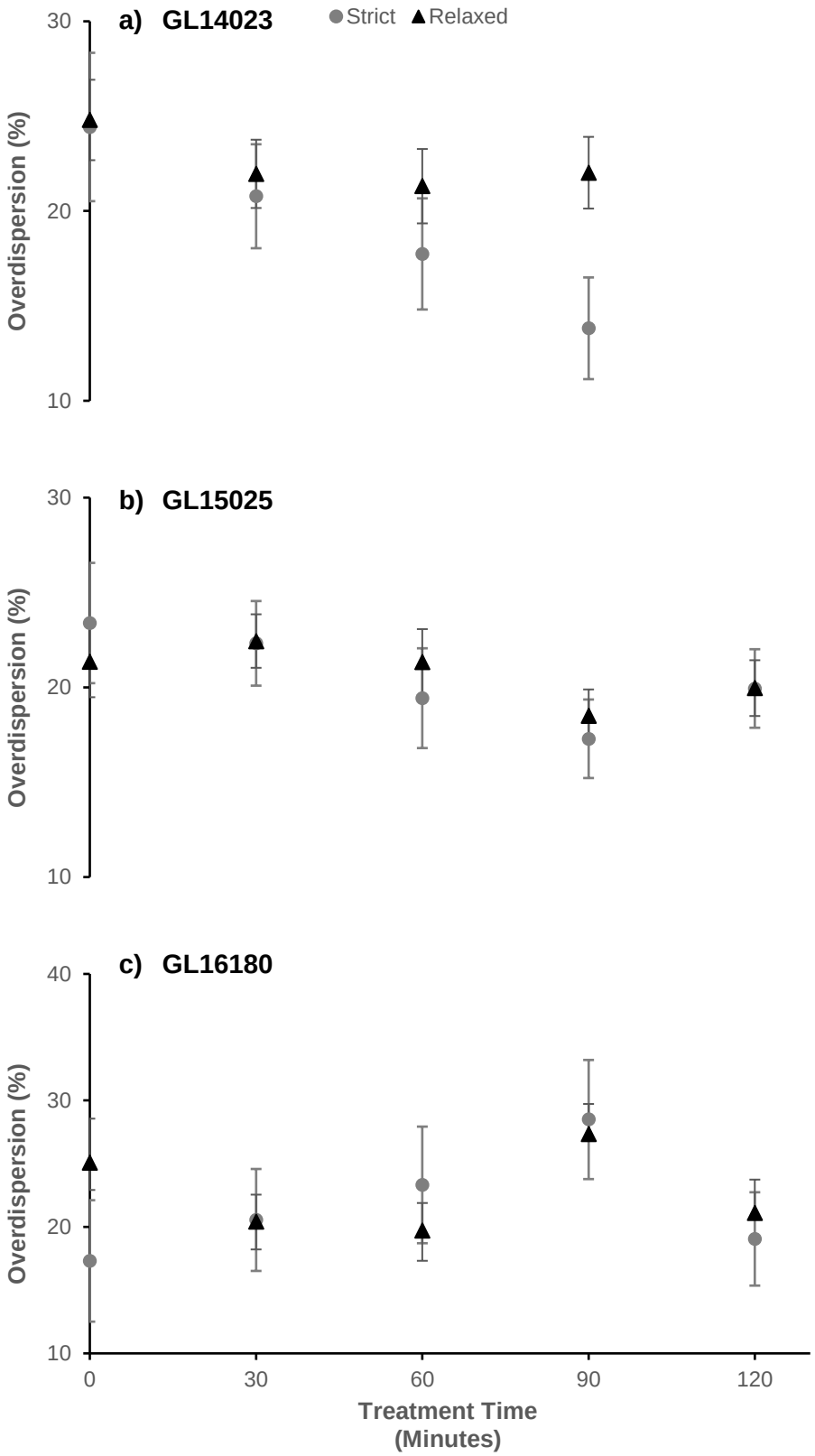


**Figure 4.4.13:** Overdispersion of $D_e$ estimates obtained for a) GL14023, b) GL15025 and c) GL16180 using 'strict' and 'relaxed' rejection criteria for various HF treatment durations.

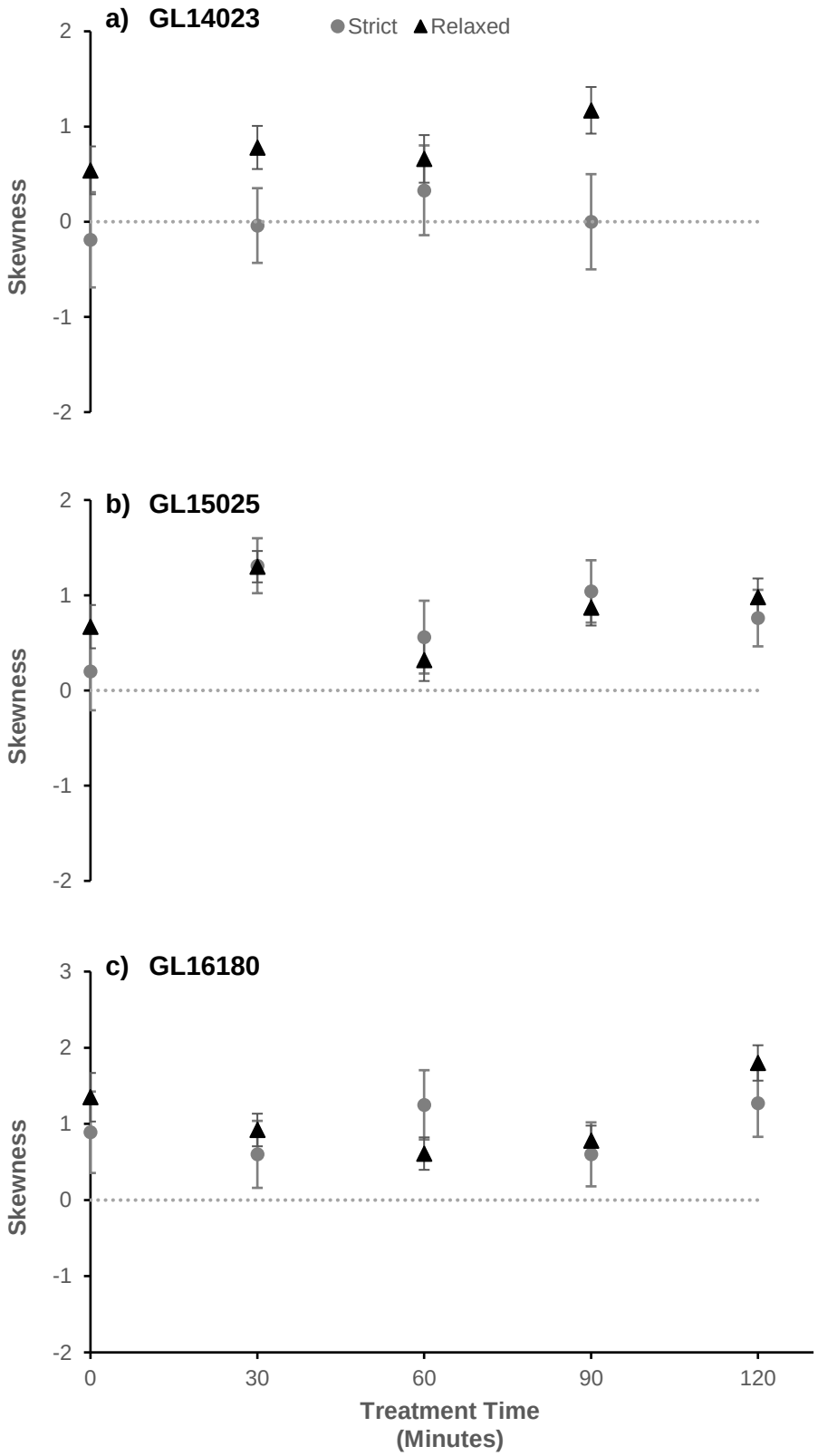


**Figure 4.4.14:** Skewness of $D_e$ estimates obtained for a) GL14023, b) GL15025 and c) GL16180 using 'strict' and 'relaxed' rejection criteria for various HF treatment durations.

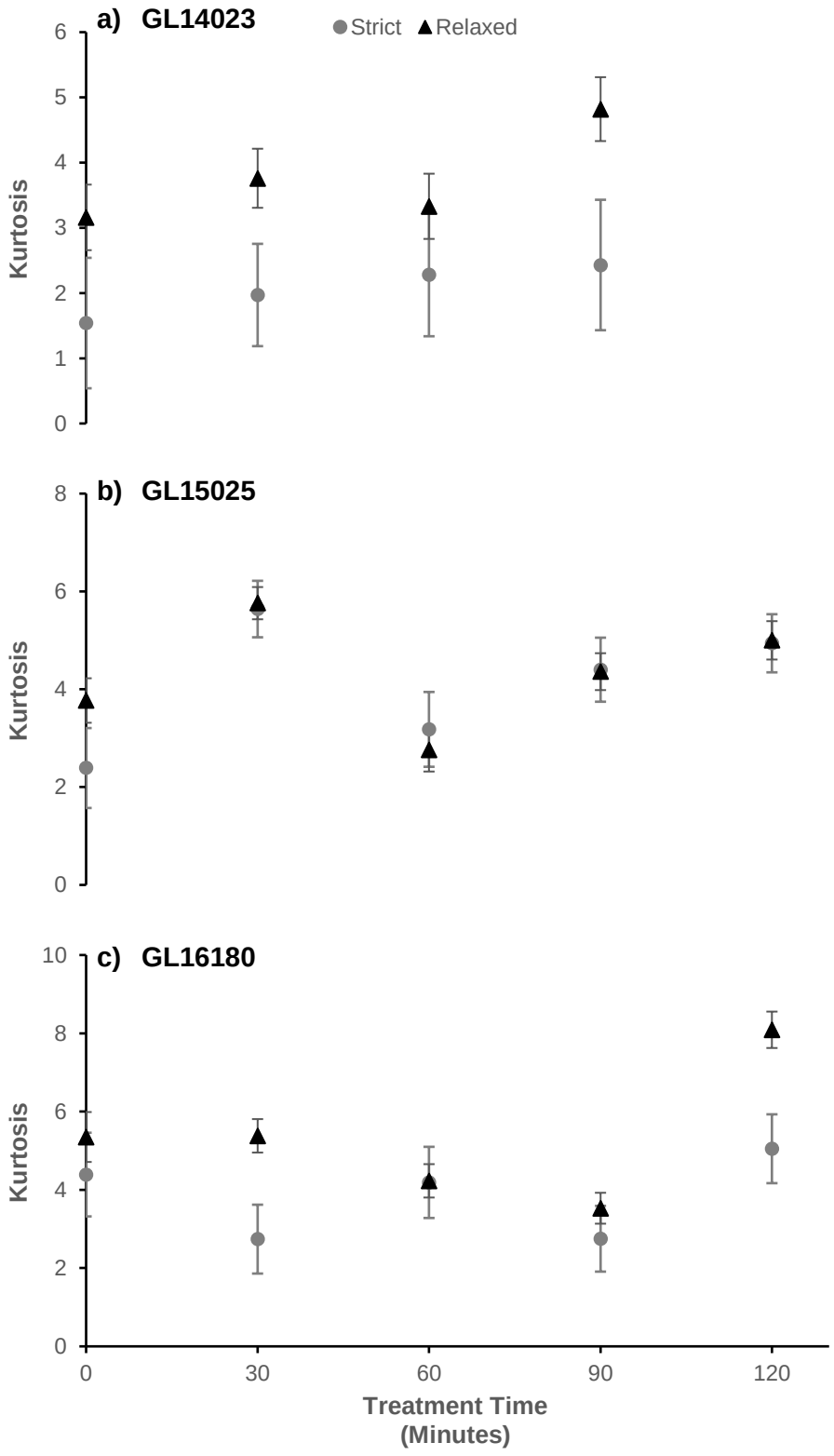


**Figure 4.4.15:** Kurtosis of $D_e$ estimates obtained for a) GL14023, b) GL15025 and c) GL16180 using 'strict' and 'relaxed' rejection criteria for various HF treatment durations.

*4.4.4. Discussion*

By assuming homogenous etching, spherical grains and a density of 2.65 g $cm^{-3}$ it is possible to hypothetically model mass loss to approximate the percentage mass change required to eliminate the outer *c.* 10 µm of quartz grains. The change in mass of a 180 and 250 µm spherical grain can be calculated using Eqn. 4.8, results of which are summarised in Table 4.4.10. Given the slight variations in grain density, shape, size and presence of preferential etching, mass loss could be expected to fall outside of the bounds highlighted in Table 4.4.10.

**Eqn. 4.8**

$$Grain\ Mass = Grain\ Density \times \left(\frac{4}{3}\pi r^3\right)$$

**Table 4.4.10:** Hypothetical mass loss for 180 and 250 µm diameter spherical quartz grains with 2.65 g $cm^{-3}$ density following removal of a 10 µm rind.

| Grain Radius (µm) | | Grain Mass (mg) | | Mass |
|---|---|---|---|---|
| **Pre-HF** | **Post-HF** | **Pre-HF** | **Post-HF** | **Loss (%)** |
| 90 | 80 | 0.00809 | 0.00568 | 29.79 |
| 125 | 115 | 0.02168 | 0.01688 | 22.14 |

The HF treatments examined in this chapter uncover some variations in mass loss and $D_e$ distribution. The impact of varying sample mass treated with 100 ml of HF appears to have a profound effect on percentage mass loss, with a reduction in treated mass displaying a greater percentage loss following the same treatment duration. The treatment of 4.92 and 9.84 g of material exhibited similar mass losses (*c.* 30%) following a 60 minute treatment and such losses are comparable to those modelled in Table 4.4.10,

whilst the treatment of 2.46 g of material exhibited a much greater percentage loss (*c.* 57%). 2D image analysis of grains isolated for measurement (re-sieved) displayed a reduction in grain area and perimeter following HF treatment (Figure 4.4.4), yet no systematic change with treated sample mass was observed, most likely owing to analysis being conducted following re-sieving. Accepting that only a single sample has been examined, it appears that a minimum of 5 g of material should be treated with 100 ml of HF (i.e. 20 ml per gram of quartz).

The impact of varying the mass of quartz treated with 100 ml of HF upon $D_e$ values appears minimal and for most scenarios modelled $D_e$ values are in agreement with the untreated fraction. One exception appears to be the treatment of 4.92 g of material, MAM and FMM estimates from $D_e$ populations obtained using both strict and relaxed rejection criteria produce elevated $D_e$ estimates. This scenario produced the least dispersed $D_e$ distribution (OD = 17.74%) and strong evidence that the $D_e$ population represents a log-normal distribution. Given the distribution of $D_e$ estimates it is likely that minimum age modelling is not suited, hence the discrepancy of minimum $D_e$ with the other treated masses.

The distribution of $D_e$ appears to become less dispersed with reduction in sample mass with a higher proportion of grains falling within 2σ of the median and, when strict rejection criteria are adopted, an increase in kurtosis towards that expected for a normal distribution (i.e. 3). Although not reflected in systematic changes of OD, it could be argued that HF has a normalising effect upon $D_e$ distributions when smaller quantities of material are treated, however the analysis of further samples is required to confirm the consistency of this.

Although the variation in HF treated mass has been highlighted as a potential influence upon $D_e$ distribution, the predominant focus of this chapter is the effect of HF treatment duration upon material used for single-grain quartz OSL. Samples GL15025 and GL16180 displayed linear increases in mass loss with increased HF treatment duration whilst the pattern observed for GL14023 appeared less progressive displaying a similar mass loss following

30 and 60 minute treatments. GL16180 appeared to be the most resistant to HF displaying the least percentage change for each treatment duration. This resistance could be rooted in the mineralogical maturity of the sample as highlighted by Porat *et al.* (2015), whereby less mature samples are less resistant and lose a greater proportion of their rind through etching process. GL14023 displayed the greatest mass loss (55% pre-re-sieve) following a 90 minute HF treatment, using Eqn. 4.8 and the assumptions adopted for calculating data in Table 4.4.10, such losses would equate to a 20-30 μm homogenous etch depth for the 180-250 μm quartz fraction. Etch depths of up to 20 μm have negligible effects upon the beta dose rate for quartz grains (Duval *et al.,* 2018) and would be considered an upper bound for OSL analysis. A homogenous 20 μm etch depth would equate to mass losses of *c.* 53% and 41% for spherical 180 and 250 μm grains respectively. All samples explored in this chapter displayed mass losses well below this upper bound for treatment times of up to 60 minutes.

For the re-sieved fractions taken forward for single-grain $D_e$ analysis, 2D image analysis revealed variable impacts upon the average grain size. GL14023 displayed a drop in average grain area and perimeter following HF treatment and GL16180 displayed an overall increase for treatments exceeding 30 minutes. No systematic change was observed for GL15025. The pattern observed for GL14023 would be expected as grains are being progressively etched, however, the increase displayed by GL16180 suggests a large proportion of grains that would have been close to 180 μm in size had been removed, truncating the grain size distribution being used for $D_e$ analysis. Although Porat *et al.* (2015) attempt to overcome any potential bias created by altering grain size distribution by not re-sieving or using a smaller mesh size, careful consideration should be taken before adopting such an approach as it has the potential to compromise the reliability of β-source calibration.

The impact of increasing HF duration upon central measures of $D_e$ is negligible with all HF treated samples producing median and CAM values statistically consistent with that of the untreated fractions, both when strict and relaxed rejection criteria were adopted. In most instances similar $D_e$

values were calculated using MAM, one notable exception are the $D_e$ values obtained using strict rejection criteria for GL14023 where a progressive increase in MAM $D_e$ is observed with increased treatment time. FMM produced some variability across the treatment scenarios for samples GL14023 and GL15025, whilst those values available for GL16180 appeared to be consistent.

$D_e$ populations obtained for each sample using relaxed rejection criteria display minimal variation in distribution and no systematic change in OD with increased HF treatment duration. However, where strict criteria are adopted systematic changes in OD are observed for treatment durations ranging from 0 to 90 minutes for all samples. GL14023 and GL15025 display a progressive reduction in OD with increased treatment time whilst GL16180 displays an increase in OD. Two questions arise from these observations on distribution; 1) why are systematic changes only observed for $D_e$ estimates obtained using strict rejection criteria, and 2) if the systematic changes observed in data obtained using strict rejection criteria are representative, how does HF treatment duration drive changes in distribution/OD?

Using a heterogeneously-bleached fluvial sample, Rodnight (2008) demonstrates the impact of varying the total number of $D_e$ values when undertaking modelling to identify representative burial doses. Within the work it is suggested that a minimum of 50 $D_e$ values are required to isolate reproducible burial doses through modelling. With the exception of GL15025, for most treatment scenarios the total number of $D_e$ values isolated using strict criteria is well below 50, each $D_e$ value therefore has a heavy weighting on dose modelling and OD. Given that Rodnight (2008) also demonstrates having <50 $D_e$ values can be misleading and a sample can appear well-bleached when it is not, the low yield of $D_e$ values obtained through strict rejection criteria could be producing the observed patterns and the discrepancies with FMM. However, as a systematic pattern is observed within all samples it is necessary to consider the potential for HF influencing $D_e$ distributions. It could be that the impact of altering HF treatment is so minimal that only the most precise estimates detect any changes.

As both positive and negative changes in OD have been observed for datasets following increased HF treatment duration, attempting to isolate processes driving changes in distribution becomes complicated. However, it remains a concern that changes in OD can be systematic with variations in HF treatment. The key aim of the HF treatment is to eradicate the α-irradiated rind of quartz grains through etching. All quartz grains should therefore be expected to reduce in size, yet this is not reflected in the average grain size data for the re-sieved fractions in this research. Guerin *et al.* (2015) identify grain size, K content and overall $D_r$ as sources of OD within quartz single-grain OSL measurements. Within their study it is suggested that grain size determines the distances between dosimeters (i.e. quartz grains) and emitters (e.g. K feldspar grains) thus influencing the $D_r$ distribution within a sediment matrix. Modelling within their work indicates that increases in average grain size are accompanied by increased skewness and OD within single-grain $D_e$ datasets. Although the three sources of OD highlighted by Guerin *et al.* (2015) are heavily interlinked and changes in each parameter drive OD, the changes in OD as a function of HF treatment time observed in this research could be related to grain size and $D_r$.

In most instances $D_r$ calculation is based upon the assumption of an infinite matrix and average radionuclide content values. However, $D_r$ is grain-size dependent and within isolated grain fractions there will be, albeit minimal, a $D_r$ gradient. For example, Hansen *et al.* (2018) calculated that for β-irradiated samples there is a 5% difference in $D_r$ between 180 and 250 μm diameter grains. The HF treatment and re-sieve combination is expected to truncate grain size distributions. In this research the grains closest to 180 μm in size prior to treatment would be expected to be lost through the two-stage process and by increasing etching duration it is anticipated that progressively larger grains will be removed. By increasing etching time the original grain size distribution effectively becomes more refined (if relatively similar etching rates are assumed), reducing the $D_r$ gradient created by grain size variability. If the assumption of a homogenous $D_r$ within a sediment matrix is correct, OD would be expected to reduce with a refining of grain size (or increase in HF treatment time), as the grain size range and therefore the variability created

by a $D_r$ gradient is reduced. $D_e$ distributions obtained using strict rejection criteria for samples GL14023 and GL15025 support these expectations and display a systematic reduction in OD with increased HF treatment time. However, $D_e$ distributions for GL16180 displayed a systematic increase in OD with increased treatment time. This indicates that there may be other underlying processes (e.g. microdosimetry) driving changes in distribution, or that the effects of HF treatment and grain size alteration upon $D_e$ distributions are sample-dependent.

In the early TL work upon α-irradiated quartz grains, Goedicke (1984) discovered that a 55% residual of a given α dose could be recovered following a 40 minute HF treatment. A further possible cause for the systematic changes in OD observed in this research could be rooted in the completeness of α-dose removal. Given that OD has been shown to be dose-dependent (Thomsen *et al.,* 2012), the positive/negative change in OD could be determined by the size of the natural dose. Further investigations using α-irradiated material and single-grain quartz OSL would be beneficial to test the assumption that the α-component is reduced to a negligible level following HF treatment and to observe any variability in OD.

Although the investigations in this chapter focus on the impact of various HF treatments upon $D_e$ distribution, it is important to consider that, in addition to removing the α-irradiated rind of quartz grains, HF is also used in OSL dating to remove any contaminating feldspars. The untreated fractions of GL15025 and GL16180 both produced IRSL signals following laboratory β-irradiation (Appendix B: Figure B3.1), indicating that feldspars were still present following density separation. No IRSL signal was detected from any of the fractions treated with HF, suggesting that 30 minutes of etching is long enough to remove feldspar grains.

### *4.4.5. Conclusions*

The initial purpose of this section was to examine whether HF treatment has any influence upon the $D_e$ distributions of naturally-dosed quartz OSL samples. Two orders of $D_e$ precision based upon recycling ratio rejection

criteria were explored. The relaxed criteria displayed minimal change in OD whilst strict criteria produced OD values that changed progressively with increased HF submersion time. It is likely that these observed changes are either a result of altering grain size distribution or through smaller grain yields producing $D_e$ populations which are not representative. Given the minimal variability in modelled $D_e$ values and statistical parameters (skewness, kurtosis, OD) observed in datasets obtained using the more relaxed rejection criteria, patterns observed for the strict rejection criteria datasets with relatively low grain yields should be interpreted cautiously.

Increased etching duration has been shown to cause significant reduction in the total mass of quartz returned following treatment, as has altering the initial mass of quartz treated with 100 ml of HF. Though based on a single sample, the ratio of HF to quartz appears to have a threshold of 20 ml/g above which mass loss appears to become more significant. For the Mfolozi sediments analysed in the subsequent chapters, continuous agitation of 5 g of 180-250 μm quartz in 100 ml of HF (40%) for 60 minutes has been selected as the most suitable treatment. The mass lost by GL15025 following a 60 minute treatment in this chapter suggests that <20 μm will be removed from Mfolozi quartz grains when using the same HF treatment conditions. Treatments of 40 minutes are retained for the smaller diameter grain fractions not explored in this chapter.

Given the minimal change in central $D_e$ observed across the HF treatment scenarios (including the untreated) examined in this chapter, it would appear that the α-component either has a negligible impact upon central $D_e$ or can not be effectively removed using HF. Further investigation using single-grain OSL and laboratory α-dosed material would seem a sensible avenue to explore in subsequent research, particularly given the findings in early TL work undertaken by Goedicke (1984).

# Chapter 5: Optical Dating of Mfolozi Sediments

## 5.1. Overview

This chapter focuses upon the quartz OSL dating of sediments collected from the Mfolozi floodplain. For each sampling location an overview of $D_e$, $D_r$ and age calculation is provided. All samples evaluated in this chapter have been subject to the preparation and measurement procedures outlined in Chapter 3, whilst hydrofluoric acid treatments of the 180-250 μm quartz fraction were informed by the investigations in Chapter 4.

## 5.2. South Lake

### *5.2.1. Sample Overview*

The South Lake site is the blocked-valley wetland situated on the southern margin of the Mfolozi floodplain. Initially 21 samples were collected from core lengths for OSL dating, however, three fine silt samples which were collected from the organic rich region of the cores were disregarded as insufficient quantities of 5-15 μm quartz could be isolated. Multi-grain dose recovery tests were conducted for all samples. The use of single or multi-grain aliquots for $D_e$ measurement was determined by grain size. Table 5.2.1 provides an overview of the samples prepared and measured for the South Lake site.

### *5.2.2. Initial OSL Signal Evaluation and Dose-Recovery Results*

Prior to conducting single-grain $D_e$ analysis, two sets of measurements were conducted upon multi-grain aliquots of each sample. These measurements assessed the relative size/intensity of the natural OSL signal and to identify suitable SAR preheat temperatures using dose-recovery experiments. Figure 5.2.1 provides an example of the data acquired from the initial measurements for GL15015. Applying a 5 Gy test dose produced an $L_x/T_x$ ratio of 0.566, which by linear calculation directed use of 2.8 Gy for the Dose Recovery test.

**Table 5.2.1:** South Lake OSL sample overview (ordered by depth)

| Sample | Depth (m) | Moisture Content (%) | Grain Fraction (μm) | Single-Grain/Aliquot |
|---|---|---|---|---|
| GL15157 | 0.17 | 28 | 180-250 | Single-Grain |
| GL15158 | 0.32 | 22 | 180-250 | Single-Grain |
| GL15015 | 0.48 | 17 | 180-250 | Single-Grain |
| GL16099 | 0.72 | 35 | 5-15 | Multi-Grain |
| GL15016 | 0.85 | 42 | 5-15 | Multi-Grain |
| GL15020 | 1.58 | 45 | 5-15 | Multi-Grain |
| GL15021 | 1.68 | 52 | 5-15 | Multi-Grain |
| GL15022 | 1.81 | 41 | 5-15 | Multi-Grain |
| GL15023 | 2.09 | 39 | 180-250 | Single-Grain |
| GL15024 | 2.58 | 44 | 180-250 | Single-Grain |
| GL15025 | 2.88 | 20 | 180-250 | Single-Grain |
| GL15026 | 3.13 | 17 | 180-250 | Single-Grain |
| GL15027 | 3.27 | 15 | 180-250 | Single-Grain |
| GL15028 | 3.74 | 17 | 180-250 | Single-Grain |
| GL15029 | 3.87 | 16 | 180-250 | Single-Grain |
| GL15030 | 4.10 | 21 | 125-180 | Single-Grain |
| GL15031 | 4.33 | 22 | 125-180 | Single-Grain |
| GL15032 | 4.62 | 31 | 125-180 | Single-Grain |

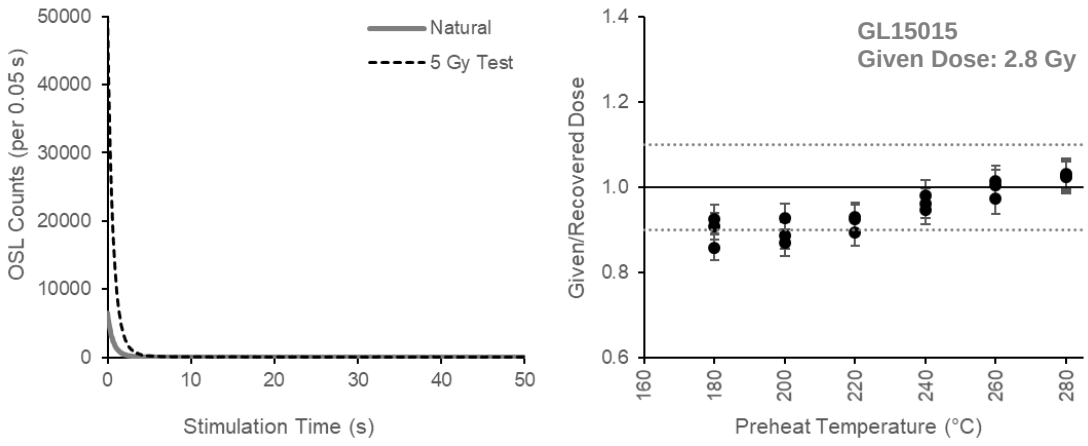


**Figure 5.2.1:** Test disc natural/5 Gy test OSL signal and 2.8 Gy dose-recovery test for GL15015.

Dose-recovery tests were conducted upon all samples and the recovered ratio x-y plots for all of these are presented in Appendix C (Figures C1.1-3). A summary of the dose-recovery test results is presented in Table 5.2.2. All dose-recovery measurements on sand-sized material indicated that preheats ≥240°C were appropriate, whilst fine silt measurements indicated preheats of ≤240°C were most suitable. Cut heat temperatures of 180°C were used for preheats ≤220°C whilst 220°C cut heats were used for preheat temperatures ≥240°C. With the exception of GL15022, which across each preheat temperature recovered doses slightly higher than that applied, the selected preheats for all samples had given/recovered dose ratios statistically consistent with unity. For some samples minimal material was available for $D_e$ analysis and only one aliquot per preheat was measured.

**Table 5.2.2:** South Lake test disc and dose-recovery test result summary

| Sample | Test Disc $L_x/T_x$ | Given Dose (Gy) | Selected Preheat (°C) | Given/Recovered Dose Ratio* |
|---|---|---|---|---|
| GL15157 | 0.739 | 3.7 | 280 | *1.00 ± 0.03* |
| GL15158 | 1.143 | 7.1 | 260 | *1.00 ± 0.03* |
| GL15015 | 0.566 | 2.8 | 260 | 1.00 ± 0.04 |
| GL16099 | 0.841 | 4.2 | 220 | 1.00 ± 0.03 |
| GL15016 | 1.201 | 6.0 | 220 | 1.00 ± 0.03 |
| GL15020 | 1.723 | 8.6 | 240 | 0.99 ± 0.03 |
| GL15021 | 1.460 | 7.3 | 240 | 1.00 ± 0.03 |
| GL15022 | 0.666 | 3.3 | 180 | 1.06 ± 0.03 |
| GL15023 | 1.881 | 9.4 | 260 | 1.00 ± 0.04 |
| GL15024 | 1.319 | 6.6 | 240 | 0.99 ± 0.03 |
| GL15025 | 1.935 | 9.7 | 240 | 0.98 ± 0.03 |
| GL15026 | 2.310 | 11.6 | 240 | 0.99 ± 0.03 |
| GL15027 | 2.259 | 11.3 | 240 | 1.00 ± 0.03 |
| GL15028 | 2.440 | 12.2 | 240 | 0.98 ± 0.03 |
| GL15029 | 2.268 | 11.3 | 240 | 0.98 ± 0.04 |
| GL15030 | 2.800 | 14.0 | 240 | 1.00 ± 0.03 |
| GL15031 | 2.598 | 13.0 | 240 | 0.99 ± 0.04 |
| GL15032 | 2.518 | 12.6 | 240 | 1.00 ± 0.03 |

*Given/Recovered Dose Ratio typically based on average of 3 aliquots per preheat – italicised values indicate only 1 aliquot available per preheat.

*5.2.3. Single-Grain $D_e$ Results*

In total, thirteen single-grain samples were analysed from the South Lake site, a summary of $D_e$ results is provided in Table 5.2.4 whilst $D_e$ summary diagrams are presented for each individual sample in Figures 5.2.2 to 5.2.14. The $D_e$ components isolated by FMM and the proportion of grains within each are summarised in Table 5.2.3. A similar approach to Rodnight *et al.* (2006) was adopted for FMM, whereby components containing less than 10% of $D_e$ values were disregarded.

The near-surface samples; GL15157, GL15158 and GL15015, display very similar patterns within their respective radial plots (Figure 5.2.2c-5.2.4c). FMM identifies that the majority of grains are held within two distinct populations and isolates $FMM_{max}$ high-dose peaks between 0.56 and 0.62 Gy and $FMM_{min}$ low-dose peaks between 0.10 and 0.12 Gy. All three samples feature a similar proportion of zero-dose grains and similar magnitude of OD (77-86%). The proportion of grains within the high-dose peak increases from 42% to 58% with increasing depth. Central measures of $D_e$ (median and CAM) are statistically consistent for GL15157 and GL15158 whilst values for GL15015 are slightly elevated (Table 5.2.4). All three samples are highly positively skewed and GL15015 displays an exaggerated kurtosis driven by the longer high-dose tail of the distribution.

GL15023 was collected from a thin laminated sand unit and produced a very different $D_e$ distribution relative to samples of a similar (and greater) depth (Figure 5.2.5). The relatively broad $D_e$ distribution for GL15023 has an OD of 42% and displays moderate positive skewness (0.91). Median and CAM $D_e$ values (11.46±0.41 & 10.65±0.40 Gy) are around double the size of the values calculated for MAM and $FMM_{min}$ (Table 5.2.4), for which only 7 and 10% of grains accepted fall within the bounds of the respective minimum $D_e$ estimates. For heterogeneously bleached sediments Rodnight *et al.* (2006) suggest that MAM tends to underestimate $D_e$ whilst CAM leads to an overestimate. Given that for GL15023 $FMM_{min}$<MAM, consideration of other doses isolated by the 4-component FMM is worthwhile. $FMM_{k=2}$ (7.80±0.52; Table 5.2.3) isolates a dose population between MAM and CAM and incorporates 23% of all grains, when considering the suggestion by Rodnight

*et al.* (2006) this would appear more suitable value than that produced for $FMM_{min}$. Median and CAM $D_e$ values are elevated relative to samples situated below GL15023.

Samples GL15024 to GL15032 display similar inter-grain $D_e$ dispersion with all having OD between 21 and 24%, but some subtle differences exist between each distribution. GL15024 is highly positively skewed (*c* = 3.50) and has elevated kurtosis (25.14) which appears to be driven by a small number of high dose grains (Figure 5.2.6d). Central (Median & CAM) and Minimum (MAM & $FMM_{min}$) $D_e$ estimates are significantly different and are separated by *c.* 1 Gy. $FMM_{maj}$ identifies $FMM_{max}$ (7.07±0.43 Gy) as the $D_e$ component containing the highest proportion (57%) of values for GL15024, this is *c.* 0.8 Gy greater than central measures of $D_e$.

GL15025-26 have similar, near-symmetric distributions which display minimal skewness (Figure 5.2.7 & 8). For both samples central and minimum $D_e$ values are statistically inconsistent and differences of *c.* 2 Gy are observed between these for both samples. Fitting of FMM to GL15025 identified a minimum dose population containing 11% of grains which was *c.* 1.7 Gy lower than the estimate for MAM, whilst $FMM_{max}$ identified a $D_e$ component (9.91±0.30 Gy) which is statistically consistent with central measures of $D_e$ and encapsulates 89% of all values. It was not possible to fit FMM to GL15026 indicating that the $D_e$ distribution is comprised of a single dose population.

GL15027 has a highly skewed distribution (Figure 5.2.9) which features a long high-dose tail. Central and minimum $D_e$ values are significantly different with a *c.* 1.5-2.2 Gy discrepancy being observed. The $FMM_{min}$ component (9.45±0.62 Gy) which incorporates 52% of all grains is situated between MAM and CAM $D_e$. The high-dose component $FMM_{max}$ produced an estimate *c.* 2 Gy greater than central measures of $D_e$, however, a significant proportion of grains (48%) do fall within this component.

Samples GL15028-31 (Figure 5.2.10-13) display similar distributions with moderate positive skewness and featuring high-dose tails with similar kurtosis values. Central and minimum $D_e$ values are significantly different for

all samples in this cluster with a *c.* 1.5-3.2 Gy discrepancy being observed between central and minimum doses. The $FMM_{min}$ components for GL15028 (9.63±0.78 Gy) and GL15029 (11.26±0.44 Gy) are situated between the median/CAM and MAM values calculated for each respective sample. For samples GL15030 and GL15031 $FMM_{min}$ (10.84±0.73 & 11.91±1.00 Gy respectively) is less than both the central and MAM $D_e$. For GL15029 the $FMM_{maj}$ component (11.26±0.44 Gy) is situated between the CAM and $FMM_{max}$, with $FMM_{maj}$ containing 71% of all $D_e$ values. The $FMM_{maj}$ components for GL15028 (12.34±0.52 Gy), GL15030 (15.37±0.41 Gy) and GL15031 (15.92±0.88 Gy) all correspond to $FMM_{max}$ with 73, 76 and 66% of values falling within the respective components.

The basal sample GL15032 (Figure 5.2.14) produced a near-symmetric distribution with minimal skewness. Central and minimum (both MAM & $FMM_{min}$) $D_e$ estimates are significantly different and are separated by *c.* 2.5 Gy. The $FMM_{max}$ component (14.86±0.51 Gy) accounts for 59% of all $D_e$ values and is *c.* 1.7 Gy greater than central doses.

**Table 5.2.3:** FMM components fitted to South Lake single-grain $D_e$ distributions (*k** = total components, σ = 0.15 (15%) and *p* = proportion of grains in each component)

| | | FMM Component | | | | | | | |
|---|---|---|---|---|---|---|---|---|---|
| | | ***k* = 1** | | ***k* = 2** | | ***k* = 3** | | ***k* = 4** | |
| **Sample** | ***k**** | **$D_e$ (Gy)** | ***p* (%)** | **$D_e$ (Gy)** | ***p* (%)** | **$D_e$ (Gy)** | ***p* (%)** | **$D_e$ (Gy)** | ***p* (%)** |
| GL15157 | 4 | 0.11±0.01 | 34 | 0.33±0.04 | 18 | 0.59±0.02 | 42 | 1.54±0.15 | 6 |
| GL15158 | 4 | 0.12±0.01 | 30 | 0.21±0.03 | 14 | 0.56±0.01 | 51 | 1.28±0.13 | 5 |
| GL15015 | 4 | 0.10±0.01 | 15 | 0.32±0.03 | 22 | 0.62±0.01 | 58 | 5.46±0.37 | 5 |
| GL15023 | 4 | 4.61±0.19 | 10 | 7.80±0.52 | 24 | 12.50±0.24 | 55 | 21.13±0.83 | 11 |
| GL15024 | 2 | 5.22±0.42 | 43 | 7.07±0.43 | 57 | - | - | - | - |
| GL15025 | 2 | 5.99±0.92 | 11 | 9.91±0.30 | 89 | - | - | - | - |
| GL15026 | - | - | - | - | - | - | - | - | - |
| GL15027 | 2 | 9.45±0.62 | 52 | 13.08±0.85 | 48 | - | - | - | - |
| GL15028 | 2 | 9.63±0.78 | 27 | 12.34±0.52 | 73 | - | - | - | - |
| GL15029 | 2 | 11.26±0.44 | 71 | 16.53±1.32 | 29 | - | - | - | - |
| GL15030 | 2 | 10.84±0.73 | 24 | 15.37±0.41 | 76 | - | - | - | - |
| GL15031 | 2 | 11.91±1.00 | 34 | 15.92±0.88 | 66 | - | - | - | - |
| GL15032 | 2 | 10.79±0.48 | 41 | 14.86±0.51 | 59 | - | - | - | - |

**Table 5.2.4:** Summary of South Lake single-grain $D_e$ analysis (errors reported within 1σ confidence; for age modelling σ = 0.15 (15%))

| Sample | Depth (m) | Grains Accepted (Number (%))* | $\sigma_{OD}$ (%) | Skewness (c) | Kurtosis (*k*) | $D_e$ Values (Gy) | | | | | | |
|---|---|---|---|---|---|---|---|---|---|---|---|---|
| | | | | | | Median | CAM | MAM | FMM *k*** | $FMM_{min}$ | $FMM_{max}$ | $FMM_{maj}$ |
| GL15157 | 0.17 | 87 (8.7) | 85 | 1.49 | 6.33 | 0.36 ± 0.04 | 0.30 ± 0.03 | 0.09 ± 0.01 | 4 | 0.11 ± 0.01 | 0.59 ± 0.02 | 0.59 ± 0.02 |
| GL15158 | 0.32 | 106 (10.6) | 77 | 1.15 | 4.55 | 0.38 ± 0.03 | 0.32 ± 0.02 | 0.11 ± 0.01 | 4 | 0.12 ± 0.01 | 0.56 ± 0.01 | 0.56 ± 0.01 |
| GL15015 | 0.48 | 115 (11.5) | 86 | 3.16 | 20.20 | 0.47 ± 0.12 | 0.44 ± 0.02 | 0.14 ± 0.02 | 4 | 0.10 ± 0.01 | 0.62 ± 0.01 | 0.62 ± 0.01 |
| GL15023 | 2.09 | 140 (14.0) | 42 | 0.91 | 4.34 | 11.46 ± 0.41 | 10.65 ± 0.40 | 5.48 ± 0.31 | 4 | 4.61 ± 0.19 | 21.13 ± 0.83 | 12.50 ± 0.24 |
| GL15024 | 2.58 | 136 (13.6) | 22 | 3.50 | 25.14 | 6.29 ± 0.19 | 6.20 ± 0.13 | 5.07 ± 0.29 | 2 | 5.22 ± 0.42 | 7.07 ± 0.43 | 7.07 ± 0.43 |
| GL15025 | 2.88 | 127 (12.7) | 23 | 0.28 | 2.98 | 9.41 ± 0.22 | 9.40 ± 0.22 | 7.67 ± 0.38 | 2 | 5.99 ± 0.92 | 9.91 ± 0.30 | 9.91 ± 0.30 |
| GL15026 | 3.13 | 152 (15.2) | 21 | 0.44 | 3.75 | 12.29 ± 0.25 | 11.92 ± 0.24 | 10.05 ± 0.47 | - | - | - | - |
| GL15027 | 3.27 | 148 (14.8) | 23 | 1.02 | 4.42 | 10.90 ± 0.27 | 11.05 ± 0.24 | 8.87 ± 0.48 | 2 | 9.45 ± 0.62 | 13.08 ± 0.85 | 9.45 ± 0.62 |
| GL15028 | 3.74 | 170 (17.0) | 24 | 0.81 | 4.64 | 11.32 ± 0.25 | 11.21 ± 0.23 | 9.00 ± 0.41 | 2 | 9.63 ± 0.78 | 12.34 ± 0.52 | 12.34 ± 0.52 |
| GL15029 | 3.87 | 143 (14.3) | 24 | 0.97 | 4.26 | 12.58 ± 0.34 | 12.60 ± 0.29 | 9.87 ± 0.61 | 2 | 11.26 ± 0.44 | 16.53 ± 1.32 | 11.26 ± 0.44 |
| GL15030 | 4.10 | 187 (18.7) | 21 | 0.84 | 4.23 | 14.13 ± 0.28 | 14.14 ± 0.25 | 11.76 ± 0.53 | 2 | 10.84 ± 0.73 | 15.37 ± 0.41 | 15.37 ± 0.41 |
| GL15031 | 4.33 | 129 (12.9) | 21 | 0.95 | 4.60 | 14.20 ± 0.34 | 14.44 ± 0.30 | 12.17 ± 0.63 | 2 | 11.91 ± 1.00 | 15.92 ± 0.88 | 15.92 ± 0.88 |
| GL15032 | 4.62 | 184 (18.4) | 22 | 0.50 | 3.28 | 13.20 ± 0.25 | 13.04 ± 0.23 | 10.75 ± 0.46 | 2 | 10.79 ± 0.48 | 14.86 ± 0.51 | 14.86 ± 0.51 |

*1000 grains measured per sample

** *k* = number of components fitted for the FMM

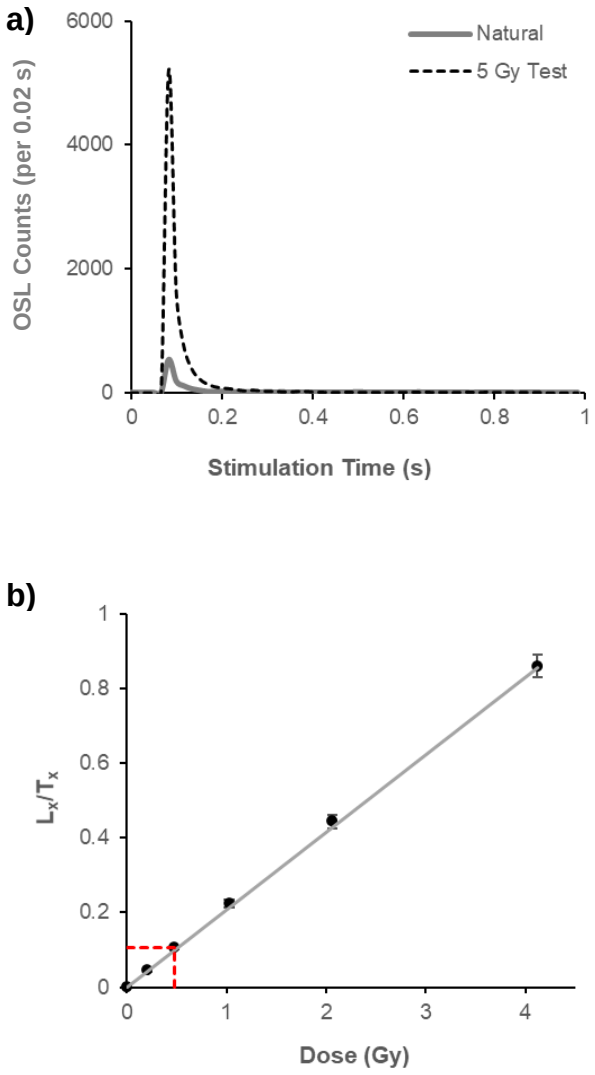


**Figure 5.2.2:** Single-grain $D_e$ summary diagrams for GL15157

a) Example single-grain decay curves for the natural and 5 Gy test dose signals of grain 14.

b) Dose-response curve for grain 14 with regenerative doses; 0, 0.2, 0.5, 1.0, 2.1, & 4.1 Gy. Interpolation of the natural $L_x/T_x$ recovered a $D_e$ of 0.48 Gy.

c) Radial plot of 87 $D_e$ values which passed rejection criteria. Coloured areas represent age models applied to the $D_e$ dataset; CAM (**red**), MAM (**grey**), $FMM_{min}$ (**green**) and $FMM_{maj}$ (**blue**). $FMM_{max}$ is equivalent to the $FMM_{maj}$ component for this sample.

d) Histogram of $D_e$ values with bin width 0.1. Dataset is highly positively skewed (c) and features a small proportion of zero-dose grains

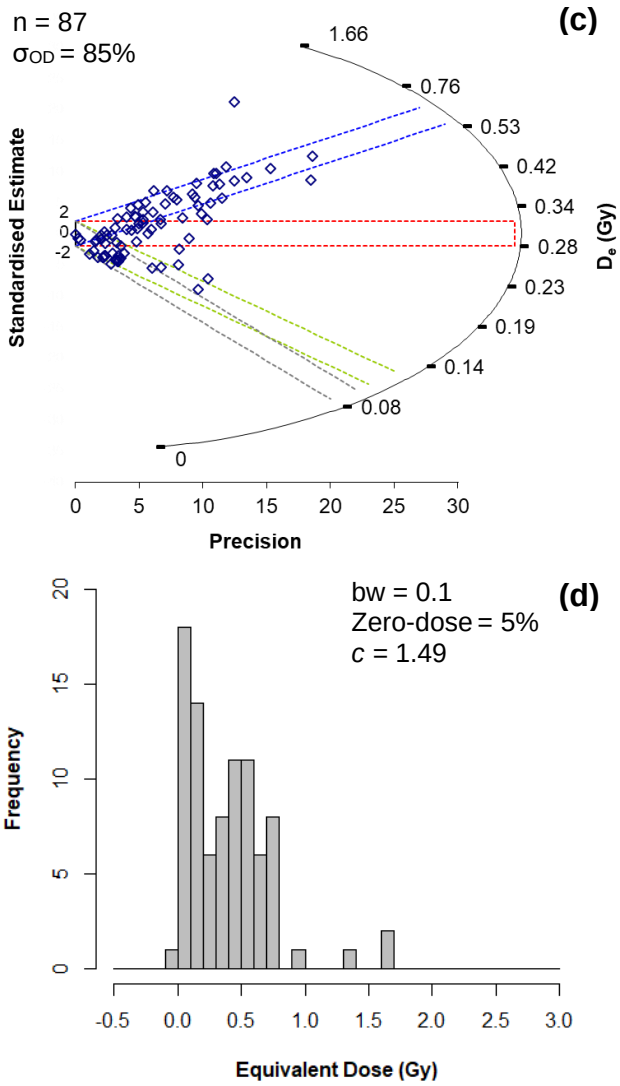

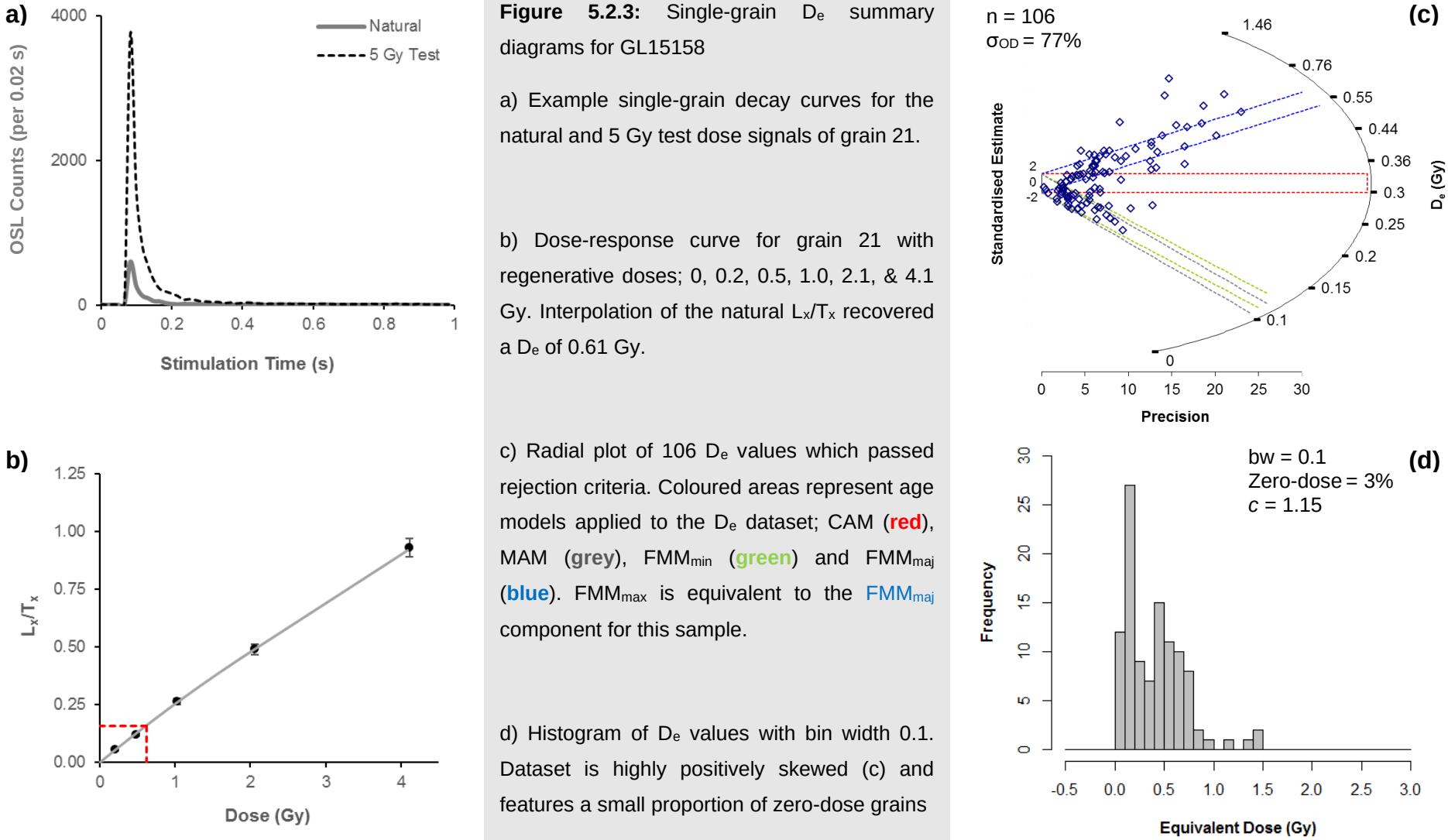


**Figure 5.2.3:** Single-grain $D_e$ summary diagrams for GL15158

a) Example single-grain decay curves for the natural and 5 Gy test dose signals of grain 21.

b) Dose-response curve for grain 21 with regenerative doses; 0, 0.2, 0.5, 1.0, 2.1, & 4.1 Gy. Interpolation of the natural $L_x/T_x$ recovered a $D_e$ of 0.61 Gy.

c) Radial plot of 106 $D_e$ values which passed rejection criteria. Coloured areas represent age models applied to the $D_e$ dataset; CAM (**red**), MAM (**grey**), $FMM_{min}$ (**green**) and $FMM_{maj}$ (**blue**). $FMM_{max}$ is equivalent to the $FMM_{maj}$ component for this sample.

d) Histogram of $D_e$ values with bin width 0.1. Dataset is highly positively skewed (c) and features a small proportion of zero-dose grains

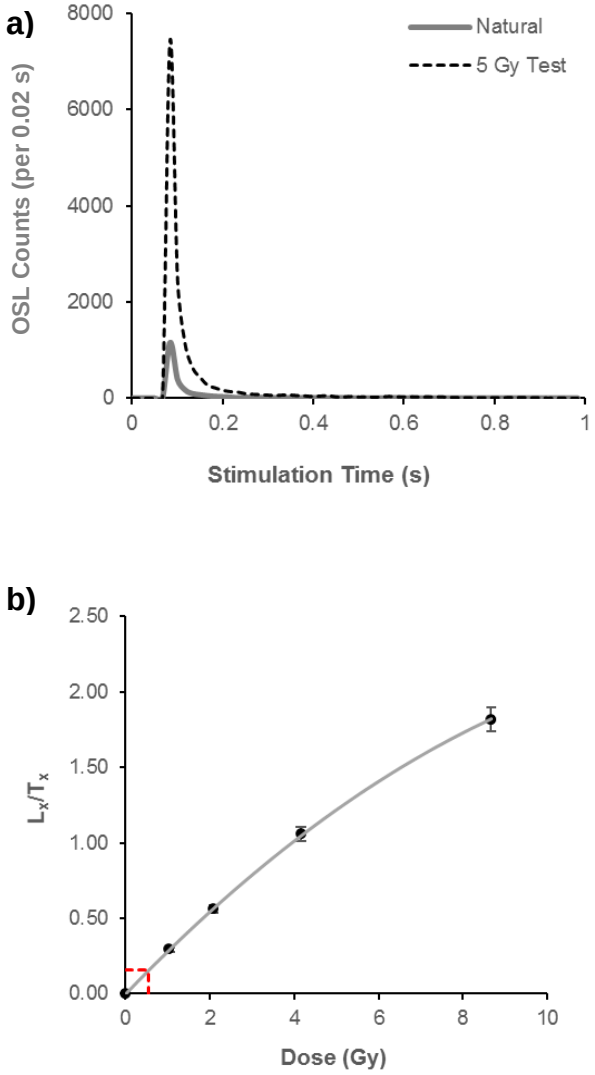


**Figure 5.2.4:** Single-grain $D_e$ summary diagrams for GL15015

a) Example single-grain decay curves for the natural and 5 Gy test dose signals of grain 2.

b) Dose-response curve for grain 2 with regenerative doses; 0, 1, 2.1, 4.2, & 8.7 Gy. Interpolation of the natural $L_x/T_x$ recovered a $D_e$ of 0.54 Gy.

c) Radial plot of 115 $D_e$ values which passed rejection criteria. Coloured areas represent age models applied to the $D_e$ dataset; CAM (**red**), MAM (**grey**), $FMM_{min}$ (**green**) and $FMM_{maj}$ (**blue**). $FMM_{max}$ is equivalent to the $FMM_{maj}$ component for this sample.

d) Histogram of $D_e$ values with bin width 0.2. Dataset is highly positively skewed (*c*) and features a small proportion of zero-dose grains

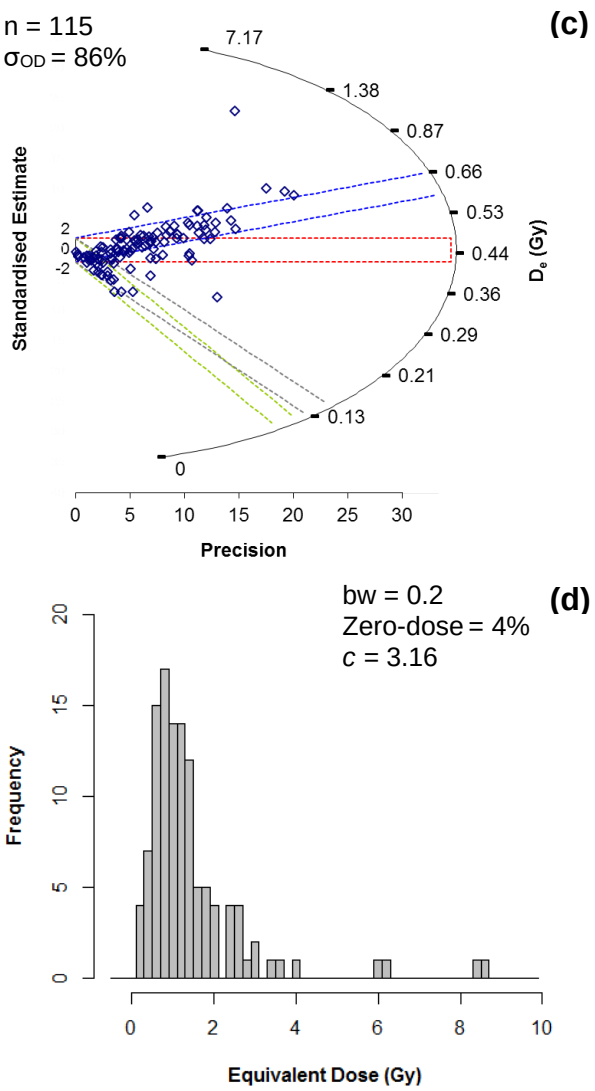

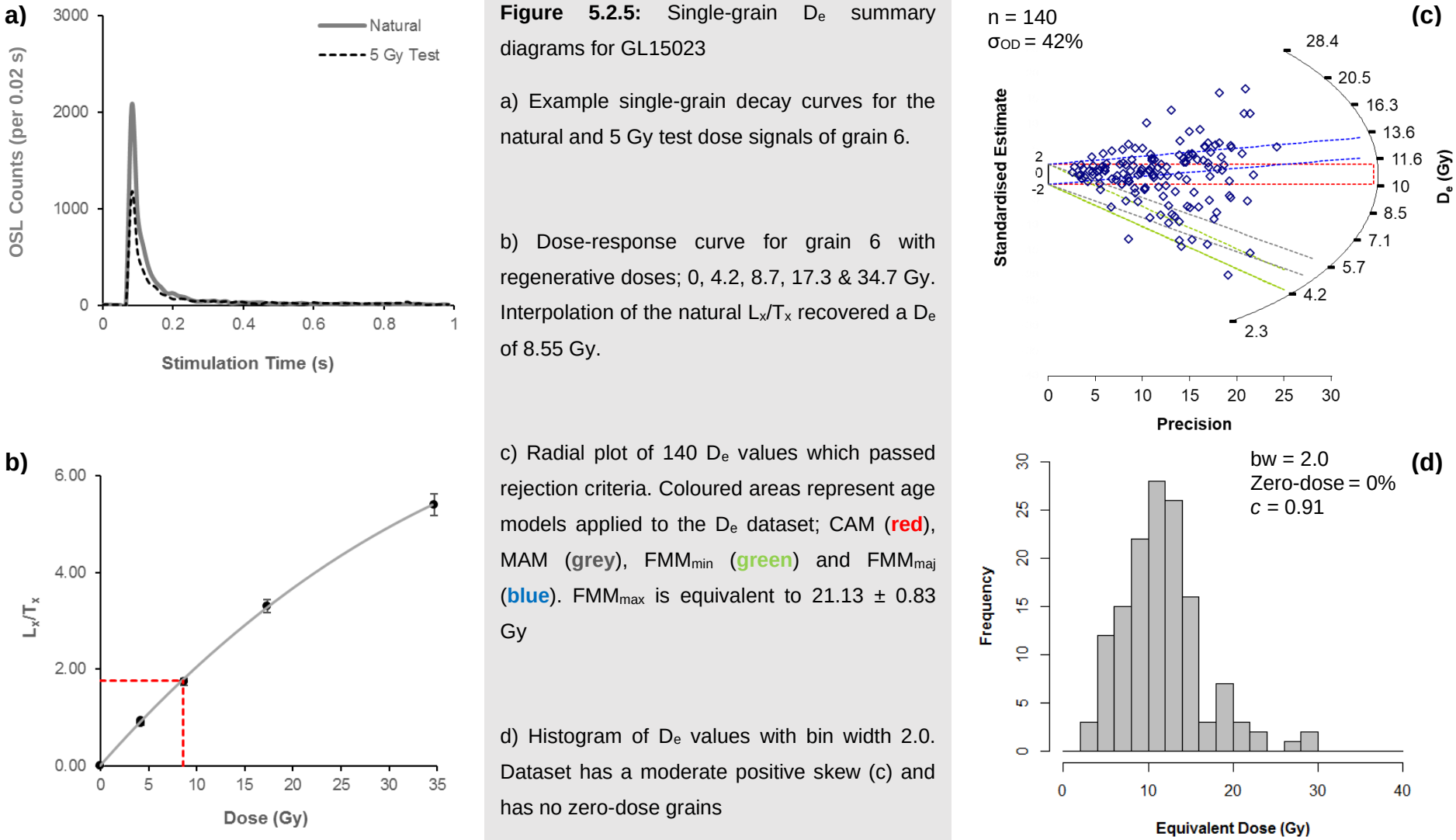


**Figure 5.2.5:** Single-grain $D_e$ summary diagrams for GL15023

a) Example single-grain decay curves for the natural and 5 Gy test dose signals of grain 6.

b) Dose-response curve for grain 6 with regenerative doses; 0, 4.2, 8.7, 17.3 & 34.7 Gy. Interpolation of the natural $L_x/T_x$ recovered a $D_e$ of 8.55 Gy.

c) Radial plot of 140 $D_e$ values which passed rejection criteria. Coloured areas represent age models applied to the $D_e$ dataset; CAM (**red**), MAM (**grey**), $FMM_{min}$ (**green**) and $FMM_{maj}$ (**blue**). $FMM_{max}$ is equivalent to 21.13 ± 0.83 Gy

d) Histogram of $D_e$ values with bin width 2.0. Dataset has a moderate positive skew (c) and has no zero-dose grains

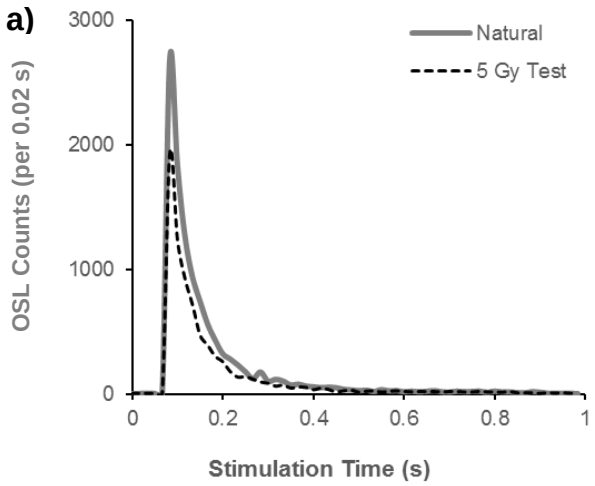


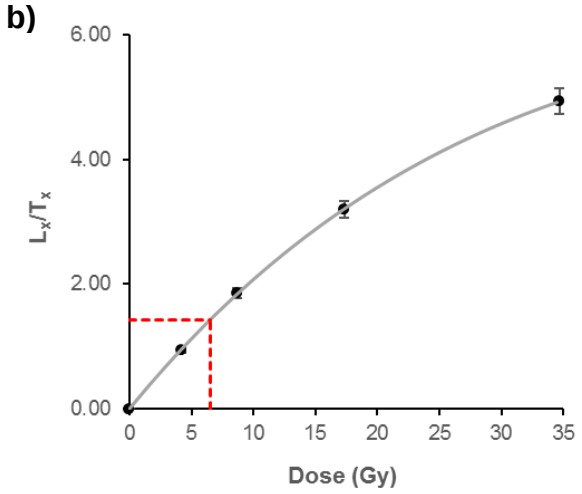


**Figure 5.2.6:** Single-grain $D_e$ summary diagrams for GL15024

a) Example single-grain decay curves for the natural and 5 Gy test dose signals of grain 5.

b) Dose-response curve for grain 5 with regenerative doses; 0, 4.2, 8.7, 17.3 & 34.7 Gy. Interpolation of the natural $L_x/T_x$ recovered a $D_e$ of 6.52 Gy.

c) Radial plot of 136 $D_e$ values which passed rejection criteria. Coloured areas represent age models applied to the $D_e$ dataset; CAM (**red**), MAM (**grey**), $FMM_{min}$ (**green**) and $FMM_{maj}$ (**blue**). $FMM_{max}$ is equivalent to the $FMM_{maj}$ component for this sample.

d) Histogram of $D_e$ values with bin width 1.0. Data is highly positively skewed (c). No zero-dose grains.

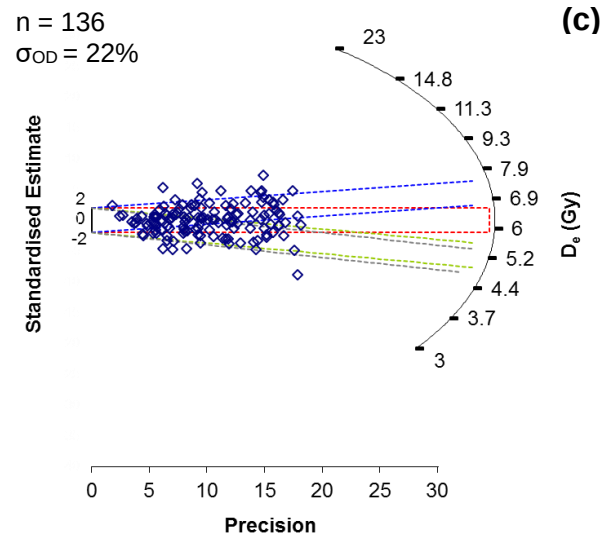


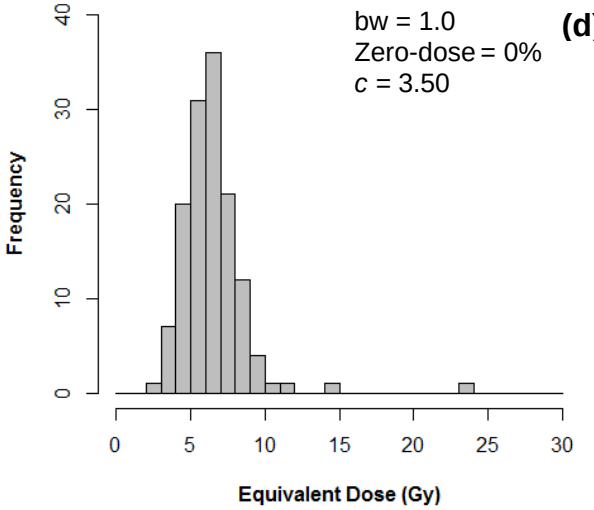

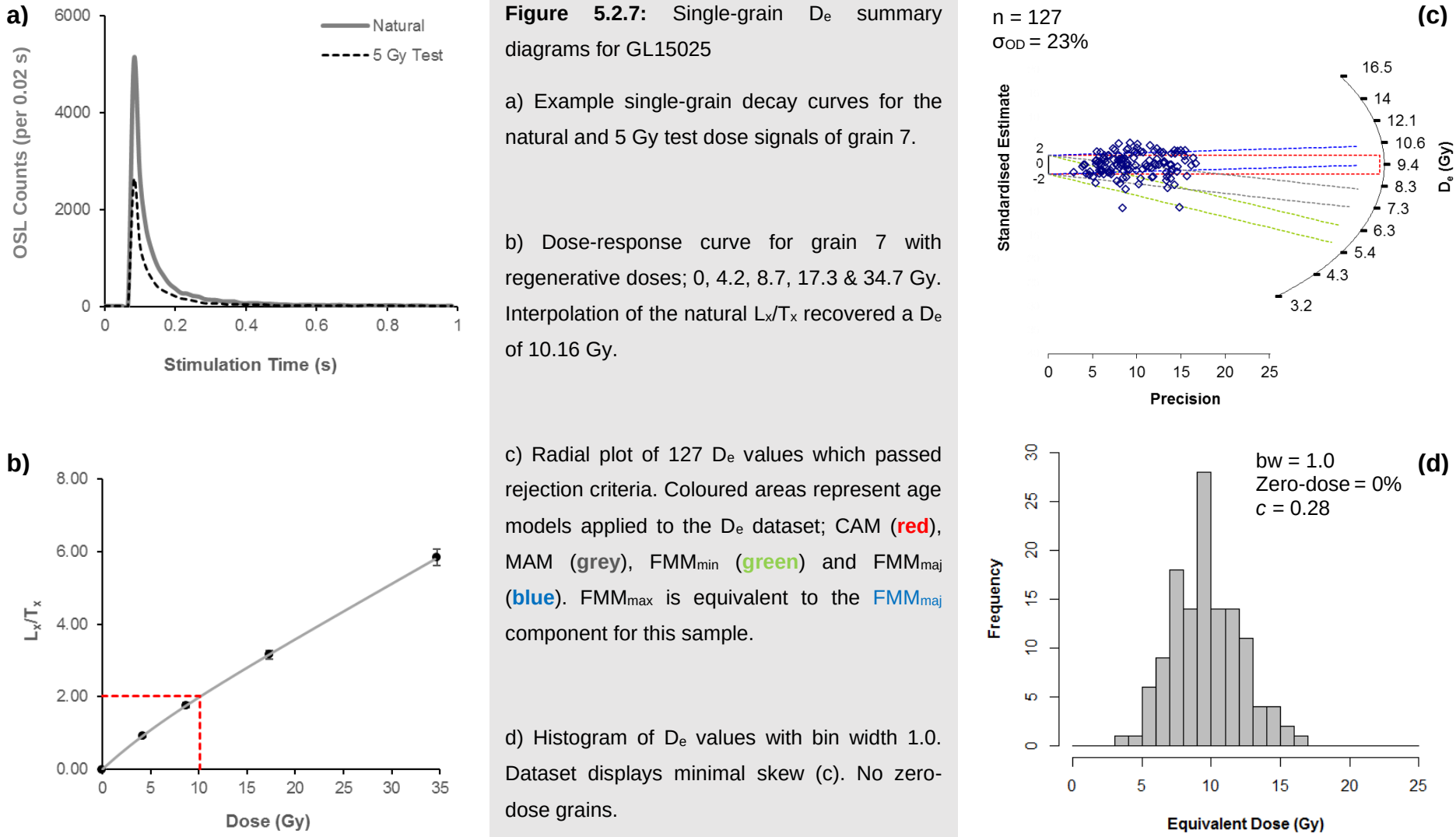


**Figure 5.2.7:** Single-grain $D_e$ summary diagrams for GL15025

a) Example single-grain decay curves for the natural and 5 Gy test dose signals of grain 7.

b) Dose-response curve for grain 7 with regenerative doses; 0, 4.2, 8.7, 17.3 & 34.7 Gy. Interpolation of the natural $L_x/T_x$ recovered a $D_e$ of 10.16 Gy.

c) Radial plot of 127 $D_e$ values which passed rejection criteria. Coloured areas represent age models applied to the $D_e$ dataset; CAM (**red**), MAM (**grey**), $FMM_{min}$ (**green**) and $FMM_{maj}$ (**blue**). $FMM_{max}$ is equivalent to the $FMM_{maj}$ component for this sample.

d) Histogram of $D_e$ values with bin width 1.0. Dataset displays minimal skew (c). No zero-dose grains.

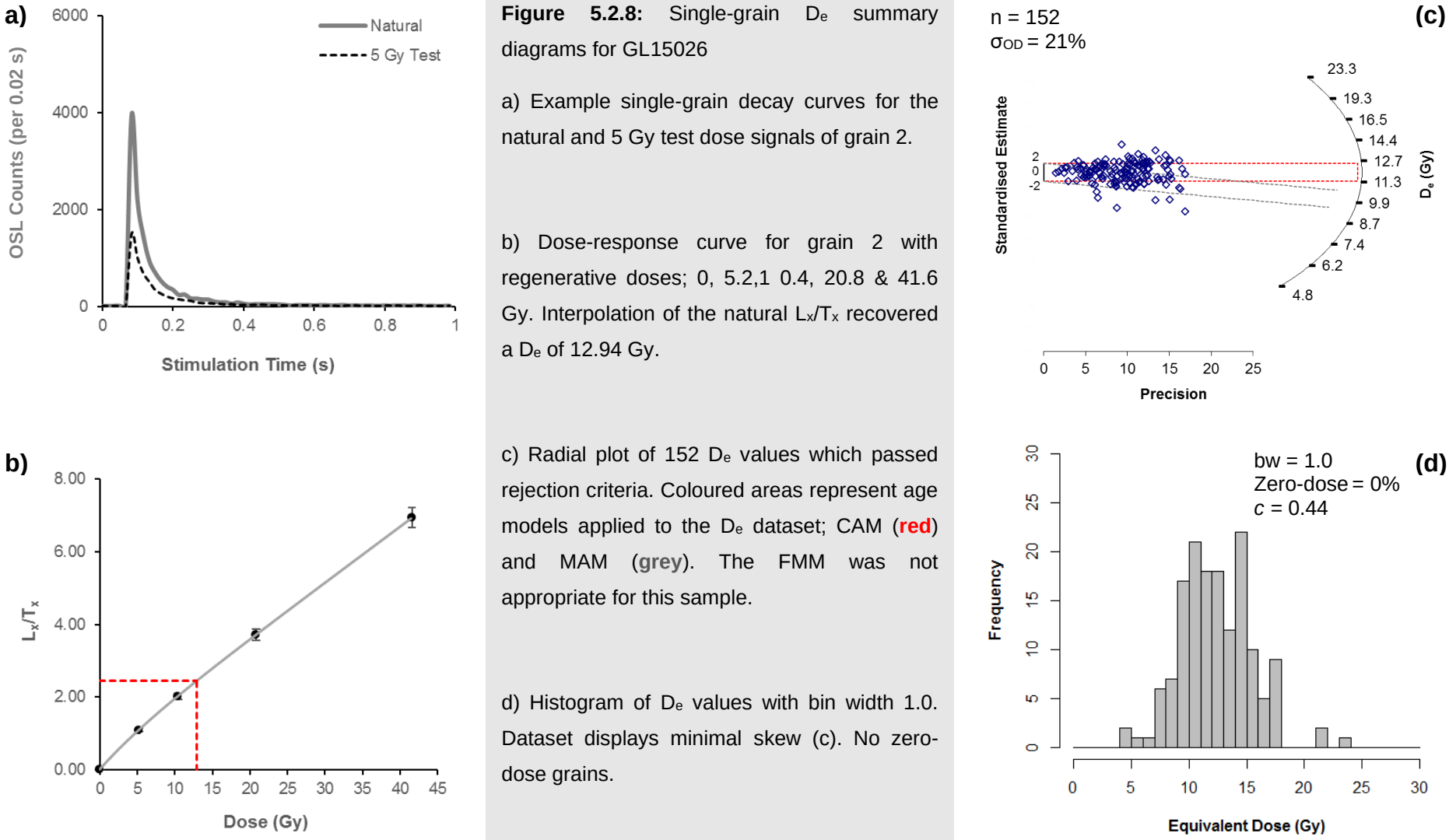


**Figure 5.2.8:** Single-grain $D_e$ summary diagrams for GL15026

a) Example single-grain decay curves for the natural and 5 Gy test dose signals of grain 2.

b) Dose-response curve for grain 2 with regenerative doses; 0, 5.2,1 0.4, 20.8 & 41.6 Gy. Interpolation of the natural $L_x/T_x$ recovered a $D_e$ of 12.94 Gy.

c) Radial plot of 152 $D_e$ values which passed rejection criteria. Coloured areas represent age models applied to the $D_e$ dataset; CAM (**red**) and MAM (**grey**). The FMM was not appropriate for this sample.

d) Histogram of $D_e$ values with bin width 1.0. Dataset displays minimal skew (c). No zero-dose grains.

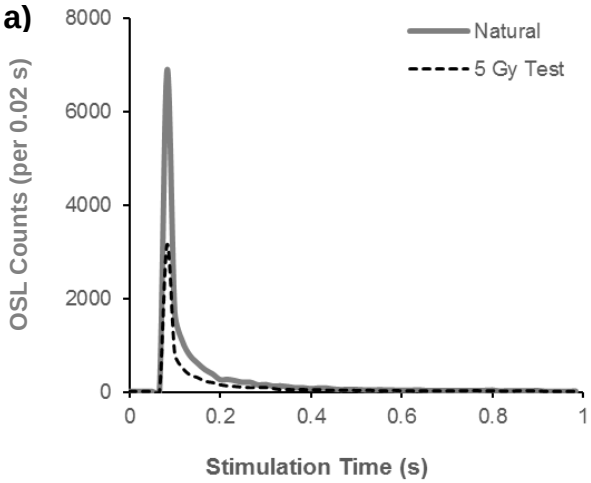


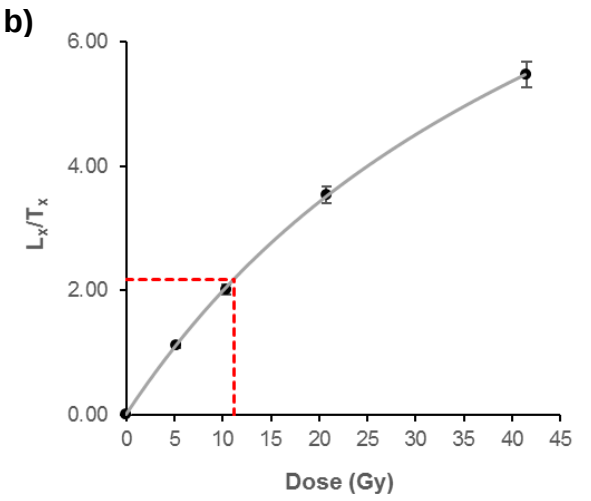


**Figure 5.2.9:** Single-grain $D_e$ summary diagrams for GL15027

a) Example single-grain decay curves for the natural and 5 Gy test dose signals of grain 9.

b) Dose-response curve for grain 9 with regenerative doses; 0, 5.2,1 0.4, 20.8 & 41.6 Gy. Interpolation of the natural $L_x/T_x$ recovered a $D_e$ of 11.11 Gy.

c) Radial plot of 148 $D_e$ values which passed rejection criteria. Coloured areas represent age models applied to the $D_e$ dataset; CAM (**red**), MAM (**grey**), $FMM_{min}$ (**green**) and $FMM_{maj}$ (**blue**). $FMM_{max}$ is equivalent to 13.08 ± 0.85 Gy.

d) Histogram of $D_e$ values with bin width 1.0. Dataset is highly positively skewed (c). No zero-dose grains.

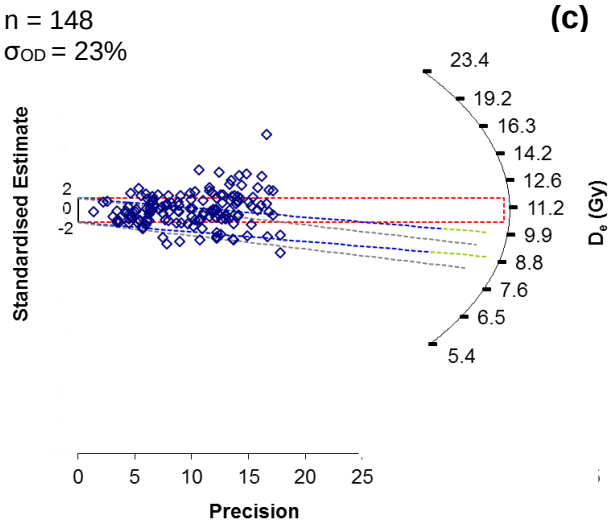


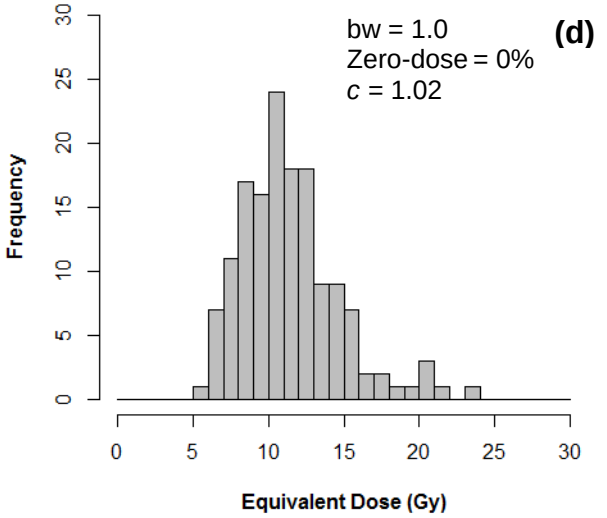

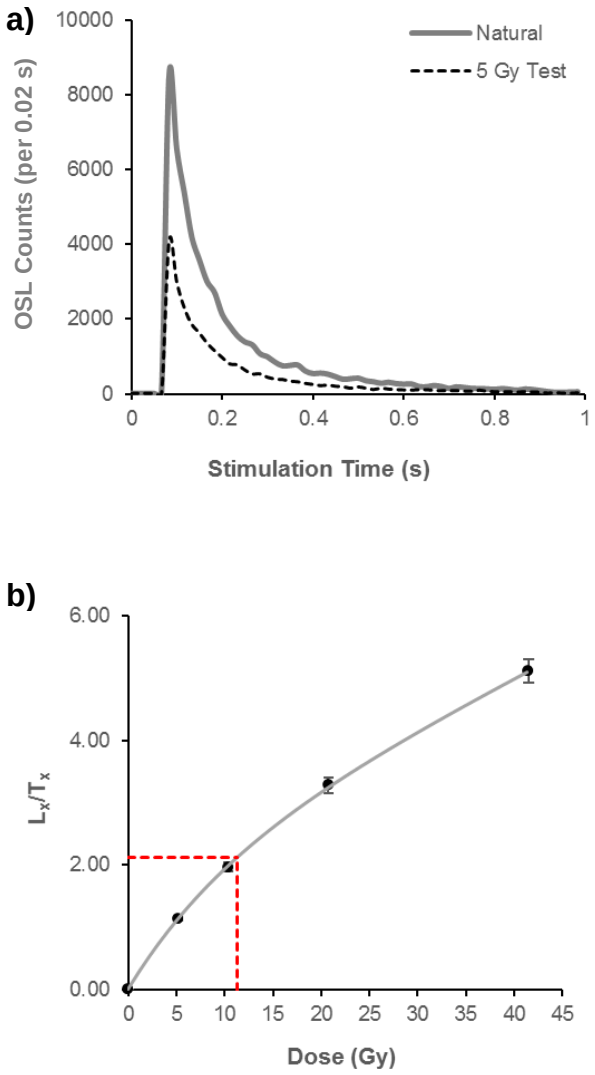


**Figure 5.2.10:** Single-grain $D_e$ summary diagrams for GL15028

a) Example single-grain decay curves for the natural and 5 Gy test dose signals of grain 38.

b) Dose-response curve for grain 38 with regenerative doses; 0, 5.2,1 0.4, 20.8 & 41.6 Gy. Interpolation of the natural $L_x/T_x$ recovered a $D_e$ of 11.31 Gy.

c) Radial plot of 170 $D_e$ values which passed rejection criteria. Coloured areas represent age models applied to the $D_e$ dataset; CAM (**red**), MAM (**grey**), $FMM_{min}$ (**green**) and $FMM_{maj}$ (**blue**). $FMM_{max}$ is equivalent to the $FMM_{maj}$ component for this sample.

d) Histogram of $D_e$ values with bin width 1.0. Dataset has a moderate positive skew (c). No zero-dose grains.

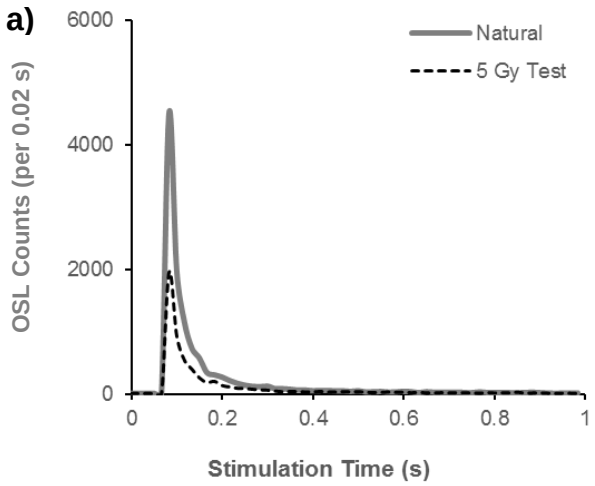


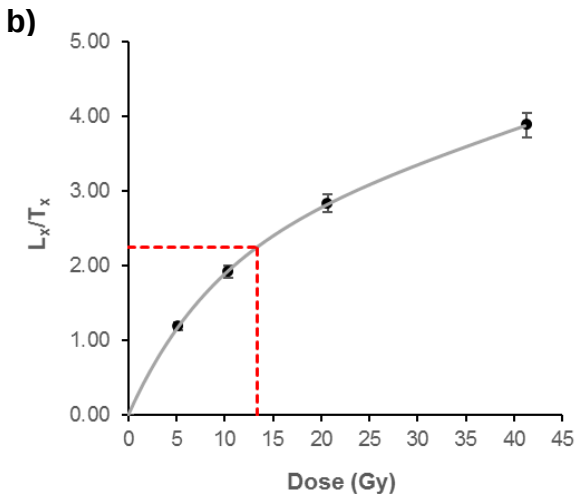


**Figure 5.2.11:** Single-grain $D_e$ summary diagrams for GL15029

a) Example single-grain decay curves for the natural and 5 Gy test dose signals of grain 9.

b) Dose-response curve for grain 9 with regenerative doses; 0, 5.2, 10.3, 20.7 & 41.3 Gy. Interpolation of the natural $L_x/T_x$ recovered a $D_e$ of 13.32 Gy.

c) Radial plot of 143 $D_e$ values which passed rejection criteria. Coloured areas represent age models applied to the $D_e$ dataset; CAM (**red**), MAM (**grey**), $FMM_{min}$ (**green**) and $FMM_{maj}$ (**blue**). $FMM_{max}$ is equivalent to 16.53 ± 1.32 Gy.

d) Histogram of $D_e$ values with bin width 1.0. Dataset has a moderate positive skew (c). No zero-dose grains.

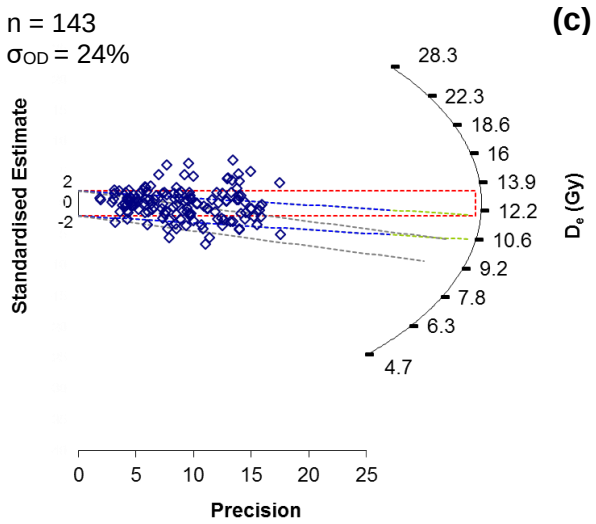


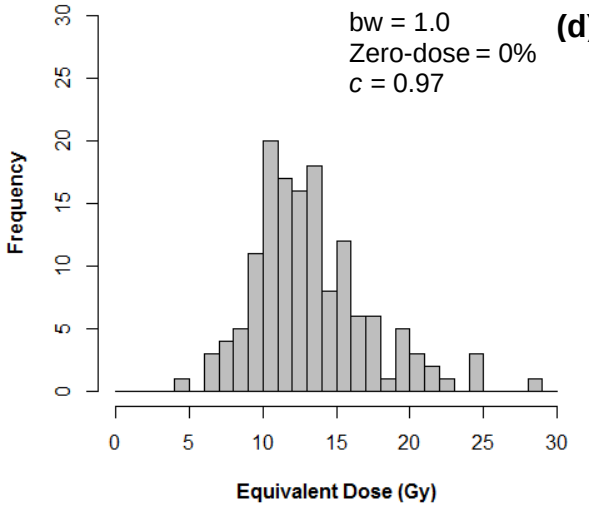

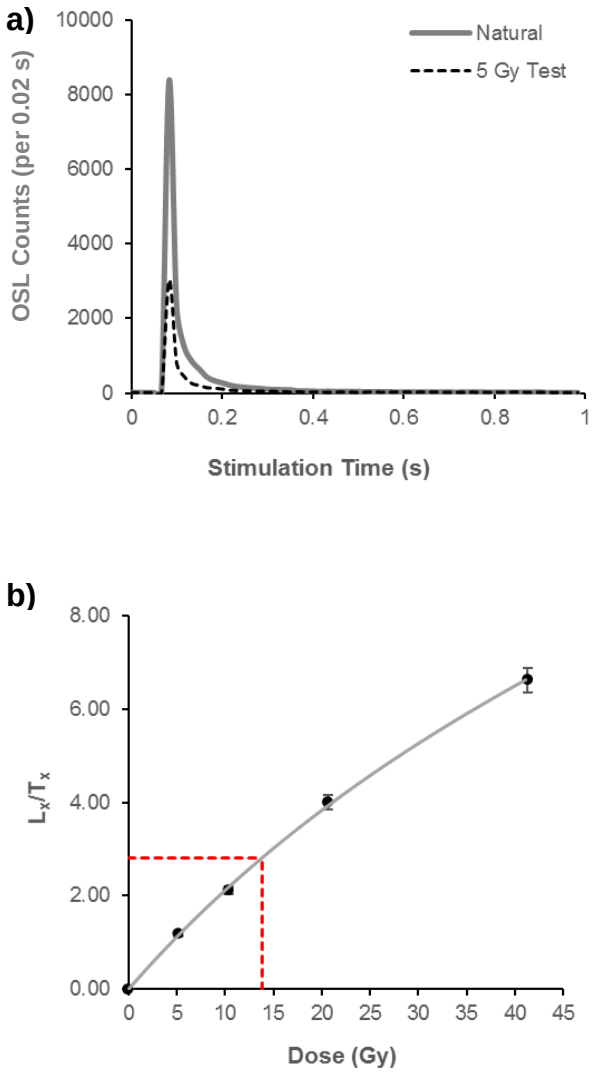


**Figure 5.2.12:** Single-grain $D_e$ summary diagrams for GL15030

a) Example single-grain decay curves for the natural and 5 Gy test dose signals of grain 13.

b) Dose-response curve for grain 13 with regenerative doses; 0, 5.2, 10.3, 20.7 & 41.3 Gy. Interpolation of the natural $L_x/T_x$ recovered a $D_e$ of 13.78 Gy.

c) Radial plot of 187 $D_e$ values which passed rejection criteria. Coloured areas represent age models applied to the $D_e$ dataset; CAM (**red**), MAM (**grey**), $FMM_{min}$ (**green**) and $FMM_{maj}$ (**blue**). $FMM_{max}$ is equivalent to the $FMM_{maj}$ component for this sample.

d) Histogram of $D_e$ values with bin width 1.0. Dataset has a moderate positive skew (c). No zero-dose grains.

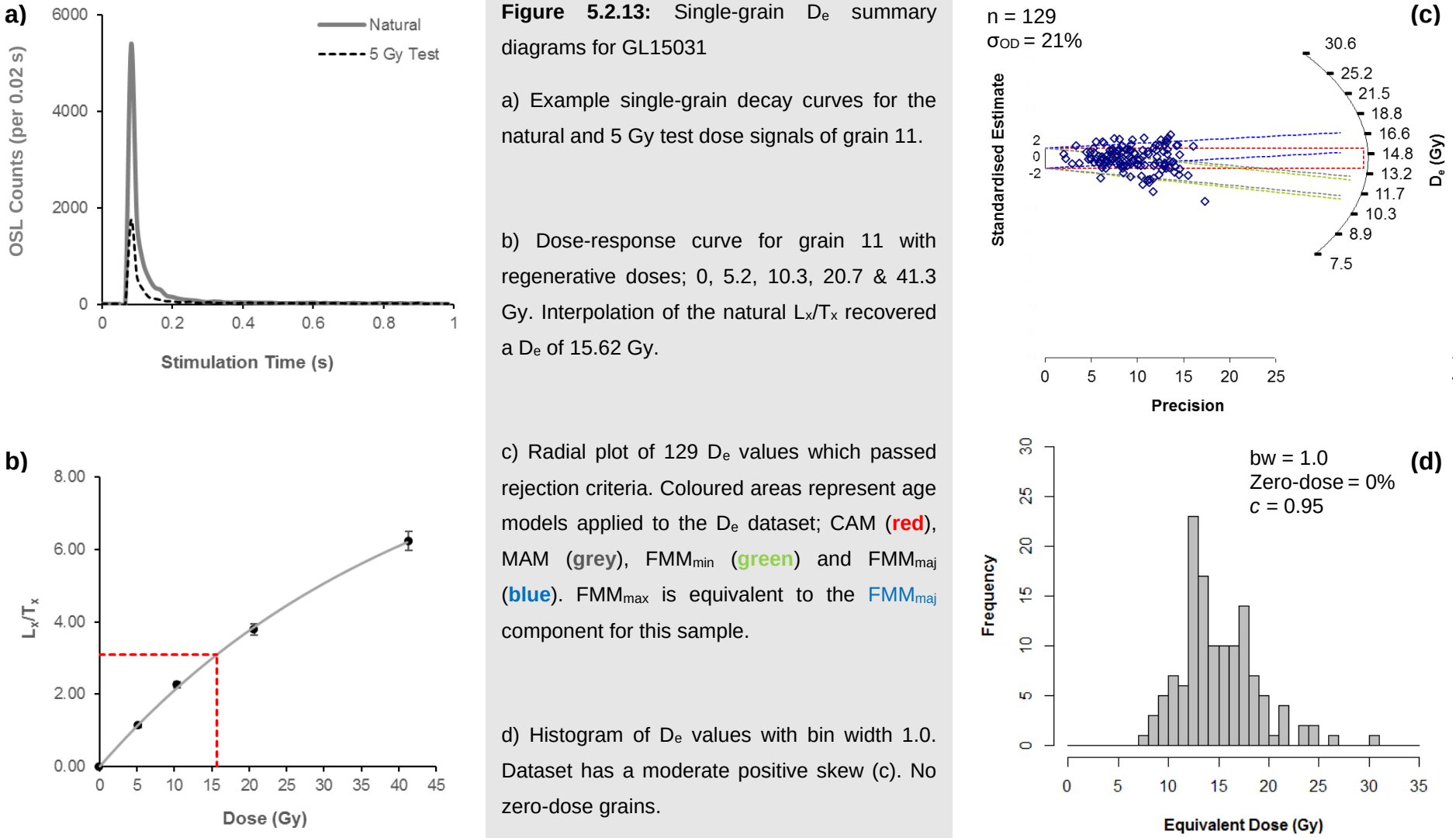


**Figure 5.2.13:** Single-grain $D_e$ summary diagrams for GL15031

a) Example single-grain decay curves for the natural and 5 Gy test dose signals of grain 11.

b) Dose-response curve for grain 11 with regenerative doses; 0, 5.2, 10.3, 20.7 & 41.3 Gy. Interpolation of the natural $L_x/T_x$ recovered a $D_e$ of 15.62 Gy.

c) Radial plot of 129 $D_e$ values which passed rejection criteria. Coloured areas represent age models applied to the $D_e$ dataset; CAM (**red**), MAM (**grey**), $FMM_{min}$ (**green**) and $FMM_{maj}$ (**blue**). $FMM_{max}$ is equivalent to the $FMM_{maj}$ component for this sample.

d) Histogram of $D_e$ values with bin width 1.0. Dataset has a moderate positive skew (c). No zero-dose grains.

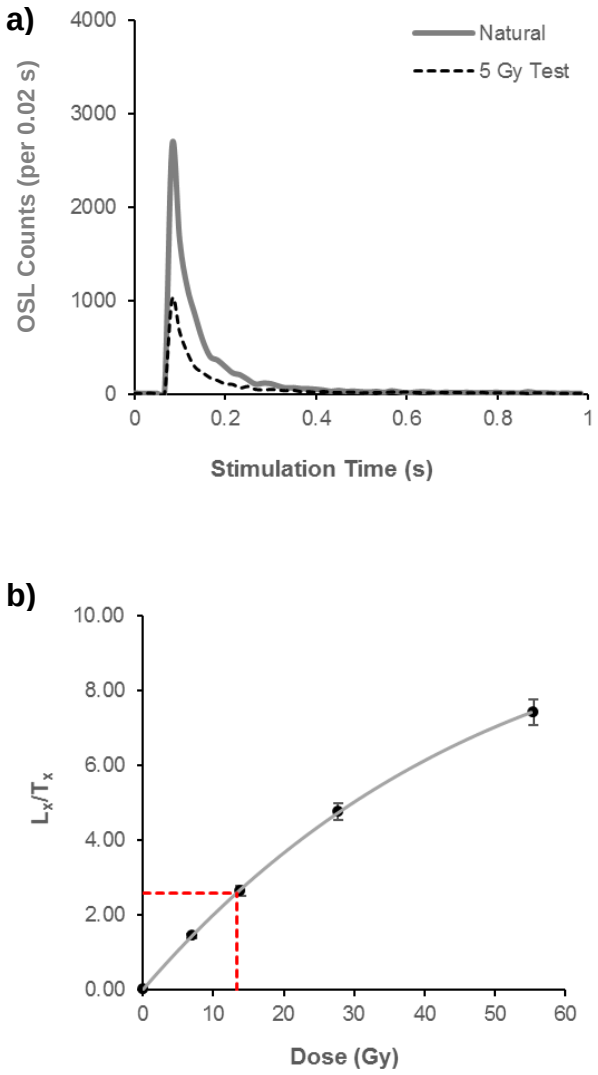


**Figure 5.2.14:** Single-grain $D_e$ summary diagrams for GL15032

a) Example single-grain decay curves for the natural and 5 Gy test dose signals of grain 10.

b) Dose-response curve for grain 10 with regenerative doses; 0, 6.9, 13.9, 27.7 & 55.5 Gy. Interpolation of the natural $L_x/T_x$ recovered a $D_e$ of 13.36 Gy.

c) Radial plot of 184 $D_e$ values which passed rejection criteria. Coloured areas represent age models applied to the $D_e$ dataset; CAM (**red**), MAM (**grey**), $FMM_{min}$ (**green**) and $FMM_{maj}$ (**blue**). $FMM_{max}$ is equivalent to the $FMM_{maj}$ component for this sample.

d) Histogram of $D_e$ values with bin width 1.0. Dataset displays minimal skew (c). No zero-dose grains.

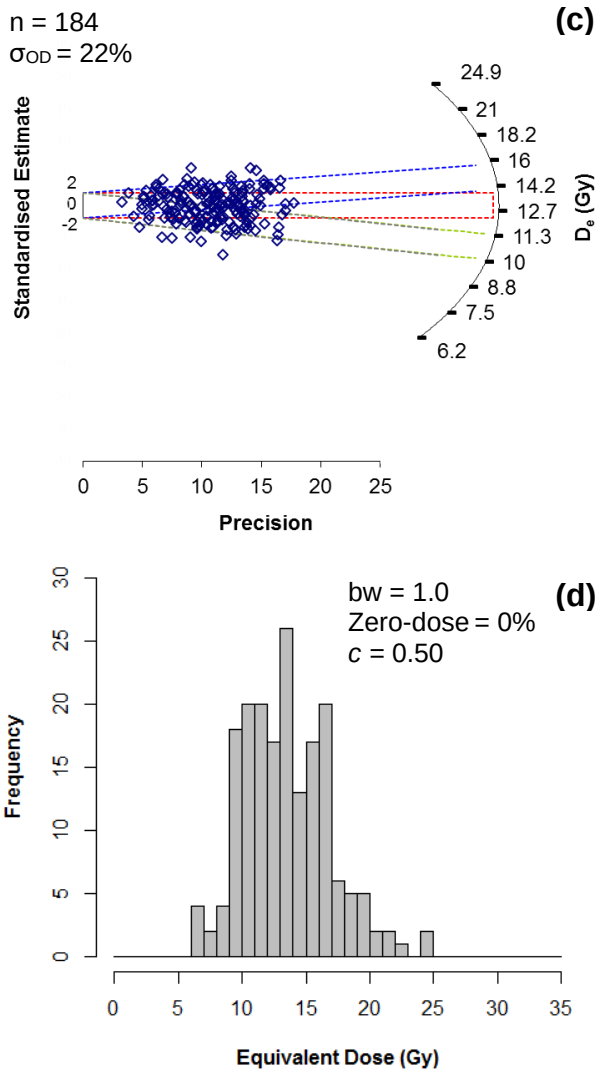

### *5.2.4. Fine silt $D_e$ Results*

Five fine silt samples were prepared and analysed from the South Lake sequence, a summary of $D_e$ results is displayed in Table 5.2.5 whilst diagrams for each of the samples are presented in Figures 5.2.15 to 5.2.19. Central $D_e$ values are statistically consistent, however, it is notable that $D_e$ is not depth-dependent and that the two samples producing the smallest $D_e$ values bracket the highest dose values.

**Table 5.2.5:** Summary of South Lake fine silt (5-15 μm quartz) $D_e$ analysis (errors reported within 1σ confidence)

| Sample | Depth (m) | Aliquots (n) | $D_e$ Values (Gy) | |
|---|---|---|---|---|
| | | | Median | CAM |
| GL16099 | 0.72 | 12 | 4.15 ± 0.03 | 4.13 ± 0.05 |
| GL15016 | 0.85 | 12 | 6.11 ± 0.06 | 6.09 ± 0.07 |
| GL15020 | 1.58 | 12 | 8.50 ± 0.03 | 8.52 ± 0.10 |
| GL15021 | 1.68 | 12 | 7.57 ± 0.07 | 7.57 ± 0.09 |
| GL15022 | 1.81 | 12 | 3.02 ± 0.01 | 3.02 ± 0.03 |

Repeat measurements of both high- and low-dose regenerative dose points produced recycling ratios consistent with 1.00 for all samples and no IRSL depletion was observed across all aliquots. Signal analysis was conducted using $D_e(t)$ plots (Figure 5.2.15c-19c) to assess the likelihood of partial bleaching. No plots displayed a significant increase in the natural $D_e$ with increased illumination time.

One key difference observed for GL15022 relative to other fine silt samples was the sensitivity change experienced by aliquots during SAR measurement. Whilst most samples displayed an increase in OSL sensitivity across measurements cycles, GL15022 displayed a significant reduction (Appendix C - Figure C1.4). Such changes have been observed upon quartz from southern Africa (Armitage *et al.,* 2000) whereby changes in the direction of sensitivity are induced by high/low preheat temperatures.

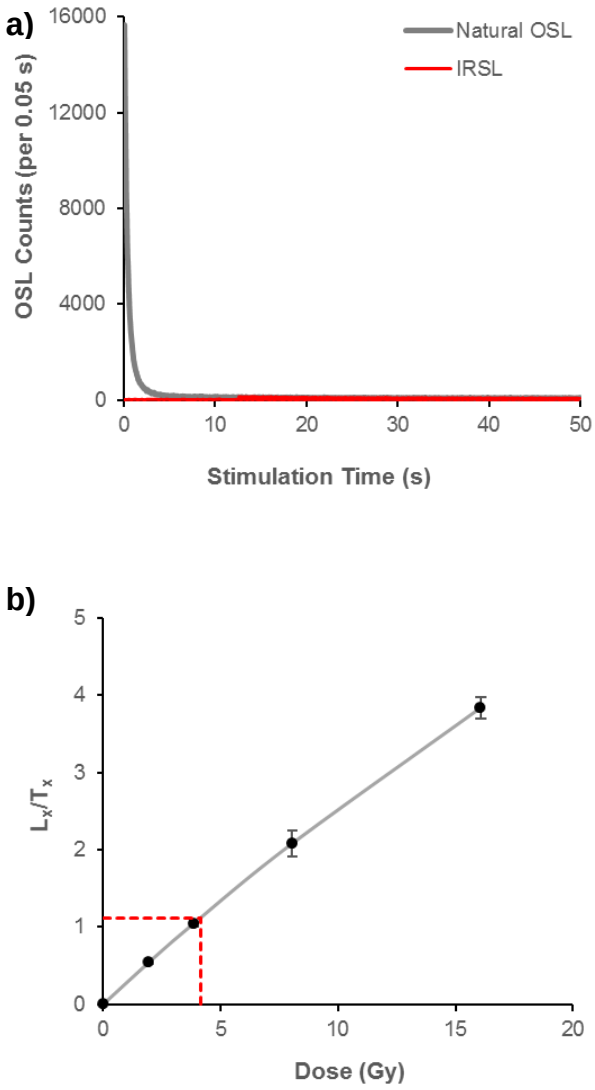


**Figure 5.2.15:** Multi-grain $D_e$ summary diagrams for GL16099

a) Example multi-grain decay curves for the natural OSL signal plus the IRSL signal following a 1.9 Gy regenerative dose.

b) Dose-response curve for aliquot 1 with regenerative doses; 0, 1.9, 3.9, 8.0 & 16.1 Gy. Interpolation of the natural $L_x/T_x$ recovered a $D_e$ of 4.15 Gy.

c) Cumulative frequency plot for 12 $D_e$ values obtained for multi-grain aliquots of 5-15 µm quartz. Coloured area represents CAM (**red**).

d) An example $D_e(t)$ plot for a natural signal. Absence of a significant rise in $D_e$ with increased illumination time indicates the sample is fully-bleached.

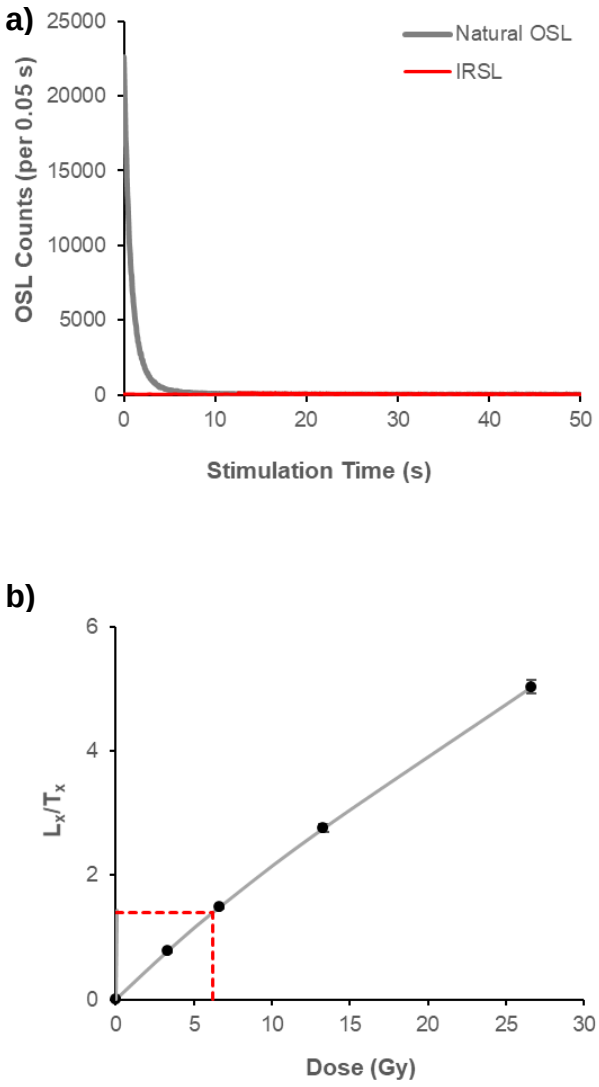


**Figure 5.2.16:** Multi-grain $D_e$ summary diagrams for GL15016

a) Example multi-grain decay curves for the natural OSL signal plus the IRSL signal following a 3.3 Gy regenerative dose.

b) Dose-response curve for aliquot 1 with regenerative doses; 0, 3.3, 6.7, 13.3 & 26.6 Gy. Interpolation of the natural $L_x/T_x$ recovered a $D_e$ of 6.19 Gy.

c) Cumulative frequency plot for 12 $D_e$ values obtained for multi-grain aliquots of 5-15 µm quartz. Coloured area represents CAM (**red**).

d) An example $D_e(t)$ plot for a natural signal. Absence of a significant rise in $D_e$ with increased illumination time indicates the sample is fully-bleached.

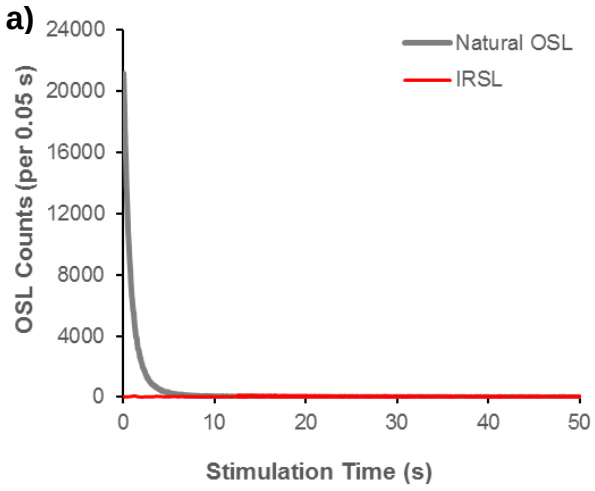


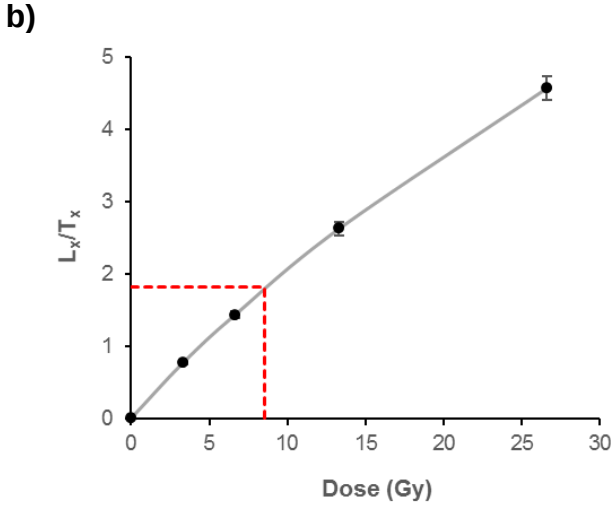


**Figure 5.2.17:** Multi-grain $D_e$ summary diagrams for GL15020

a) Example multi-grain decay curves for the natural OSL signal plus the IRSL signal following a 3.3 Gy regenerative dose.

b) Dose-response curve for aliquot 1 with regenerative doses; 0, 3.3, 6.7, 13.3 & 26.6 Gy. Interpolation of the natural $L_x/T_x$ recovered a $D_e$ of 8.51 Gy.

c) Cumulative frequency plot for 12 $D_e$ values obtained for multi-grain aliquots of 5-15 µm quartz. Coloured area represents CAM (**red**).

d) An example $D_e(t)$ plot for a natural signal. Absence of a significant rise in $D_e$ with increased illumination time indicates the sample is fully-bleached.

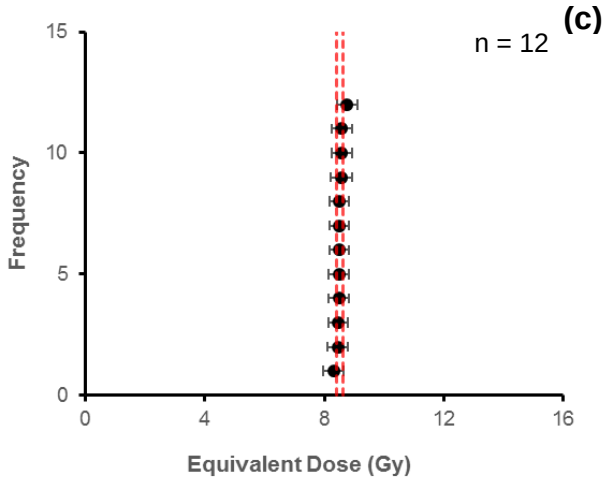


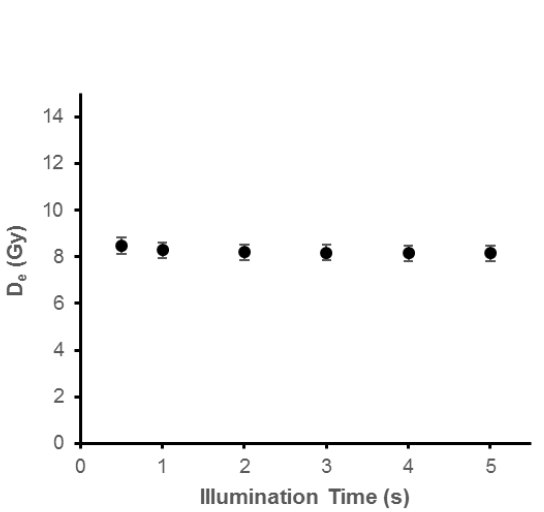

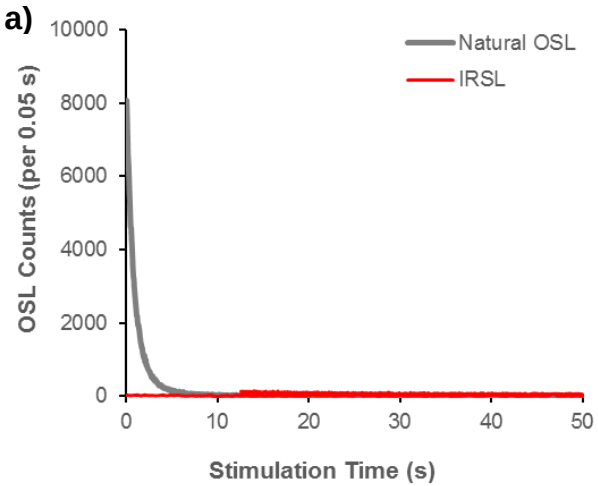


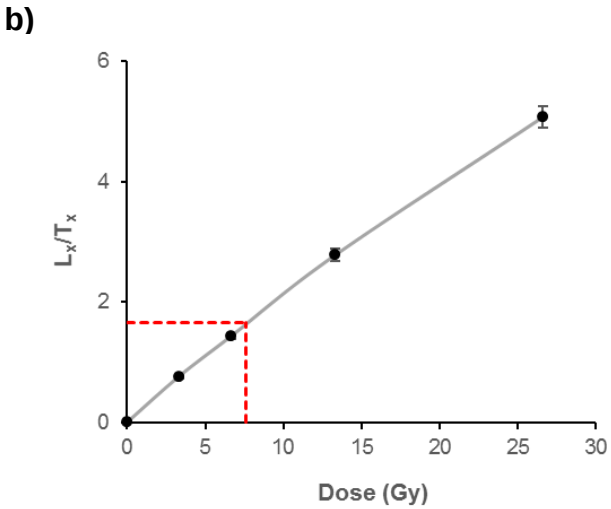


**Figure 5.2.18:** Multi-grain $D_e$ summary diagrams for GL15021

a) Example multi-grain decay curves for the natural OSL signal plus the IRSL signal following a 3.3 Gy regenerative dose.

b) Dose-response curve for aliquot 1 with regenerative doses; 0, 3.3, 6.7, 13.3 & 26.6 Gy. Interpolation of the natural $L_x/T_x$ recovered a $D_e$ of 7.63 Gy.

c) Cumulative frequency plot for 12 $D_e$ values obtained for multi-grain aliquots of 5-15 µm quartz. Coloured area represents CAM (**red**).

d) An example $D_e(t)$ plot for a natural signal. Absence of a significant rise in $D_e$ with increased illumination time indicates the sample is fully-bleached.

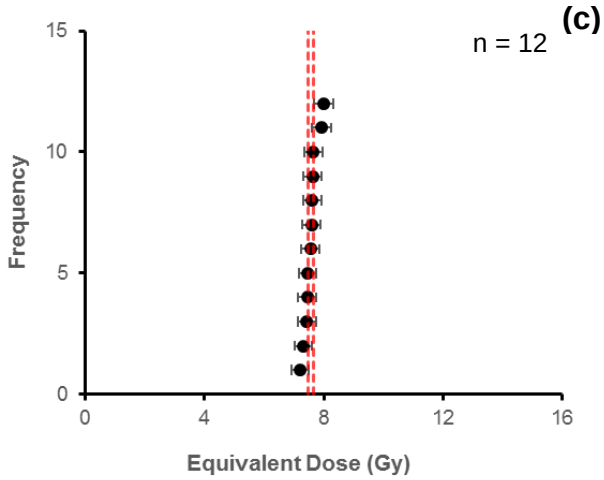


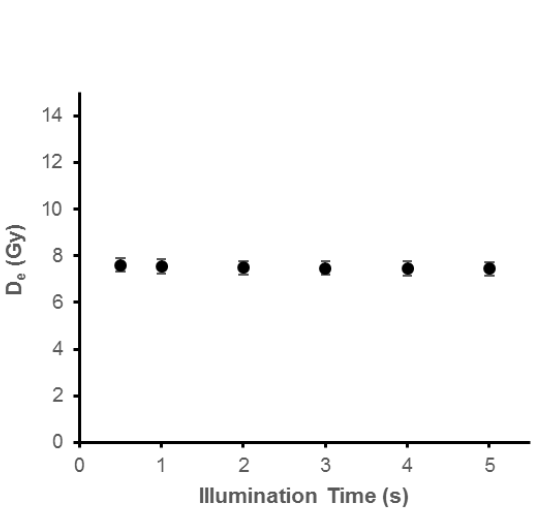

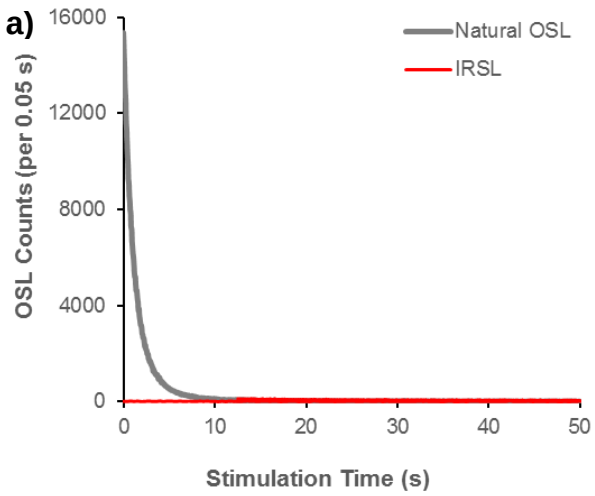


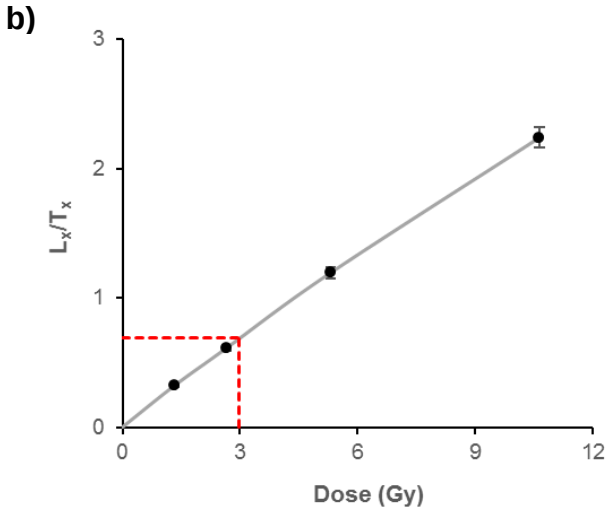


**Figure 5.2.19:** Multi-grain $D_e$ summary diagrams for GL15022

a) Example multi-grain decay curves for the natural OSL signal plus the IRSL signal following a 3.3 Gy regenerative dose.

b) Dose-response curve for aliquot 1 with regenerative doses; 0, 1.3, 2.7, 5.3 & 10.6 Gy. Interpolation of the natural $L_x/T_x$ recovered a $D_e$ of 2.99 Gy.

c) Cumulative frequency plot for 12 $D_e$ values obtained for multi-grain aliquots of 5-15 µm quartz. Coloured area represents CAM (**red**).

d) An example $D_e(t)$ plot for a natural signal. Absence of a significant rise in $D_e$ with increased illumination time indicates the sample is fully-bleached.

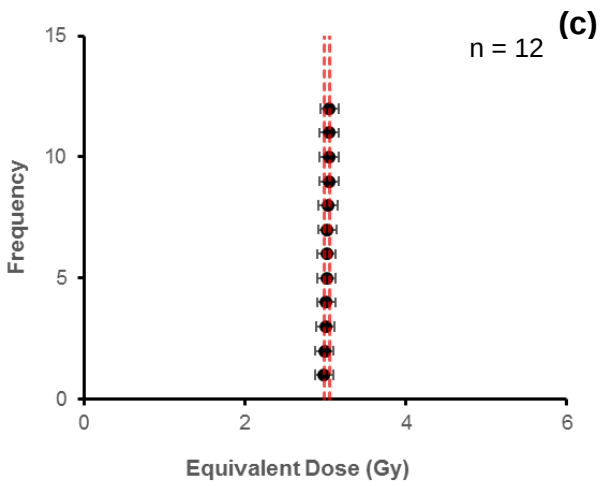


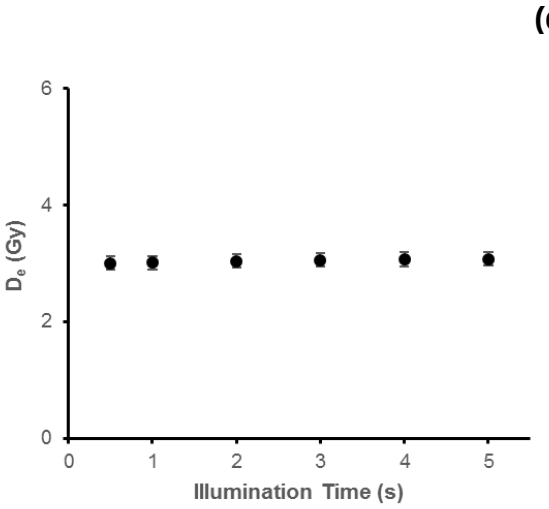

*5.2.5. Dosimetry*

The complex sedimentology of the South Lake core required careful consideration for $D_r$ calculation, Figure 5.2.20 provides an overview of the key variables required for calculation. For most of the sequence modelled density fluctuated between 1.40 and 1.90 g $cm^{-3}$ but between 0.90 and 1.55 m modelled density was significantly lower owing to the elevated organic content. For most of the sequence moisture content exceeds 20%, with deposits between 0.90 and 2.88 m having particularly high contents (30 and 89%).

Radionuclide concentrations obtained through high-resolution Ge gamma spectrometry display some variability throughout the South Lake sequence. K appears to be the least variable throughout the sequence with most values falling between 1.5 and 2.0%. The greatest variability for K occurs between 1.00 and 2.00 m where some values dip close to zero. Th and U concentrations have similar patterns throughout the sequence, however, their range in concentrations (Th: 0.65-14.44 ppm; U: 0.23-2.70 ppm) are significantly different. A sharp peak in both concentrations is observed at *c.* 0.72 m, whilst a broader peak is centred around 2.25 m. As with K, great variability is observed between 1.00 and 2.00 m.

Radionuclide and $D_r$ data for all South Lake samples are presented in Table 5.2.6. The calculated $D_r$ for all samples ranges from 1.64 to 2.67 Gy $ka^{-1}$. The highest $D_r$ is observed for sample GL16099 at 0.72 m, this coincides with a peak in Th and U. The lowest calculated $D_r$ for GL15022 coincides with a drop in K content at 1.81 m. The errors for all calculated $D_r$ values fall between 12 and 15%, with uncertainty in core compaction and subsequent $\gamma$-modelling contributing to this overall uncertainty in $D_r$.

Overall, 73 $^{226}Ra/^{238}U$ ratios were calculated for assessment of U-series disequilibrium throughout the South Lake sequence (Figure 5.2.20), 55 of which (74%) are consistent with unity. Eight (11%) of the calculated ratios were statistically less than unity, with single values identified at 0.40, 1.06 and 3.54 m whilst troughs in $^{226}Ra/^{238}U$ containing multiple values inconsistent with unity are centred on 2.57 and 3.84 m. The remaining 11

(15%) values were statistically greater than unity with single values identified at 0.75, 1.31 and 3.13 m whilst peaks in $^{226}Ra/^{238}U$ containing multiple values inconsistent with unity are centred on 0.30 and 1.88 m. At most $D_e$ sampling locations $^{226}Ra/^{238}U$ ratios are consistent with unity, however, four samples are statistically greater than unity (GL15021, 22, 23 & 26) whilst two are statistically less than unity (GL15024 & 29). The depths of GL15021-23 are consistent with an observed peak in $^{226}Ra/^{238}U$ whilst GL15029 is consistent with a trough (Figure 5.2.20).

Despite the variability in $^{226}Ra/^{238}U$ throughout the sequence, all ratios fall within 0.5 of unity (Figure 5.2.20) suggesting U-series disequilibria should not present a significant issue (Olley *et al.* ,1996). Although equilibrium is assumed for all OSL age estimates from the South Lake sequence, the potential for disequilibrium to have occurred following deposition remains. Particularly given that groundwater flow dominates drainage elsewhere on the catchment (Grenfell *et al.,* 2010). Groundwater mobilisation of the U-series could have created the excess $^{226}Ra$ and marginal $^{226}Ra/^{238}U$ ratios observed in some regions of the sequence.

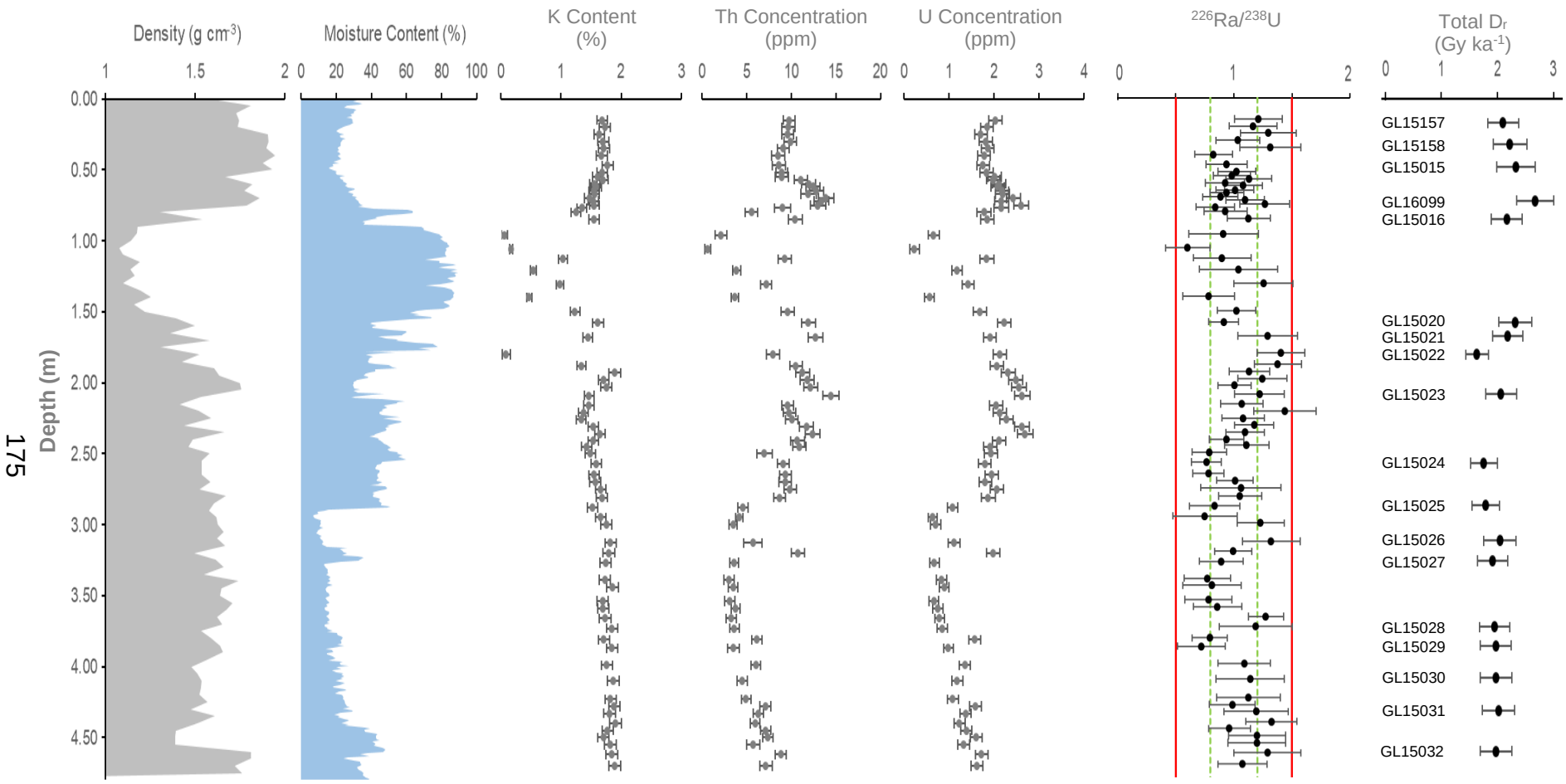


**Figure 5.2.20:** Key variables used for South Lake γ-modelling and $D_r$ calculation. $^{226}Ra/^{238}U$ ratios are presented for assessment of U-series disequilibria - 20% (green/dashed line) and 50% (red/solid line) margins highlighted.

**Table 5.2.6:** Summary of South Lake dosimetry data ([a]: radionuclide values obtained at $D_e$ sampling location; [b]: values obtained following γ-modelling)

| Sample | Depth (m) | Grain Fraction (μm) | Moisture Content (%) | Radionuclide Content[a] | | | | $D_r$ Components (Gy $ka^{-1}$) | | | | Total $D_r$ (Gy $ka^{-1}$) |
|---|---|---|---|---|---|---|---|---|---|---|---|---|
| | | | | K (%) | Th (ppm) | U (ppm) | $^{226}Ra/^{238}U$ | α | β | γ[b] | Cosmic | |
| GL15157 | 0.17 | 180-250 | 28 | 1.73±0.09 | 9.68±0.71 | 1.85±0.14 | 1.17±0.20 | - | 1.11±0.23 | 0.76±0.16 | 0.23±0.04 | 2.10±0.28 |
| GL15158 | 0.32 | 180-250 | 22 | 1.70±0.09 | 9.91±0.70 | 1.82±0.15 | 1.03±0.19 | - | 1.16±0.24 | 0.87±0.18 | 0.19±0.04 | 2.22±0.30 |
| GL15015 | 0.48 | 180-250 | 17 | 1.78±0.09 | 8.59±0.74 | 1.76±0.14 | 0.94±0.18 | - | 1.24±0.25 | 0.90±0.20 | 0.19±0.03 | 2.33±0.34 |
| GL16099 | 0.72 | 5-15 | 35 | 1.54±0.09 | 13.39±0.81 | 2.17±0.15 | 1.10±0.17 | 0.32±0.07 | 1.33±0.27 | 0.84±0.17 | 0.18±0.03 | 2.67±0.33 |
| GL15016 | 0.85 | 5-15 | 42 | 1.55±0.09 | 10.44±0.76 | 1.85±0.14 | 1.13±0.18 | 0.24±0.05 | 1.17±0.24 | 0.58±0.12 | 0.18±0.03 | 2.17±0.28 |
| GL15020 | 1.58 | 5-15 | 45 | 1.62±0.09 | 11.91±0.79 | 2.23±0.15 | 0.91±0.13 | 0.28±0.06 | 1.24±0.25 | 0.64±0.13 | 0.17±0.03 | 2.32±0.29 |
| GL15021 | 1.68 | 5-15 | 52 | 1.44±0.08 | 12.71±0.81 | 1.91±0.14 | 1.29±0.26 | 0.26±0.05 | 1.07±0.22 | 0.69±0.14 | 0.17±0.03 | 2.18±0.27 |
| GL15022 | 1.81 | 5-15 | 41 | 0.09±0.06 | 7.95±0.76 | 2.13±0.15 | 1.40±0.21 | 0.22±0.05 | 0.39±0.09 | 0.85±0.17 | 0.17±0.03 | 1.64±0.20 |
| GL15023 | 2.09 | 180-250 | 39 | 1.47±0.08 | 14.44±0.87 | 2.63±0.17 | 1.22±0.21 | - | 1.02±0.21 | 0.89±0.18 | 0.16±0.03 | 2.06±0.28 |
| GL15024 | 2.58 | 180-250 | 44 | 1.58±0.09 | 9.08±0.64 | 1.80±0.14 | 0.76±0.13 | - | 0.90±0.18 | 0.71±0.15 | 0.15±0.03 | 1.76±0.24 |
| GL15025 | 2.88 | 180-250 | 20 | 1.53±0.09 | 4.56±0.57 | 1.08±0.12 | 0.83±0.22 | - | 0.95±0.20 | 0.70±0.14 | 0.15±0.03 | 1.79±0.25 |
| GL15026 | 3.13 | 180-250 | 17 | 1.83±0.10 | 5.69±0.99 | 1.11±0.13 | 1.32±0.25 | - | 1.15±0.24 | 0.78±0.16 | 0.14±0.03 | 2.05±0.29 |
| GL15027 | 3.27 | 180-250 | 15 | 1.74±0.09 | 3.60±0.50 | 0.67±0.11 | 0.89±0.36 | - | 1.06±0.22 | 0.71±0.15 | 0.14±0.03 | 1.91±0.27 |
| GL15028 | 3.74 | 180-250 | 17 | 1.85±0.10 | 3.62±0.53 | 0.85±0.12 | 1.19±0.31 | - | 1.11±0.23 | 0.71±0.15 | 0.13±0.03 | 1.95±0.27 |
| GL15029 | 3.87 | 180-250 | 16 | 1.85±0.10 | 3.51±0.67 | 0.99±0.11 | 0.72±0.21 | - | 1.13±0.23 | 0.71±0.15 | 0.13±0.03 | 1.97±0.28 |
| GL15030 | 4.10 | 125-180 | 21 | 1.87±0.10 | 4.50±0.55 | 1.19±0.12 | 1.14±0.29 | - | 1.18±0.24 | 0.67±0.14 | 0.13±0.03 | 1.98±0.28 |
| GL15031 | 4.33 | 125-180 | 22 | 1.81±0.10 | 6.31±0.56 | 1.37±0.13 | 1.19±0.28 | - | 1.18±0.24 | 0.71±0.15 | 0.13±0.02 | 2.02±0.29 |
| GL15032 | 4.62 | 125-180 | 31 | 1.84±0.10 | 8.82±0.62 | 1.73±0.14 | 1.29±0.29 | - | 1.17±0.24 | 0.69±0.14 | 0.12±0.02 | 1.98±0.28 |

### *5.2.6. Selection of Modelled $D_e$ and Age Calculation*

The OSL ages produced for South Lake are summarised in Table 5.2.7, these are discussed in-line with the sedimentology core units described in Chapter 2. All modelled $D_e$ values were divided by the average $D_r$ and associated errors were combined in quadrature. As highlighted in Chapter 4, the decision tree developed Bailey & Arnold (2006) can be used to isolate a $D_e$ based on statistical parameters. However, given that more recent single-grain work by Thomsen et al. (2016) highlights significant $D_e$ underestimation with application of the decision tree, it is not adopted for the samples in this study. Ages are instead interpreted using statistical measures (OD, skewness and proportion of zero-dose grains), stratigraphic order and the consistency between calculated age models (Figure 5.2.22).

Figure 5.2.21 includes most of the highlighted parameters and outlines the decision process used for age model selection in this study. The decision process is based in part on the success of dating known age deposits at the UCOSP site (Section 5.3), it also accounts for the tendency of CAM to overestimate and MAM to underestimate the age of heterogeneously bleached fluvial sediments (Rodnight *et al.,* 2006). Although the decision process discriminates between $FMM_{min}$ and $FMM_{maj}$, in some instances these components will represent the same $D_e$ population.

For all multi-grain samples in this study only CAM is used for calculation of $D_e$ to avoid the identification of phantom dose populations arising from averaging, as observed for very small multi-grain aliquots (pseudo single-grain) by Arnold *et al.* (2012). Multi-grain aliquots provide a measure of central tendency as OSL emissions arise from multiple grains. Deeper consideration is required for single-grain $D_e$ estimates. For the South Lake sequence interpretation of all single-grain samples below 2.09 m (GL15024-32) is relatively straightforward as $D_e$ distributions display minimal OD and skewness, in addition most age models produce age estimates which are statistically consistent. Single-grain samples above 2.09 m (GL15157-8, GL15015 & GL15023) present a greater challenge as $D_e$ distributions display significant OD, elevated skewness and produce modelled ages which are statistically distinct.

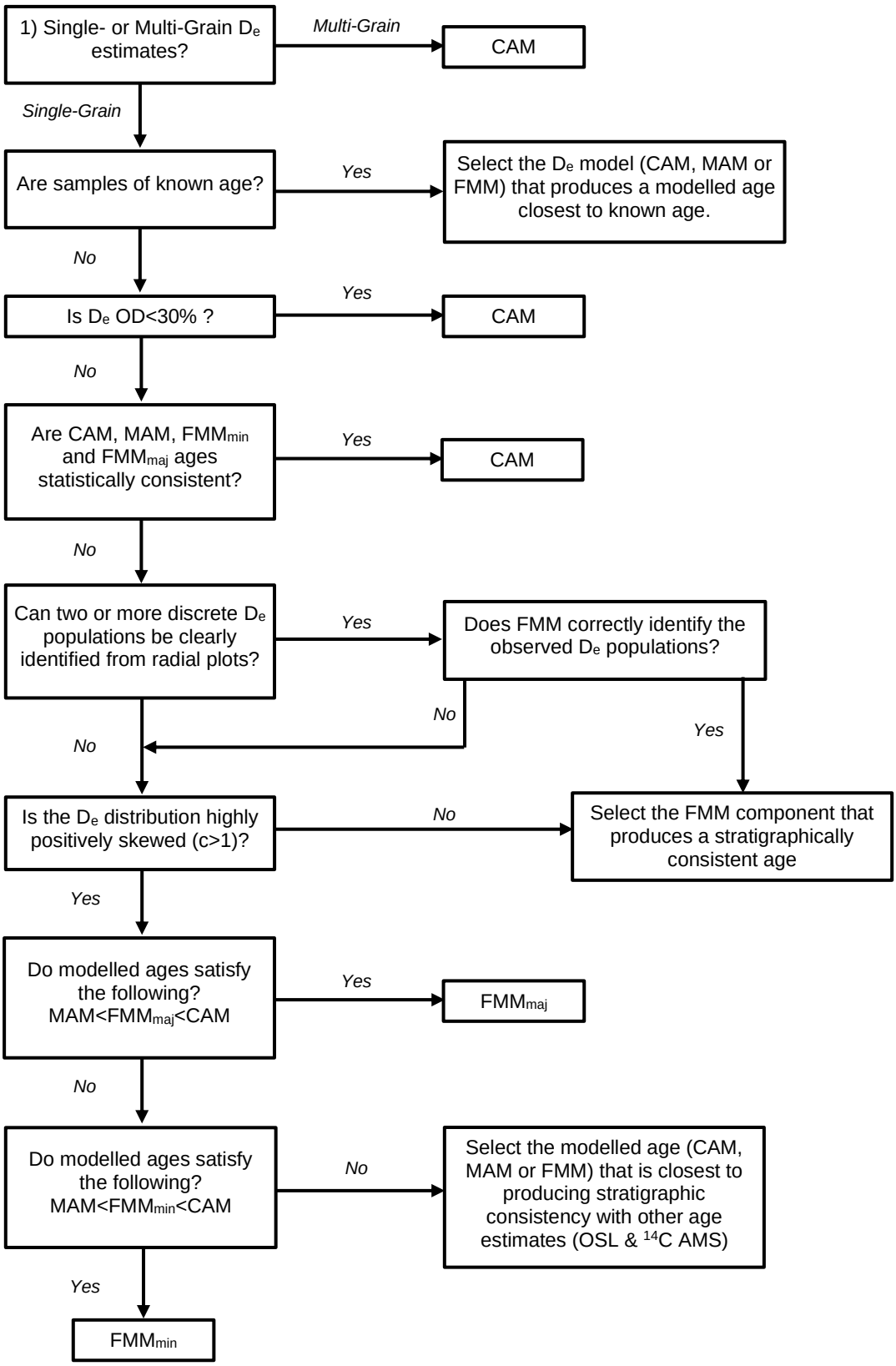


**Figure 5.2.21:** The decision process used for age model selection (starting point is 1).

*Unit 1*

Samples from unit 1 (GL15025-32; 4.78-2.85 m; Figure 5.2.22) all fall below 2.09 m and were taken from the earliest material deposited at the South Lake site dominated by sand. Single age estimates were produced for thin sand beds from unit 1 (GL15025 and GL15032) whilst upper and lower ages (GL15026-27, GL15028-29 and GL15030-31) were produced for the thicker beds to confirm that each unit represents a distinct sedimentary event. All samples within unit 1 have an OD (21-24%) which is just over the 20% ascribed to well-bleached sediments (Olley *et al.,* 2004; Arnold & Roberts, 2009) and minimal variations are observed in skewness. For most samples both MAM and FMM produce ages which are statistically indistinguishable from CAM confirming that the $D_e$ distributions are formed of a single dose population, hence CAM is adopted for all samples from unit 1. The errors associated with all CAM ages from unit 1 is *c.* 14%. The only exception in unit 1 where an age model is statistically inconsistent with CAM is the $FMM_{min}$ age produced for GL15024, a small proportion of low-dose grains appear to have a heavy weighting on this $D_e$ component resulting in a younger age.

The OSL ages for unit 1 display good stratigraphic consistency and indicate that deposition of the South Lake sediments initiated at *c.* 7 ka with 5 phases of sand bed deposition ensuing until a maximum of *c.* 5 ka (Figure 5.2.23). A $^{14}C$ AMS sample (SL_AMS_5) was taken from the boundary of unit 1 and 2 and dates this region of the sequence to 4.73 ± 0.14 cal ka BP, this is statistically consistent with the uppermost OSL sample from unit 1 (GL15025; 5.24 ± 0.73 ka) and supports the upper OSL age limit. All samples within unit 1 produced OD close to 20% suggesting that partial bleaching does not present a significant issue. Age models produced statistically indistinct estimates, confirming that $D_e$ distributions are formed of single dose populations and that the influence of extrinsic forcing upon $D_e$ is minimal. No significant differences in age are observed for dual (upper and lower) estimates produced for the thicker sand beds, confirming that each bed represents a single depositional event.

*Unit 2*

Unit 2 (2.85-1.48 m) of the South Lake sequence observes interlamination of organic and clastic units. Some pure sand beds are preserved but upward fining is observed across the clastic matrix. Two single-grain (GL15023 & GL15024) and three fine silt (GL15020-22) age were calculated from unit 2.

GL15024 is the lowermost sample from unit 2 and is another of the single-grain samples which falls below 2.09 m, displaying minimal OD (22%) and modelled ages which are statistically indistinct. A significant increase in skewness is observed relative to the samples in unit 1, however, on inspection of the $D_e$ histogram for this sample (Figure 5.2.6d) this appears to be driven by a small number of high-dose grains separated from the main population. Given the minimal OD and the consistency observed between age models, GL15024 appears to be well-bleached and features a single significant grain population. CAM is selected (3.58 ± 0.49 ka) and displays stratigraphic consistency relative to ages in unit 1. Error margins for CAM are the same magnitude (14%) observed in unit 1.

GL15023 was also collected from a well-preserved sand bed in unit 2 and produced a $D_e$ distribution that has a high OD (42%) relative to the samples explored at greater depths (Figure 5.2.22). $FMM_{min}$ and MAM are lower and statistically distinct relative to CAM indicating partial bleaching could have had a significant influence upon the observed $D_e$ distribution. Given MAM tends to underestimate and CAM overestimate age for heterogeneously bleached sediments (Rodnight *et al.*, 2006), most age estimates reported in Table 5.2.7 are not suitable as $FMM_{min} \leq MAM$, $FMM_{maj} \geq CAM$ and $FMM_{max} > CAM$. As the true $D_e$ for heterogeneously bleached sediments is anticipated to fall between MAM and CAM, selection of $FMM_{k=2}$ is most suitable as it produces an age (3.78±0.57 ka) that is situated between MAM and CAM. $FMM_{k=2}$ encapsulates 24% of grains and the associated age is statistically consistent with that adopted for GL15024. The error margin for the adopted age is *c.* 15%.

The remaining OSL ages from unit 2 are all based on multi-grain aliquots of fine silt quartz. GL15022 produces an age (1.85±0.23 ka) which is

stratigraphically consistent, the estimate is younger than single-grain ages situated lower in the sequence and is older than an AMS age (SL_ AMS_3A: 1.39 ± 0.02 cal ka BP) which was taken from 9 cm above the OSL sample (Figure 5.2.23). The final two fine silt ages from unit 2 (GL15020 and GL15021) are situated above SL_AMS_3A and produce age estimates (3.67±0.47 & 3.47±0.43 ka) which are significantly greater than the AMS age and GL15022.

Potential causes of what appears to be age overestimates for GL15020 and GL15021 could either be rooted in $D_e$ or $D_r$. Whilst this region of the core provides complexity for $D_r$ calculation, owing to elevated moisture and organic content, in order for ages to fall within stratigraphic consistency $D_r$ would have to double. This seems unlikely given the range of radionuclide concentrations and calculated $D_r$ values observed for other regions of the sequence where moisture and organic content is less. It seems more likely that $D_e$ overestimation is the source of age discrepancy. Overestimation of $D_e$ could be attributed to the environmental settings, particularly if during the deposition of unit 2 the blocked-valley wetland was similar to present day Lake Futululu and featured floating reed beds (Grenfell *et al.,* 2010). Coupled with the attenuation of light through the water column, reed beds would restrict light exposure to suspended or reworked sediment within the basin and would increase the likelihood of incomplete bleaching. Equally, given that samples within this region of the sequence featured a significant clay fraction and material is very cohesive, clumping of sediments could have reduced the likelihood of complete bleaching.

As partial bleaching is determined to be the most likely cause of age overestimation for GL15020 and GL15021, it is appropriate to highlight the $D_e(t)$ plots produced for the samples (Figures 5.2.17d & 5.2.18d). Samples which have been partially bleached are expected to display an increase in $D_e$ with stimulation time, however, the $D_e(t)$ plots for GL15020 and GL15021 display no significant change in $D_e$. Although this may appear inconsistent with the interpretation of age overestimation, $D_e(t)$ plots are also dependant on the relative sizes of the pre- and post-burial doses and the fast and medium OSL components (Bailey, 2003). Given that multiple factors

contribute to the form of $D_e(t)$ plots, partial bleaching cannot be ruled out based only on the absence of a rise in $D_e$ with stimulation time.

In summary, the OSL samples within unit 2 presented some challenges for age interpretation. Two sand-laden clastic beds preserved within the lower portion of the unit produced statistically consistent ages and were deposited between *c.* 3.5 and 4 ka. However, $D_e$ modelling was required for GL15023 as it was highly overdispersed (42%) and likely to have experienced significant partial bleaching. Fine silt OSL ages indicate that deposition of the finer clastic material in unit 2 ensued until at least 1.85 ka, however, an AMS age indicates this could be as late as 1.4 cal ka BP. The two uppermost samples within unit 2 appear to be overestimates of age relative to other samples in the sequence and it is suggested that this overestimate has been caused by partial bleaching given the significant increase in $D_r$ required to align ages with the rest of the sequence.

*Unit 3*

Only one fine silt OSL sample could be isolated from unit 3 (1.48-0.76 m). GL15016 was taken from a clastic lamination at the top of unit 3 and produced an age (2.81±0.36 ka) which pre-dates GL15022 and the AMS age from unit 2. The age for GL15016 is also significantly greater than two further AMS ages (SL_AMS_1 & _AMS_2) taken from the lower portions of unit 3 dated to 1.19±0.06 and 1.30±0.05 cal ka BP. The apparent age overestimation appears to be similar in nature to that discussed for GL15020 and GL15021. The $D_r$ for GL15016 is statistically consistent with the values obtained for all other samples and would need to double to produce an age estimate falling within stratigraphic consistency. As with other fine silt samples from the sequence the $D_e(t)$ plot for GL15016 does not display a rise in $D_e$ with increased stimulation time. However, overestimation is again attributed to partial bleaching as $D_e(t)$ plots cannot confirm that it is absent, and a significant underestimation of $D_r$ seems unlikely.

*Unit 4*

Unit 4 (0.76-0 m) forms the uppermost material from the South Lake sequence. GL16099 was collected from the base of the unit at the transition

from unit 3. Whilst the age (1.55±0.19 ka) is stratigraphically consistent with OSL samples GL15022 and below, it pre-dates the AMS ages produced for unit 3 and may be considered a maximum age for the deposition of unit 4.

The remaining three OSL samples from unit 4 are considered near-surface and were taken from 0.48 m upwards. Samples GL15015, GL15158 and GL15157 are interpreted simultaneously given their similar characteristics. GL15015 was collected from a distinct sand lense whilst the prevalence of sand was less obvious for GL15157 and GL15158. All $D_e$ distributions for the near-surface samples are significantly overdispersed, positively skewed and feature zero-dose grains. Recent reworking is suggested as being a contributor to the observed distributions owing to the presence of zero-dose grains within all samples and the increase (with depth) in the proportion of grains falling within $FMM_{max}$ and $FMM_{maj}$. Both of these dose components are statistically consistent for all three samples.

If compared to the recent conceptual framework outlined by Gliganic *et al.* (2016), the South Lake near-surface samples fall within 'zone 1' when classified by depth, this is an active mixing zone where zero-dose grains are actively being introduced. However, comparison of the proportion of zero-dose grains between South Lake and the data presented by Gliganic *et al.* (2016) suggests that the South Lake samples actually fall within 'zone 2' of the framework, as the proportion of zero-dose grains falls between 2 and 15%. In zone 2 zero-dose grains can be introduced but it is not consistently observed in $D_e$ distributions for samples of similar depths. Skewness values calculated for GL15157 and GL15158 are also less than those calculated by Gliganic *et al.* (2016) for samples falling within zone 1. The skewness for the upper two samples from the South Lake sequence are more comparable ($k$<2) to 'zone 3' of the framework which is classified as being disconnected from surface reworking. Differences would be expected in this study given that it is a lacustrine environment as opposed to the dune and sandsheet deposits discussed by Gliganic *et al.* (2016). Despite the differences in environment, the low proportion of zero-dose grains suggest that although recent pedoturbation may have occurred it is not actively influencing the near-surface samples.

The two distinct $D_e$ populations are interpreted as representing separate depositional events, with post-burial reworking creating the bimodal $D_e$ distributions for the three near-surface samples. Given the increase with depth in the proportion of grains falling within $FMM_{max}$ and $FMM_{maj}$, it is suggested that this dose component is selected for age calculation of GL15015 (0.27±0.04 ka). This represents the dominant $D_e$ population and the deposition of the sand lense. Samples GL15157 and GL15158 are believed to represent recent phases of deposition and reworking, potentially created by flood intrusions onto the basin, $FMM_{min}$ (0.05±0.01 ka) is suggested as the most suitable age bracket for these.

The OSL ages from unit 4 suggest sediments record deposition spanning from the present day to a maximum of *c.* 1.5 ka. The lowermost sample from unit 4 indicates the accumulation of unit 3 occurred over a relatively short timeframe (<500 years). Near-surface samples suggest a large flood event, depositing sand across the basin (preserved at 0.48 m depth), occurred at a maximum of *c.* 0.27 ka. Deposition and potential reworking of surface sediments has occurred over the last century, with GL15157 and 158 recording the more significant events.

Incorporation of all OSL and AMS ages into a simple age-depth plot (Figure 5.2.23) shows that a majority of ages from the South Lake sequence fall in stratigraphic order, providing a continuous sedimentary record spanning the past *c.* 7 ka. Upper and lower ages from preserved sand beds in unit 1 are statistically indistinguishable suggesting each sand bed represents a singular depositional event. The three fine silt OSL ages which appear to be overestimates are clearly offset relative to other ages within the sequence. This indicates that OSL sampling within close proximity to hyper-organic sediments, at least within this environment, is challenging and unlikely to be successful. Given the significant elevation in $D_r$ required to produce fine silt ages which fall in stratigraphic order, partial bleaching and the overestimation of $D_e$ is believed to be creating the age discrepancies in the South Lake chronology.

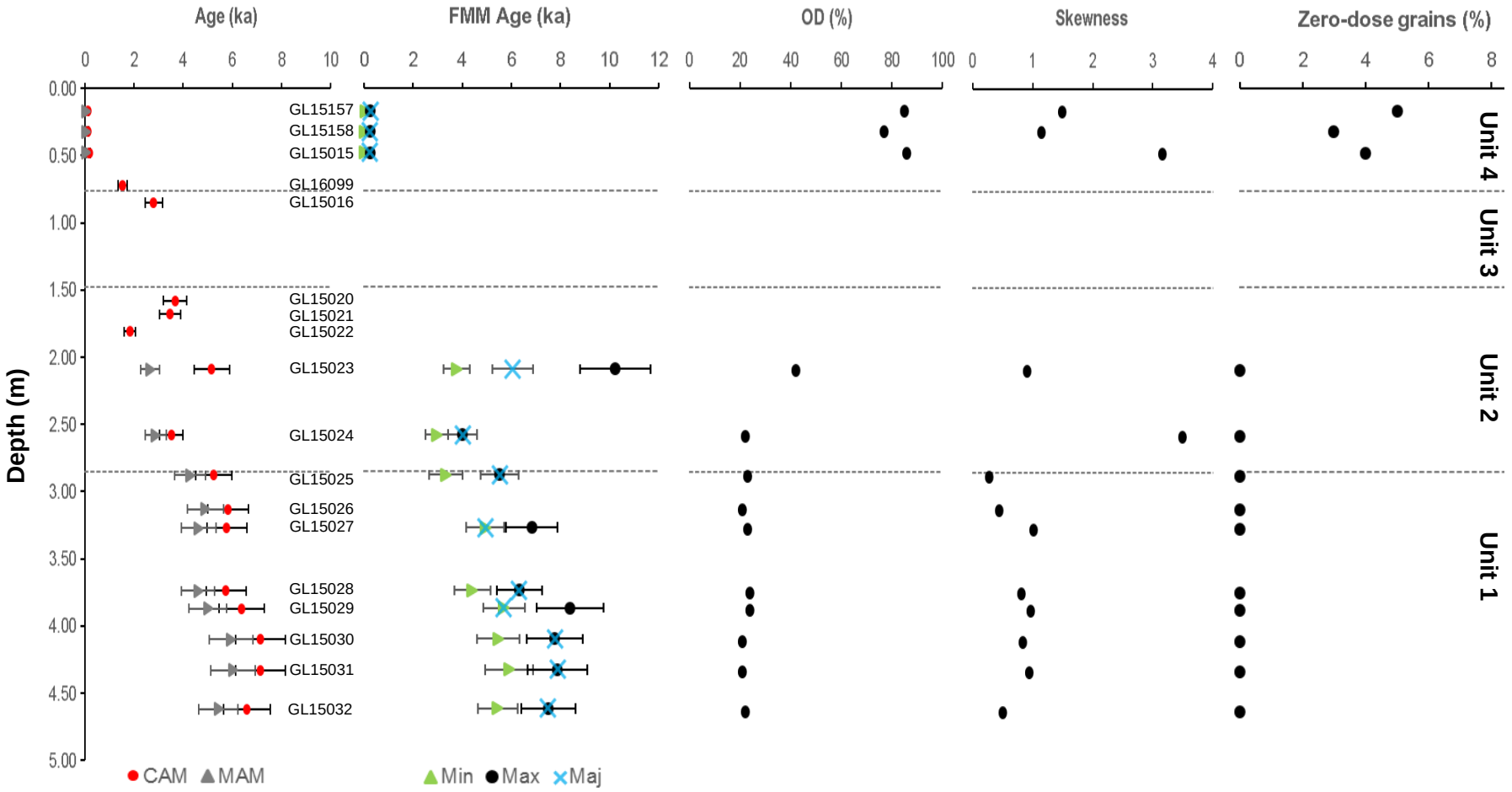


**Figure 5.2.22:** Modelled quartz OSL ages and key statistical parameters used to assist with selection of $D_e$ for South Lake samples.

**Table 5.2.7:** Summary South Lake quartz OSL ages (all reported with 1σ confidence and relative to sampling year 2014) – suggested age models for use in Chapter 6 Bayesian models.

| Sample | Unit | Depth (m) | Age (ka) | | | | | | | Suggested Age Model/s |
|---|---|---|---|---|---|---|---|---|---|---|
| | | | Median | CAM | MAM | $FMM_{min}$ | $FMM_{max}$ | $FMM_{maj}$ | Other (Model & ka) | |
| GL15157 | 4 | 0.17 | 0.17±0.02 | 0.14±0.02 | 0.04±0.01 | 0.05±0.01 | 0.28±0.04 | 0.28±0.04 | | $FMM_{min}$ |
| GL15158 | 4 | 0.32 | 0.17±0.02 | 0.14±0.02 | 0.05±0.01 | 0.05±0.01 | 0.25±0.03 | 0.25±0.03 | | $FMM_{min}$ |
| GL15015 | 4 | 0.48 | 0.20±0.06 | 0.19±0.03 | 0.06±0.01 | 0.04±0.01 | 0.27±0.04 | 0.27±0.04 | | $FMM_{maj}$ |
| GL16099 | 4 | 0.72 | 1.55±0.19 | 1.54±0.19 | - | - | - | - | - | CAM |
| GL15016 | 3 | 0.85 | 2.81±0.36 | 2.81±0.36 | - | - | - | - | - | CAM |
| GL15020 | 2 | 1.58 | 3.66±0.47 | 3.67±0.47 | - | - | - | - | - | CAM |
| GL15021 | 2 | 1.68 | 3.47±0.43 | 3.47±0.43 | - | - | - | - | - | CAM |
| GL15022 | 2 | 1.81 | 1.85±0.23 | 1.85±0.23 | - | - | - | - | - | CAM |
| GL15023 | 2 | 2.09 | 5.55±0.72 | 5.16±0.72 | 2.65±0.39 | 2.23±0.32 | 10.23±1.44 | 6.05±0.83 | $FMM_{k=2}$ = 3.78±0.57 | $FMM_{k=2}$ |
| GL15024 | 2 | 2.58 | 3.58±0.49 | 3.53±0.48 | 2.88±0.42 | 2.97±0.47 | 4.02±0.59 | 4.02±0.59 | - | CAM |
| GL15025 | 1 | 2.88 | 5.25±0.73 | 5.24±0.73 | 4.28±0.62 | 3.34±0.69 | 5.53±0.77 | 5.53±0.77 | - | CAM |
| GL15026 | 1 | 3.13 | 6.01±0.83 | 5.82±0.83 | 4.91±0.73 | - | - | - | - | CAM |
| GL15027 | 1 | 3.27 | 5.70±0.81 | 5.77±0.81 | 4.63±0.69 | 4.94±0.76 | 6.83±1.05 | 4.94±0.76 | - | CAM |
| GL15028 | 1 | 3.74 | 5.80±0.81 | 5.74±0.81 | 4.61±0.68 | 4.42±0.74 | 6.32±0.92 | 6.32±0.92 | - | CAM |
| GL15029 | 1 | 3.87 | 6.38±0.92 | 6.39±0.91 | 5.01±0.77 | 5.71±0.83 | 8.38±1.36 | 5.71±0.83 | - | CAM |
| GL15030 | 1 | 4.10 | 7.14±1.09 | 7.15±1.02 | 5.94±0.89 | 5.48±0.86 | 7.77±1.13 | 7.77±1.13 | - | CAM |
| GL15031 | 1 | 4.33 | 7.03±1.03 | 7.15±1.02 | 6.02±0.91 | 5.90±0.97 | 7.88±1.20 | 7.88±1.20 | - | CAM |
| GL15032 | 1 | 4.62 | 6.67±0.94 | 6.59±0.94 | 5.43±0.80 | 5.45±0.81 | 7.51±1.10 | 7.51±1.10 | - | CAM |

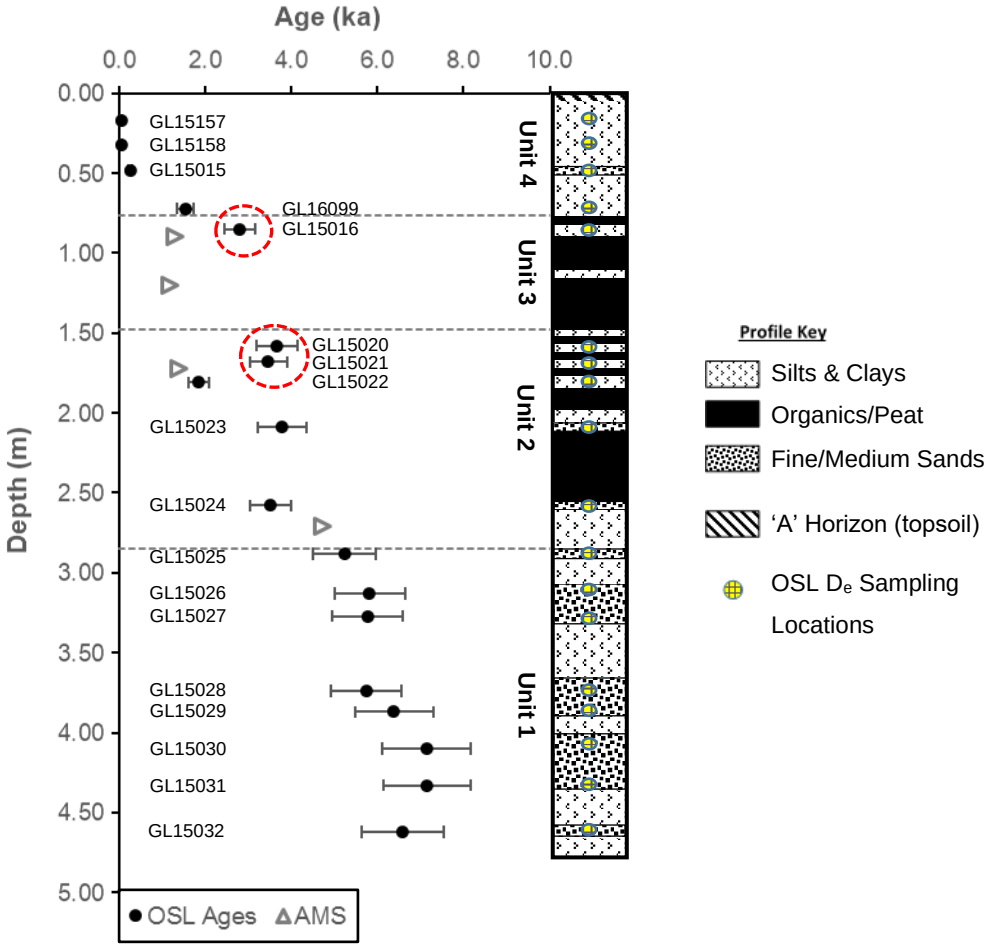


**Figure 5.2.23:** Quartz OSL ages adopted for the South Lake sequence, AMS ages included for comparison (all ages reported with 1σ confidence; overestimated fine silt OSL ages circled).

## 5.3. UCOSP

### *5.3.1. Sample Overview*

The UCOSP site acts as a modern analogue for this study as it features at least four recent flood deposits suitable for dating. Four samples (GL14001, 003, 004 & 006) were taken in section from sand dominated flood units, whilst five (GL15116-120) were sampled from equivalent units within cores. Sample details are provided in Table 5.3.1.

**Table 5.3.1:** UCOSP sample details

| Sample | Depth (m) | Unit Type | Moisture Content (%) | Grain Fraction (μm) |
|---|---|---|---|---|
| GL14001 | 0.69 | Flood (section) | 9 | 180-250 |
| GL14003 | 1.55 | Flood (section) | 6 | 180-250 |
| GL14004 | 1.95 | Flood (section) | 3 | 180-250 |
| GL14006 | 3.00 | Flood (section) | 4 | 180-250 |
| GL15116 | 5.15 | Flood (core) | 11 | 180-250 |
| GL15117 | 6.15 | Flood (core) | 15 | 180-250 |
| GL15118 | 6.35 | Flood (core) | 17 | 180-250 |
| GL15119 | 6.75 | Flood (core) | 11 | 180-250 |
| GL15120 | 7.35 | Flood (core) | 9 | 180-250 |

*5.3.2. Initial OSL Signal Evaluation and Dose-Recovery Results*

Figure 5.3.1 provides an example of the data acquired from the initial measurements for GL15116. An $L_x/T_x$ ratio of 0.215 was produced for a test aliquot following measurement of the natural and a 5 Gy test dose (a), this indicated that an appropriate artificial dose for the subsequent dose recovery test (b) was 1 Gy. Dose-recovery tests were conducted upon all UCOSP samples and the recovered ratio x-y plots for all of these are presented in Appendix C (Figures C3.1-2). A summary of the dose-recovery test results is presented in Table 5.3.2.

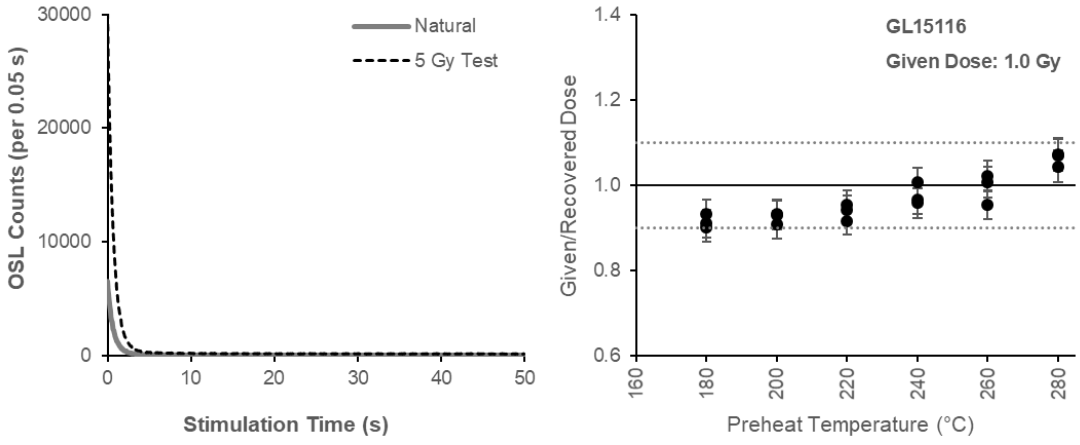


**Figure 5.3.1:** Test disc natural/5 Gy test OSL signal and 1.0 Gy dose-recovery test for GL15116

Most dose-recovery tests for UCOSP samples indicated that a 260°C preheat was most suitable for SAR $D_e$ acquisition. The only exceptions were GL15116 and GL15120 for which 240°C preheats were selected. A cut heat of 220°C was used for every sample. All samples produced given/recovered dose ratios consistent with unity.

**Table 5.3.2:** UCOSP test disc and dose-recovery test result summary

| Sample | Test Disc $L_x/T_x$ | Given Dose (Gy) | Selected Preheat (°C) | Given/Recovered Dose Ratio |
|---|---|---|---|---|
| GL14001 | 0.082 | 0.4 | 260 | 0.99 ± 0.03 |
| GL14003 | 0.094 | 0.5 | 260 | 1.00 ± 0.03 |
| GL14004 | 0.081 | 0.4 | 260 | 1.00 ± 0.03 |
| GL14006 | 0.131 | 0.7 | 260 | 1.00 ± 0.04 |
| GL15116 | 0.215 | 1.0 | 240 | 0.99 ± 0.04 |
| GL15117 | 0.450 | 2.3 | 260 | 0.98 ± 0.03 |
| GL15118 | 0.627 | 3.1 | 260 | 1.00 ± 0.04 |
| GL15119 | 2.292 | 11.5 | 260 | 1.00 ± 0.04 |
| GL15120 | 1.331 | 6.7 | 240 | 1.00 ± 0.04 |

### *5.3.3. Single-Grain $D_e$ Results*

In total, nine single-grain samples were analysed from the UCOSP site, a summary of $D_e$ results is provided in Table 5.3.4 whilst $D_e$ summary diagrams are presented for each individual sample in Figures 5.3.2 to 5.3.10. The $D_e$ components isolated by FMM and the proportion of grains within each are summarised in Table 5.3.3.

Statistically, all samples from the UCOSP site are highly positively skewed, however, the severity of skewness within $D_e$ datasets appears to decrease with increase in depth/dose. With the exception of GL15117, $D_e$ populations also display significant OD and kurtosis. All samples collected from the section contained a small population (4-7%) of zero-dose grains, samples collected from core samples did not feature any.

The three uppermost samples (GL14001, 003 & 004; Figure 5.3.2-4) collected from the UCOSP section all produced central $D_e$ values (median & CAM) which are statistically consistent, whilst MAM $D_e$ estimates increase with depth from 0.07±0.01 to 0.19±0.01 Gy. The distribution of all three samples features a strong low-dose peak with a long high-dose tail. Although fewer grains were accepted for GL14004, the high-dose tail appears to be less significant which is marked by a drop in OD and kurtosis. Application of FMM to the distributions indicated that 4 and 5 components were most suited. $FMM_{min}$ were consistent for GL14001 (0.15±0.01 Gy) and GL14003 (0.14±0.01 Gy) containing 48 and 33% of grains respectively, whilst a slightly higher dose incorporating a higher proportion of grains (69%) is observed for GL14004 (0.20±0.01 Gy). All $FMM_{min}$ and $FMM_{maj}$ values fall between estimates for CAM and MAM. GL14004 is relatively unique compared to the other section samples as median, MAM and $FMM_{min}$ and $FMM_{maj}$ are statistically consistent.

GL14006 was taken from the base of the UCOSP section and produced central $D_e$ values which were double those obtained for the upper three samples. The distribution includes a distinct low-dose peak with some zero-dose grains and a significant number of high-dose grains are also observed (Figure 5.3.5c-d). A 4-component FMM isolates $FMM_{min}$ (0.25±0.01 Gy) and $FMM_{maj}$ (0.42±0.01 Gy) dose populations situated between CAM and MAM.

GL15116 was taken from the uppermost flood unit contained within core samples. Central measures of $D_e$ are lower than those obtained for GL14006, however, the OD and high-dose peak is less significant for GL15116 (Figure 5.3.6) as a few high-dose grains feature within the distribution. Minimum $D_e$ estimates (MAM & $FMM_{min}$) and $FMM_{maj}$ are statistically consistent (*c.* 0.38 Gy) and account for 67% of all values.

GL15117 has the lowest OD (23%) from the UCOSP sequence with a minimal number of high-dose grains (Figure 5.3.7) creating a strong positive skew. Application of a two-component FMM confirmed the $D_e$ distribution is only formed of one significant grain population, having identified a $FMM_{min}$, $FMM_{maj}$ and $FMM_{max}$ of 1.33±0.03 Gy which incorporates 92% of all values.

$FMM_{k=2}$ is comprised of <10% of all values and so is dismissed as a discrete $D_e$ population. $FMM_{k=1}$ (min, maj & max) is statistically consistent with MAM and the median $D_e$, whilst CAM only overlaps with the median.

The remaining samples (GL15118-120; Figure 5.3.8-10) from the UCOSP sequence all display similar distributions with high-dose tails. OD ranges from 46 to 60%, all have strong positive skew and values for kurtosis are similar. All modelled $D_e$ values increase systematically with depth and both CAM and median $D_e$ are statistically consistent for all samples, as too are MAM and $FMM_{min}$. Central doses increase from *c.* 2 Gy for GL15118 to *c.* 4 Gy for GL15120. The increase in minimum doses is less significant increasing from *c.* 1.2 to 2.5 Gy. Four-component FMM was deemed most suitable for all samples and $FMM_{min}$ formed the $FMM_{maj}$ component for GL15119 and GL15120, however, for GL15118 $FMM_{maj}$ produced a $D_e$ value statistically consistent with CAM. $FMM_{maj}$ accounts for between 36 and 49% of all $D_e$ values for the three samples.

**Table 5.3.3:** FMM components fitted to UCOSP single-grain $D_e$ distributions ($k^*$ = total components, σ = 0.15 (15%) and $p$ = proportion of grains in each component)

| | | FMM Component | | | | | | | | | |
|---|---|---|---|---|---|---|---|---|---|---|---|
| | | ***k* = 1** | | ***k* = 2** | | ***k* = 3** | | ***k* = 4** | | ***k* = 5** | |
| **Sample** | ***k**** | **$D_e$ (Gy)** | ***p* (%)** | **$D_e$ (Gy)** | ***p* (%)** | **$D_e$ (Gy)** | ***p* (%)** | **$D_e$ (Gy)** | ***p* (%)** | **$D_e$ (Gy)** | ***p* (%)** |
| GL14001 | 4 | 0.15±0.01 | 48 | 0.19±0.02 | 28 | 0.86±0.05 | 15 | 2.58±0.18 | 9 | - | - |
| GL14003 | 5 | 0.14±0.01 | 33 | 0.26±0.01 | 40 | 0.53±0.02 | 15 | 1.48±0.11 | 8 | 7.28±0.85 | 4 |
| GL14004 | 4 | 0.20±0.01 | 69 | 0.35±0.05 | 15 | 0.76±0.06 | 12 | 1.63±0.19 | 4 | - | - |
| GL14006 | 4 | 0.25±0.01 | 21 | 0.42±0.01 | 36 | 0.72±0.05 | 20 | 1.70±0.05 | 23 | - | - |
| GL15116 | 3 | 0.38±0.01 | 67 | 0.55±0.05 | 22 | 1.39±0.07 | 11 | - | - | - | - |
| GL15117 | 2 | 1.33±0.03 | 92 | 2.48±0.25 | 8 | - | - | - | - | - | - |
| GL15118 | 4 | 1.32±0.08 | 31 | 2.02±0.10 | 49 | 3.31±0.27 | 13 | 6.46±0.41 | 7 | - | - |
| GL15119 | 4 | 1.58±0.10 | 43 | 2.65±0.29 | 31 | 5.20±0.46 | 20 | 10.62±1.03 | 6 | - | - |
| GL15120 | 4 | 2.54±0.08 | 36 | 3.96±0.40 | 33 | 5.70±0.69 | 20 | 11.52±0.52 | 11 | - | - |

**Table 5.3.4:** Summary of UCOSP single-grain $D_e$ analysis (errors reported within 1σ confidence; for age modelling σ = 0.15/15%)

| Sample | Depth (m) | Grains Accepted (Number (%))* | $\sigma_{OD}$ (%) | Skewness (c) | Kurtosis (*k*) | $D_e$ Values (Gy) | | | | | | |
|---|---|---|---|---|---|---|---|---|---|---|---|---|
| | | | | | | Median | CAM | MAM | FMM *k*** | $FMM_{min}$ | $FMM_{max}$ | $FMM_{maj}$ |
| GL14001 | 0.69 | 107 (7.1) | 107 | 4.02 | 22.91 | 0.23±0.09 | 0.29±0.03 | 0.07±0.01 | 4 | 0.15±0.01 | 0.86±0.05 | 0.15±0.01 |
| GL14003 | 1.55 | 124 (8.3) | 84 | 5.86 | 40.35 | 0.22±0.09 | 0.27±0.02 | 0.10±0.01 | 5 | 0.14±0.01 | 0.53±0.02 | 0.26±0.01 |
| GL14004 | 1.95 | 62 (4.1) | 68 | 2.55 | 10.39 | 0.21±0.05 | 0.27±0.03 | 0.19±0.01 | 4 | 0.20±0.01 | 0.76±0.06 | 0.20±0.01 |
| GL14006 | 3.00 | 139 (9.3) | 74 | 2.78 | 14.31 | 0.45±0.07 | 0.57±0.04 | 0.22±0.02 | 4 | 0.25±0.01 | 1.70±0.05 | 0.42±0.01 |
| GL15116 | 5.15 | 112 (7.5) | 47 | 2.11 | 16.77 | 0.42±0.02 | 0.47±0.02 | 0.39±0.01 | 3 | 0.38±0.01 | 1.39±0.07 | 0.38±0.01 |
| GL15117 | 6.15 | 109 (7.3) | 23 | 2.97 | 17.37 | 1.35±0.05 | 1.40±0.04 | 1.31±0.04 | 2 | 1.33±0.03 | 1.33±0.03 | 1.33±0.03 |
| GL15118 | 6.35 | 106 (7.1) | 46 | 2.31 | 8.72 | 1.93±0.14 | 2.06±0.10 | 1.18±0.11 | 4 | 1.32±0.08 | 3.31±0.27 | 2.02±0.10 |
| GL15119 | 6.75 | 104 (6.9) | 60 | 2.10 | 7.47 | 2.32±0.25 | 2.66±0.16 | 1.49±0.12 | 4 | 1.58±0.10 | 5.20±0.46 | 1.58±0.10 |
| GL15120 | 7.35 | 112 (7.5) | 49 | 1.88 | 6.27 | 3.69±0.27 | 4.04±0.19 | 2.44±0.16 | 4 | 2.54±0.08 | 11.52±0.52 | 2.54±0.08 |

*1500 grains measured per sample

** *k* = number of components fitted for the FMM

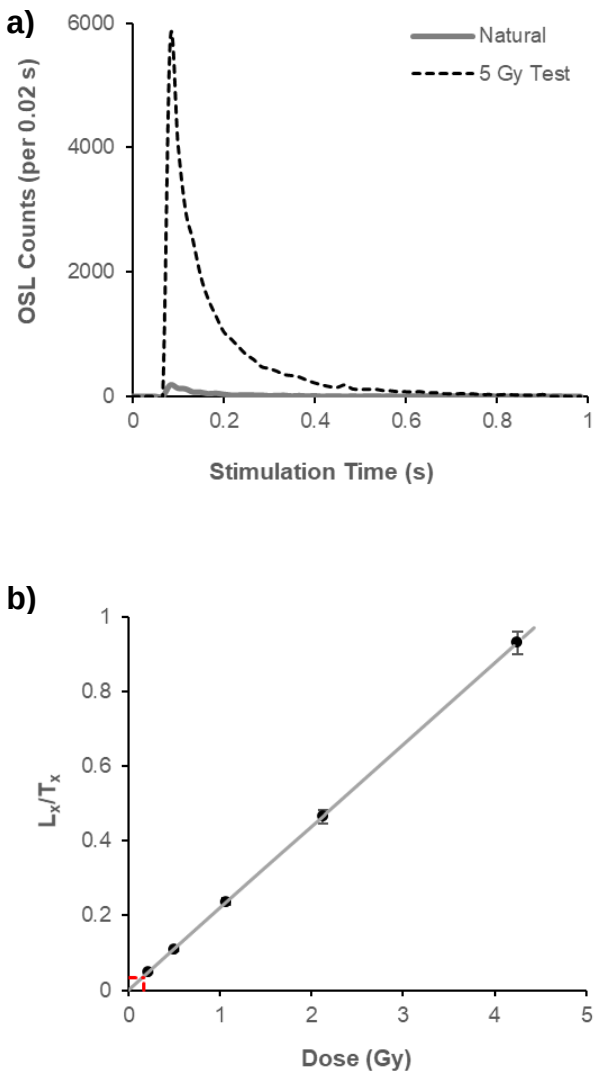


**Figure 5.3.2:** Single-grain $D_e$ summary diagrams for GL14001

a) Example single-grain decay curves for the natural and 5 Gy test dose signals of grain 28.

b) Dose-response curve for grain 28 with regenerative doses; 0, 0.2, 0.5, 1.1, 2.1 & 4.3 Gy. Interpolation of the natural $L_x/T_x$ recovered a $D_e$ of 0.16 Gy.

c) Radial plot of 94 $D_e$ values which passed rejection criteria. Coloured areas represent age models applied to the $D_e$ dataset; CAM (**red**), MAM (**grey**), $FMM_{min}$ (**green**) and $FMM_{maj}$ (**blue**). $FMM_{max}$ is equivalent to 0.86 ± 0.05 Gy.

d) Histogram of $D_e$ values with bin width 0.1. Data is highly positively skewed (c) and features a small proportion of zero-dose grains.

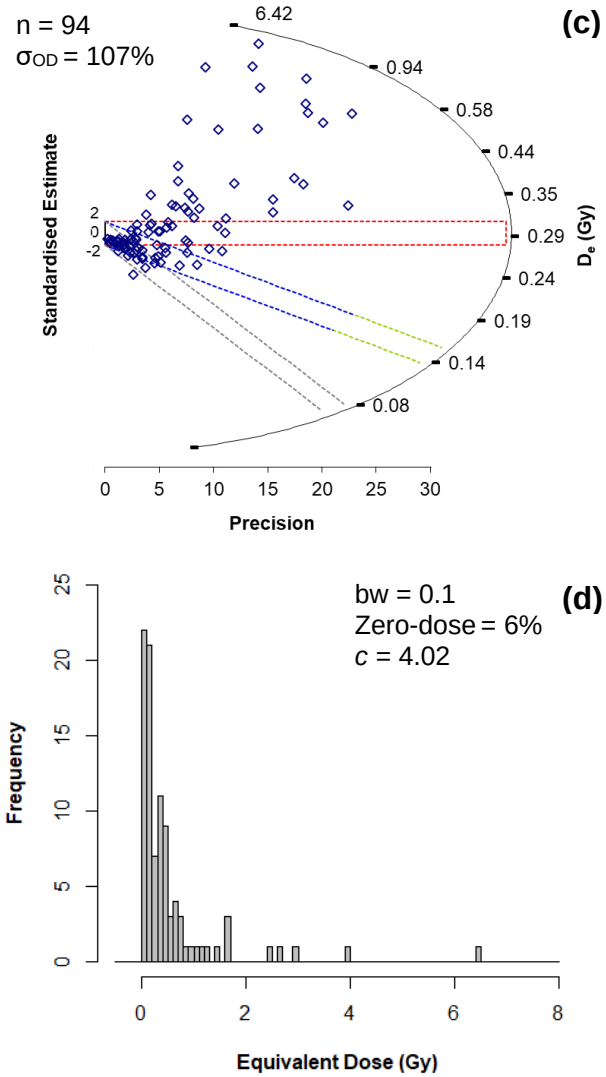

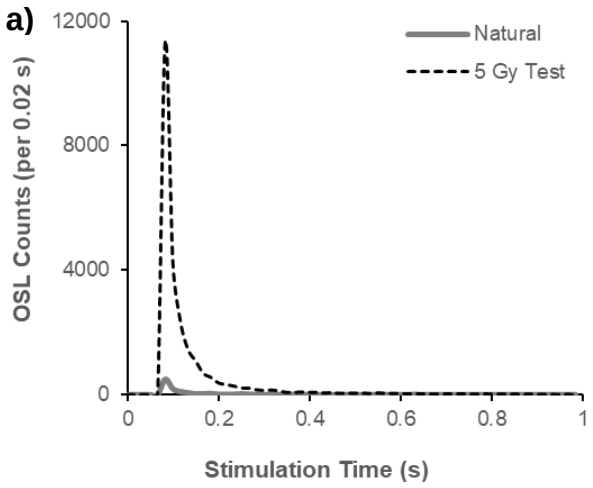


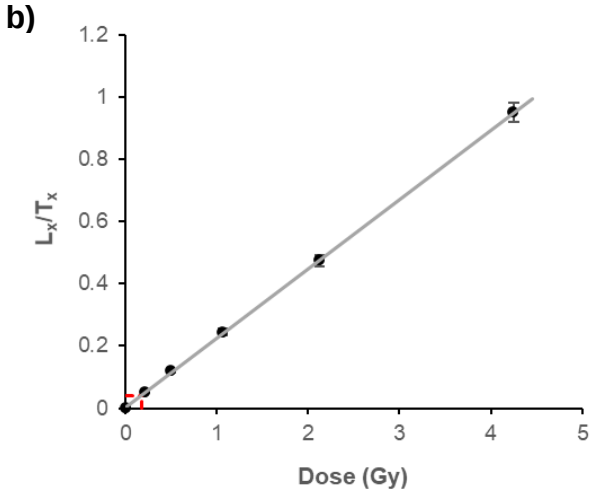


**Figure 5.3.3:** Single-grain $D_e$ summary diagrams for GL14003

**a)** Example single-grain decay curves for the natural and 5 Gy test dose signals of grain 44.

**b)** Dose-response curve for grain 44 with regenerative doses; 0, 0.2, 0.5, 1.1, 2.1 & 4.3 Gy. Interpolation of the natural $L_x/T_x$ recovered a $D_e$ of 0.18 Gy.

**c)** Radial plot of 124 $D_e$ values which passed rejection criteria. Coloured areas represent age models applied to the $D_e$ dataset; CAM (**red**), MAM (**grey**), $FMM_{min}$ (**green**) and $FMM_{maj}$ (**blue**). $FMM_{max}$ is equivalent to 0.53 ± 0.02 Gy.

d) Histogram of $D_e$ values with bin width 0.1. Data is highly positively skewed (c) and features a small proportion of zero-dose grains.

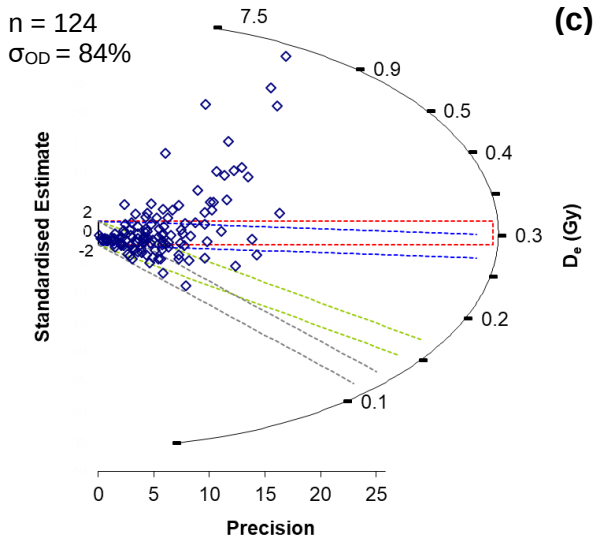


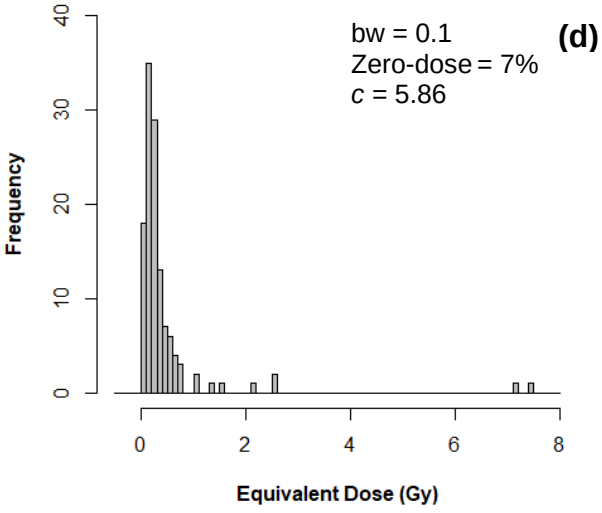

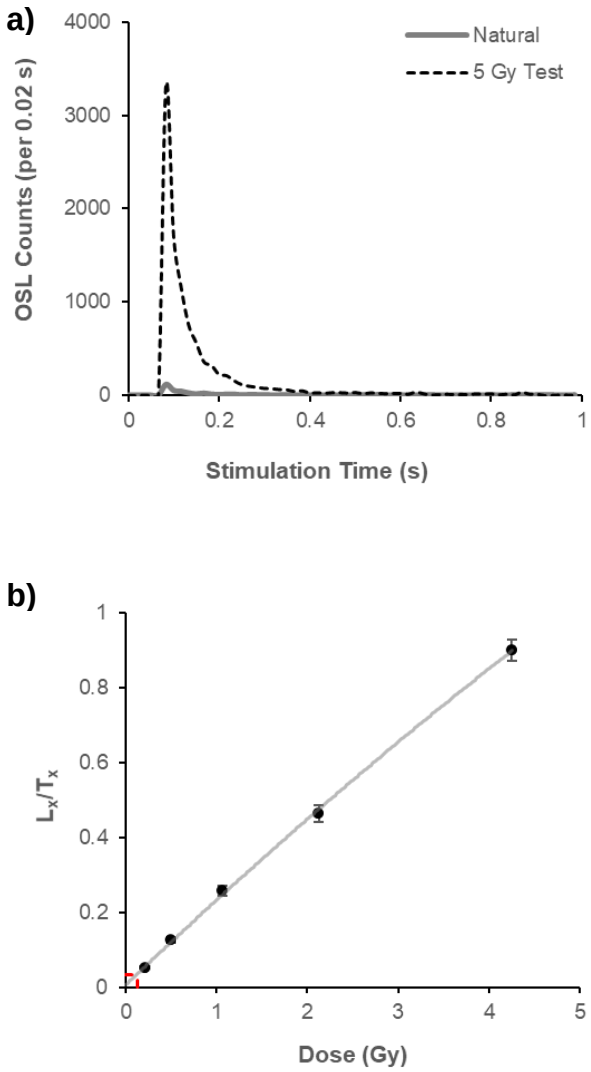


**Figure 5.3.4:** Single-grain $D_e$ summary diagrams for GL14004

**a)** Example single-grain decay curves for the natural and 5 Gy test dose signals of grain 1.

**b)** Dose-response curve for grain 1 with regenerative doses; 0, 0.2, 0.5, 1.1, 2.1 & 4.3 Gy. Interpolation of the natural $L_x/T_x$ recovered a $D_e$ of 0.13 Gy.

**c)** Radial plot of 62 $D_e$ values which passed rejection criteria. Coloured areas represent age models applied to the $D_e$ dataset; CAM (**red**), MAM (**grey**), $FMM_{min}$ (**green**) and $FMM_{maj}$ (**blue**). $FMM_{max}$ is equivalent to 0.76 ± 0.06 Gy.

d) Histogram of $D_e$ values with bin width 0.1. Data is highly positively skewed (c) and features a small proportion of zero-dose grains.

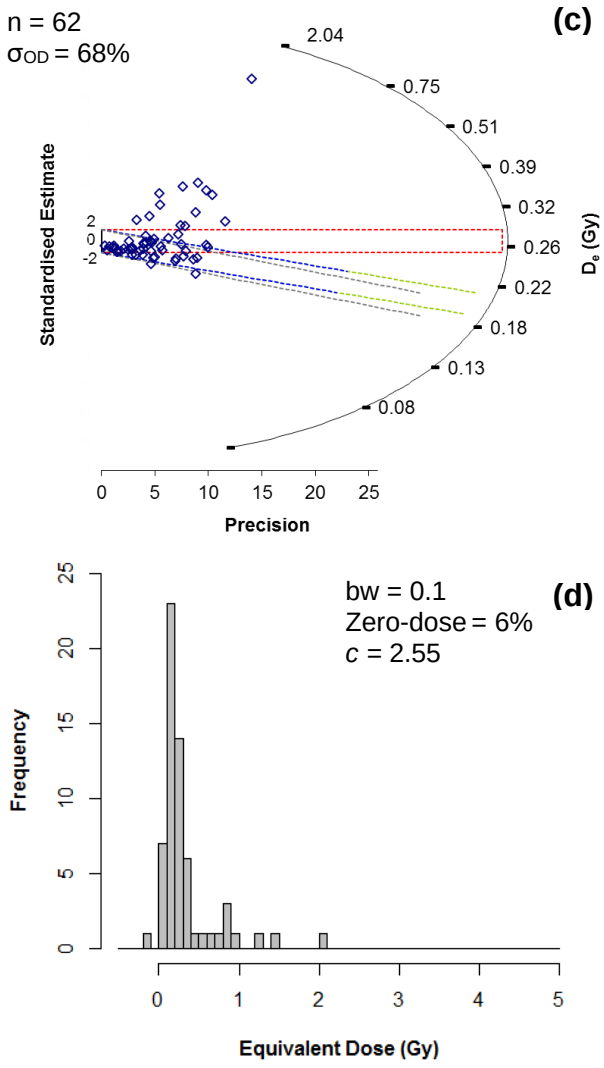

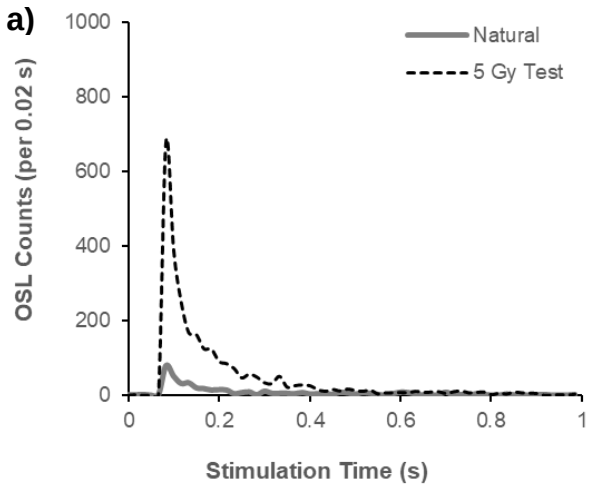


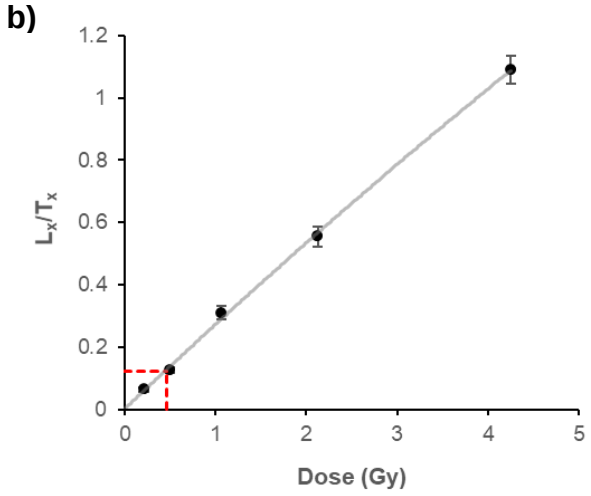


**Figure 5.3.5:** Single-grain $D_e$ summary diagrams for GL14006

**a)** Example single-grain decay curves for the natural and 5 Gy test dose signals of grain 6.

**b)** Dose-response curve for grain 6 with regenerative doses; 0, 0.2, 0.5, 1.1, 2.1 & 4.3 Gy. Interpolation of the natural $L_x/T_x$ recovered a $D_e$ of 0.46 Gy.

**c)** Radial plot of 139 $D_e$ values which passed rejection criteria. Coloured areas represent age models applied to the $D_e$ dataset; CAM (**red**), MAM (**grey**), $FMM_{min}$ (**green**) and $FMM_{maj}$ (**blue**). $FMM_{max}$ is equivalent to 1.70 ± 0.05 Gy.

d) Histogram of $D_e$ values with bin width 0.1. Data is highly positively skewed (c) and features a small proportion of zero-dose grains.

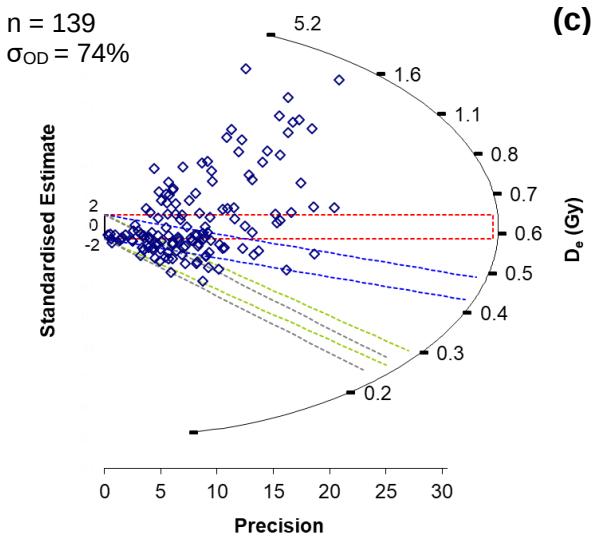


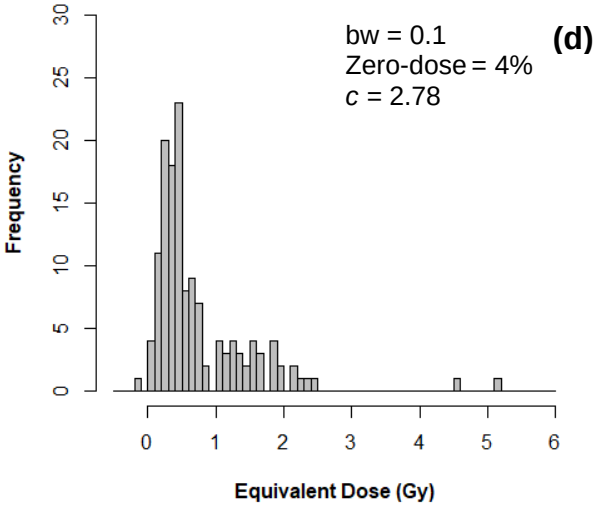

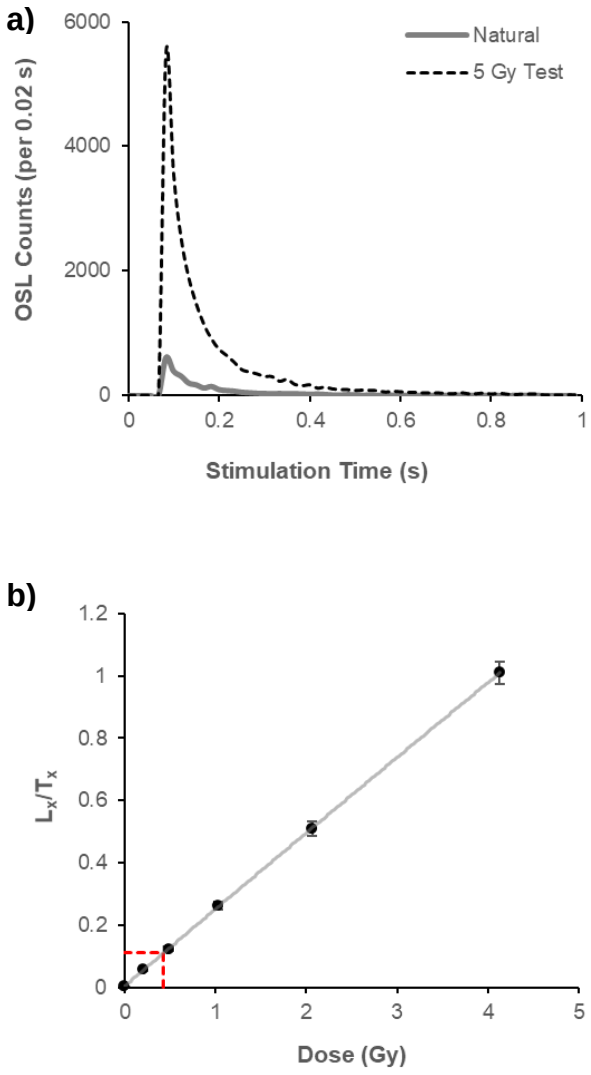


**Figure 5.3.6:** Single-grain $D_e$ summary diagrams for GL15116

**a)** Example single-grain decay curves for the natural and 5 Gy test dose signals of grain 67.

**b)** Dose-response curve for grain 67 with regenerative doses; 0, 0.2, 0.5, 1.0, 2.1 & 4.1 Gy. Interpolation of the natural $L_x/T_x$ recovered a $D_e$ of 0.43 Gy.

**c)** Radial plot of 112 $D_e$ values which passed rejection criteria. Coloured areas represent age models applied to the $D_e$ dataset; CAM (**red**), MAM (**grey**), $FMM_{min}$ (**green**) and $FMM_{maj}$ (**blue**). $FMM_{max}$ is equivalent to 1.39 ± 0.07 Gy.

d) Histogram of $D_e$ values with bin width 0.1. Data is highly positively skewed (c). No zero-dose grains.

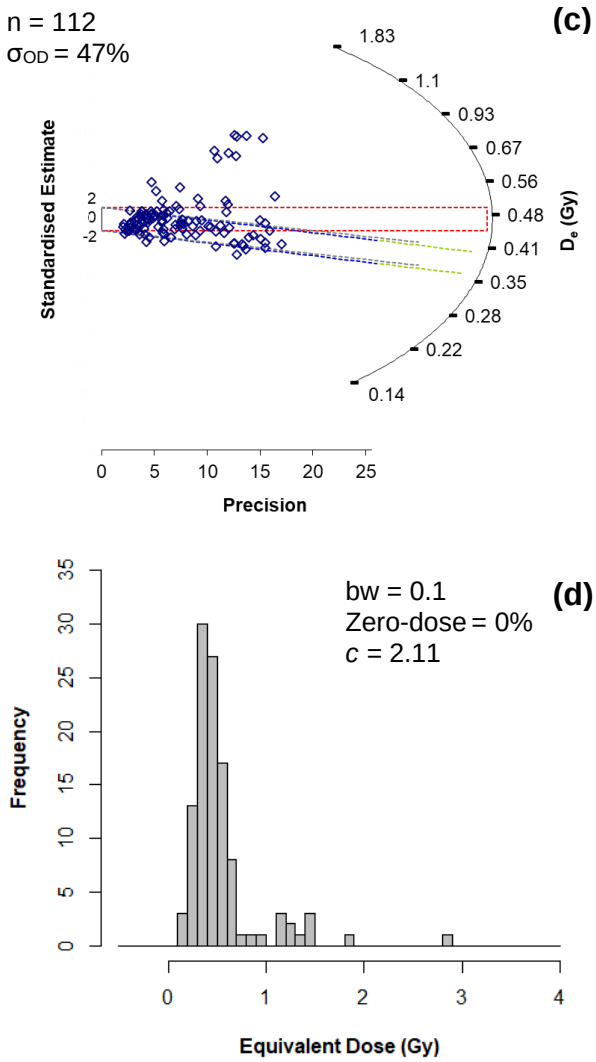

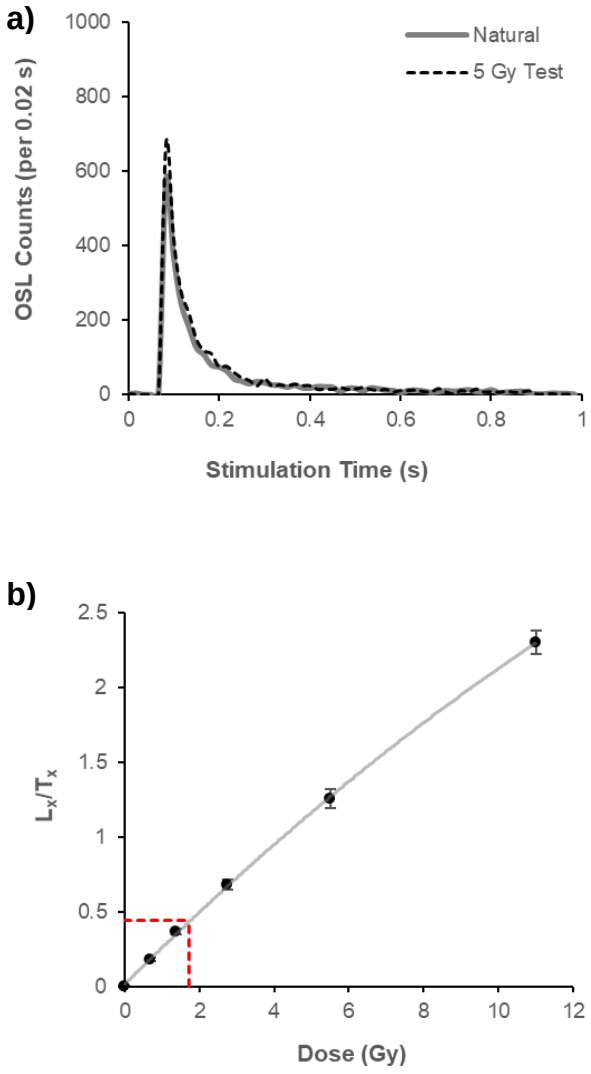


**Figure 5.3.7:** Single-grain $D_e$ summary diagrams for GL15117

**a)** Example single-grain decay curves for the natural and 5 Gy test dose signals of grain 11.

**b)** Dose-response curve for grain 11 with regenerative doses; 0, 0.7, 1.4, 2.8, 5.5 & 11.0 Gy. Interpolation of the natural $L_x/T_x$ recovered a $D_e$ of 1.72 Gy.

**c)** Radial plot of 109 $D_e$ values which passed rejection criteria. Coloured areas represent age models applied to the $D_e$ dataset; CAM (**red**), MAM (**grey**), $FMM_{min}$ (**green**) and $FMM_{maj}$ (**blue**). $FMM_{max}$ produced a dose with <10% of values.

d) Histogram of $D_e$ values with bin width 0.2. Data is highly positively skewed (c). No zero-dose grains.

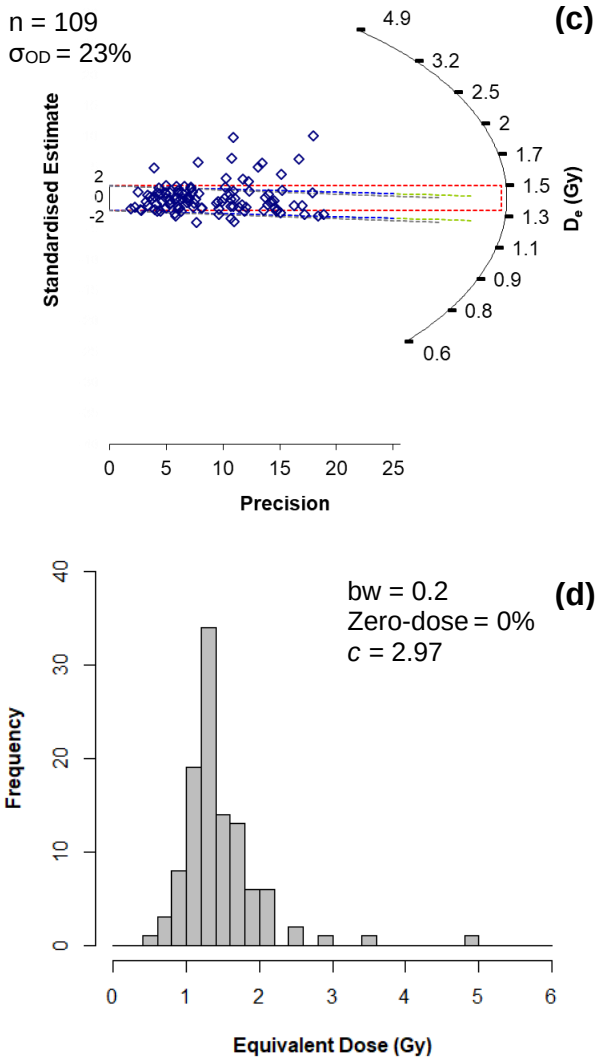

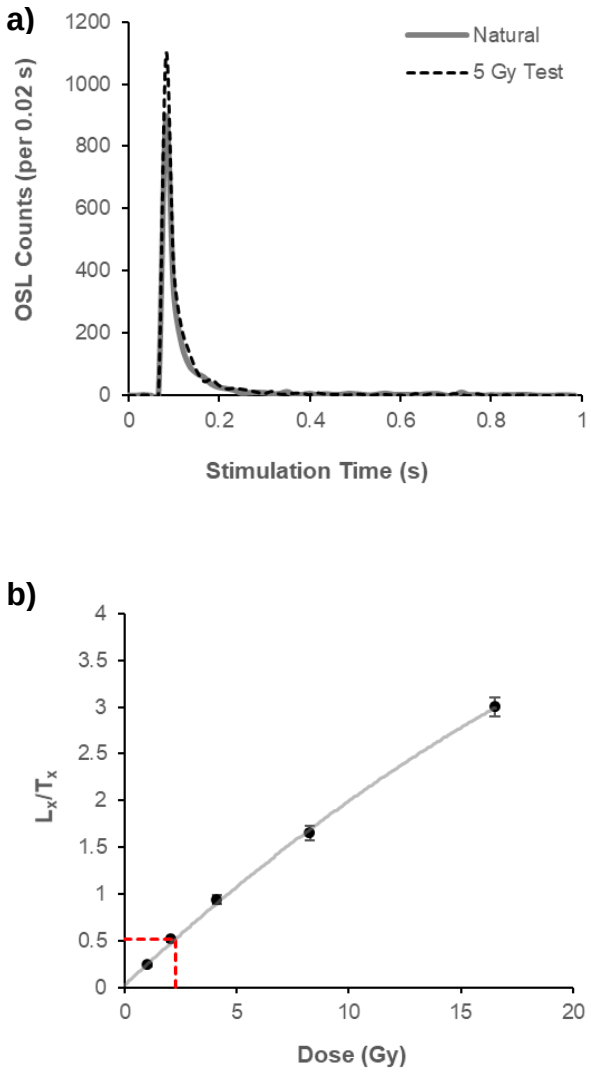


**Figure 5.3.8:** Single-grain $D_e$ summary diagrams for GL15118

**a)** Example single-grain decay curves for the natural and 5 Gy test dose signals of grain 68.

**b)** Dose-response curve for grain 68 with regenerative doses; 0, 1.0, 2.1, 4.1, 8.3 & 16.5 Gy. Interpolation of the natural $L_x/T_x$ recovered a $D_e$ of 2.30 Gy.

**c)** Radial plot of 106 $D_e$ values which passed rejection criteria. Coloured areas represent age models applied to the $D_e$ dataset; CAM (**red**), MAM (**grey**), $FMM_{min}$ (**green**) and $FMM_{maj}$ (**blue**). $FMM_{max}$ is equivalent to 3.31 ± 0.27 Gy.

d) Histogram of $D_e$ values with bin width 0.2. Data is highly positively skewed (c). No zero-dose grains.

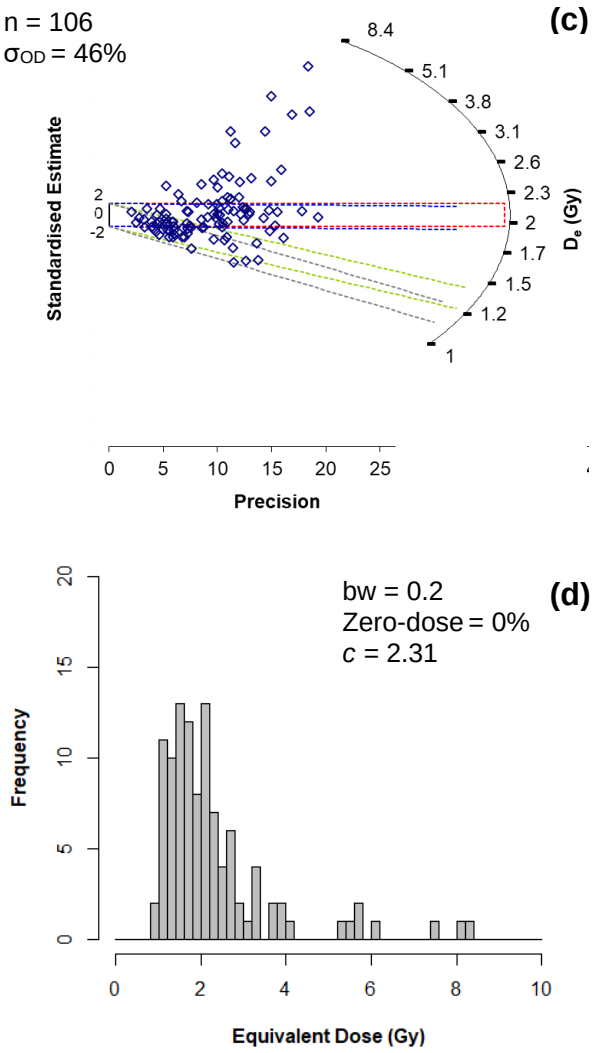

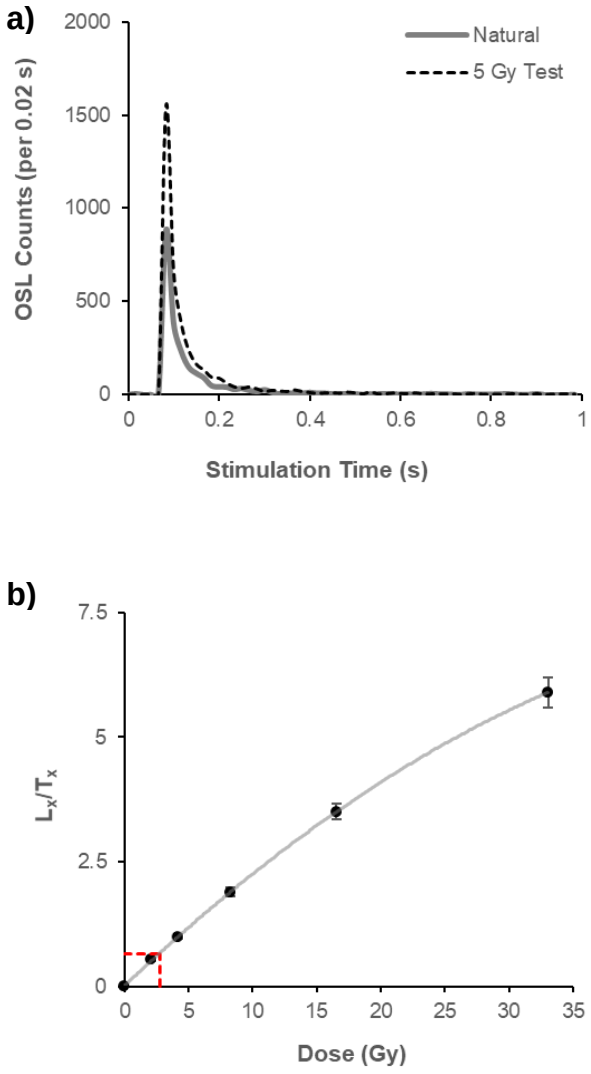


**Figure 5.3.9:** Single-grain $D_e$ summary diagrams for GL15119

**a)** Example single-grain decay curves for the natural and 5 Gy test dose signals of grain 4.

**b)** Dose-response curve for grain 4 with regenerative doses; 0, 2.1, 4.1, 8.3, 16.5 & 33.0 Gy. Interpolation of the natural $L_x/T_x$ recovered a $D_e$ of 2.77 Gy.

**c)** Radial plot of 104 $D_e$ values which passed rejection criteria. Coloured areas represent age models applied to the $D_e$ dataset; CAM (**red**), MAM (**grey**), $FMM_{min}$ (**green**) and $FMM_{maj}$ (**blue**). $FMM_{max}$ is equivalent to 5.20 ± 0.46 Gy.

d) Histogram of $D_e$ values with bin width 0.2. Data is highly positively skewed (c). No zero-dose grains.

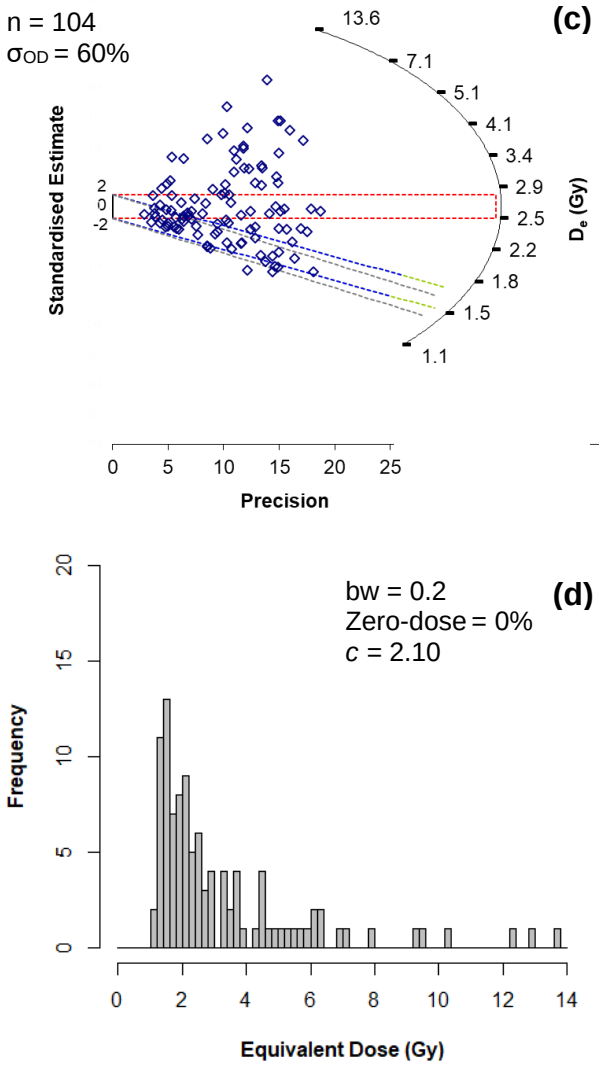

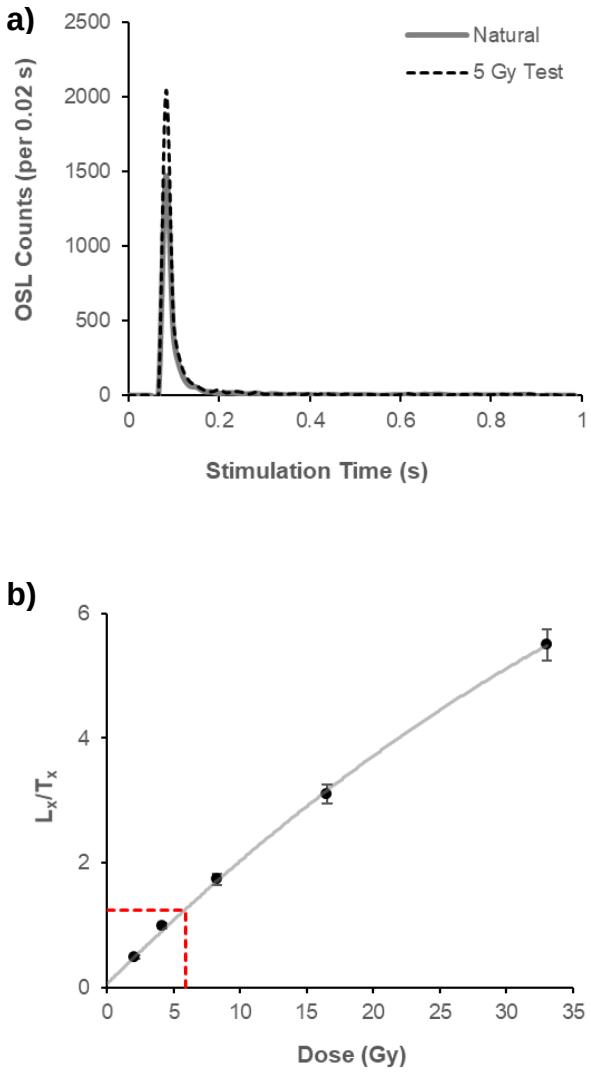


**Figure 5.3.10:** Single-grain $D_e$ summary diagrams for GL15120

**a)** Example single-grain decay curves for the natural and 5 Gy test dose signals of grain 19.

**b)** Dose-response curve for grain 19 with regenerative doses; 0, 2.1, 4.1, 8.3, 16.5 & 33.0 Gy. Interpolation of the natural $L_x/T_x$ recovered a $D_e$ of 5.85 Gy.

**c)** Radial plot of 112 $D_e$ values which passed rejection criteria. Coloured areas represent age models applied to the $D_e$ dataset; CAM (**red**), MAM (**grey**), $FMM_{min}$ (**green**) and $FMM_{maj}$ (**blue**). $FMM_{max}$ is equivalent to 11.52 ± 0.52 Gy.

d) Histogram of $D_e$ values with bin width 0.5. Data is highly positively skewed (c). No zero-dose grains.

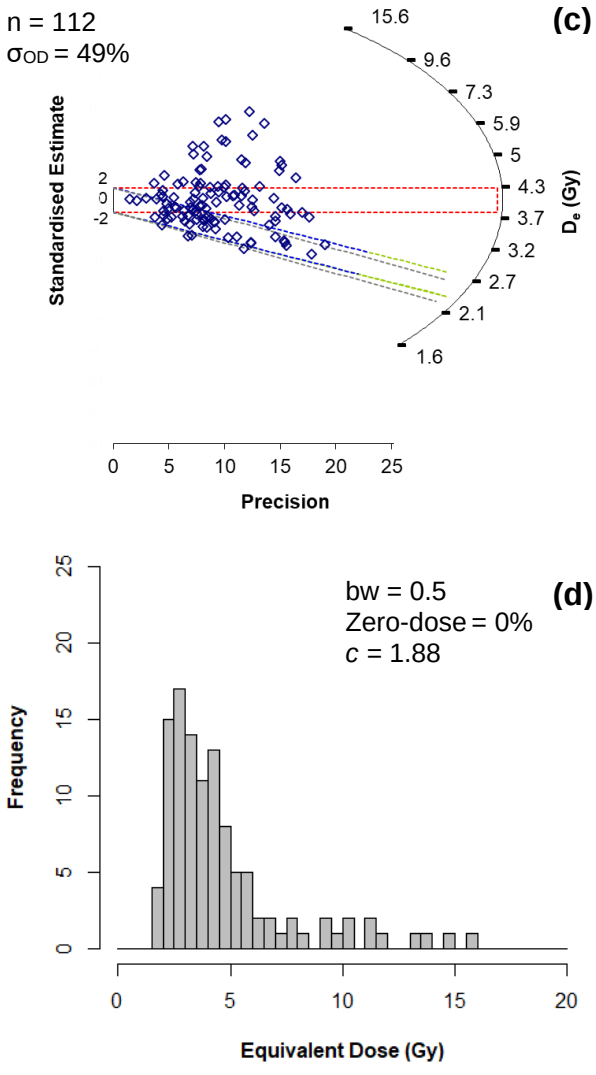

*5.3.4. Dosimetry*

The sedimentology of the UCOSP sequence was less complex than that at the South Lake site. Therefore, $\gamma$-modelling was not conducted and $D_r$ values are based on radionuclide concentrations obtained at each sampling location (Table 5.3.5).

The mean $D_r$ for UCOSP samples ranges from 1.52 to 2.76 Gy $ka^{-1}$ with relative errors ranging between 13.5 and 15%. Section samples produced the highest $D_r$ values. These units contained the highest concentrations of K, Th and U, and moisture contents were slightly lower than the values obtained for core samples. K contents for the whole sequence ranged from 1.47 to 1.98% with the highest content being observed for GL14006 at 3.00 m and the lowest at 6.15 m for GL15117. Concentrations of Th range from 2.41 to 9.98 ppm, GL14003 displays the highest concentration at 1.55 m whilst the lowest concentration is observed at 6.75 m for GL15119. U concentrations range from 0.63 to 1.79 ppm, GL14003 displays the highest concentration at 1.55 m whilst GL15120 displays the lowest value at 7.35 m.

The two lower-most samples from the UCOSP sequence (GL15119 & GL15120) had Th and U concentrations which were significantly lower than other samples in the sequence. In addition, for GL15119 the U-series appears to be in disequilibrium (Figure 5.3.11) with $^{226}Ra/^{238}U$ falling outside of the 50% margin. The excess radon within GL15119 and the lower concentrations of Th and U indicate that radionuclides could be mobile within the lower core regions, as with South Lake this could be attributed to groundwater flow.

With the exception of GL14001 and GL15119, all samples produce $^{226}Ra/^{238}U$ ratios which are consistent with unity and radioactive equilibrium is assumed. Equilibrium is also assumed for GL14001 as the $^{226}Ra/^{238}U$ ratio falls within the 50% margin and is statistically consistent within 10% of unity. Ages produced for GL15119 are used with caution owing to the presence of U-series disequilibrium.

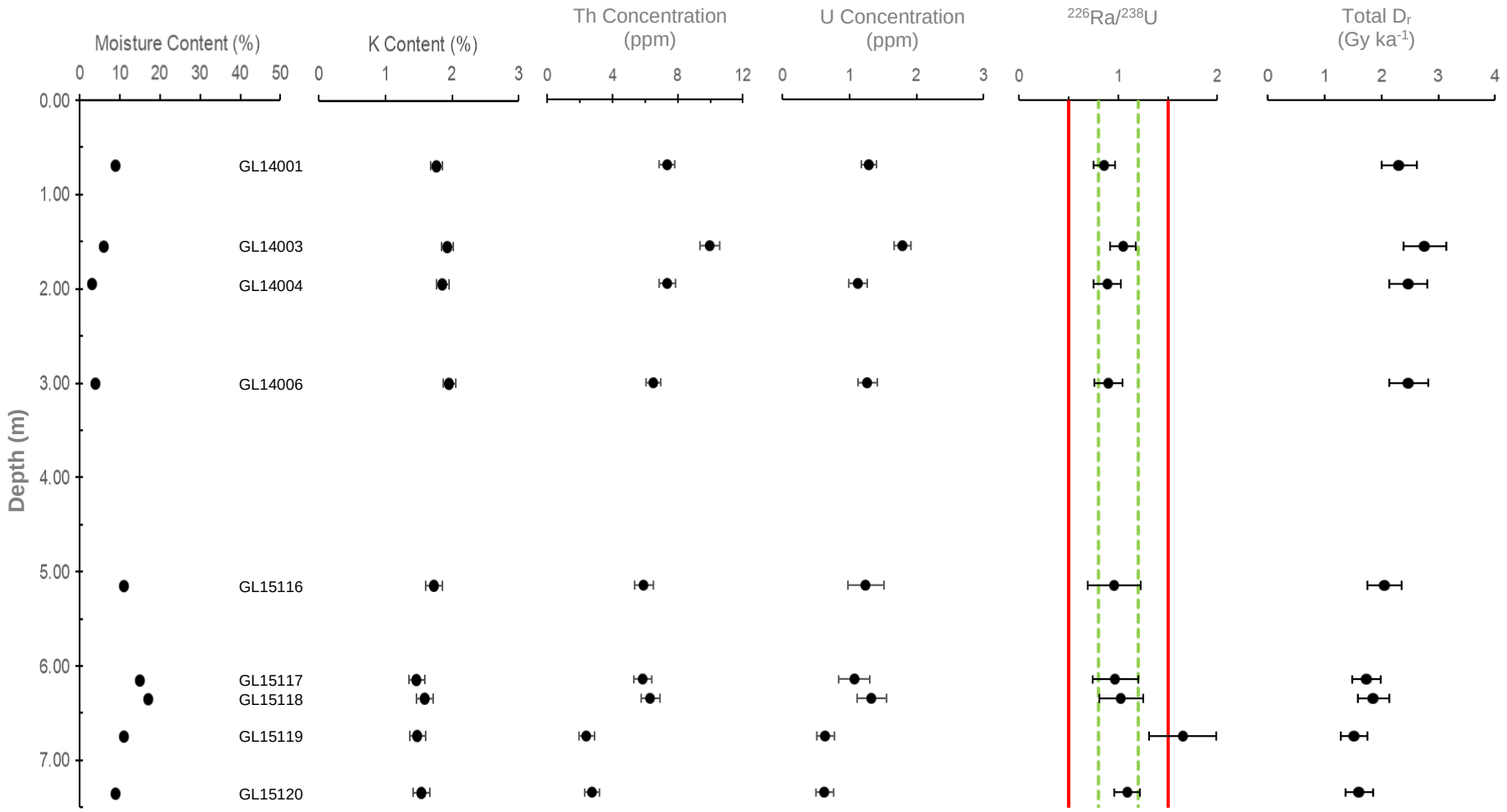


**Figure 5.3.11:** Key variables used for UCOSP $D_r$ calculation. $^{226}Ra/^{238}U$ ratios are presented for assessment of U-series disequilibria - 20% (green/dashed line) and 50% (red/solid line) margins highlighted.

**Table 5.3.5:** Summary of UCOSP dosimetry data

| Sample | Depth (m) | Grain Fraction (μm) | Moisture Content (%) | Radionuclide Content | | | | $D_r$ Components (Gy $ka^{-1}$) | | | Total $D_r$ (Gy $ka^{-1}$) |
|---|---|---|---|---|---|---|---|---|---|---|---|
| | | | | K (%) | Th (ppm) | U (ppm) | $^{226}Ra/^{238}U$ | β | γ | Cosmic | |
| GL14001 | 0.69 | 180-250 | 9 | 1.77±0.09 | 7.35±0.48 | 1.29±0.10 | 0.86±0.11 | 1.27±0.26 | 0.85±0.17 | 0.18±0.01 | 2.31±0.31 |
| GL14003 | 1.55 | 180-250 | 6 | 1.93±0.09 | 9.98±0.59 | 1.79±0.11 | 1.05±0.13 | 1.51±0.31 | 1.09±0.22 | 0.16±0.01 | 2.76±0.38 |
| GL14004 | 1.95 | 180-250 | 3 | 1.86±0.09 | 7.37±0.49 | 1.13±0.09 | 0.89±0.14 | 1.40±0.29 | 0.91±0.19 | 0.16±0.01 | 2.47±0.34 |
| GL14006 | 3.00 | 180-250 | 4 | 1.96±0.09 | 6.51±0.46 | 1.27±0.09 | 0.90±0.14 | 1.44±0.30 | 0.90±0.18 | 0.14±0.01 | 2.48±0.35 |
| GL15116 | 5.15 | 180-250 | 11 | 1.73±0.13 | 5.93±0.58 | 1.24±0.15 | 0.96±0.27 | 1.19±0.25 | 0.76±0.16 | 0.11±0.01 | 2.06±0.30 |
| GL15117 | 6.15 | 180-250 | 15 | 1.47±0.12 | 5.87±0.56 | 1.07±0.17 | 0.97±0.23 | 0.98±0.21 | 0.66±0.14 | 0.10±0.01 | 1.74±0.25 |
| GL15118 | 6.35 | 180-250 | 17 | 1.59±0.12 | 6.33±0.59 | 1.33±0.17 | 1.03±0.22 | 1.06±0.22 | 0.71±0.15 | 0.09±0.01 | 1.86±0.27 |
| GL15119 | 6.75 | 180-250 | 11 | 1.48±0.12 | 2.41±0.49 | 0.64±0.13 | 1.65±0.34 | 0.93±0.20 | 0.50±0.11 | 0.09±0.01 | 1.52±0.23 |
| GL15120 | 7.35 | 180-250 | 9 | 1.54±0.12 | 2.74±0.46 | 0.63±0.13 | 1.09±0.13 | 0.99±0.21 | 0.53±0.11 | 0.08±0.01 | 1.61±0.24 |

*5.3.5. Selection of Modelled $D_e$ and Age Calculation*

The UCOSP section samples provided the opportunity to test OSL upon known-age deposits. The four most significant flood events documented upon the catchment by the Umfolozi Sugar Mill (2015) occurred in 1918, 1925, 1963 and 1984 (Domoina). Section samples collected from the deposits at the UCOSP site would be expected to bracket some of these events. To produce the OSL ages presented in Table 5.3.6 all modelled $D_e$ values were divided by the average $D_r$ and associated errors were combined in quadrature. Ages are interpreted using statistical measures (OD, skewness and proportion of zero-dose grains), stratigraphic order, the consistency between calculated age models (Figure 5.3.12) and the known-age of flood events impacting the catchment (See Figure 5.2.21).

GL14001 was collected from a unit deposited by the floodwaters created by Tropical Storm Domoina in 1984 (0.03 ka). The significant positive skew and long-tail of the $D_e$ distribution are likely symptomatic of partial-bleaching. The proportion of zero-dose grains is small (<8%) and given that all samples were collected from below 0.6 m, pedoturbation and the interaction with surface sediments can be ruled out. The presence of zero-dose grains could indicate low $D_r$ regions within the sediment matrix, however, given the relatively short burial time, the significance of microdosimetry is likely to be minimal for all of the known age flood units. Adopting central measures of $D_e$ and all dose populations identified by the FMM results in an overestimation of age for GL14001, the magnitude of overestimation is significantly greater when central measures of $D_e$ are used. Use of MAM produces an age of 31 ± 7 years resulting in a calendar year age bracket of AD 1976-1990 which encapsulates the flood event associated with Domoina. Whilst MAM correctly identifies an age for GL14001, it has an ability to underestimate age for heterogeneously bleached sediments (Rodnight *et al.,* 2006). If this unit was of unknown age $FMM_{min}$ is likely to be selected as it falls between CAM and MAM. Selection of this $D_e$ component overestimates age and produces a calendar year age bracket of AD 1941-1959. In this instance it could be by chance that MAM successfully isolates to correct age.

GL14003 was collected from the unit associated with the 1963 (0.05 ka) flood. The $D_e$ distribution for this sample also had a strong positive skewness indicating the material has been partially-bleached. Central $D_e$ estimates overestimate expected age, but the magnitude of overestimation is less than that observed for GL14001. $FMM_{min}$ produces an age of 50 ± 8 years and a calendar year age bracket of AD 1956-1972 thus successfully estimating the age of the deposit. However, it is important to note that if MAM were adopted the accompanying age bracket (AD 1976-1984) would not incorporate the 1963 event and the unit could instead be interpreted as an additional phase of flooding induced by the 1984 floods.

Statistically consistent ages were produced for GL14004 when the median, MAM and $FMM_{min/maj}$ $D_e$ values were adopted. MAM produces an age of 76 ± 12 years (AD 1926-1950), slightly underestimating the age of the deposit associated with the 1925 (0.09 ka) floods. $FMM_{min}$ and $FMM_{maj}$ account for 69% of all $D_e$ values producing an age of 80 ± 12 years (AD 1922-1945), thus bracketing the actual age of the samples. $FMM_{min}$ and $FMM_{maj}$ ages are also statistically indistinct from CAM suggesting heterogeneously bleached samples do not always require age modelling. The median (AD 1906-1952) is also consistent with the age of the deposit, however, the error margins are much larger for this estimate. The impact of partial bleaching appears less significant for GL14004 relative to the samples situated higher in the section, the sample has lower OD and there are fewer high-dose grains. As with GL14003, zero-dose grains are attributed to microdosimetry and low-$D_r$ regions within the sediment matrix owing to the depth of the sample.

For the final known age deposit (GL14006) use of the FMM was again most suited to isolating the correct age. Using the $D_e$ for $FMM_{min}$ an OSL age of 99 ± 15 years (AD 1900-1930) is produced, however this envelope covers both the 1918 (*c.* 0.10 ka) and 1925 floods. Central $D_e$ values result in an overestimation of age, whilst MAM produces a younger age than $FMM_{min}$ but still encapsulates the known age of the deposit.

Most ages for the UCOSP section support the findings of Rodnight *et al.* (2006) whereby MAM tends to underestimate age whilst CAM overestimates

age for heterogeneously bleached sediments. For most of the UCOSP section samples $FMM_{min}$ appears to be the most suited to isolating a $D_e$ that falls between CAM and MAM, resulting in the estimation of a correct age. Despite MAM calculating the correct age for the most recent large flood event (1984), the coupling of MAM $D_e$ with mean $D_r$ is not considered suitable for the partially bleached samples explored here. Given the errors associated with each of the known-age samples, it is likely that the chronology for samples extending back into the Holocene will be limited to a centennial resolution and phases of frequent flooding are likely to be observed as clusters of statistically consistent ages.

Despite a 24% difference in OD, visually the two uppermost samples from the UCOSP core produce a similar $D_e$ distribution. They appear to have a dominant grain population with a small number of high-dose grains which make up the high-dose tail and produce the positive skew. Partial bleaching appears to have had less of an effect upon the observed $D_e$ distributions relative to other samples from the site. Excluding $FMM_{max}$, all ages produced are statistically consistent across the age models for GL15116 and GL15117. Although the decision process used for age model selection in this study (Figure 5.2.21) suggests that CAM should be used for GL15116, given the success of FMM in isolating $D_e$ values for section samples, $FMM_{min}$ is adopted for age calculation accounting for 67% of values and producing an age of 184 ± 27 years. GL15117 has low OD (23%) and FMM confirmed the presence of a single significant ($p$ = 92%) $D_e$ component, CAM is therefore selected for age calculation producing an age of 807 ± 118 years.

The remaining samples from the UCOSP core all displayed similar $D_e$ distributions with significant OD (46-60%) and positive skewness. Whilst partial bleaching is attributed to some of the observed OD for all UCOSP samples given their waterlain origin, further significant contributors are believed to be responsible for the OD observed for GL15118 to GL15120. The effect of partial bleaching upon $D_e$ distributions is expected to lessen with burial time (Rittenour, 2008) as residual doses become less statistically significant with growth in $D_e$. However, for the UCOSP samples of unknown age CAM and MAM ages diverge with an increase in depth, as do ages

calculated using $FMM_{min}$ and $FMM_{max}$ (Figure 5.3.12). From GL15117 to GL15120 there is a systematic increase in the difference between CAM and MAM ages, with age discrepancies increasing from 0.05 to 1.00 ka. For $FMM_{min}$ and $FMM_{max}$ the differences in age are more significant, rising from 0 to 5.59 ka for the same sample range. The divergence of ages can be attributed to microdosimetry and the dose rate multiplier effect. In such instances the $D_e$ for grains within low $D_r$ regions becomes further separated from those in high $D_r$ regions (hotspots) with increased burial time.

The drop in radionuclide concentration and $D_r$ for the lower three samples suggests there may also be some mobility within the sequence, particularly given the excess $^{226}Ra$ and potential for U-series disequilibrium observed for GL15119. This makes selection of appropriate age for samples GL15118 to GL15120 complex as it is not possible to separate the relative contributions of microdosimetry, temporal shifts in $D_r$ and partial bleaching to the observed $D_e$ distributions. Given the complexities associated with these samples, $FMM_{maj}$ was deemed to be the most appropriate model for age calculation as it isolates the $D_e$ component which satisfies most of the $D_e$ population ($p$ = 36 to 49%). For all three samples $FMM_{maj}$ falls between CAM and MAM, for GL15119 and GL15120 it is also the same component used for $FMM_{min.}$ Ages of 1.09±0.17 (1087±166 years), 1.04±0.24 (1042±169 years) and 1.58±0.24 ka (1583±242 years) are calculated for GL15118, GL15119 and GL15120 respectively. All ages satisfy stratigraphic consistency, however, each estimate should be used cautiously given the complexities associated with both $D_e$ and $D_r$.

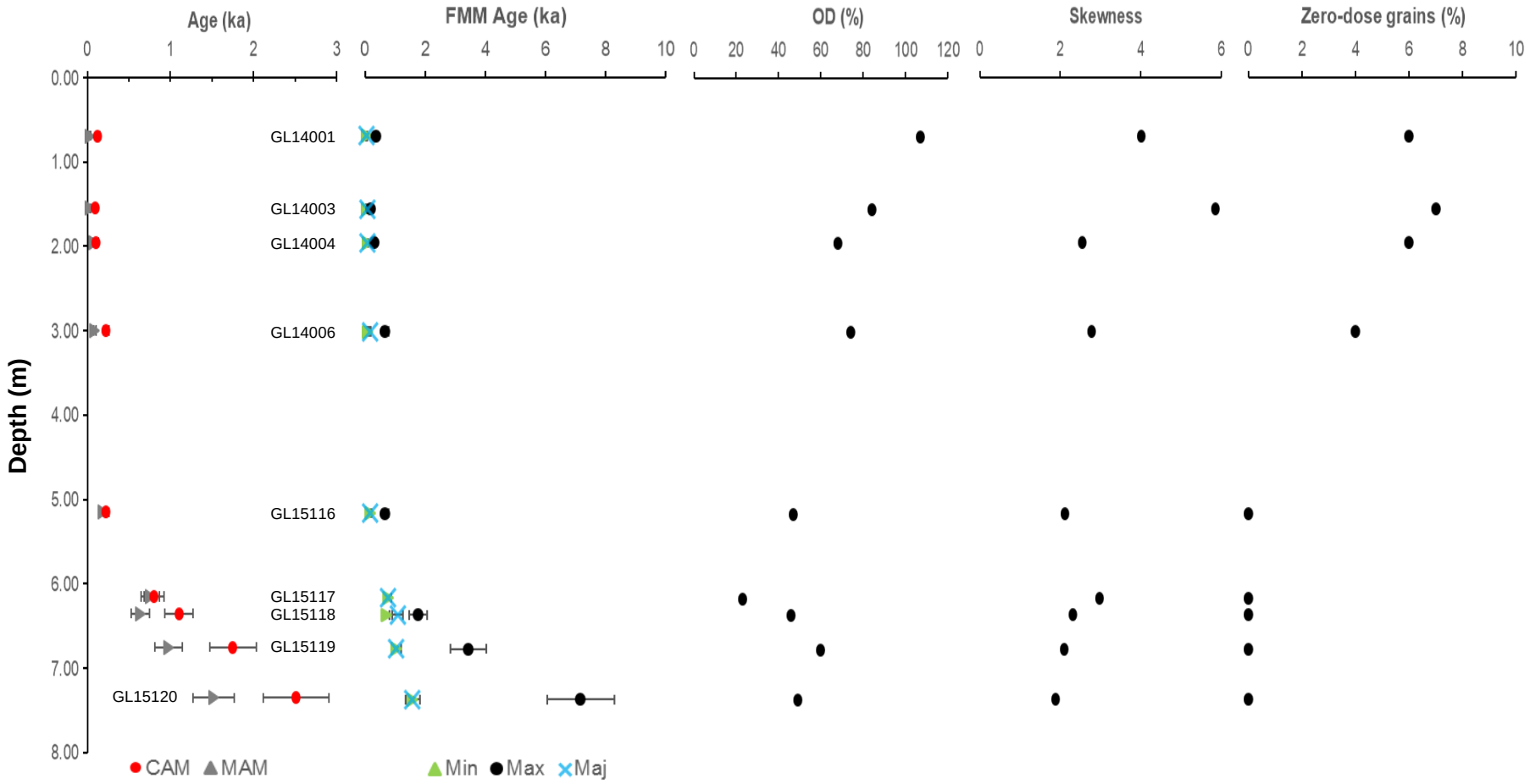


**Figure 5.3.12:** Modelled quartz OSL ages and key statistical parameters used to assist with selection of $D_e$ for UCOSP samples.

**Table 5.3.6:** Summary UCOSP quartz OSL ages (all reported with 1σ confidence and relative to sampling year 2014) – suggested age models for use in Chapter 6 Bayesian models.

| Sample | Depth (m) | Age (ka) | | | | | | Known Age (ka) | Suggested Age Model/s |
|---|---|---|---|---|---|---|---|---|---|
| | | Median | CAM | MAM | $FMM_{min}$ | $FMM_{max}$ | $FMM_{maj}$ | | |
| GL14001 | 0.69 | 0.10±0.04 | 0.13±0.02 | 0.03±0.01 | 0.06±0.01 | 0.37±0.06 | 0.06±0.01 | 0.03 | MAM |
| GL14003 | 1.55 | 0.08±0.03 | 0.10±0.02 | 0.04±0.01 | 0.05±0.01 | 0.19±0.03 | 0.09±0.01 | 0.05 | $FMM_{min}$ |
| GL14004 | 1.95 | 0.08±0.02 | 0.11±0.02 | 0.08±0.01 | 0.08±0.01 | 0.31±0.05 | 0.08±0.01 | 0.09 | $FMM_{min}$ |
| GL14006 | 3.00 | 0.18±0.04 | 0.23±0.04 | 0.09±0.01 | 0.10±0.01 | 0.68±0.10 | 0.17±0.02 | 0.10 | $FMM_{min}$ |
| GL15116 | 5.15 | 0.20±0.03 | 0.23±0.03 | 0.19±0.03 | 0.18±0.03 | 0.68±0.10 | 0.18±0.03 | Unknown | $FMM_{min}$ |
| GL15117 | 6.15 | 0.78±0.12 | 0.81±0.12 | 0.76±0.11 | 0.77±0.11 | 0.77±0.11 | 0.77±0.11 | Unknown | CAM |
| GL15118 | 6.35 | 1.04±0.17 | 1.10±0.17 | 0.64±0.11 | 0.71±0.11 | 1.77±0.29 | 1.09±0.17 | Unknown | $FMM_{maj}$ |
| GL15119 | 6.75 | 1.53±0.28 | 1.75±0.28 | 0.98±0.17 | 1.04±0.17 | 3.43±0.60 | 1.04±0.17 | Unknown | $FMM_{maj}$ |
| GL15120 | 7.35 | 2.30±0.38 | 2.51±0.39 | 1.52±0.25 | 1.58±0.24 | 7.17±1.12 | 1.58±0.24 | Unknown | $FMM_{maj}$ |

Incorporation of all OSL ages into a simple age-depth plot (Figure 5.3.13) shows that ages from the UCOSP sequence fall in stratigraphic order, providing a flood record spanning the past c. 1.6 ka. Deposition of flood units appears to have been most frequent over the last *c.* 200 years with six events being observed, whilst for the four lowermost flood units event frequency appears reduced with ages spanning *c.* 800 years. Despite microdosimetry, temporal variations in $D_r$ and partial bleaching causing issues for interpretation of GL15118 to GL15120, age estimates appear sensible relative to the stratigraphy and other age estimates. However, GL15119 (6.75 m) does appear slightly offset and slight underestimation could have been created by U-series disequilibrium.

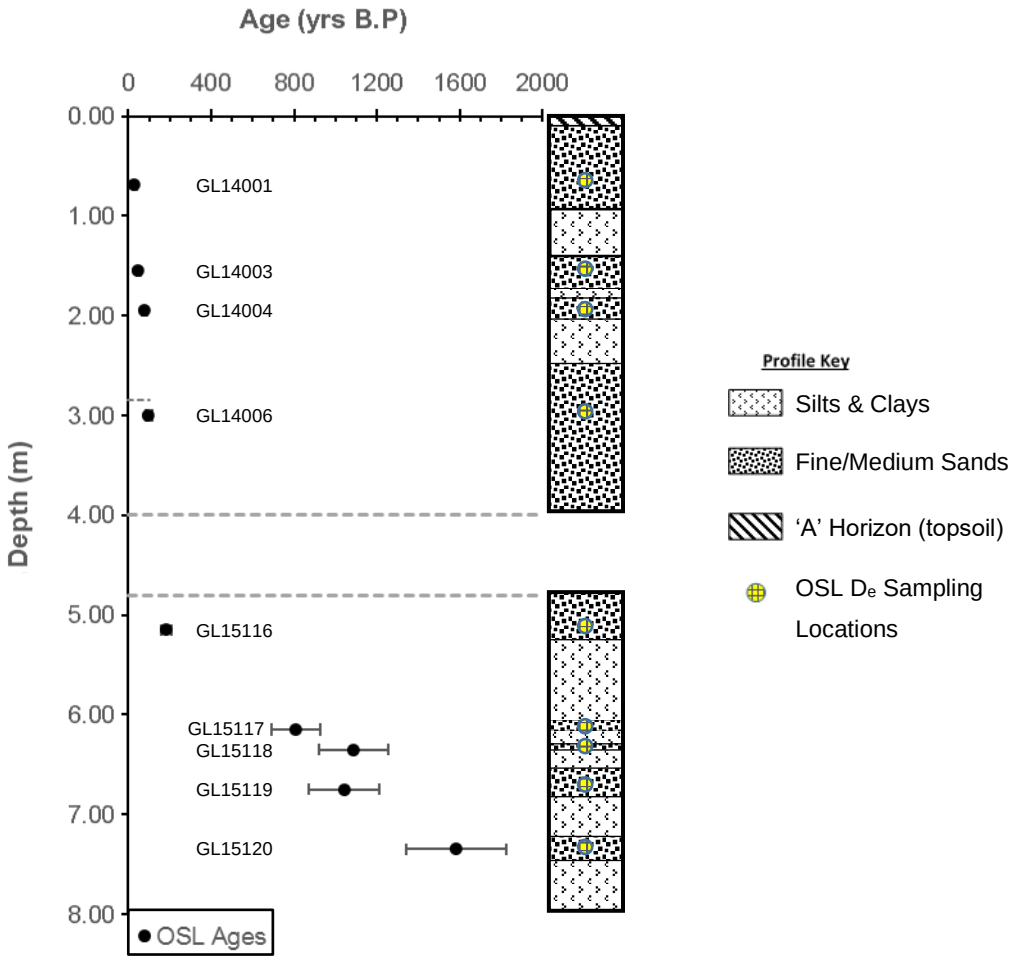


**Figure 5.3.13:** Quartz OSL ages adopted for the UCOSP sequence (all ages reported with 1σ confidence; dashed lines represent the region between the section and the top of the core sample).

## 5.4. Futululu

### *5.4.1. Sample Overview*

Samples from the Futululu site were collected from a crevasse splay feature which had encroached onto the blocked-valley lake basin via a channel upon the Mfolozi floodplain. Five sand beds, interpreted as avulsion events which had occurred during periods of significant flooding were sampled for OSL dating (Table 5.4.1). Single-grain $D_e$ analysis was conducted on two samples (GL15122 & GL15123) whilst 8 mm aliquots were prepared for Multi-Grain $D_e$ analysis of samples dominated by the 90-125 µm quartz fraction (GL15124-6).

**Table 5.4.1:** Futululu sample details

| Sample | Depth (m) | Moisture Content (%) | Grain Fraction (µm) | Single-Grain/Aliquot |
|---|---|---|---|---|
| GL15122 | 0.75 | 11 | 180-250 | Single-Grain |
| GL15123 | 1.67 | 16 | 125-180 | Single-Grain |
| GL15124 | 2.77 | 16 | 90-125 | Multi-Grain |
| GL15125 | 2.90 | 18 | 90-125 | Multi-Grain |
| GL15126 | 3.82 | 22 | 90-125 | Multi-Grain |

### *5.4.2. Initial OSL Signal Evaluation and Dose-Recovery Results*

Figure 5.4.1 provides an example of the data acquired from the initial measurements for GL15122. An $L_x/T_x$ ratio of 0.166 was produced for a test aliquot following measurement of the natural and a 5 Gy test dose (a), this indicated that an appropriate artificial dose for the subsequent dose recovery test (b) was 0.8 Gy. Dose-recovery tests were conducted upon all Futululu samples and the recovered ratio x-y plots for all of these are presented in Appendix C (Figures C4.1). A summary of the dose-recovery test results is presented in Table 5.4.2.

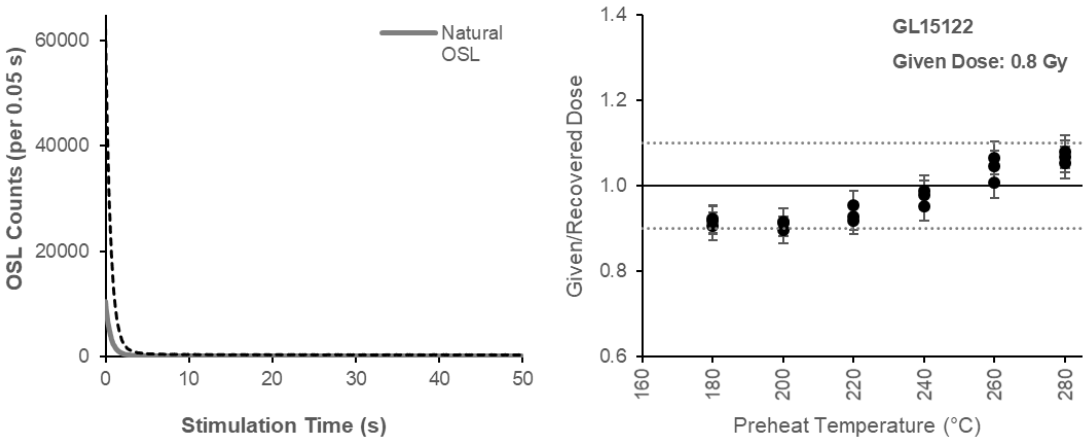


**Figure 5.4.1:** Test disc natural/5 Gy test OSL signal and 0.8 Gy dose-recovery test for GL15122

All Futululu samples successfully recovered known doses during dose-recovery tests, with all given/recovered dose ratios consistent with unity. The most appropriate preheat temperatures isolated for SAR $D_e$ acquisition were 240 and 260°C. A cut heat of 220°C was used for all samples. Material availability limited the number of aliquots used for the dose-recovery tests of GL15124.

**Table 5.4.2:** Futululu test disc and dose-recovery test result summary

| Sample | Test Disc $L_x/T_x$ | Given Dose (Gy) | Selected Preheat (°C) | Given/Recovered Dose Ratio* |
|---|---|---|---|---|
| GL15122 | 0.166 | 0.8 | 240 | 0.97 ± 0.04 |
| GL15123 | 0.306 | 1.5 | 260 | 1.00 ± 0.04 |
| GL15124 | 0.925 | 4.6 | 240 | *0.99 ± 0.04* |
| GL15125 | 1.199 | 6.0 | 240 | 1.00 ± 0.03 |
| GL15126 | 1.111 | 5.6 | 260 | 1.01 ± 0.04 |

*Given/Recovered Dose Ratio typically based on average of 3 aliquots per preheat – italicised values indicate only 1 aliquot available per preheat.

### *5.4.3. Single-Grain $D_e$ Results*

Single-grain analysis was undertaken upon two samples from the Futululu sequence, GL15122 and GL15123. A summary of $D_e$ results is provided in Table 5.4.4 whilst $D_e$ summary diagrams are presented for each of the samples in Figures 5.4.2 and 5.4.3. The $D_e$ components isolated by FMM and the proportion of grains within each are summarised in Table 5.4.3.

GL15122 is the uppermost sample from the sequence, its $D_e$ distribution appears normally distributed (Figure 5.4.2d) displaying minimal skew and OD (17%). All modelled $D_e$ values are statistically consistent (CAM = 0.51±0.01 Gy) and the OD indicates that the sample was well-bleached upon deposition and has remained undisturbed following burial.

The $D_e$ distribution for GL15123 has a significant OD value (39%) which is driven by the incorporation of numerous high-dose values. This has produced a distribution with a strong positive skew which features a slight high-dose tail. All modelled $D_e$ values, bar $FMM_{max}$ which identifies the high-dose population (1.31±0.11 Gy; *p* = 10%), are statistically consistent (CAM = 0.54±0.03 Gy). The high-dose tail of GL15123 could be attributed to partial bleaching.

Despite the differences in distribution, modelled central and minimum $D_e$ values are consistent for both samples. Depending on $D_r$, this could indicate that they were either deposited during a single flood event or, represent two closely spaced events. The observed consistency is fairly remarkable, particularly given the significant differences in OD.

**Table 5.4.3:** FMM components fitted to Futululu single-grain $D_e$ distributions (*k** = total components, σ = 0.15 (15%) and *p* = proportion of grains in each component)

| | | FMM Component | | | |
|---|---|---|---|---|---|
| | | ***k* = 1** | | ***k* = 2** | |
| **Sample** | ***k**** | **$D_e$ (Gy)** | ***p*** **(%)** | **$D_e$ (Gy)** | ***p*** **(%)** |
| GL15122 | 2 | 0.41±0.12 | 16 | 0.52±0.03 | 84 |
| GL15123 | 2 | 0.51±0.01 | 90 | 1.31±0.51 | 10 |

**Table 5.4.4:** Summary of Futululu single-grain $D_e$ analysis (errors reported within 1σ confidence; for age modelling σ = 0.15/15%)

| Sample | Depth (m) | Grains Accepted (Number (%))* | $\sigma_{OD}$ (%) | Skewness (c) | Kurtosis (*k*) | $D_e$ Values (Gy) | | | | | | |
|---|---|---|---|---|---|---|---|---|---|---|---|---|
| | | | | | | Median | CAM | MAM | FMM *k*** | $FMM_{min}$ | $FMM_{max}$ | $FMM_{maj}$ |
| GL15122 | 0.75 | 80 (8.0) | 17 | 0.47 | 3.41 | 0.51±0.02 | 0.51±0.01 | 0.47±0.03 | 2 | 0.41±0.12 | 0.52±0.03 | 0.52±0.03 |
| GL15123 | 1.67 | 77 (7.7) | 39 | 2.09 | 7.79 | 0.51±0.03 | 0.54±0.03 | 0.48±0.02 | 2 | 0.51±0.01 | 1.31±0.11 | 0.51±0.01 |

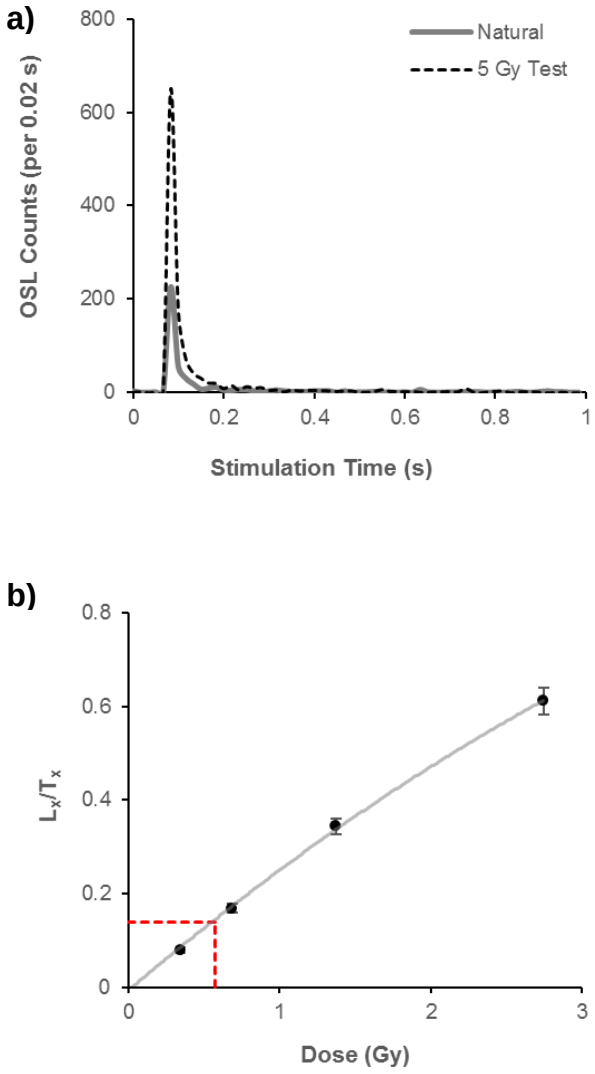


**Figure 5.4.2:** Single-grain $D_e$ summary diagrams for GL15122

a) Example single-grain decay curves for the natural and 5 Gy test dose signals of grain 29.

b) Dose-response curve for grain 29 with regenerative doses; 0, 0.3, 0.7, 1.4, & 2.7 Gy. Interpolation of the natural $L_x/T_x$ recovered a $D_e$ of 0.57 Gy.

c) Radial plot of 80 $D_e$ values which passed rejection criteria. Coloured areas represent age models applied to the $D_e$ dataset; CAM (**red**), MAM (**grey**), $FMM_{min}$ (**green**) and $FMM_{maj}$ (**blue**). $FMM_{max}$ is equivalent to $FMM_{maj}$.

d) Histogram of De values with bin width 0.1. Dataset displays minimal skew (c). No zero-dose grains.

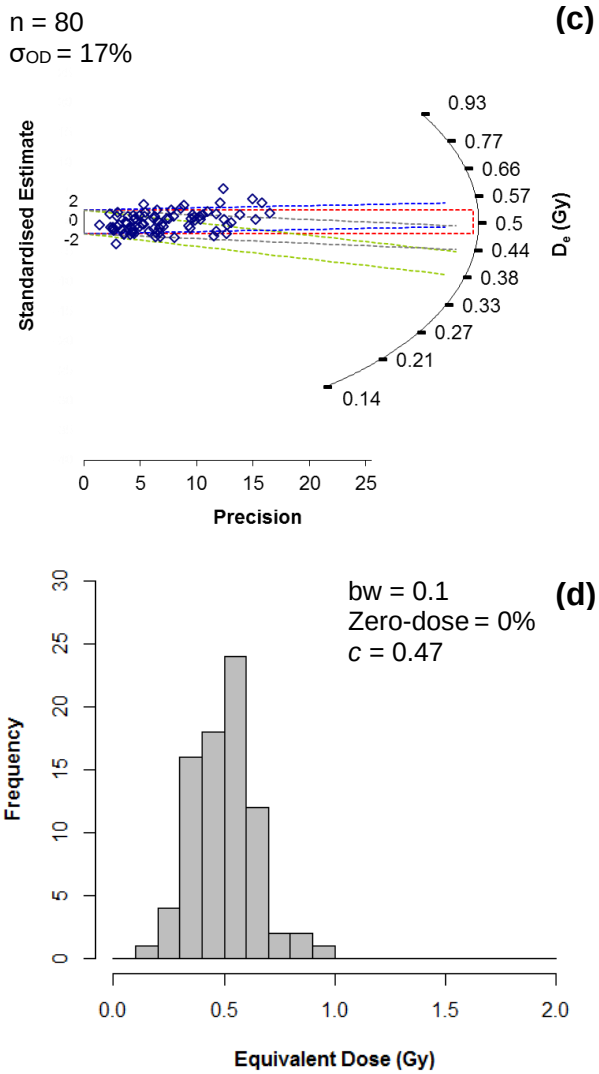

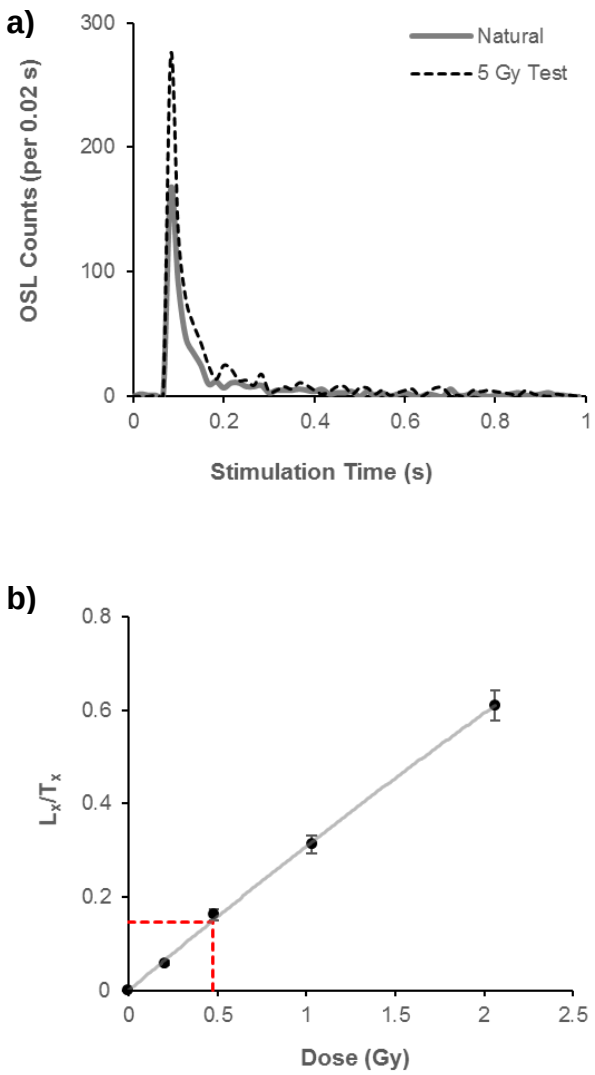


**Figure 5.4.3:** Single-grain $D_e$ summary diagrams for GL15123

a) Example single-grain decay curves for the natural and 5 Gy test dose signals of grain 24.

b) Dose-response curve for grain 24 with regenerative doses; 0, 0.2, 0.5, 1.0 & 2.1 Gy. Interpolation of the natural $L_x/T_x$ recovered a $D_e$ of 0.47 Gy.

c) Radial plot of 77 $D_e$ values which passed rejection criteria. Coloured areas represent age models applied to the $D_e$ dataset; CAM (**red**), MAM (**grey**), $FMM_{min}$ (**green**) and $FMM_{maj}$ (**blue**). $FMM_{max}$ is equivalent to 1.31 Gy.

d) Histogram of De values with bin width 0.1. Data is highly positively skewed (c). No zero-dose grains.

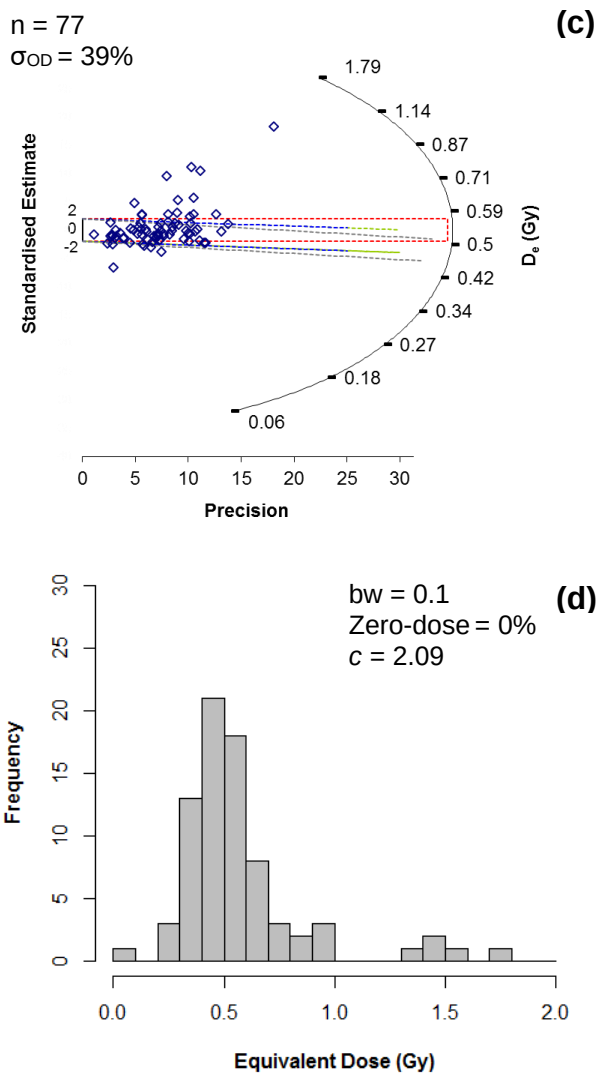

### *5.4.4. Multi-Grain $D_e$ Results*

$D_e$ results for the three multi-grain samples taken from the Futululu site are summarised in Table 5.4.5, whilst $D_e$ summary diagrams are presented in Figures 5.4.4 to 5.4.6. For all samples only $D_e$ values obtained for the CAM are considered to avoid the identification of phantom dose populations (Arnold *et al.,* 2012). Stimulation had to be reduced to 15% power for all measurements because of the intensity of the natural and laboratory-dosed OSL signal.

**Table 5.4.5:** Summary of Futululu multi-grain $D_e$ analysis (errors reported within 1σ confidence; for MAM σ = 0.15/15%)

| Sample | Depth (m) | Aliquots (n) | $\sigma_{OD}$ (%) | $D_e$ Values (Gy) | |
|---|---|---|---|---|---|
| | | | | Median | CAM |
| GL15124 | 2.77 | 12 | 23 | 4.52±0.30 | 4.38±0.30 |
| GL15125 | 2.90 | 48 | 21 | 4.74±0.20 | 4.98±0.15 |
| GL15126 | 3.82 | 48 | 18 | 4.91±0.14 | 4.98±0.13 |

Only 12 aliquots were measured for GL15124 $D_e$ acquisition (Figure 5.4.4) owing to limited sample mass. All aliquots produced recycling ratios consistent with unity and no IRSL depletion was detected. $D_e$ values were 23% OD with statistically consistent median and CAM. No increase in $D_e$ was observed with an increase in stimulation time, suggesting aliquots are not partially-bleached.

CAM $D_e$ values isolated for GL15125 (Figure 5.4.5) and GL15126 (Figure 5.4.6) are statistically consistent (4.98 Gy) and some OD is observed for both samples. All aliquots produced recycling ratios consistent with unity and no IRSL depletion was detected. Signal analysis provided no indication of partial bleaching.

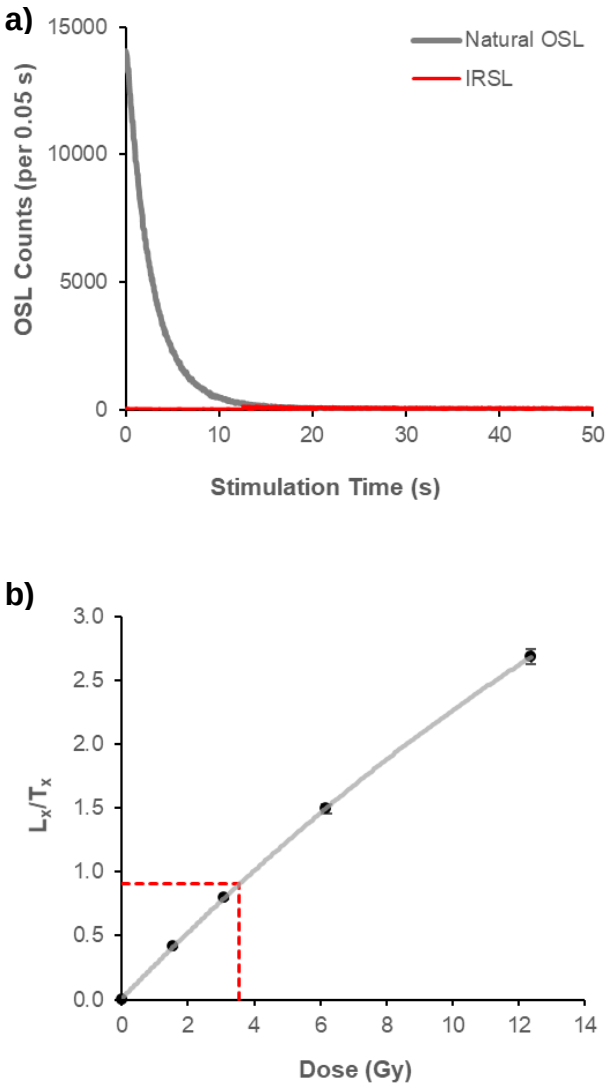


**Figure 5.4.4:** Multi-grain $D_e$ summary diagrams for GL15124

a) Example multi-grain decay curves for the natural OSL signal plus the IRSL signal following a 1.5 Gy regenerative dose.

b) Dose-response curve for aliquot 5 with regenerative doses; 0, 1.5, 3.1, 6.2 & 12.4 Gy. Interpolation of the natural $L_x/T_x$ recovered a $D_e$ of 3.55 Gy.

c) Rank order plot for 12 $D_e$ values obtained for multi-grain aliquots of 90-125 μm quartz. Coloured area represents CAM (**red**).

d) An example $D_e(t)$ plot for a natural signal. Absence of a significant rise in $D_e$ with increased illumination time indicates the sample is fully-bleached.

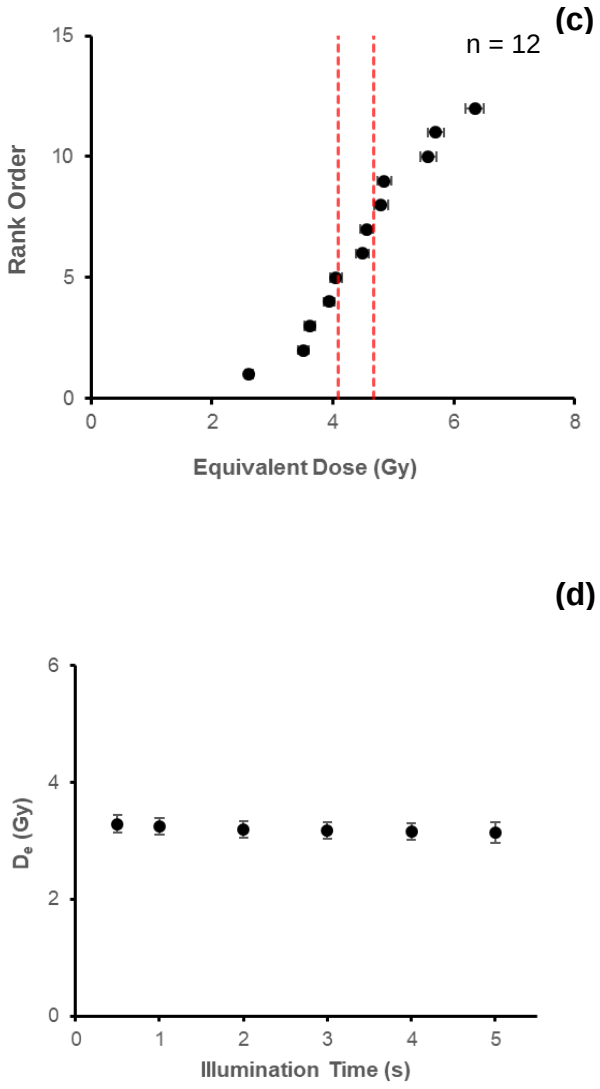

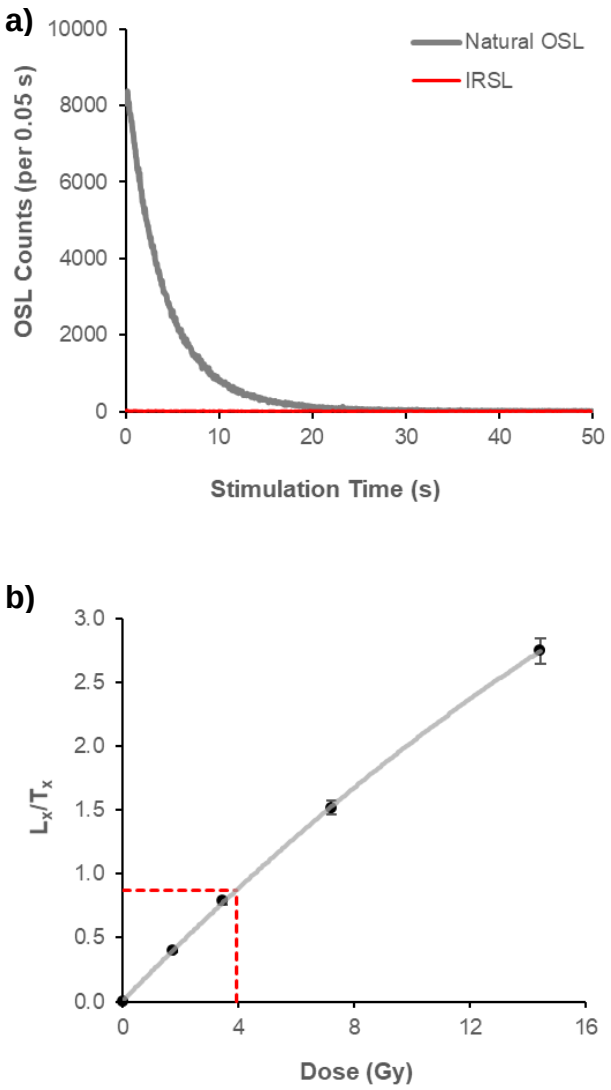


**Figure 5.4.5:** Multi-grain $D_e$ summary diagrams for GL15125

a) Example multi-grain decay curves for the natural OSL signal plus the IRSL signal following a 1.7 Gy regenerative dose.

b) Dose-response curve for aliquot 1 with regenerative doses; 0, 1.7, 3.5, 7.2 & 14.4 Gy. Interpolation of the natural $L_x/T_x$ recovered a $D_e$ of 3.91 Gy.

c) Rank order plot for 48 $D_e$ values obtained for multi-grain aliquots of 90-125 µm quartz. Coloured area represents CAM (**red**).

d) An example $D_e(t)$ plot for a natural signal. Absence of a significant rise in $D_e$ with increased illumination time indicates the sample is fully-bleached.

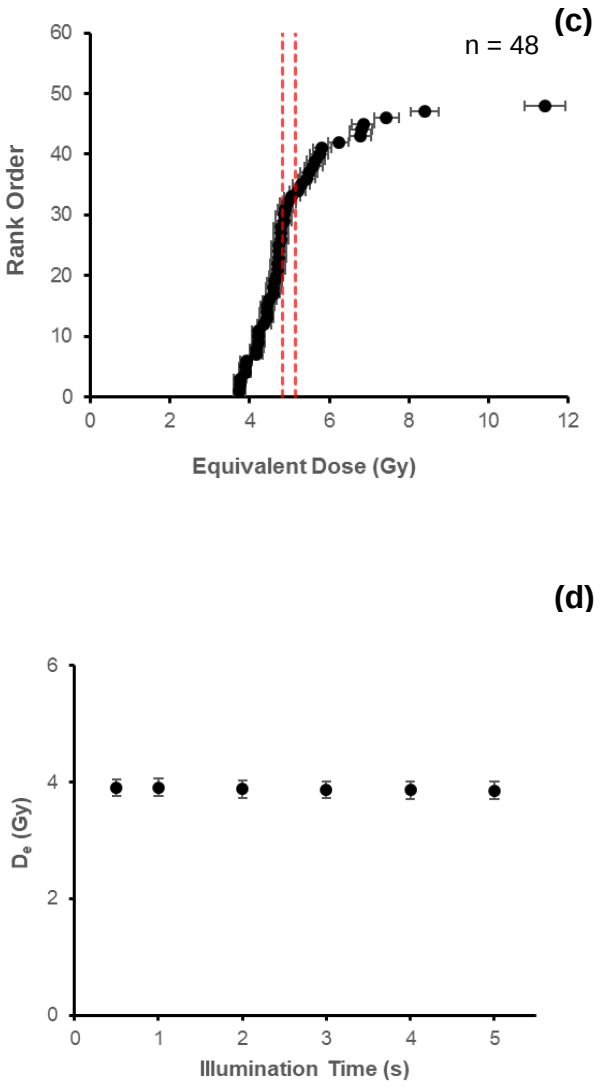

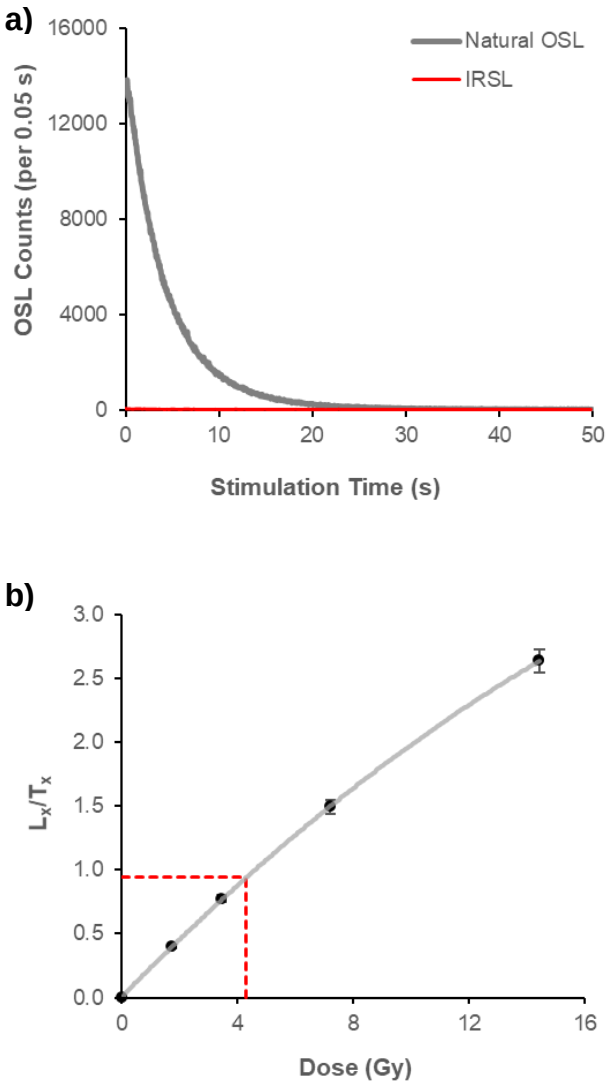


**Figure 5.4.6:** Multi-grain $D_e$ summary diagrams for GL15126

a) Example multi-grain decay curves for the natural OSL signal plus the IRSL signal following a 1.7 Gy regenerative dose.

b) Dose-response curve for aliquot 25 with regenerative doses; 0, 1.7, 3.5, 7.2 & 14.4 Gy. Interpolation of the natural $L_x/T_x$ recovered a $D_e$ of 4.43 Gy.

c) Rank order plot for 48 $D_e$ values obtained for multi-grain aliquots of 90-125 µm quartz. Coloured area represents CAM (**red**).

d) An example $D_e(t)$ plot for a natural signal. Absence of a significant rise in $D_e$ with increased illumination time indicates the sample is fully-bleached.

### *5.4.5. Dosimetry*

The overall $D_r$ for Futululu samples displays minimal variation throughout the sequence (Table 5.4.6; Figure 5.4.7), all values are statistically consistent with average total $D_r$ values ranging from 2.32 to 2.39 Gy $ka^{-1}$. Each estimate has an uncertainty of *c.* 14%.

There is an increase in moisture content with depth from 11 to 22%. Minimal variability is observed in estimated radionuclide concentration, with concentration ranges of; 1.53 to 1.89% for K, 7.94 to 9.53 ppm for Th and 1.72 to 2.17 ppm for U. Many of the radionuclide concentrations are statistically consistent, which would be expected given the similar $D_r$. All $^{226}Ra/^{238}U$ fall within 10% of unity indicating U-series disequilibrium should not present an issue for the Futululu samples.

### *5.4.6. Selection of Modelled $D_e$ and Age Calculation*

All ages produced for the Futululu site are presented in Table 5.4.7. Modelled $D_e$ values were divided by the average $D_r$ and associated errors were combined in quadrature.

GL15124, GL15125 and GL15126 were taken from the earliest material deposited on the Futululu site. Ages calculated using CAM are statistically consistent and represent three closely spaced depositional events occurring between 1.89 and 2.10 ka. Although OD was *c.* 20% for each of the samples, the smaller grain size coupled with the use of multi-grain aliquots would suggest that a higher OD could be expected at the single grain level. However, this does not necessarily indicate that CAM is unsuitable for isolation of the correct age, as demonstrated at the UCOSP site (GL14004). The fluvial origin of samples would suggest that partial bleaching has contributed to some of the observed OD. $D_e(t)$ plots did not display a significant rise in $D_e$ with stimulation time, but as highlighted in section 5.2.6 numerous factors contribute to the form of a $D_e(t)$ plot and the lack of a rise in $D_e$ with stimulation time cannot be used to confirm the absence of partial bleaching.

Single-grain measurements for GL15123 produced a highly skewed $D_e$ distribution featuring a high-dose tail. Such distributions can be attributed to partial bleaching or the incorporation of older material through post-depositional reworking. All age models apart from $FMM_{max}$, produced statistically consistent ages, despite the elevated the OD observed for GL15123. CAM is therefore adopted producing an age of 0.23±0.03 ka.

The uppermost sample GL15122 displays minimal OD and produces a $D_e$ distribution which is unimodal and appears symmetric. All adopted age models produce $D_e$ values which are statistically consistent. CAM is suggested for age calculation resulting in an age of 0.22±0.03 ka, this is statistically consistent with the age produced for GL15123.

The Futululu sequence spans *c.* 2.10 ka and age estimates produced for sand beds preserved within the sedimentology indicate that the crevasse splay feature has experienced two main phases of deposition at *c.* 2.00 and 0.22 ka. Incorporation of all OSL ages into a simple age-depth plot (Figure 5.4.8) highlights these two distinct phases. The preservation of sand beds suggests that phases of encroachment onto the blocked-valley lake basin are comprised of multiple events or ‘pulses’ which occurred over relatively short timescales.

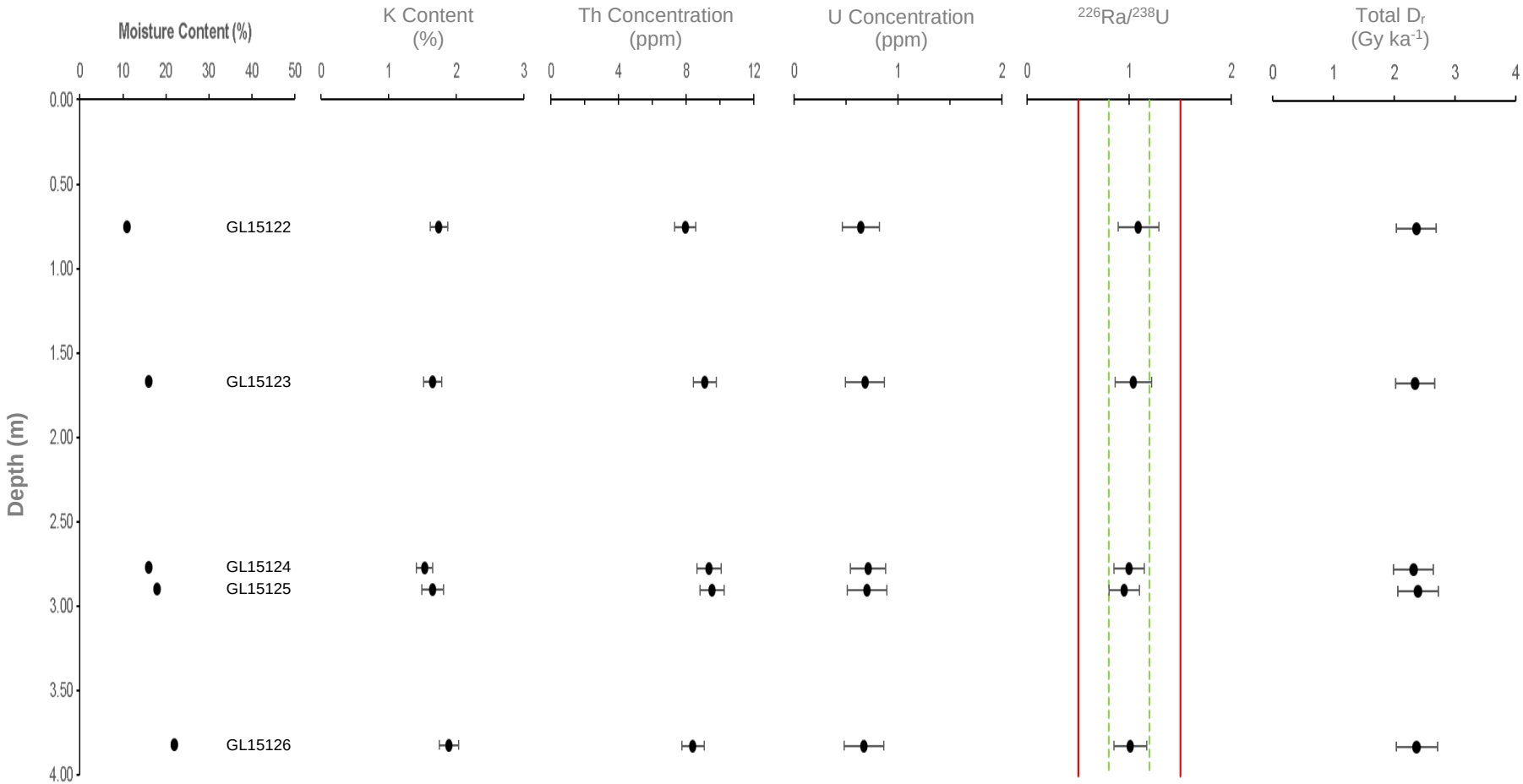


**Figure 5.4.7:** Key variables used for Futululu $D_r$ calculation. $^{226}Ra/^{238}U$ ratios are presented for assessment of U-series disequilibria - 20% (green/dashed line) and 50% (red/solid line) margins highlighted.

**Table 5.4.6:** Summary of Futululu dosimetry data

| Sample | Depth (m) | Grain Fraction (μm) | Moisture Content (%) | Radionuclide Content | | | | $D_r$ Components (Gy $ka^{-1}$) | | | Total $D_r$ (Gy $ka^{-1}$) |
|---|---|---|---|---|---|---|---|---|---|---|---|
| | | | | K (%) | Th (ppm) | U (ppm) | $^{226}Ra/^{238}U$ | β | γ | Cosmic | |
| GL15122 | 0.75 | 180-250 | 11 | 1.74±0.13 | 7.94±0.64 | 1.72±0.18 | 1.09±0.20 | 1.28±0.27 | 0.89±0.19 | 0.18±0.01 | 2.36±0.33 |
| GL15123 | 1.67 | 125-180 | 16 | 1.65±0.13 | 9.09±0.68 | 2.00±0.19 | 1.04±0.18 | 1.27±0.27 | 0.91±0.19 | 0.16±0.01 | 2.34±0.33 |
| GL15124 | 2.77 | 90-125 | 16 | 1.53±0.12 | 9.35±0.71 | 2.07±0.17 | 1.00±0.15 | 1.28±0.27 | 0.90±0.19 | 0.14±0.01 | 2.32±0.33 |
| GL15125 | 2.90 | 90-125 | 18 | 1.65±0.13 | 9.53±0.70 | 2.17±0.19 | 0.95±0.15 | 1.33±0.28 | 0.92±0.19 | 0.14±0.01 | 2.39±0.34 |
| GL15126 | 3.82 | 90-125 | 22 | 1.89±0.14 | 8.40±0.67 | 1.97±0.19 | 1.01±0.16 | 1.37±0.29 | 0.88±0.18 | 0.12±0.01 | 2.37±0.34 |



**Table 5.4.7:** Summary Futululu quartz OSL ages (all reported with 1σ confidence and relative to sampling year 2014) – suggested age models for use in Chapter 6 Bayesian models.

| Sample | Depth (m) | Age (ka) | | | | | | Suggested Age Model/s |
|---|---|---|---|---|---|---|---|---|
| | | Median | CAM | MAM | $FMM_{min}$ | $FMM_{max}$ | $FMM_{maj}$ | |
| GL15122 | 0.75 | 0.22±0.03 | 0.22±0.03 | 0.20±0.03 | 0.17±0.06 | 0.22±0.03 | 0.22±0.03 | CAM |
| GL15123 | 1.67 | 0.22±0.03 | 0.23±0.03 | 0.20±0.03 | 0.22±0.03 | 0.56±0.09 | 0.22±0.03 | CAM |
| GL15124 | 2.77 | 1.95±0.30 | 1.89±0.30 | - | - | - | - | CAM |
| GL15125 | 2.90 | 1.98±0.29 | 2.08±0.30 | - | - | - | - | CAM |
| GL15126 | 3.82 | 2.07±0.30 | 2.10±0.31 | - | - | - | - | CAM |

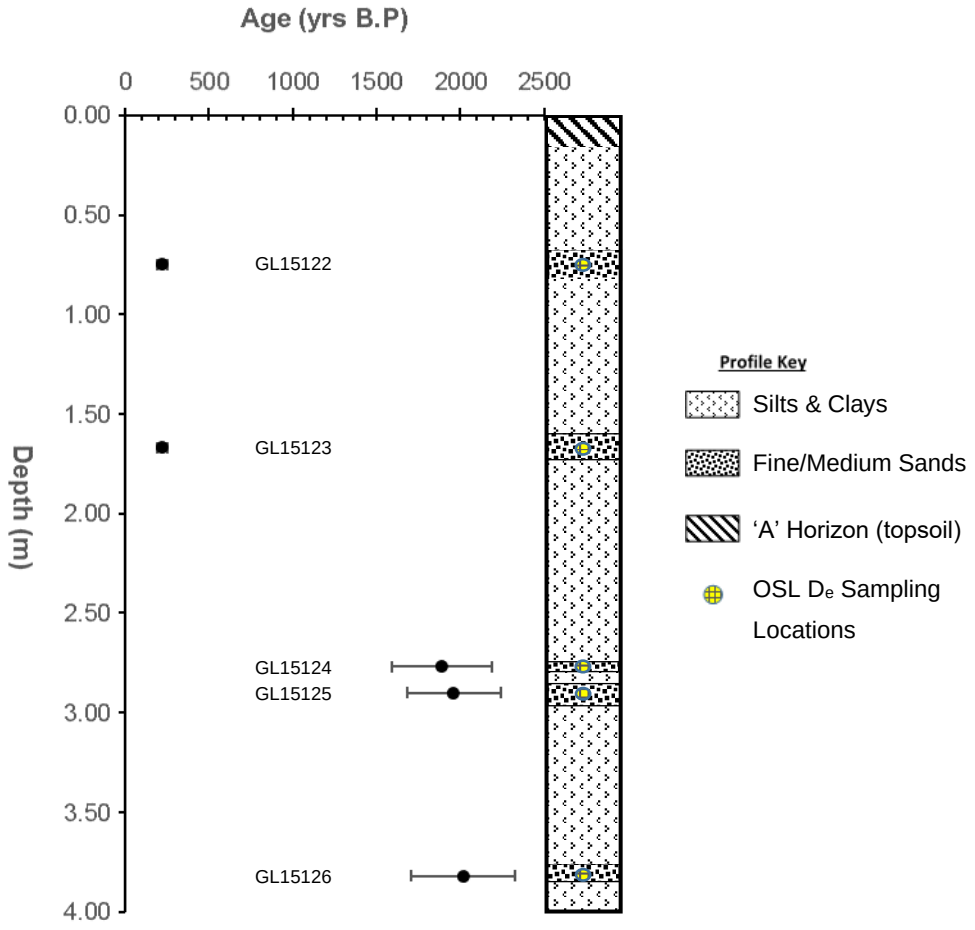


**Figure 5.4.8:** Quartz OSL ages adopted for the Futululu sequence (all ages reported with 1σ confidence).

# Chapter 6: Bayesian Modelling of Mfolozi Chronologies

## 6.1. Overview

As outlined in Chapter 3, Bayesian statistics provide a means to assess the probability of an event occurring based on given, related parameters. In this Chapter chronologies produced for South Lake, UCOSP and Futululu are subject to Bayesian depositional modelling using OxCal (v4.2). For each site the suitability of both the raw (unmodelled) and modelled chronologies is considered; subsequently the utility of the Bayesian models is discussed.

Numerous depositional models are available in OxCal but for all chronologies assessed in this study the 'P_Sequence' function is used. This function assumes that deposition is a random process which can occur at various rates, as opposed to the 'U_Sequence' function where the deposition rate is set as a constant (Bronk Ramsey, 2008). Given the sporadic nature of large flood events and the influence of the main river trunk upon blocked-valley lake sedimentation, variability in deposition rate is expected.

## 6.2. South Lake

### *6.2.1. Suitability of Chronology*

Most OSL ages isolated in Chapter 5 for the South Lake sequence are consistent with their relative stratigraphic position and the inclusion of $^{14}C$ AMS dates contributes to good chronological coverage. For chronologies to be enhanced by Bayesian modelling it is important that age estimates overlap (Rhodes *et al.,* 2003), however, this is not the case for the whole of the South Lake sequence. Whilst all samples from unit 1 provide overlap (Figure 5.2.23), discontinuity is observed for the transition into unit 2 with a gap in the unmodelled chronology occurring between 2.58 (GL15024) and 2.71 m (SL_AMS_5). The upper part of unit 2 also displays no overlap

between 1.81 (GL15022) and 2.09 m (GL15023), which marks the transition into the region of the sequence where fine silt OSL had to be adopted.

Further concern arises from the samples collected from organic-rich regions of the sequence (0.85-1.72 m), particularly the fine grain OSL ages which were highlighted as potential age overestimates in the previous chapter (GL15016, 020 & 021). AMS ages for this region of the sequence produced the youngest ages but these are not statistically consistent with OSL age estimates produced for similar depths. However, GL15022 (1.81 m) and GL16099 (0.72 m) bracket the organic-rich region of the core and the age estimates for both of these are statistically consistent. This provides overlap and should aid the development of a Bayesian model.

The near-surface samples in the South Lake sequence appear detached from the rest of the chronology, they are significantly younger and display no overlap with samples at greater depths. GL15157 and GL15158 are statistically indistinct whilst GL15015 is statistically distinct from the adjacent near-surface samples. There is a *c.* 1.3 ka gap between the base of unit 1 (GL16099) and the oldest near-surface sample (GL15015).

Although the South Lake sequence has good chronological coverage, the highlighted gaps and discrepancies have the potential to hamper successful modelling. Two modelling approaches are therefore investigated for the South Lake sequence. Firstly, all age estimates are included within the Bayesian model, and secondly the proposed fine silt overestimates are omitted and a revised model is produced.

### *6.2.2. Results*

Incorporation of all ages from the South Lake sequence into a P_Sequence produced the modelled ages outlined in Table 6.2.1, these are also represented schematically as an age-depth model in Figure 6.2.1. It is evident both from the numerical values and the schematic that all outliers have been adjusted so that they fall within the correct stratigraphic order. However, this represents a significant (22 to 62%) reduction in age for

samples GL15016, 020, 021 and GL16099. The unmodelled and modelled ages for each of these samples are statistically distinct.

Of the remaining OSL samples in the sequence, four (GL15022, 023, 024 and 032) experienced age adjustments between 10 and 18% whilst the remaining 10 samples had adjustments which were <10%. All OSL samples which experienced age adjustments of ≤18% had statistically consistent unmodelled and modelled ages. This is also the case for most AMS ages which experienced age adjustments between 1 and 8%. However, the unmodelled and modelled ages produced for $^{14}C$ sample SL_AMS_1 are statistically distinct.

Most OSL ages observe a significant reduction in percentage error following modelling, the two exceptions to this are GL15015 which displayed minimal change whilst GL15022 displayed a slight increase (3%) in relative error. The greatest reduction in error (*c.* 10%) is displayed by the three samples (GL15016, 020, 021) that experienced the greatest age adjustments and had statistically inconsistent unmodelled and modelled ages. Errors associated with samples GL15025 to GL15032 and GL16099 displayed reductions of between 7 and 9% following modelling, whilst the remaining OSL ages experienced reductions in relative error of ≤5%. Given that the initial unmodelled OSL ages incorporated errors of 13 to 15%, the observed reductions in percentage error highlight a significant refining of the South Lake OSL chronology. AMS ages displayed minimal change (0-2%) in percentage error.

The overall agreement index for the South Lake deposition model incorporating all ages is 0.1%, this falls well below the recommended 60% (Bronk Ramsey, 1995). Assessment of the agreement index for individual ages highlights GL15016, 020 and 021, as having 0% agreement with the model. Poor agreement is also reported for GL16099 (27.3%) and SL_AMS_1 (40.8%).

**Table 6.2.1:** All South Lake ages incorporated into a P_Sequence deposition model (All ages reported with 1σ confidence and are relative to sampling year – 2014).

| Sample | Unmodelled Age (Years BP) | Modelled Age (Years BP) | Age Adjustment (%)[a] | Rel. Error Change (%)[b] |
|---|---|---|---|---|
| GL15157 | 55 ± 8 | 52 ± 7 | -6 | -2 |
| GL15158 | 54 ± 8 | 58 ± 6 | 8 | -4 |
| GL15015 | 266 ± 39 | 269 ± 41 | -1 | <1 |
| GL16099 | 1543 ± 192 | 1198 ± 65 | -22 | -7 |
| GL15016 | 2805 ± 358 | 1238 ± 38 | -56 | -10 |
| SL_AMS_2 | 1291 ±46 | 1246 ± 35 | -3 | -1 |
| SL_AMS_1 | 1182 ± 55 | 1279 ± 36 | 8 | -2 |
| GL15020 | 3671 ± 467 | 1390 ± 45 | -62 | -10 |
| GL15021 | 3466 ± 430 | 1404 ± 32 | -59 | -10 |
| SL_AMS_3A | 1392 ± 23 | 1411 ± 23 | 1 | 0 |
| GL15022 | 1847 ± 230 | 1663 ± 253 | -10 | 3 |
| GL15023 | 3780 ± 570 | 3170 ± 431 | -16 | -1 |
| GL15024 | 3525 ± 481 | 4173 ± 380 | 18 | -5 |
| SL_AMS_5 | 4725 ± 135 | 4682 ± 132 | -1 | 0 |
| GL15025 | 5244 ± 728 | 4910 ± 248 | -6 | -9 |
| GL15026 | 5824 ± 827 | 5295 ± 286 | -9 | -9 |
| GL15027 | 5773 ± 812 | 5503 ± 317 | -5 | -8 |
| GL15028 | 5741 ± 813 | 6111 ± 370 | 6 | -8 |
| GL15029 | 6389 ± 913 | 6248 ± 416 | -2 | -8 |
| GL15030 | 7146 ± 1025 | 6617 ± 415 | -7 | -8 |
| GL15031 | 7149 ± 1023 | 6919 ± 461 | -3 | -8 |
| GL15032 | 6590 ± 941 | 7272 ± 513 | 10 | -7 |

[a] Percentage change in age from unmodelled to modelled. Negative values represent a reduction in age whilst positive represent an increase.

[b] Change in relative error (%) following modelling (i.e. Modelled relative error minus Unmodelled relative error). Negative values represent a drop in % error whilst positive represent an increase.

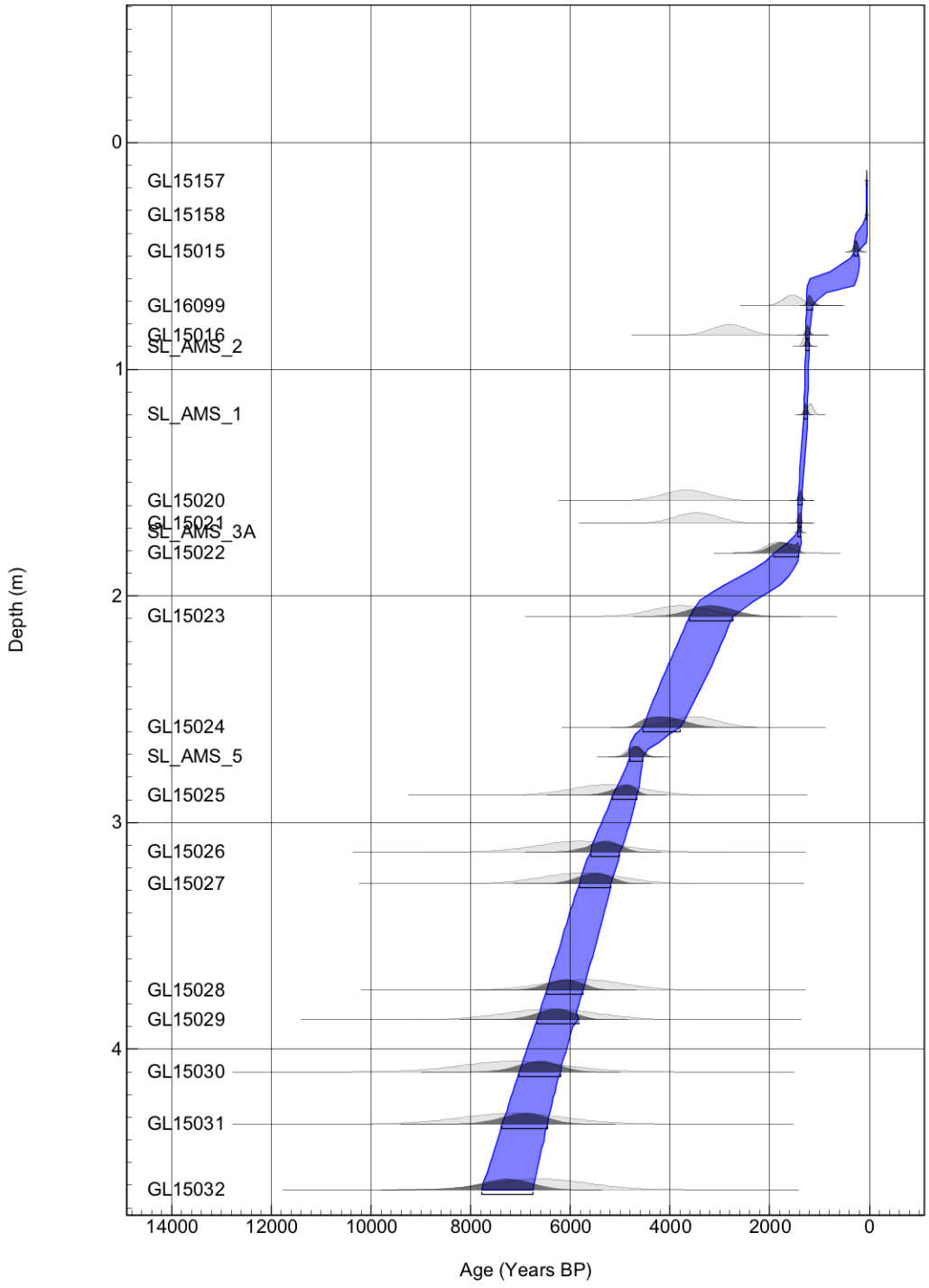


**Figure 6.2.1:** An OxCal P_Sequence deposition model for all South Lake age estimates. Unmodelled age distributions (inputs) are shown as light grey probability density functions (PDFs). Modelled age distributions (outputs) are shown as dark grey PDFs (All ages reported with 1σ confidence and are relative to sampling year – 2014).

Omission of the most significant outliers (GL15016, 020, 021) highlighted in the first model results in a significant improvement in agreement, with the revised model (Table 6.2.2 & Figure 6.2.2) producing an overall agreement index of 69.4%. This falls above the 60% threshold suggested for Bayesian deposition models, indicating the revised chronology is more suitable. Some minor discrepancies still exist despite the improvement in agreement. Poor individual agreement is again reported for GL16099 (23.6%) and SL_AMS_1 (54.8%), however, both appear to have been suitably accommodated within the age-depth model.

GL16099 experiences the greatest age adjustment in the revised model with age being lowered by 23%. The remaining OSL samples display age adjustments of ≤18% and all have unmodelled and modelled ages which are statistically consistent. AMS ages experience similar adjustments (0-7%) to the initial model, however, the unmodelled and modelled ages for SL_AMS_1 are statistically indistinct for the revised chronology.

As with the initial deposition model, most OSL ages experience a significant refining of age margins with relative errors reducing by between 1 and 9%. The most significant reduction in error (7-9%) is again experienced by samples GL15025 to GL15032 and GL16099. GL15022 is the only sample which observes an increase in error (3%) following modelling. Refining of AMS ages is again minimal with changes in relative error falling between 0 and 2%.

**Table 6.2.2:** Ages from a revised P_Sequence deposition model for the South Lake sequence with outlying OSL ages omitted. (All ages reported with 1σ confidence and are relative to sampling year – 2014)

| Sample | Unmodelled Age (Years BP) | Modelled Age (Years BP) | Age Adjustment (%)[a] | Rel. Error Change (%)[b] |
|---|---|---|---|---|
| GL15157 | 55 ± 8 | 52 ± 7 | -6 | -2 |
| GL15158 | 54 ± 8 | 58 ± 7 | 6 | -4 |
| GL15015 | 266 ± 39 | 268 ± 41 | -1 | 0 |
| GL16099 | 1543 ± 192 | 1184 ± 66 | -23 | -7 |
| SL_AMS_2 | 1291 ±46 | 1232 ± 36 | -5 | -1 |
| SL_AMS_1 | 1182 ± 55 | 1264 ± 37 | 7 | -2 |
| SL_AMS_3A | 1392 ± 23 | 1399 ± 23 | 0 | 0 |
| GL15022 | 1847 ± 230 | 1657 ± 261 | -10 | 3 |
| GL15023 | 3780 ± 570 | 3210 ± 454 | -15 | -1 |
| GL15024 | 3525 ± 481 | 4168 ± 395 | 18 | -4 |
| SL_AMS_5 | 4725 ± 135 | 4687 ± 133 | -1 | 0 |
| GL15025 | 5244 ± 728 | 4906 ± 252 | -6 | -9 |
| GL15026 | 5824 ± 827 | 5303 ± 294 | -9 | -9 |
| GL15027 | 5773 ± 812 | 5467 ± 386 | -5 | -7 |
| GL15028 | 5741 ± 813 | 6103 ± 370 | 6 | -8 |
| GL15029 | 6389 ± 913 | 6261 ± 420 | -2 | -8 |
| GL15030 | 7146 ± 1025 | 6607 ± 426 | -8 | -8 |
| GL15031 | 7149 ± 1023 | 6898 ± 460 | -4 | -8 |
| GL15032 | 6590 ± 941 | 7249 ± 537 | 10 | -7 |

[a] Percentage change in age (independent of errors) from unmodelled to modelled. Negative values represent a reduction in age whilst positive represent an increase.

[b] Change in relative error (%) following modelling (i.e. Modelled relative error minus Unmodelled relative error). Negative values represent a drop in % error whilst positive represent an increase.

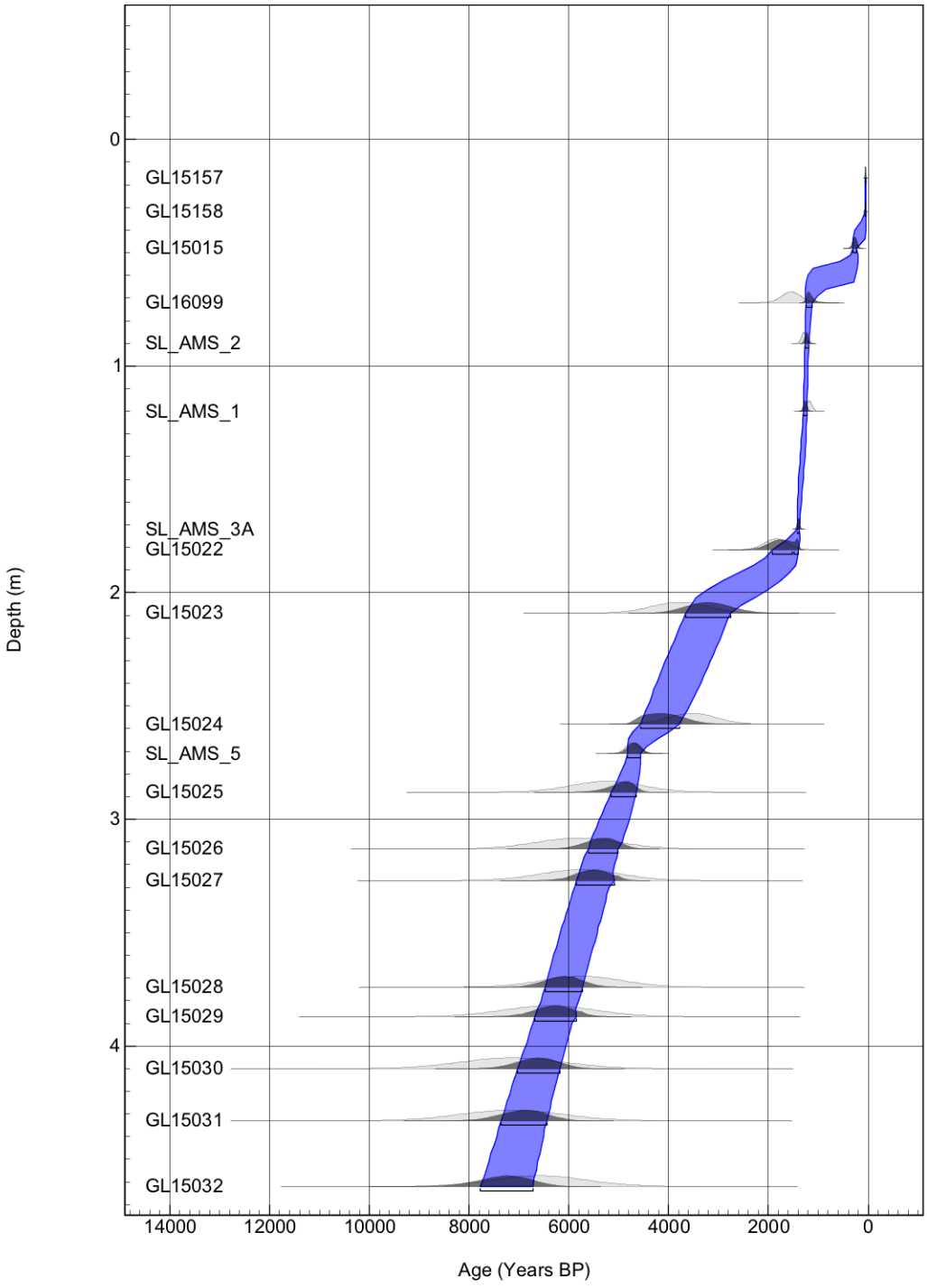


**Figure 6.2.2:** A revised OxCal P_Sequence deposition model for South Lake age estimates with outliers removed. Unmodelled age distributions (inputs) are shown as light grey probability density functions (PDFs). Modelled age distributions (outputs) are shown as dark grey PDFs (All ages reported with 1σ confidence and are relative to sampling year – 2014).

*6.2.3. Discussion*

Two Bayesian deposition models were created for the South Lake chronology, the initial model included all OSL and $^{14}C$ AMS ages but it did not produce a significant overall agreement index (0.1%). Removal of the fine silt OSL ages which had 0% individual agreement with the initial model and had previously been highlighted as overestimates, resulted in the production of a deposition model with an overall agreement of 69.4%, surpassing the recommended threshold of 60%. Although the omission of outliers triggered an increase in agreement, modelled values included in both Bayesian plots are statistically inseparable (Figure 6.2.3).

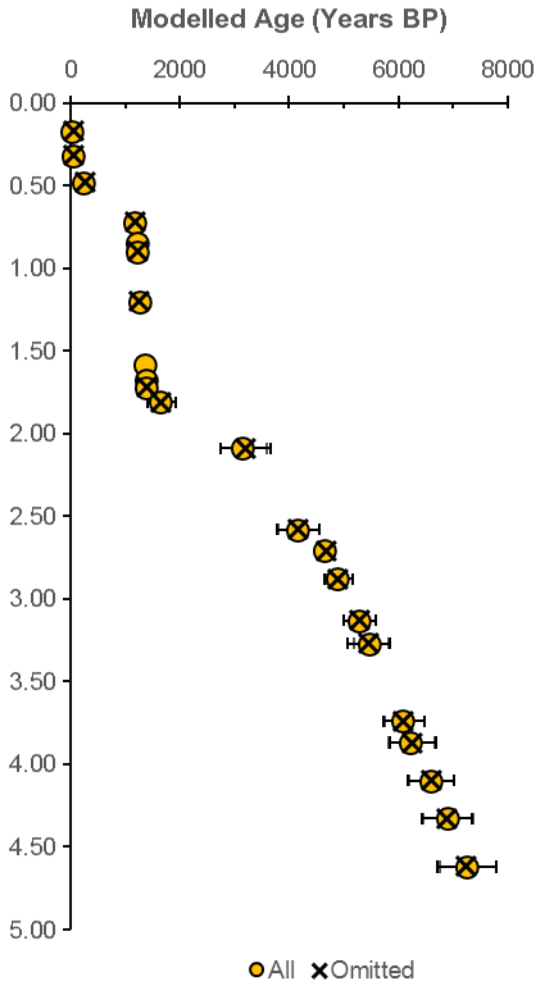


**Figure 6.2.3**: Comparison of South Lake modelled ages produced through Bayesian analysis with i) all age estimates included and ii) outliers omitted.

The Bayesian deposition model produced for the South Lake sequence (outliers omitted – Figure 6.2.2) significantly refined the chronology by producing tighter age constraints for most OSL age estimates. The significant reductions in uncertainty observed for some modelled ages indicate that a maximum achievable chronological resolution of 5% is possible at the 1σ confidence level. However, the resolution is variable throughout the sequence and of the 15 modelled OSL ages included within the model, 10 incorporate errors between 5 and 9% whist the remaining five have uncertainties falling between 10 and 16%. AMS ages experienced minimal changes during modelling, both to age estimates and the attached uncertainties. The consistency of these independent chronological controls provides confidence for the constructed Bayesian model.

In addition to refining South Lake chronology and coupling AMS and OSL dates, the Bayesian model provides further utility as ages can be produced for undated regions of the core through interpolation of the 1σ fitting. For the South Lake sequence this is particularly useful as temporal constraints can be produced for each of the stratigraphic units; the age boundaries isolated for units 1 to 4 are outlined in Table 6.2.3. Both the interpolated age and the gradient of the 1σ fitting in Figure 6.2.2 suggest that unit 3 represents a very short depositional phase upon the South Lake basin. An OSL age could not be produced for a thin clastic band within unit 3 at 1.13 m owing to limited sample mass, interpolation produced an age of 1260±36 years BP.

**Table 6.2.3:** Interpolated ages for sedimentary units identified for the South Lake sequence (*Bayesian model did not extend to contemporary surface)

| | | Interpolated Age (years BP) | |
|---|---|---|---|
| **Unit** | **Depth (m)** | **Maximum** | **Minimum** |
| 1 | 4.62 - 2.85 | 7249 ± 537 | 4906 ± 252 |
| 2 | 2.85 - 1.48 | 4906 ± 252 | 1347 ± 44 |
| 3 | 1.48 - 0.76 | 1347 ± 44 | 1212 ± 50 |
| 4 | 0.76 - Surface | 1212 ± 50 | 54 ± 8* |

Interpolation can also be used to assess the scale of age overestimation for the fine silt samples omitted from the deposition model. Interpolated ages for GL15016 (1236±36), GL15020 (1382±33) and GL15021 (1496±137 years BP) indicate that fine silt samples overestimate age by *c.* 1600 to 2300 years (127 to 166%). Whilst this marks a significant overestimation it is interesting to note that the interpolated ages are statistically indistinct from the modelled ages produced in the first deposition model, where GL15016, 020 and 021 were included. The statistical consistency of ages produced by the models with and without significant overall agreement suggests that, in the case of the South Lake sequence, the presence or lack of agreement does not necessarily define the utility of a Bayesian deposition model.

## 6.3. UCOSP

### *6.3.1. Suitability of Chronology*

The OSL chronology developed for the UCOSP sequence successfully dated four known age flood events which have occurred upon the Mfolozi catchment. The sequence also includes five OSL ages which were collected from flood units of unknown age. Whilst all ages fall in the correct stratigraphic order, a potential issue for Bayesian modelling of the sequence is the significant lack of overlap. Four (GL14001, GL14002, GL15116 & GL15120) of the nine samples are statistically distinct and display no overlap with adjacent estimates, this could restrict the effectiveness of modelling. No AMS ages were collected from this sequence so the consistency of modelled OSL ages can only be compared to the flood units of known age.

### *6.3.2. Results*

Incorporation of all UCOSP OSL ages into a P_Sequence produced the modelled ages outlined in Table 6.3.1 and the age-depth model in Figure 6.3.1. Unlike the South Lake sequence there are no obvious outliers, however, the modelled sequence highlights a significant age gap between 5.15 (GL15116) and 6.15 m (GL15117). Age estimates for the sequence are adjusted between 1 and 21% with GL15119 and GL15120 experiencing the

least and greatest percentage changes respectively. All modelled ages are statistically consistent with unmodelled age estimates, despite the varying magnitudes of adjustments.

Most known age samples displayed minimal change following modelling with 2 to 4% adjustments in age only representing <1 to 2 year. However, GL14004 experienced a reduction in age of 10% (8 years) and the modelled age does not encapsulate the known age of the deposit. For the flood units of unknown age, an increase age is observed for GL15116 (8%) and GL15117 (6%) whilst reductions in age are observed for GL15118 (4%) and GL15120 (21%). GL15119 experiences negligible change following modelling.

Errors associated with the unmodelled UCOSP age estimates ranged from 14 to 16%, most of which were reduced by between 1 and 4% through modelling. The refining of GL14001 and GL14003 is minimal and reduction in relative error does not translate to a change in error margins owing to the young age of the deposits. Only GL15120 displays an increase in relative error, but this is because of the significant reduction in age (21%), in absolute terms the uncertainty reduces from 242 to 205 years.

Despite the significant lack of overlapping age estimates, the overall agreement index for the UCOSP model is 91.7% and no significant issues are highlighted by the individual agreements of each modelled age. All ages displayed individual agreements of >60%, GL15120 displayed the lowest agreement of 69.3% whilst all others exceeded 93%.

**Table 6.3.1:** Ages from a P_Sequence deposition model for all UCOSP samples. (All ages reported with 1σ confidence and are relative to sampling year – 2014)

| Sample | Unmodelled Age (Years BP) | Modelled Age (Years BP) | Known Age (Years BP) | Age Adjustment (%)[a] | Rel. Error Change (%)[b] |
|---|---|---|---|---|---|
| GL14001 | 31 ± 7 | 31 ± 7 | 30 | -2 | -1 |
| GL14003 | 50 ± 8 | 52 ± 8 | 51 | 4 | -2 |
| GL14004 | 80 ± 12 | 72 ± 10 | 89 | -10 | -1 |
| GL14006 | 99 ± 15 | 101 ± 14 | 96 | 2 | -2 |
| GL15116 | 184 ± 27 | 200 ± 26 | - | 8 | -2 |
| GL15117 | 807 ± 118 | 854 ± 106 | - | 6 | -2 |
| GL15118 | 1087 ± 166 | 946± 110 | - | -13 | -4 |
| GL15119 | 1042 ± 169 | 1049 ± 124 | - | 1 | -4 |
| GL15120 | 1583 ± 242 | 1256 ± 205 | - | -21 | 1 |

[a] Percentage change in age from unmodelled to modelled. Negative values represent a reduction in age whilst positive represent an increase.

[b] Change in relative error (%) following modelling (i.e. Modelled relative error minus Unmodelled relative error). Negative values represent a drop in % error whilst positive represent an increase.

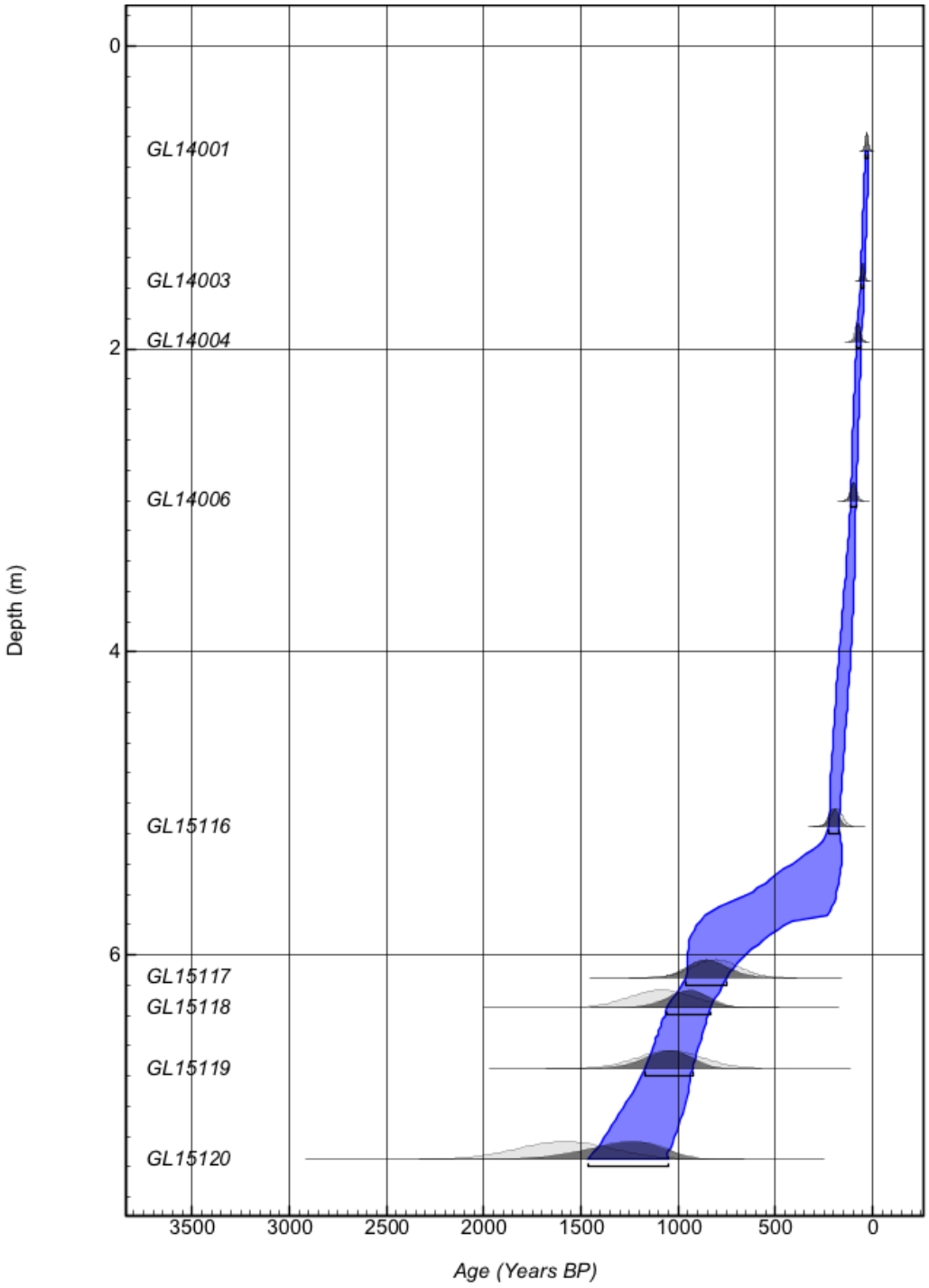


**Figure 6.3.1:** An OxCal P_Sequence deposition model for all UCOSP age estimates. Unmodelled age distributions (inputs) are shown as light grey probability density functions (PDFs). Modelled age distributions (outputs) are shown as dark grey PDFs (All ages reported with 1σ confidence and are relative to sampling year – 2014).

*6.3.3. Discussion*

The Bayesian deposition model created for the UCOSP sequence produced very good overall agreement (91.7%) and surpassed the 60% threshold. No significant outliers were highlighted and modelled ages are statistically consistent with the initial OSL age estimates.

No $^{14}C$ AMS ages were collected for this site and the known age samples GL14001, 003, 004, & 006) act as independent age controls. Most known age samples displayed minimal change following modelling with ages being adjusted between 0 and 8 years and associated errors experiencing negligible change (0 to 2 years). The most significant change in age is displayed by GL14004, where an 8 year adjustment results in a statistically significant underestimation of age for the 1925 flood event. Whilst the overall agreement of the model provides confidence in the UCOSP OSL chronology, there appears to be minimal benefit to Bayesian modelling young, known age deposits. There is minimal refining of error margins for this section of the chronology and in the one instance where age adjustment is significant the resultant modelled age is an underestimate. Furthermore, OSL ages were produced for all known age flood units and interpolation of the 1σ fitting (Figure 6.3.1) is not required.

Modelling appeared to be more beneficial for the remaining UCOSP samples (GL15116-120). All experienced some age adjustment (1-21%) and a reduction in absolute error margins, thus producing tighter age constraints. Reductions in uncertainty observed for this cluster of modelled ages indicate that a maximum achievable chronological resolution of 12% is possible at the 1σ confidence level. A significant age gap (c. 0.65 ka) is highlighted between GL15116 and GL15117; this represents a portion of the sequence where no flood units were preserved.

The utility of the UCOSP model appears limited relative to the one produced for South Lake. Refinement of the UCOSP chronology is only of benefit to those samples that have ages >0.2 ka and the ability to date all flood units means interpolation of the 1σ fitting on the age-depth plot is not required. Two broad phases of flooding are highlighted for the sequence, with four

events occurring between *c.* 1.26 and 0.85 ka and five events occurring between 0.20 ka and the present day.

## 6.4. Futululu

### *6.4.1. Suitability of Chronology*

The Futululu chronology comprises five OSL ages (GL15122-126) for sand based flood units preserved within the sedimentology of a crevasse splay. Some overlap is observed throughout the sequence, GL15122 and GL15123 are statistically indistinct as are the age estimates for GL15124 to GL15126. However, there is a significant age gap (*c.* 1.7 ka) between the two sets of age estimates which could hamper the development of a Bayesian model.

### *6.4.2. Results*

Incorporation of all Futululu OSL ages into a P_Sequence produced the modelled ages outlined in Table 6.4.1 and the age-depth model in Figure 6.4.1. Age estimates for the sequence are adjusted between 4 and 11% with GL15124 and GL15123 experiencing the least and greatest percentage changes respectively. All modelled ages are statistically consistent with unmodelled age estimates. Errors associated with the unmodelled ages ranged from 14 to 16% and for a majority of samples relative errors were reduced by 4% following modelling. The only exception was GL15023 which experienced a 1% reduction in relative error.

The overall agreement index of the Futululu model is 101.3% and no significant issues are highlighted by the individual agreements for each modelled age with all values exceeding 92%. All modelled ages remained in stratigraphic order but the significant age gap highlighted between GL15123 and GL15124 creates a significant broadening of the 1σ fitting on the age-depth plot (Figure 6.4.1) from GL15125 to GL15123.

**Table 6.4.1:** Ages from a P_Sequence deposition model for all Futululu samples. (All ages reported with 1σ confidence and are relative to sampling year – 2014)

| Sample | Unmodelled Age (Years BP) | Modelled Age (Years BP) | Age Adjustment (%)[a] | Rel. Error Change (%)[b] |
|---|---|---|---|---|
| GL15122 | 214 ± 30 | 195 ± 26 | -9 | -1 |
| GL15123 | 218 ± 32 | 241 ± 27 | 11 | -4 |
| GL15124 | 1891 ± 296 | 1822 ± 215 | -4 | -4 |
| GL15125 | 2083 ± 301 | 1888 ± 202 | -9 | -4 |
| GL15126 | 2102 ± 306 | 2222 ± 245 | 6 | -4 |

[a] Percentage change in age from unmodelled to modelled. Negative values represent a reduction in age whilst positive represent an increase.

[b] Change in relative error (%) following modelling (i.e. Modelled relative error minus Unmodelled relative error). Negative values represent a drop in % error whilst positive represent an increase.

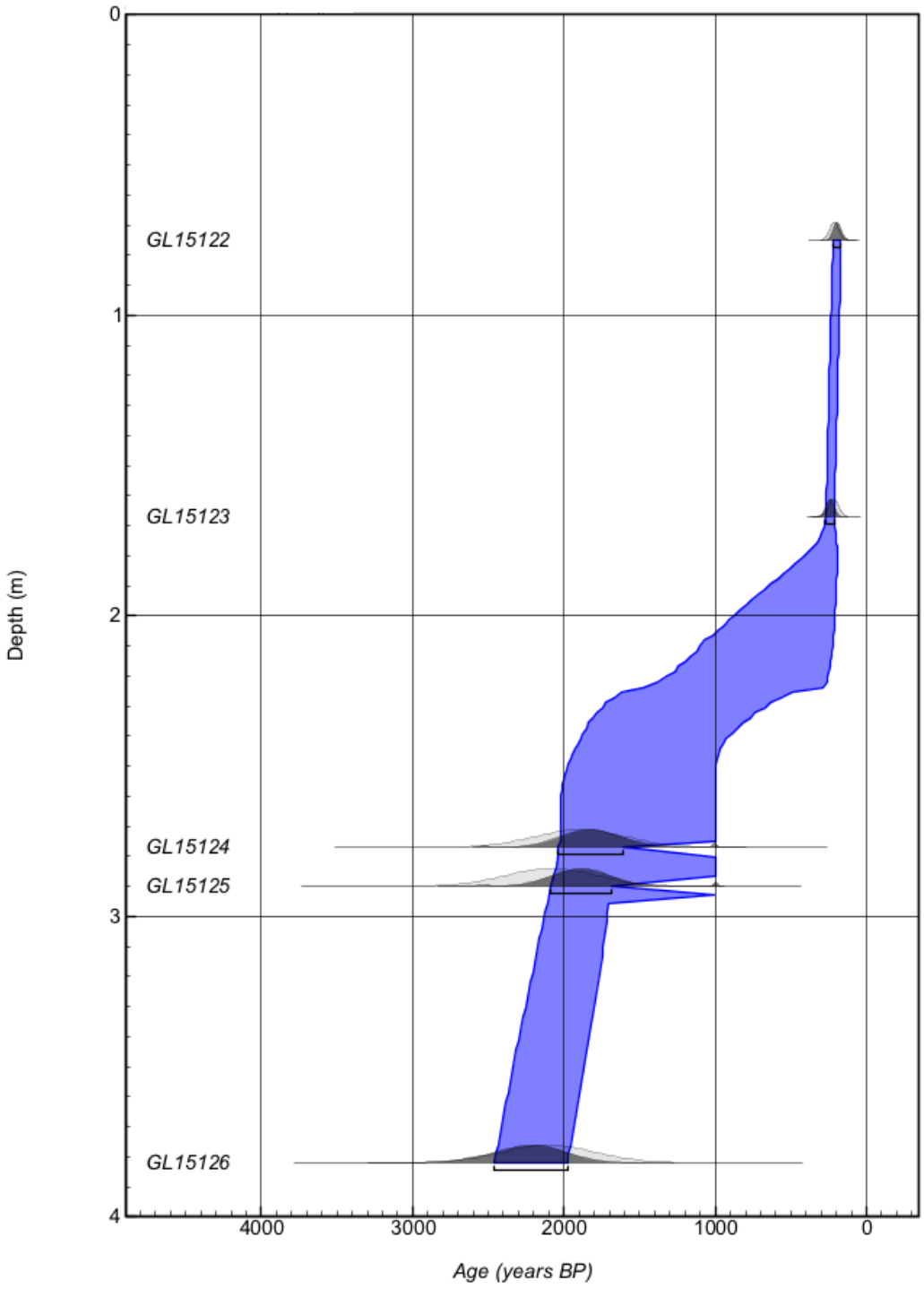


**Figure 6.4.1:** An OxCal P_Sequence deposition model for all Futululu age estimates. Unmodelled age distributions (inputs) are shown as light grey probability density functions (PDFs). Modelled age distributions (outputs) are shown as dark grey PDFs (All ages reported with 1σ confidence and are relative to sampling year – 2014).

### *6.4.3. Discussion*

The Bayesian model produced for the Futululu site surpassed the 60% threshold for overall agreement and also produced the highest agreement value (101.3%) of the three sites explored. No outliers were observed in the chronology and all modelled ages are statistically consistent with the initial OSL age estimates.

A significant age gap (*c.* 1.6 ka) created an issue for the 1σ fitting of the Futululu age-depth plot (Figure 6.4.1). Despite this site producing the highest overall agreement, the lack of overlap in the chronology creates a broadening of age boundaries between 1.67 and 2.90 m. If required, interpolation of this region of the sequence would require careful consideration, particularly given there are no independent age controls to ratify the modelled chronology. Further OSL age estimates between GL15123 and GL15124 would be required to confirm whether these sediments represents a single depositional event or, as indicated by the Bayesian model, a continuous phase of accumulation. Despite some issues with the 1σ fitting, modelling of the Futululu sequence refined the error margins associated with each OSL estimate between 1 and 4%, producing tighter age constraints. Reductions in uncertainty observed for the Futululu ages indicate that a maximum achievable chronological resolution of 11% is possible at the 1σ confidence level.

As with the initial OSL age estimates, the Futululu Bayesian model highlights two phases of flooding onto the crevasse splay feature. Three flood units are deposited between *c.* 2.2 and 1.8 ka whilst a further two units are deposited at *c.* 0.2 ka. Modelled ages within each of the two phases are statistically indistinct, indicating events were temporally closely spaced. However, it should be considered that $D_e$ values for GL15124 to GL15126 were obtained from a smaller grain fraction and from multi-grain aliquots. The presence of *c.* 20% OD at the multi-grain level could be indicative of high inter-grain $D_e$ dispersion and the potential for multi-grain age overestimation. This is a particular concern for GL15126 where an increase in age is observed following Bayesian modelling.

# Chapter 7: Outcomes

## 7.1. Overview

In this chapter the three modelled chronologies produced for Mfolozi sediments are discussed. Whilst the main focus is to isolate flood chronologies and evaluate OSL as a technique for dating of clastic sediment within blocked-valley lake deposits, comparisons with existing palaeoenvironmental work also aids the interpretation of blocked-valley lake formation and flood-driven sedimentation. Further discussion explores the implications of this study for the luminescence dating community, summarising the challenges associated with dating blocked-valley lake sediments and also the implications of the Hydrofluoric acid treatment investigation in Chapter 4.

## 7.2. Floodplain Chronostratigraphy

### *7.2.1. South Lake*

The sedimentology of the South Lake blocked-valley wetland features four distinct units (1-4; Figure 7.2.1) representing different phases of deposition. Unit 1 represents the earliest phase of deposition and contains five sand beds preserved amongst clay rich sediments. The deposition of sand beds initiated in the early-Holocene at 7.2 ± 0.5 ka until 4.9 ± 0.3 ka, with ages for the three intervening sand beds centred on 6.8 ± 0.4, 6.2 ± 0.4 and 5.4 ± 0.3 ka. This coincides with rising sea levels on the South African coast and warming associated with the Holocene Altithermal (8 to 6 ka; Chapter 2: Figure 2.4.5). During this period the Mfolozi floodplain experienced a switch from river incision to aggradation owing to the higher base level created by rising sea levels. The sand beds in unit 1 represent this initial phase of aggradation across the floodplain which is characterised by the fluvial reworking and deposition of aeolian sands (Grenfell *et al.*, 2010).

Although the sand beds deposited between 7.2 and 4.9 ka precede the formation of the blocked-valley lake basin, they do highlight the episodic nature

of fluvial reworking and deposition. In the adjacent Lake Teza, Neumann *et al.* (2010) observe a phase of increased sedimentation at *c.* 6.5 ka and propose that this could have been caused by increased flood and tropical cyclone frequency resulting from a spike in sea surface temperatures (SST) in the Mozambique Channel (Bard *et al.,* 1997). Given their similar age, the phases of sand deposition recorded by the lower regions of the South Lake sequence could represent flood events which are also associated with elevated SST and increased flood frequency.

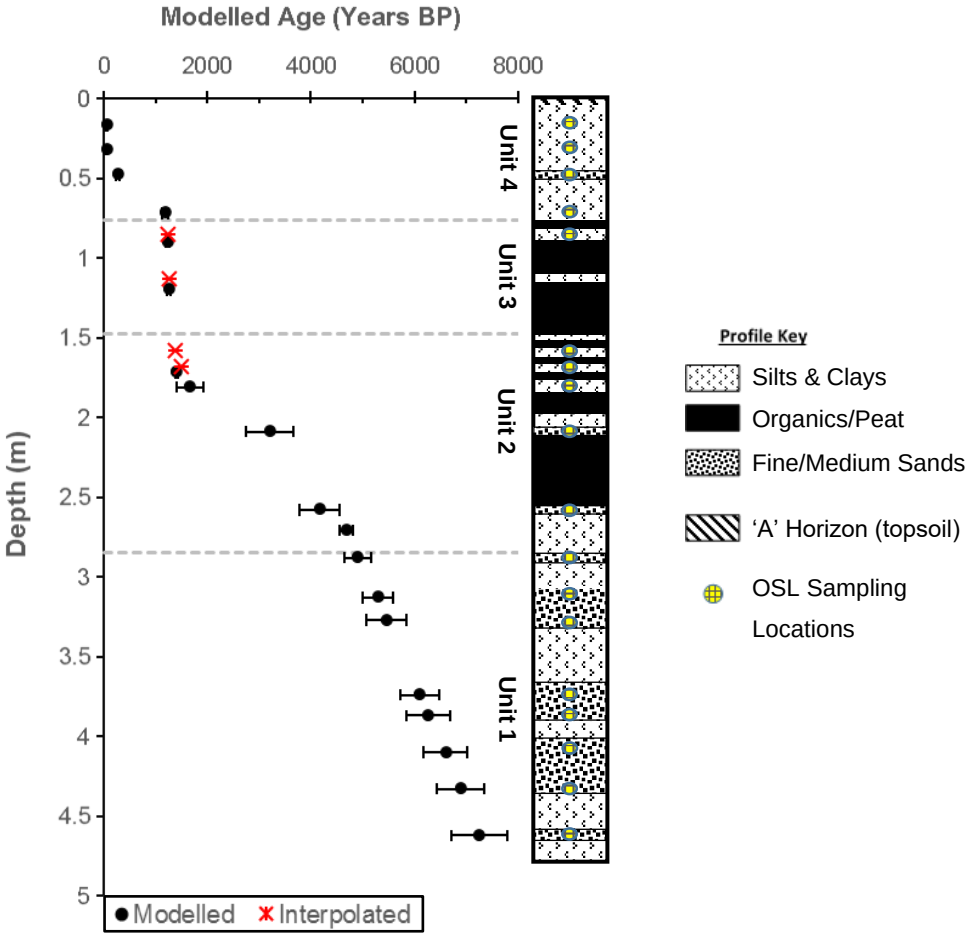


**Figure 7.2.1:** Combined OSL and $^{14}C$ AMS chronology for South Lake following Bayesian modelling. Both modelled and interpolated ages are provided.

From 4.7 ± 0.1 ka organic matter begins to accumulate at the South Lake site marking the shift from a fluvial to lacustrine environment and the initial

formation of the blocked-valley lake basin. This closely corresponds to other observations upon the floodplain, including the *c.* 4.5 ka initiation of tributary impoundment for Lake Futululu (Grenfell *et al.,* 2010) and the development of a freshwater dominated environment at Lake Teza (4.7 ka). Following formation of the basin an alternating pattern of organic and clastic accumulation/deposition is observed at South Lake until 1.35 ± 0.04 ka. As with previous work at Futululu, the clastic bands bound by organics within unit 2 of the South Lake sequence are interpreted as flood deposits, these are formed predominantly of silt or fine/medium sands. Two sand-based flood units were deposited at 4.17 ± 0.40 and 3.21 ± 0.50 ka whilst flood units formed of silt were deposited at 1.66 ± 0.26, 1.50 ± 0.14 and 1.38 ± 0.03 ka. The two earliest of the silt flood units are consistent with ages produced for flood events (1.70 and 1.47 ka) identified at Lake Futululu by Grenfell *et al.* (2010).

Existing work upon the Mfolozi suggest that overbank flood deposits formed of silts are indicative of normal flooding whilst coarser sand units can be attributed to larger flood events (Grenfell *et al.,* 2009). However, it is not appropriate to adopt such inferences for the South Lake basin as variability in sediment source or availability could also contribute to these differences. This is particularly relevant given the cross-floodplain mobility of the Mfolozi channel and its previous avulsions into the Msunduze River and onto the southern reaches of the floodplain during large flood events.

Following 1.35 ka there was a short phase (*c.* 0.1 ka) of heightened organic accumulation at South Lake with minimal clastic input (Unit 3). Preliminary charcoal and pollen analysis of the sequence indicates that this represents the establishment of swamp forest vegetation within the margins of the basin (Reddy & Finch, pers. comm.). Swamp forest is typically found in drainage channels and requires a relatively high water table (Clulow *et al.,* 2013), indicating a temporary elevation in the water table across the basin and potentially a temporary reconnection of South Lake with the Msunduze via a tie channel. Two flood intrusions onto the basin are recorded as silt units within the sedimentology (1.13 and 0.85 m) during this short phase, occurring at 1.26 ± 0.04 and 1.24 ± 0.04 ka. However, it should be considered that the mode of deposition at this time could have been different should South Lake have been

temporarily reconnected to the main river trunk. Flood units could represent tie channel exchange rather than overbank sedimentation.

At 1.21 ± 0.05 ka South Lake experiences another abrupt change, there is a significant drop in the accumulation of organics and the deposition of clastic sediment becomes dominant (unit 4). The abundance of swamp forest is lost (Reddy & Finch, pers. comm.) indicating a drop in the water table and potentially the loss of connectivity to the main river trunk. During the late-Holocene Finch and Hall (2008) infer a general trend of drying from the pollen sequence at the Mfabeni wetland. This could have contributed to the drop in water table and reduction in organic accumulation observed at South Lake. Furthermore, at Lake St Lucia a period of extreme drought and desiccation induced by a strong El Niño is identified at 1.1 ka (Humphries *et al.,* 2016). Given its locality and similar age, this extreme event could have exacerbated the initial desiccation of South Lake. Deposition of clastic rich sediment ensues from 1.21 ka until the present day with the combination of drying and infilling appearing to induce the transition of the basin margins into a terrestrial environment. Three flood deposits comprising fine sands were deposited in the basin at 0.27 ± 0.04, 0.06 ± 0.01 and 0.05 ± 0.01 ka.

The South Lake chronology extends back to 7.2 ka encapsulating the whole development of the blocked-valley lake plus the preceding phases of fluvial deposition. Five phases of sand deposition, interpreted as flood events, are recorded prior to the development of the blocked-valley lake (7.2 to 4.9 ka) and a further ten flood events are preserved within the basin sedimentology following the initial disconnection from the main river trunk (4.7 ka to present day).

### *7.2.2. UCOSP*

The sediments preserved in the UCOSP avulsion sequence provide relatively straightforward interpretation in comparison to South Lake. The avulsion channel sediments featured an alternation of palaeosols (silt and clays; Figure 7.2.2) and flood deposits (fine/medium sands). In total, nine flood events are

recorded within the sequence and the four most recent events are of known age, occurring in AD 1918, 1925, 1963 and 1984 (0.03, 0.05, 0.09 & 0.10 ka).

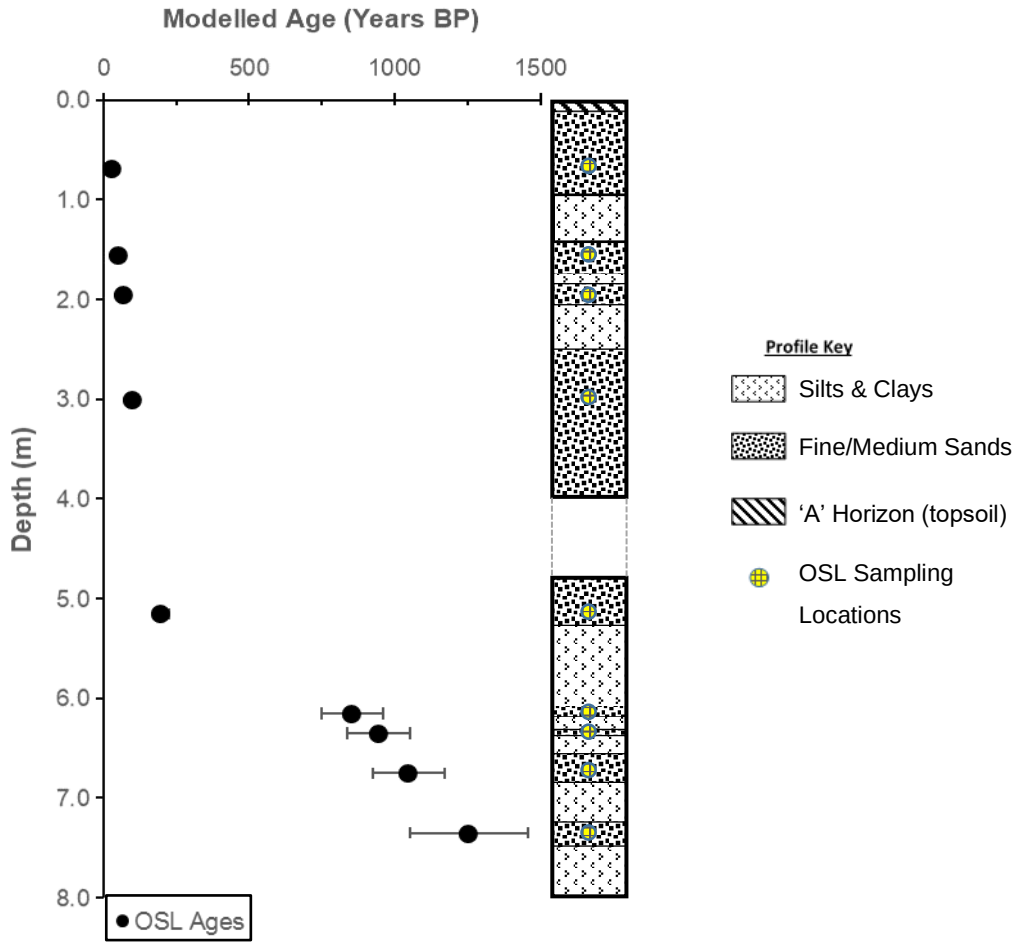


**Figure 7.2.2:** OSL chronology for UCOSP following Bayesian modelling (blank area on profile key represents area not covered by core or section samples).

The flood chronology for UCOSP appears to display two periods of significant flooding for the central floodplain. Between *c.* 1.26 and 0.85 ka four avulsions are recorded by the sequence with ages centred on 1.26 ± 0.21, 1.05 ± 0.12, 0.95 ± 0.11 and 0.85 ± 0.11 ka. Following these floods there is a *c.* 0.6 ka hiatus where no avulsion events occur. Another period of increased flooding initiates at 0.20 ka and spans to the present day. There are five flood units for this period, this includes the four known age events and an additional flood event at 0.20 ± 0.03 ka.

*7.2.3. Futululu*

The Futululu sequence represents the development of a crevasse splay feature which had encroached onto the blocked-valley lake basin via a drainage channel. The sequence was formed predominantly of silt and clay units but it also featured five fine/medium sand-based beds that represented flood events (Figure 7.2.3).

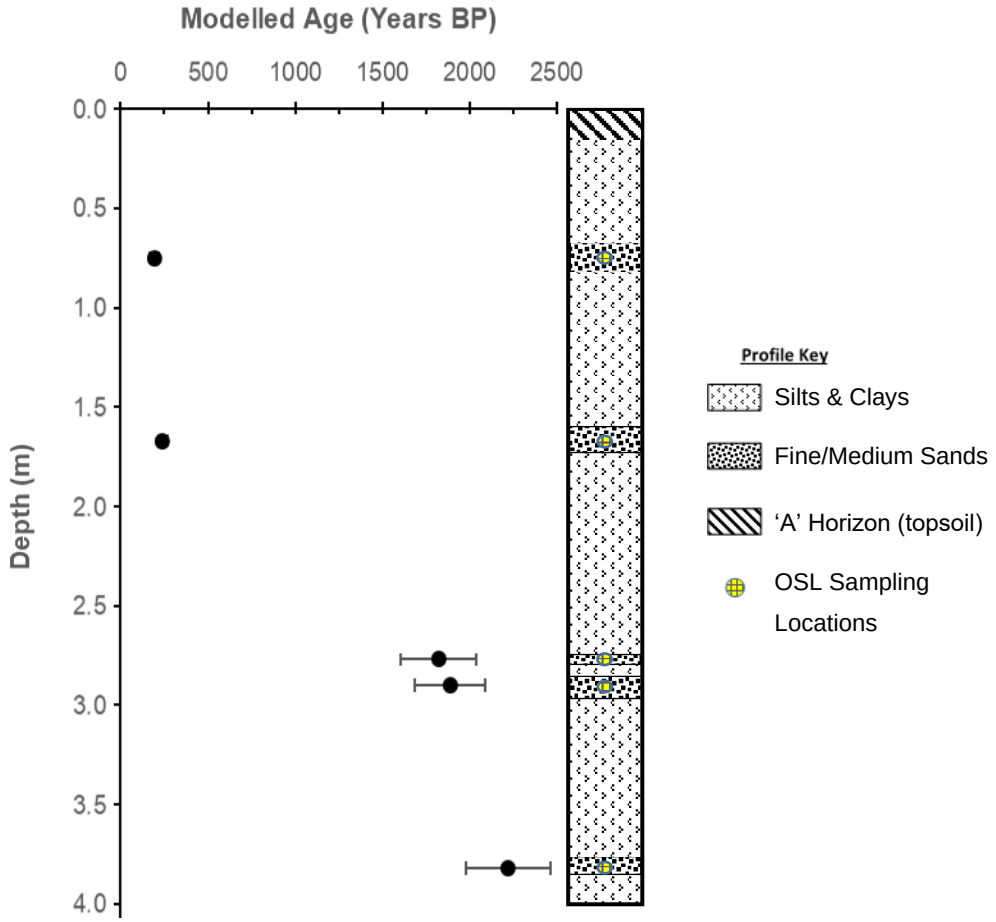


**Figure 7.2.3:** OSL chronology for Futululu following Bayesian modelling.

Two periods of increased flooding are also observed for the Futululu sequence. The three earliest flood events occurred at 2.22 ± 0.25, 1.89 ± 0.20 and 1.82 ± 0.22 ka, following which there is a *c.* 1.6 ka hiatus where no flood intrusions are recorded. After the hiatus two further flood events are detected at 0.24 ± 0.03 and 0.20 ± 0.03 ka. The flood chronology indicates that encroachment of the crevasse splay onto the Futululu basin is comprised of two depositional phases.

*7.2.4. Comparison of Flood Chronologies*

Each of the three flood chronologies developed for the Mfolozi floodplain represent different depositional settings. The South Lake sequence represents blocked-valley lake formation and overbank flood sedimentation whilst flood sediments preserved within the UCOSP and Futululu sequences represent avulsions from the Mfolozi and connected drainage channels onto the respective sites. Despite the differences in depositional processes, all chronologies isolate phases of flooding and provide cross-floodplain coverage of events. Chronicled flood events from all sites are displayed for comparison in Figure 7.2.4.

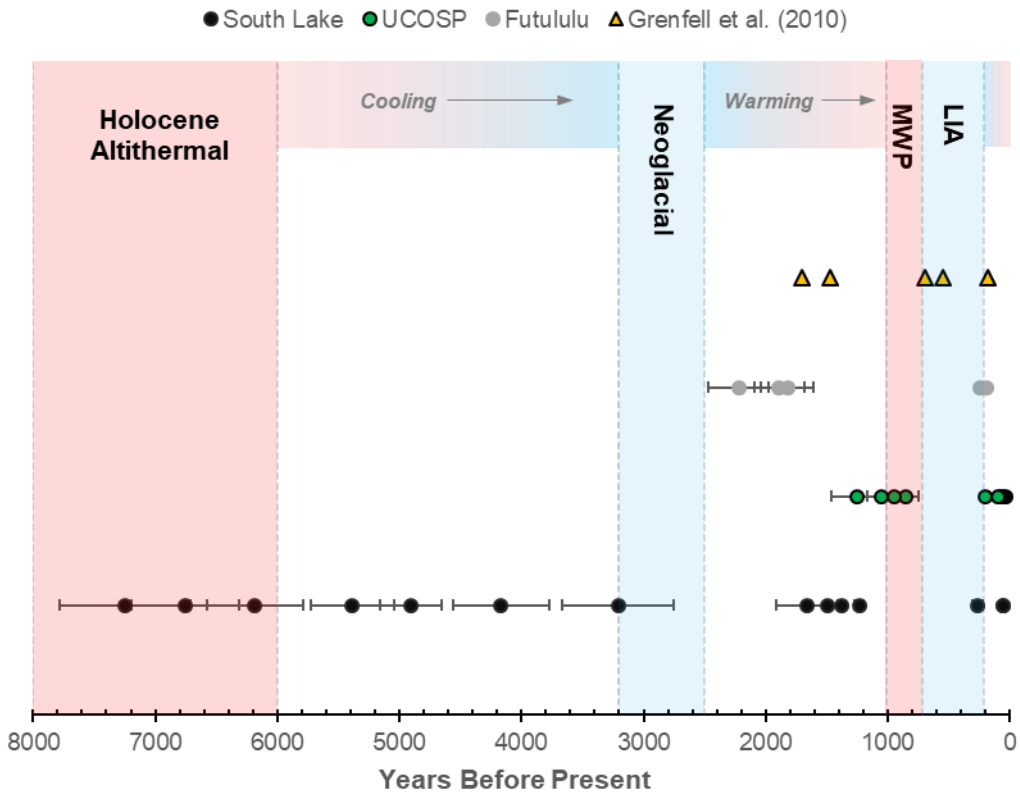


**Figure 7.2.4:** A timeline for flood events occurring across the Mfolozi floodplain using ages from South Lake, UCOSP and Futululu. Flood events identified by Grenfell *et al.* (2010) also included. Highlighted climatic phases/events represent those identified in Chapter 2.

The South Lake sequence provides the greatest temporal coverage and is the only flood chronology to extend past 2.5 ka. The three earliest floods upon the catchment (7.2, 6.8 and 6.2 ka) occurred at *c.* 0.5 ka intervals between 7.2 and

6.2 ka during climatic warming associated with the Holocene Altithermal. Following this interval a trend of gradual cooling is observed across eastern South Africa through to 3.2 ka. In that time four flood events occurred within the catchment at 5.4, 4.9, 4.2 and 3.2 ka. It appears that flood frequency reduces with the cooling climate as the interval between flood events increases from *c.* 0.5 to 1 ka. From 3.2 to 2.5 ka there are no floods recorded across the of whole floodplain, this reflects the mid-Holocene neoglacial period during which conditions on the catchment were much cooler and drier (Grenfell *et al.,* 2010).

Following the neoglacial period climatic warming is observed across the region, which persists until the termination of the medieval warm period (MWP) at 0.7 ka. During this warming phase flooding resumes within the catchment and events are recorded across all three sites. The earliest flood events for this phase are recorded at Lake Futululu with three events occurring at 2.22, 1.89 and 1.82 ka. Ages for the final two flood events recorded at Futululu during this warming phase are consistent with floods resuming around the South Lake basin at 1.66 ka. Between 1.66 and 1.24 ka four flood events are recorded at South Lake, with the average interval between events being 0.14 ka. All four flood ages from the South Lake sequence for this phase are statistically consistent with the onset of avulsions recorded by the UCOSP sequence at 1.26 ka, indicating that high frequency flooding was experienced across most of the floodplain. Three further avulsions at the UCOSP site (1.05, 0.95 and 0.85 ka) occur at 0.1 ka intervals and coincide with the onset of the MWP at 1 ka. In South Africa the MWP is generally considered to have produced warmer and wetter conditions with the climate being up to 3°C warmer than present day (Tyson *et al.,* 2000; Curt Stager *et al.,* 2013).

Whilst all ages have been subject to Bayesian depositional modelling, it should be considered that for flood events occurring between 2.5 and 0.7 ka only those deposited at UCOSP underwent single-grain $D_e$ analysis. South Lake ages for this phase comprised of one fine silt multi-grain age and three ages interpolated from the deposition model whilst all Futululu estimates were from multi-grain aliquots. This represents a potential source of error in both $D_e$ and age. The earlier onset of flooding recorded at Futululu and South Lake (Figure

7.2.4) could either be a function of age overestimation or spatial variations in flooding.

Following the MWP a significant cooling was observed across South Africa between 0.7 and 0.2 ka, associated with the Little Ice Age (LIA). During LIA the climate was up to 1°C cooler than the present day and conditions were generally drier (Tyson *et al.,* 2000; Curt Stager *et al.,* 2013). During this cool event there is another hiatus where no flood events are recorded across the Mfolozi floodplain. Towards the end of the LIA all sampled sequences identify a flood event between *c.* 0.27 and 0.20 ka. This was preserved as a distinct sand bed and represents a significant floodplain-wide event (Figure 7.2.5). At Futululu the final two flood units recorded within the sedimentology correspond to this floodplain-wide event. These units could either represent two closely spaced events or pulses of sediment laden floodwater associated with the same event. Grenfell *et al.* (2010) highlight the occurrence of a flood at 0.18 ka in the Futululu basin which could correspond to the most recent event that is recorded by the crevasse splay.

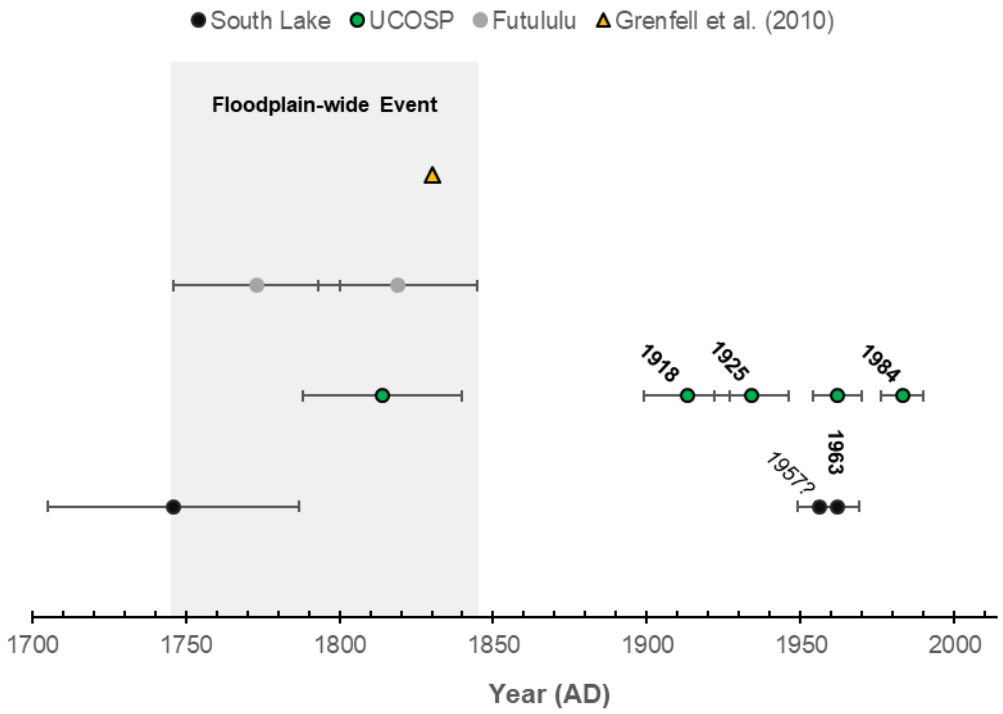


**Figure 7.2.5:** A timeline for flood events occurring post-LIA across the Mfolozi floodplain (Known ages are provided for reference and 1957 is inferred for the South Lake event).

The remaining flood events recorded by the sequences occurred over the past *c.*100 years, these most recent events are only observed at South Lake and UCOSP (Figure 7.2.5). The samples at UCOSP are all of known age (AD 1918, 1925, 1963 and 1984) and when compared to the two flood events recorded at South Lake (AD 1956 ± 7 & 1962 ± 7) it is evident that both ages are consistent with the 1963 floods. However, given that two separate units are preserved within the South Lake sedimentology it could also be inferred that the earliest of these ages relates to the 1957 flooding (Chapter 2: Figure 2.3.5).

Only one flood event appears to simultaneously impact the whole floodplain after 2.5 ka, occurring between 0.27 and 0.20 ka. Some other inter-site similarities in flood phases were evident, including the overlap in flood events observed for Futululu and South Lake between 1.89 and 1.66 ka and also the overlap between 1.66 and 1.24 ka for South Lake and UCOSP. Only South Lake and UCOSP harboured 'modern' (<100 years) flood deposits with the 1963 flood event being recorded within both sequences.

### *7.2.5. Palaeoenvironmental Comparisons and Implications for Eastern South Africa*

The palaeoflood chronologies produced for the Mfolozi floodplain in this study extend beyond the earliest event (1.70 ka) identified by Grenfell *et al.* (2010), providing a more complete long-term record of flooding and the opportunity to further explore the link between flood frequency and palaeoenvironmental change. This is particularly important for understanding the contemporary flood patterns in South Africa and the influence of human-induced climate change, as historical records are limited and often feature missing data (Kruger, 2006).

For many South African palaeoenvironmental studies, the Makapansgat speleothem record (Holmgren *et al.,* 2003; Chapter 2: Figure 2.4.3) acts as a primary proxy for inter-comparison. The stalagmite record is high resolution (~9-years), spans 25 ka and closely agrees with $\delta^{18}O$ patterns observed in the Taylor Dome Antarctic ice-cores (Steig et al., 2000). The Mfolozi palaeoflood chronologies produced in this study span 7.2 ka and for this timeframe Holmgren *et al.* (2003) highlight four broad climatic phases from their

speleothem data (Figure 7.2.4). Early Holocene warming occurs from 10.2 ka until the termination of the Holocene Altithermal at 6 ka, following this a mid-Holocene cooling prevails until the end of the neoglacial at 2.5 ka. The transition from a warm to a cooling climatic phase is accompanied by a reduction in flood frequency upon the Mfolozi, with intervals between events increasing from *c.* 0.5 to 1 ka. Flooding across the Mfolozi floodplain then appears to halt with the onset of the globally-recognised neoglacial event at 3.5 ka (Mayewski *et al*., 2004). Following the neoglacial, Holmgren *et al.* (2003) identify a warm phase between 2.5 and 0.7 ka, with evidence of the MWP between 1.0 and 0.7 ka. This warming phase is accompanied by high frequency (≥4 events per ka) flooding across the Mfolozi floodplain. Between 0.5 and 0.2 ka the speleothem record observes a pronounced cooling phase associated with the LIA. No flooding is observed until the very end of the LIA, where speleothem data observes a transition into a warming phase (Chapter 2: Figure 2.4.3). Although not discussed as a climatic phase by Holmgren *et al.* (2003), this most recent warming (0.2 ka to present) is accompanied by frequent flooding across the Mfolozi floodplain.

Comparison of the chronologies produced in this study with the inferred climatic phases from the Makapansgat record reveals a clear pattern. During phases of climatic warming flood frequency upon the Mfolozi appears to increase, whilst for climatic cooling phases flood occurrences decrease until ceasing at lowstands. In South Africa these climatic phases can be attributed to atmospheric circulation changes, with migration of the circumpolar westerlies driving climatic change (Holmgren *et al.,* 2003; Chase *et al.,* 2013). The important relationship between warm climatic phases and increased flood frequency is particularly concerning when considering contemporary climate change. In the coming decades temperatures are projected to rise more quickly over the eastern coast of South Africa (Jury, 2019), this is likely to result in the region experiencing a higher flood frequency. It is not possible to separate the influence of natural climate variability and anthropogenic global warming upon the flood frequencies observed in this study. However, given that natural climate variability alone cannot account for the large increases in record-breaking precipitation events recorded globally over the past three

decades (Lehmann *et al*., 2015), it is likely that global warming has already, and will continue to influence flood patterns in eastern South Africa.

Most of the flood events identified in the Futululu blocked-valley lake sequence by Grenfell *et al.* (2010) adhere to the observed relationship between phases of climate warming and increased flood frequency (Figure 7.2.4). A flood occurring at 0.55 ka is an exception to this pattern as it falls within the LIA. This could be an anomaly, or it could be an error associated with the indirect dating of flood deposits as ages were obtained through linear interpolation of a radiocarbon chronology for peat accumulation. Despite the anomalous LIA flood age, the general consistency of Grenfell *et al*. (2010) data with the observed patterns in this study, including the observation of a *c.* 0.2 ka floodplain-wide event (Figure 7.2.5), provides confidence for the climatic inferences drawn from the Makapansgat speleothem data.

Within their study, Grenfell *et al.* (2010) also highlight a trend of increasing flood frequency following the initiation of peat accumulation within Lake Futululu at 4 ka, however, they were unable to determine whether increased flood frequency was a result of climate change or a changing proximity of the Mfolozi River to Lake Futululu. The chronologies produced in this study also display a clear increase in flood frequency following 4 ka, however, as they represent flooding across the Mfolozi floodplain (northern, central and southern floodplain), it is likely that the pattern of increased flood frequency observed both in this study and by Grenfell *et al.* (2010) can be attributed to changing climate conditions.

The broad pattern of increased flood frequency upon the Mfolozi since 4 ka provides an interesting discussion point when compared to broad climate patterns observed in the available proxy records. The Bard *et al.* (1997) SST curve for the Mozambique Channel (Chapter 2: Figure 2.4.4) observes a net decrease of *c.* 0.5°C between 4 and 1 ka whilst speleothem records from Makapansgat suggest a slight overall cooling trend between 4 ka and the present (Holmgren *et al.,* 2003; Lee-Thorp *et al*., 2001). Whilst this appears to contradict the previous inference of increased flood frequency being driven by climatic warming phases, it should be noted that many climate proxies and

reconstructions observe an overall cooling trend following termination of the early Holocene warming at 6 ka (Liu *et al.,* 2014; Marcott *et al.,* 2013; Marcott & Shakun, 2015). Liu *et al.* (2014) suggest that the mid- to late-Holocene cooling trend observed by climate proxies and reconstructions is false and is created by significant biases, as their climate models simulate a net warming trend for the Holocene.

The discrepancies between climate reconstructions (e.g. proxies) and simulations produce some confusion for the overall Holocene climate trend. However, throughout the Holocene a globally consistent pattern of increased climatic variability is observed in palaeoclimate records, with a greater number of significant rapid climate fluctuations experienced from *c.* 4 ka (Mayewski *et al.,* 2004). This observation compliments the pattern of increased flood frequency on the Mfolozi from 4 ka and does not contradict the inferences made from Holmgren *et al.* (2003) speleothem record. Comparison of the Mfolozi palaeoflood chronologies with existing palaeoenvironmental data indicates that centennial- and millennial-scale climate variability is responsible for the Holocene flood patterns observed in eastern South Africa.

## 7.3. Implications for the Luminescence Dating Community

### *7.3.1. Optical Dating of Blocked-Valley Lake Deposits*

The main aim of study was to evaluate OSL as a technique for dating clastic sediment within blocked-valley lake deposits upon the Mfolozi catchment. Discussion on the suitability of OSL for chronicling blocked-valley lakes is limited to the South Lake site as the UCOSP site represents an avulsion channel and sediments from Lake Futululu reflect the encroachment of a crevasse splay onto the blocked-valley lake margin rather than the development of the basin itself. However, both the UCOSP and Futululu sites did provide some useful observations for interpretation of the South Lake OSL ages.

The least challenging aspect of chronicling the South Lake sequence was the single-grain dating of basal sands (GL15025-GL15032) which represented 5 phases of fluvial reworking and deposition between 7.2 and 4.9 ka. Single-

grain $D_e$ distributions displayed minimal OD (≤24%) and did not require age modelling. In addition, the sedimentology displayed similar variations resulting in statistically consistent $D_r$ values for these deposits. Ages produced for the sand-beds displayed stratigraphic consistency and were in agreement with the AMS age produced for this region of the sequence. Despite the success of OSL in chronicling the basal sand beds, it is important to note that the deposition of these units preceded the formation of the blocked-valley lake basin. However, the ages remain useful as no previous attempts have been made to chronicle these fluvial phases or highlight their episodic nature. Furthermore, these deposits helped to isolate an age for basin formation and confirmed that not all waterlain deposits are hampered by partial bleaching in this area.

Dating of sediments deposited after the formation of the blocked-valley lake basin was completed with varying degrees of success. Single-grain OSL ages were the least problematic, displaying stratigraphic consistency and having broad agreement with AMS ages produced for the sequence. Single-grain $D_e$ distributions for the blocked-valley lake deposits were variable with OD ranging from 22 to 86% and some samples requiring age modelling. Most known age deposits at the UCOSP site indicated that FMM was best suited to isolating an appropriate $D_e$ for age calculation of heterogeneously bleached sediments. The most suited FMM dose components typically fell between MAM and CAM, concurring with the observations of Rodnight *et al.* (2006), whereby MAM typically underestimates age whilst CAM overestimates age. Based on the observations from the UCOSP site, FMM was applied to overdispersed single-grain $D_e$ distributions from South Lake. The consistency of age estimates would indicate that, despite the requirement for age modelling, single-grain OSL is suitable for use upon blocked-valley lake deposits.

Ages produced using fine silt multi-grain aliquots displayed less success, with three of the five samples analysed for the South Lake sequence significantly overestimating age and not aligning with AMS and single-grain OSL ages. This is not a unique observation and in a previous comparison of coarse- and fine-grain OSL ages produced for fluvial terraces, fine silt aliquots were highlighted as having a tendency to overestimate age by up to a factor of ten (Thompson

*et al.,* 2018). In the case of South Lake it is suggested that fine silt OSL age overestimation is rooted in incomplete bleaching, particularly given the cohesive nature of the sediments and their waterlain origin. In most instances the $D_r$ calculated for fine silt samples was either similar to, or greater than that calculated for other samples within the sequence. Whilst a higher $D_r$ would be expected for the fine silt fraction, given the additional α-component and the lower β attenuation, the calculated $D_r$ would have to at least double to align the fine silt age estimates with other ages in the sequence. This seems unlikely, especially given that most of the fine silt units are surrounded by saturated sediments with an elevated (>20%) organic content. This further indicates that overestimation is rooted in $D_e$. The varying success of fine silt OSL would suggest that it is not best suited for dating blocked-valley lake deposits and ages should be interpreted cautiously and where possible, in combination with single-grain OSL and AMS dating. For this study interpolation of a Bayesian deposition model comprised of single-grain OSL and AMS ages appears the best solution for inferring the age of fine silt flood units preserved within organic rich sediment.

From the outset of this study two predominant factors were considered as potential issues for successful OSL dating of blocked-valley lake sediments. The first of these was the waterlain nature of samples and the likelihood of partial bleaching. In this study it has been demonstrated that by using single-grain quartz OSL it is possible to identify partial bleaching using $D_e$ distribution methods and make accommodations through age modelling, more specifically FMM. However, for fine silt OSL dating partial bleaching appears to be the cause of age overestimation, despite not being able to detect it through $D_e$ distribution or signal analysis methods. The second factor highlighted as a potential issue concerns $D_r$ and the complexity of the sedimentology. The significant fluctuations in organic and moisture content, plus the distinct changes in the clastic sediment matrix required careful consideration when calculating $D_r$. By conducting density and $\gamma$ modelling representative $D_r$ values appear to have been calculated for all age estimates, contributing to their stratigraphic consistency. Whilst this does not act as a replacement for *in situ*

gamma-spectrometry, it provides a useful alternative when on site measurements are not possible.

It can be concluded that quartz OSL is a useful technique for dating clastic sediment within blocked-valley lake profiles. However, it is advised that where possible single-grain $D_e$ analysis should be conducted in order to isolate representative burial doses and the resultant single-grain ages should also be ratified by an independent age control (e.g. known age deposits or $^{14}C$ AMS dating). Furthermore, where there is a combination of a high organic content and dominance of fine silt within the clastic matrix, fine silt OSL ages should be treated with caution and their suitability assessed using independent age controls. Interpolation of deposition models that are constructed using age estimates from surrounding sediments provides a useful alternative when fine silt OSL appears to misrepresent depositional age.

### *7.3.2. Hydrofluoric Acid Treatment of Quartz Grains*

Single-grain $D_e$ distributions provide a means of interpreting depositional settings and isolating representative burial doses through age modelling. Numerous factors are widely accepted to contribute to the form of $D_e$ distributions and the observed OD, but the least considered is the contribution of laboratory preparation methods. The investigations in Chapter 4 focused on the impact of Hydrofluoric acid (HF) treatment upon natural $D_e$ distributions of 180-250 µm quartz grains, with a specific focus on varying treated sample mass and treatment time.

For the investigation into varying sample mass treated with 100 ml of 40% HF for 60 minutes, no systematic changes were observed in $D_e$ values. However, minor distribution changes were observed, with the proportion of grains falling within 2σ of the median systematically increasing with a reduction in treated sample mass. For all HF investigations two levels of $D_e$ precision were explored using ‘strict’ and ‘relaxed’ rejection criteria; for both levels of precision the normalising of $D_e$ distribution (i.e. the increase in proportion of grains within 2σ) with a reduction in treated mass was observed (Table 4.4.2 and Table 4.4.3). In addition to the changes observed in $D_e$ distribution, a significant

systematic change in the percentage mass lost following treatment was observed, with a higher proportion of sample being removed when smaller masses were treated. It is likely that the effectiveness of HF is reduced by the dissolution of more material when greater masses are treated. Despite samples from different geological settings tending to display variable resistance to HF (e.g. Porat *at al.,* 2015), the patterns observed in this study suggest there is a need to standardise the HF to sample mass ratio. For this study treating 5 g of 180-250 μm quartz with 100 ml is suggested. However, it is emphasised that this part of the HF investigation only featured one sample and further work is required.

Investigations into the impact of altering HF treatment time was conducted upon three different samples with etching durations ranging between 0 and 120 minutes. Systematic changes in $D_e$ with increased treatment time were negligible for all samples using both levels of $D_e$ precision. Given that no changes were observed for central $D_e$ estimates, it is suggested that the α-component either has a negligible contribution to $D_e$ or that it cannot be effectively removed using HF. Providing quartz is successfully isolated using mineral separation techniques, this would indicate that HF treatment is not a necessity for single-grain quartz OSL.

The most concerning observation for variations in HF treatment time was the systematic change in OD observed for all samples treated for between 0 and 90 minutes. $D_e$ distributions obtained using strict rejection criteria displayed progressive decreases in OD with increased treatment time for two samples, whilst the opposite effect was observed for the remaining sample which experienced an increase in OD. Although difficult to isolate a driver for this systematic change in OD, two potential causes were outlined and included; the refining of grain size distribution with increases in OD indicative of microdosimetry, and the potential for small grain yields to misrepresent the natural distribution.

These observations have potential implications for future sample preparation and interpretation of single-grain $D_e$ distributions. Minimal changes in central $D_e$ across each of the HF treatment scenarios suggests that either the α-

component is negligible and HF treatment is not needed, or HF is unable to remove the α-component and reconsideration of this component within $D_r$ calculation is required. Furthermore, the observed systematic changes in OD suggests that HF has an influence upon natural $D_e$ distributions and should be considered when interpreting single-grain $D_e$ results. For the Mfolozi sediments which were examined using single-grain OSL in this study, submersion of 5 g of 180-250 μm quartz in 100 ml of 40% HF for 60 minutes was deemed the most suitable treatment. However, this assumed the presence of an α-irradiated rind upon quartz grains and was based on etching depths of <20 μm inferred through mass loss.

### 7.4. Future Work

Further to the OSL work upon the South Lake, the completion of pollen and charcoal analysis will strengthen current interpretation and understanding of the blocked-valley lake development. This analysis could also enhance the understanding of the environment at the time of flooding and potentially aid in isolating other climatic drivers of flood frequency within this region. Although not directly related to flooding, the isolation of fire outbreaks upon the catchment will provide an interesting alternative comparison as they will highlight phases of desiccation upon the catchment.

At the time of fieldwork the water table was relatively high across the Mfolozi floodplain and much of Lake Futululu, which was the primary target for sampling, was not accessible. Given that only one blocked-valley lake sequence is represented in this study, it would be beneficial to return to the catchment and sample the Futululu basin when conditions are favourable. This would provide further assessment on the suitability of OSL dating clastic sediment in blocked-valley lake profiles. In their work upon the Futululu basin Grenfell *et al.* (2010) suggest that overbank deposits experience fining with increased distance from the main river trunk. Thus, to increase the likelihood that flood units are represented as sand units and enable single-grain OSL analysis, sampling would be conducted upon the southern areas of the Lake Futululu basin within close proximity to the Mfolozi River.

The HF investigations in the study outline some potential influences that the acid treatment has upon $D_e$ distribution, however, further work is required to determine whether this is applicable to a wider range of samples. Repeating the matrix of experiments in Chapter 4 (both for treatment time and sample mass) upon samples from a range of depositional environments and of different dose ranges would help to determine the consistency of the interpretations in this study. It may also help to isolate the driver behind OD change with increased HF etching times. Further investigations using single-grain OSL and laboratory α-dosed quartz would also be useful, in order to identify whether it is possible to reduce the α-dose to negligible levels through HF treatment. This would help to determine an appropriate HF treatment for quartz grains, or if treatment is not required, highlight whether the α-component requires consideration in $D_r$ calculation.

# Chapter 8: Conclusions

The investigations in this study produced three key findings:

- High-precision single-grain $D_e$ estimates from naturally-dosed quartz displayed a systematic change in OD when hydrofluoric acid (HF) treatment time was increased, indicating that HF treatment has an influence upon $D_e$ distribution.
- Quartz OSL is a suitable technique for dating clastic sediment within blocked-valley lake deposits, however, $D_e$ analysis should be conducted upon sand-sized material at the single-grain level as multi-grain aliquots of fine silt are hampered by partial bleaching and tend to overestimate $D_e$.
- Palaeoflood chronologies produced for the Mfolozi floodplain reveal a clear pattern of increased flood frequency during phases of climatic warming and observe an overall trend of increasing flood frequency after 4 ka, this is likely to have been driven by increased climate variability during the mid- to late-Holocene.

Using sediments collected from the Mfolozi floodplain, eastern South Africa, this study examined the utility of OSL dating blocked-valley lake deposits. Core samples collected from South Lake, a blocked-valley wetland on the southern margin the Mfolozi floodplain, comprised an alternating pattern of organic and clastic sediments representing wetland development and episodic flooding. A combination of $D_r$ modelling, multi- and single-grain $D_e$ analysis, $^{14}C$ AMS dating and Bayesian deposition modelling produced a chronology of sedimentation at South Lake spanning *c.* 7.2 ka, with formation of the blocked-valley lake basin initiating at *c.* 4.7 ka. Whilst single-grain quartz OSL appeared successful in dating this environment, multi-grain ages for fine silt quartz (5-15 μm) significantly overestimated age owing to partial bleaching. Although some single-grain $D_e$ distributions displayed symptoms of partial bleaching, $D_e$

modelling identified representative burial doses and produced OSL age estimates that displayed stratigraphic consistency and were in agreement with independent age controls. From the work at South Lake it is concluded that OSL is a useful technique for dating blocked-valley lake sediments, however, single-grain $D_e$ analysis is required to ensure accurate ages.

This study had a particular focus on chronicling palaeoflood events which had impacted the Mfolozi floodplain. To provide floodplain-wide coverage of past flooding, OSL chronologies were produced for two additional sediment sequences that contained flood units. This included the UCOSP sequence, an avulsion channel in the centre of the floodplain, and a crevasse splay which had encroached onto Lake Futululu on the northern margin of the floodplain. Neither of the additional chronologies extended past 2.5 ka but they did adhere to the same trend as South Lake, whereby flood frequency was highest during phases of climatic warming whilst during cool climatic events (e.g. Little Ice Age) flooding would cease. This could have implications for future flooding, particularly given that current temperatures over South Africa are expected to rise more quickly in the coming decades. Although there was some degree of overlap between each of the flood chronologies, only one floodplain-wide event could be pinpointed for all sites. This was preserved as sand bed in all sequences which was deposited at the termination of the LIA (0.27-0.20 ka).

The UCOSP site had an additional benefit to this study as it contained four known age deposits that provided the opportunity to test the ability of OSL to successfully date flood units. Single-grain $D_e$ distributions for all known age flood units were highly overdispersed and for most, the minimum dose component isolated by the finite mixture model (FMM) was most suited to producing the correct age. Findings were consistent with previous studies upon heterogeneously bleached sediment, with burial dose typically falling between minimum and central $D_e$. These findings were utilised for modelling single-grain distributions from the South Lake sequence that displayed significant OD.

Further to the work upon flood deposits from the Mfolozi catchment, this study also investigated the impact of various Hydrofluoric acid (HF) treatments upon

naturally-dosed single-grain $D_e$ distributions for 180-250 μm quartz. This aspect of the study has wider implications for the luminescence dating community as it is not specific to depositional environment and for quartz OSL HF treatment is a standard preparation procedure, however, it is not necessarily standardised in its execution. The investigations in this study found that there was a systematic increase in the proportion of grains falling within 2σ of the median when the mass of quartz treated with 100 ml of 40% HF for 60 minutes was reduced. For high-precision $D_e$ estimates it was also found that OD changed systematically by increasing etching time from 0 to 90 minutes, however, change in OD was bidirectional. For all of the treatments investigated there was negligible change in central $D_e$ and it is concluded that either the α-component is negligible and HF treatment is not needed, or HF is unable to remove the α-component and reconsideration of this component within $D_r$ calculation is required. Whilst further work is needed to assess the consistency of the findings in these investigations, it is recommended that where HF treatment is used a standard mass and treatment time should be adopted for each grain fraction. In this study the treatment of 5 g of 180-250 μm quartz with 100 ml of 40% HF for 60 minutes was deemed most suitable.

# References


Adrian, R., O'Reilly, C.M., Zagarese, H., Baines, S.B., Hessen, D.O., Keller, W., Livingstone, D.M., Sommaruga, R., Straile, D., Van Donk, E., Weyhenmeyer, G.A., Winder, W. (2009) 'Lakes as sentinels of climate change', *Limnology and Oceanography,* 54(6-2), pp. 2283-2297.

Aitken, M.J. (1985) *Thermoluminescence Dating.* London: Academic Press.

Aitken, M.J. (1998) *An Introduction to Optical Dating: The Dating of Quaternary Sediments by the use of Photo-Stimulated Luminescence.* Oxford: Oxford University Press.

Armitage, S.J., Bailey, R.M. (2005) 'The measured dependence of laboratory beta dose rates on sample grain size', *Radiation Measurements,* 39(2), pp. 124-127.

Armitage, S.J., Drakes, N.A., Stokes, S., El-Hawat, A., Salem, M.J., White, K., Turner, P., McLaren, S.J. (2007) 'Multiple phases of North African humidity recorded in lacustrine sediments from the Fazzan Basin, Libyan Sahara', *Quaternary Geochronology,* 2, pp. 181-186.

Armitage, S.J., Duller, G.A.T., Wintle, A.G. (2000) 'Quartz from southern Africa: sensitivity changes as a result of thermal pretreatment', *Radiation Measurements,* 32(5-6), pp. 571-577.

Arnold, L.J., Bailey, R.M., Tucker, G.E. (2007) 'Statistical treatment of fluvial dose distributions from southern Colorado arroyo deposits', *Quaternary Geochronology,* 2(1-4), pp. 162-167.

Arnold, L.J., Demuro, M., Navazo Ruiz, M. (2012) 'Empirical insights into multi-grain averaging effects from 'pseudo' single-grain OSL measurements', *Radiation Measurements,* 47(9), pp. 652-658.

Arnold, L.J., Roberts, R.G. (2009) 'Stochastic modelling of multi-grain equivalent dose ($D_e$) distributions: implications for OSL dating of sediment mixtures', *Quaternary Geochronology,* 4(3), pp. 204-230.

Badenhorst, P., Cooper, J.A.G., Crowther, J., Gonslaves, J., Grobler, N.A., Illenberger, W.K., Laubscher, W.I., Mason, T.R., Moller, J.P., Perry, J.E., Reddering, J.S.V., van der Merwe, L. (1989) Survey of September 1987 Natal floods. Republic of South Africa: National Scientific Programmes Unit (CSIR).

Bailey, R.M. (2001) 'Towards a general kinetic model for optically and thermally stimulated luminescence of quartz', *Radiation Measurements,* 33, pp. 17-45.

Bailey, R.M. (2003a) 'Paper I: The use of measurement-time dependent single-aliquot equivalent-dose estimates from quartz in the identification of incomplete signal resetting', *Radiation Measurements,* 37(6), pp. 673-683.

Bailey, R.M. (2003b) 'Paper II: The interpretation of measurement-time-dependent single-aliquot equivalent-dose estimates using predictions from a simple empirical model', *Radiation Measurements,* 37(6), pp. 685-691.

Bailey, R.M., Arnold, L.J. (2006) 'Statistical modelling of single grain quartz $D_e$ distributions and an assessment of procedures for estimating burial dose', *Quaternary Science Reviews,* 25(19-20), pp. 2475-2502.

Bailey, R.M., Smith, B.W., Rhodes, E.J. (1997) 'Partial bleaching and the decay form characteristics of quartz OSL', *Radiation Measurements,* 27(2), pp. 123-136.

Bailey, R.M., Stokes, S., Bray, H. (2003) 'Inductively-Couples Plasma Mass Spectrometry (ICP-MS) for dose rate determination: some guidelines for sample preparation and analysis', *Ancient TL,* 21(1), pp. 11-14.

Bailey, S.D., Wintle, A.G., Duller, G.A.T., Bristow, C.S. (2001) 'Sand deposition during the last millennium at Aberffraw, Anglesey, North Wales as determined by OSL dating of Quartz', *Quaternary Science Reviews,* 20(5-9), pp. 701-704.

Bailiff, I.K., Lewis, S.G., Drinkall, H.C., White, M.J. (2013) 'Luminescence dating of sediments from a Palaeolithic site associated with a solution feature on the North Downs of Kent, U.K', *Quaternary Geochronology,* 18, pp. 135-148.

Baker, A., Routh, J., Blaauw, M., Roychoudhury, A.N. (2014) ‘Geochemical records of palaeoenvironmental controls of peat forming processes in the Mfabeni peatland, KwaZulu Natal, South Africa since the Late Pleistocene’, *Palaeogeography, Palaeoclimatology, Palaeoecology,* 395, pp. 95-106.

Barbouti, A.I., Rastin, B.C. (1983) ‘A study of the absolute intensity of muons at sea level and under various thicknesses of absorber’, *Journal of Physics G: Nuclear Physics,* 9(12), pp. 1577-1595.

Bard, E., Rostek, F., Sonzognim C. (1997) ‘Interhemispheric synchrony of the last deglaciation inferred from alkenone palaeothermometry’, *Nature,* 385, pp. 707-710.

Bateman, M.D., Boulter, C.H., Carr, A.S., Frederick, C.D., Peter, D., Wilder, M. (2007a) ‘Detecting post-depositional sediment disturbance in sandy deposits using optical luminescence’, *Quaternary Geochronology,* 2(1-4), pp. 57-64.

Bateman, M.D., Boulter, C.H., Carr, A.S., Frederick, C.D., Peter, D., Wilder, M. (2007b) ‘Preserving the palaeoenvironmental record in Drylands: Bioturbation and its significance for luminescence-derived chronologies’, *Sedimentary Geology,* 195(1-2), pp. 5-19.

Bateman, M.D., Frederick, C.D., Jaiswal, M.K., Singhvi, A.K. (2003) ‘Investigations into the potential effects of pedoturbation on luminescence dating’, *Quaternary Science Reviews,* 22(10-13) pp. 1169-1176.

Bell, F.G. (1994) ‘Floods and landslides in Natal and notably the Greater Durban Region, September 1987: a retrospective view’, *Environmental & Engineering Geoscience,* xxxi(1), pp. 59-74.

Bell, W.T., Zimmerman, D.W. (1978) ‘The effect of HF acid etching on the morphology of quartz inclusions for thermoluminescence dating’, *Archaeometry*, 20(1), pp. 63-65.

Beta Analytic (2016) *Radiocarbon Dating of Sediment or Soil.* USA. Available at: https://www.radiocarbon.com/ams-dating-sediments.htm (Accessed: September 2016)

Berger, G.W. (1990) ‘Effectiveness of natural zeroing of the thermoluminescence in sediments’, *Journal of Geophysical Research: Solid Earth,* 95(B8), pp. 12375-12397.

Berger, G.W., Mulhern, P.J., Huntley, D.J. (1980) ‘Isolation of Silt-Sized Quartz from Sediments’, *Ancient TL,* 11, pp. 8-9.

Blake, D.H., Ollier C.D. (1971) ‘Alluvial plains of the Fly River, Papua’, *Z. Geomorph. N.F*., 12, pp. 1-17.

Bøe, A-G., Dahl, S.V., Lie, O., Nesje, A. (2006) ‘Holocene river floods in the upper Glomma catchment, southern Norway: a high-resolution multiproxy record from lacustrine sediments’, *The Holocene,* 16(3), pp. 445-455.

Bonczyk, M. (2013) ‘A Determination of the Concentration Level of Lead $^{210}$Pb Isotope in Solid Samples for the Assessment of Radiation Risk Occurring in Coal Mines’, *Journal of Sustainable Mining,* 12(2), pp. 1-7.

Bøtter-Jensen, L, Bulur, E., Duller, G.A.T., Murray, A.S. (2000) ‘Advances in luminescence instrument systems’, *Radiation Measurements,* 32(5-6), pp. 523-528.

Bøtter-Jensen, L., Mejdahl, V. (1988) ‘Assessment of beta dose-rate using a GM multicounter system’, *International Journal of Radiation Applications and Instrumentation. Part D. Nuclear Tracks and Measurements,* 14(1-2), pp. 187-191.

Boyle, J. (2004) ‘A comparison of two methods for estimating the organic matter content of sediments’, *Journal of Paleolimnology,* 31, pp. 125-127.

Brennan, B.J. (2003) ‘Beta doses to spherical grains’, *Radiation Measurements,* 37(4-4), pp. 299-303.

Bronk Ramsey, C. (1995) ‘Radiocarbon calibration and analysis of stratigraphy: the OxCal program’, *Radiocarbon,* 37(2), pp. 425-430.

Bronk Ramsey, C. (2008) ‘Deposition models for chronological records’, *Quaternary Science Reviews,* 27(1-2), pp. 42-60.

Bronk Ramsey, C. (2009) ‘Bayesian analysis of radiocarbon dates’, *Radiocarbon,* 51(1), pp. 337-360.

Buylaert, J-P., Jain, M., Murray, A.S., Thomsen, K.J., Thiel, C., Sohbati, R. (2012) ‘A robust feldspar luminescence dating method for Middle and Late Pleistocene sediments’, *Boreas,* 41(3), pp. 435-451.

Chamberlain, E., Wallinga, J. (2018) ‘Fluvial sediment pathways enlightened by OSL bleaching of river sediments and deltaic deposits’, *Earth Surface Dynamics Discussions,* in review.

Chase, B.M., Meadows, M.E. (2007) ‘Late Quaternary dynamics of southern Africa’s winter rainfall zone’, *Earth-Science Reviews,* 84, pp. 103-138.

Chase, B.M., Boom, A., Carr, A.S., Meadows, M.E., Reimer, P.J. (2013) ‘Holocene climate change in southernmost South Africa: rock hyrax middens record shifts in the southern westerlies’, *Quaternary Science Reviews,* 82, pp. 199-205.

Chu, S.Y.F., Ekström, L.P., Firestone, R.B. (1999) *The Lund/LBNL Nuclear Data Search: Version 2.0.* Berkeley: USA. Available at: http://nucleardata.nuclear.lu.se/toi/nuclide.asp?iZA=380090 (Accessed: 21st May 2018).

CLIWOC (2007) ‘CLIWOC Release 2.1’, Available at: http://projects.knmi.nl/cliwoc/cliwocdata.htm (Accessed: 03 August 2016).

Clulow, A.D., Everson, C.S., Price, J.S., Jewitt, G.P.W., Scott-Shaw, B.C. (2013) ‘Water-use dynamics of a peat swamp forest and a dune forest in Maputaland, South Africa’, *Hydrology and Earth System Sciences,* 17, pp. 2053-2067.

Corella, J.P., Benito, G., Rodriguez-Lloveras, X., Brauer, A., Valero-Garcés, B.L. (2014) ‘Annually-resolved lake record of extreme hydro-meteorological events since AD 1347 in NE Iberian Peninsula’, *Quaternary Science Reviews,* 93, pp. 77-90.

Cunningham, A.C., Bakker, M.A.J., van Heteren, S., van der Valk, B., van der Spek, A.J.F., Schaart, D., Wallingam J. (2011) 'Extracting storm-surge data from coastal dunes for improved assessment of flood risk', *Geology,* 39(11), pp. 1063-1066.

Cunningham, A.C., Wallinga, J. (2010) 'Slection of integration time intervals for quartz OSL decay curves', *Quaternary Geochronology,* 5(6), pp. 657-666.

Currie, R.G. (1993) 'Luni-solar 18.6- and 10-11-year solar cycle signals in South African rainfall', *International Journal of Climatology,* 13(3), pp. 237-256.

Curt Stager, J., Ryves, D.B., King, C., Madson, J., Hazzard, M., Neumann, F.H., Maud, R. (2013) 'Late Holocene precipitation variability in the summer rainfall region of South Africa', *Quaternary Science Reviews,* 67(1), pp. 105-120.

Davies, B.E. (1974) 'Loss-on-Ignition as an Estimate of Soil Organic Matter', *Soil Science Society of America Journal,* 38(1), pp. 150-151.

Day, G., Dietrich, W.E., Rowland, J.C., Marshall, A. (2008) 'The depositional web on the floodplain of the Fly River, Papua New Guinea', *Journal of Geophysical Research,* 113, F01S02.

Dietze, M., Kreutzer, S. (2018). *plot_AbanicoPlot(): Function to create an Abanico Plot*. Function version 0.1.10. In: Kreutzer, S., Burow, C., Dietze, M., Fuchs, M.C., Schmidt, C., Fischer, M., Friedrich, J. (2018). *Luminescence: Comprehensive Luminescence Dating Data Analysis*. R package version 0.9.0. Available at: https://CRAN.R-project.org/package=Luminescence

Dietze, M., Kreutzer, S., Burow, C., Fuchs, M.C., Fischer, M., Schmidt, C. (2016) 'The abanico plot: Visualising chronometric data with individual standard errors', *Quaternary Geochronology,* 31, pp. 12-18.

Divigalpitiya, W.M.R. (1982) 'Thermoluminescence dating of sediments', Unpublished M.Sc. Thesis, Simon Fraser University, Burnaby, BC.

Donat M.G., Alexander, L.V., Yang, H., Durre, I., Vose, R., Dunn, R.J.H., Willett, K.M., Aguilar, E., Brunet, M., Caesar, J., Hewitson, B., Jack, C., Klien Tank, A.M.G., Kruger, A.C., Marengo, J., Peterson, T.C., Renom, M., Oria Rojas, C., Rusticucci, M., Salinger, J., Elrayah, A.S., Sekele, S.S., Srivastava, A.K., Trewin, B., Villarroel, C., Vincent, L.A., Zhai, P., Zhang, X., Kitching, S. (2013) 'Updated analyses of temperature and precipitation extreme indices since the beginning of the twentieth century: The HadEX2 dataset', *Journal of Geophysical Research,* 118(5), pp. 2098-2118.

Duller, G.A.T. (1994) 'Luminescence dating of poorly bleached sediments from Scotland', *Quaternary Science Reviews*, 13(5-7), pp. 521–524.

Duller, G.A.T. (2003) 'Distinguishing quartz and feldspar in single grain luminescence measurements', *Radiation Measurements,* 37(2), pp. 161-165.

Duller, G.A.T. (2007) 'Assessing the error on equivalent dose estimate derived from single aliquot regenerative dose measurements', *Ancient TL,* 23(1), pp.15-24.

Duller, G.A.T. (2008) 'Single-grain optical dating of Quaternary sediments: why aliquot size matters in luminescence dating', *Boreas*, 37, pp. 589–612.

Duller, G.A.T. (2008) *Luminescence Dating: guidelines on using luminescence dating in archaeology.* Swindon: English Heritage.

Duller, G.A.T. (2012) 'Improving the accuracy and precision of equivalent doses determined using the optically stimulated luminescence signal from single grains of quartz' *Radiation Measurements,* 47(9), pp. 770-777.

Duller, G.A.T. (2016) *Analyst v4.31.9 – User Manual.* Aberystwyth: U.K. Available at: http://users.aber.ac.uk/ggd/analyst_manual_v4_31_9.pdf (Accessed: 4th June 2016).

Duller, G.A.T., Bøtter-Jensen, L., Kohsiek, P., Murray, A.S. (1999b) 'A high sensitivity optically stimulated luminescence scanning system for measurement of single sand-size grains', *Radiation Protection Dosimetry,* 84(1-4), pp. 325-330.

Duller, G.A.T., Bøtter-Jensen, L., Murray, A.S., Truscott, A.J. (1999a) 'Single grain laser luminescence (SGLL) measurements using a novel automated reader', *Nuclear Instruments and Methods in Physics Research Section B: Beam Interactions with Materials and Atoms,* 155(4), pp. 506-514.

Durcan, J.A., King, G.E., Duller, G.A.T. (2015) 'DRAC: Dose Rate and Age Calculator for trapped charge dating', *Quaternary Geochronology,* 28, pp. 54-61.

Durcan,, J.A., Duller, G.A.T. (2011) 'The fast ratio: A rapid measure for testing the dominance of the fast component in the initial OSL signal from quartz', *Radiation Measurements,* 46(10), pp. 1065-1072.

Duval, M., Guilarte, V., Campana, I., Arnold, L.J., Miguens, L., Iglesias, J., Gonzalez-Sierra, S. (2018) 'Quantifying hydrofluoric acid etching of quartz and feldspar coarse grains based on weight loss estimates: implications for ESR and luminescence dating studies', *Ancient TL,* 36(1), pp. 1-14.

Erwin, K.L. (2009) 'Wetlands and global climate change: the role of wetland restoration in a changing world', *Wetlands Ecology and Management,* 17(1), pp. 71-84.

Fauchereau, N., Pohl, B., Reason, C.J,C., Rouault, M., Richard, Y. (2009) 'Recurrent daily OLR patterns in the Southern Africa/Southwest Indian Ocean region, implications for South African rainfall and teleconnections', *Climate Dynamics,* 32, pp. 575-591.

Finch, J.M., Hill, T.R. (2008) 'A late Quaternary pollen sequence from Mfabeni Peatland, South Africa: Reconstructing forest history in Maputaland', *Quaternary Research,* 70, pp. 442-460.

Finlayson, B., Kenyon, C. (2007) 'Lake Nuga Nuga: a Levee-dammed Lake in Central Queensland, Australia', *Geographical Research*, 45(3), pp. 246-261.

Fischer, E.M., Knutti, R. (2015) 'Anthropogenic contribution to global occurrence of heavy-precipitation and high-temperature extremes', *Nature Climate Change,* 5, pp. 560-565.

Fitchett, J.M., Grab, S.W. (2014) ‘A 66-year tropical cyclone record for south-east Africa: temporal trends in a global context’, *International Journal of Climatology,* 34, pp. 3604-3615.

Fuchs, M., Lang, A. (2001) ‘OSL dating of coarse-grain fluvial quartz using single-aliquot protocols on sediment from NE Peloponnese, Greece’, *Quaternary Science Reviews,* 20(5-9), pp. 783-787.

Galbraith, R. (2002) ‘A note on the variance of a background-corrected OSL count’, *Ancient TL,* 20(2), pp. 49-51.

Galbraith, R.F. (2005) *Statistics for Fission Track Analysis.* London: Chapman & Hall.

Galbraith, R.F., Green, P.F. (1990) ‘Estimating the component ages in a finite mixtue’, *International Journal of Radiation Applications and Instrumentation. Part D. Nuclear Tracks and Radiation Measurements,* 17(3), pp. 197-206.

Galbraith, R.F., Roberts, R.G. (2012) ‘Statistical aspects of equivalent dose and error calculation and display in OSL dating: An overview and some recommendations’, *Quaternary Geochronology,* 11, pp. 1-27.

Galbraith, R.F., Roberts, R.G., Laslett, G.M., Yoshida, H., Olley, J.M. (1999) ‘Optical dating of single and multiple grains of quartz from Jinmium rock shelter, Northern Australia: Part I, Experimental design and statistical models’, *Archaeometry,* 41(2), pp. 339-364.

Garcia-Herrera, R., Konnen, G.P., Wheeler, D.A., Prieto, M.R., Jones, P.D., Koek, F.B. (2005) CLIWOC: A climatological database for the World’s oceans 1750-1854’, *Climatic Change,* 73, pp. 1-12.

Gliganic, L.A., Cohen, T.J., Slack, M., Feathers, J.K. (2016) ‘Sediment mixing in aeolian sandsheets identified and quantified using single-grain optically stimulated luminescence’, *Quaternary Geochronology,* 32, pp. 53-66.

Godfrey-Smith, D.I., Huntley, D.J., Chen, W.H. (1988) ‘Optical dating studies of quartz and feldspar sediment extracts’, *Quaternary Science Reviews,* 7, pp. 373-380.

Goedicke, C. (1984) ‘Microscopic investigations of the quartz etching technique for TL dating’, *Nuclear Tracks and Radiation Measurements*, 9(2), 87-93.

Gray, H.J., Mahan, S. (2015) ‘Variables and potential models for the bleaching of luminescence signals in fluvial environments’, *Quaternary International,* 362, pp. 42-49.

Grenfell, S.E., Ellery, W.N. (2009) ‘Hydrology, sediment transport dynamics and geomorphology of a variable flow river: The Mfolozi River, South Africa’, *Water SA*, 35(2), pp. 271-282.

Grenfell, S.E., Ellery, W.N., Grenfell, M.C. (2009) ‘Geomorphology and dynamics of the Mfolozi River floodplain, KwaZulu-Natal, South Africa’, *Geomorphology*, 107, pp. 226-240.

Grenfell, S.E., Ellery, W.N., Grenfell, M.C., Ramsay, L.F., Flugel, T.J. (2010) ‘Sedimentary facies and geomorphic evolution of a blocked-valley lake: Lake Futululu, northern Kwazulu-Natal, South Africa’, *Sedimentology*, 57(5), pp. 1159-1174.

Grundling, A.T., van den Berg, E.C., Price, J.S. (2013) ‘Assessing the distribution of wetlands over wet and dry periods and land-use change on the Maputaland Coastal Plain, north-eastern KwaZulu-Natal, South Africa’, *South African Journal of Geomatics,* 2(2), pp. 120-139.

Guerin, G., Christophe, C., Philippe, A., Murray, A.S., Thomsen, K.J., Tribolo, C., Urbanova, P., Jain, M., Guibert, P., Mercier, N., Kreutzer, S., Lahaye, C. (2017) ‘Absorbed dose, equivalent dose, measured dose rates, and implications for OSL age estimates: Introducing the Average Dose Model’, *Quaternary Geochronology,* 41, pp. 163-173.

Guerin, G., Jain, M., Thomsen, K.J., Murray, A.S., Mercier, N. (2012) ‘Modelling dose rate to single grains of quartz in well-sorted sand samples: The dispersion arising from the presence of potassium feldspars and implications for single grain OSL dating’, *Quaternary Geochronology,* 27, pp. 52-65.

Guerin, G., Jain, M., Thomsen, K.J., Murray, A.S., Mercier, N. (2015) ‘Modelling dose rate to single grains of quartz in well-sorted sand samples: The dispersion arising from the presence of potassium feldspars and implications for single grain OSL dating’, *Quaternary Geochronology,* 27, pp. 52-65.

Hajdas, I., Lowe, D.J., Newnham, R.M., Bonani, G. (2006) ‘Timing of the late-glacial climate reversal in the Southern Hemisphere using high-resolution radiocarbon chronology for Kaipo bog, New Zealand’, *Quaternary Research,* 65(2), pp. 340-340.

Hansen, V., Murray, A., Buylaert, J-P., Yeo, E-Y., Thomsen, K. (2015) ‘A new irradiated quartz for beta source calibration’, *Radiation Measurements,* 81, pp. 123-127.

Hansen, V., Murray, A., Thomsen, K., Jain, M., Autzen, M., Buylaert, J-P. (2018) ‘Towards the origins of over-dispersion in beta source calibration’, *Radiation Measurements,* 120, pp. 157-162.

Hogg, A.G., Hua, Q., Blackwell, P.G., Niu, M., Buck, C.E., Guilderson, T.P., Heaton, T.J., Palmer, J.G., Reimer, P.J., Reimer, R.W., Turney, C.S.M., Zimmerman, S.R.H. (2013) ‘SHCAL13 Southern Hemisphere Calibration, 0-50,000 years cal BP’, *Radiocarbon,* 55(4), pp. 1889-1903.

Holmgren, K., Karlen, W., Lauritzen, S.E., Lee-Thorp, J.A., Partridge, T.C., Piketh, S., Repinski, P., Stevenson, C., Svanered, O., Tyson, P.D. (1999) ‘A 3000-year high-resolution stalagmite-based record of palaeoclimate for northeastern South Africa’, *The Holocene,* 9(3), pp. 295-309.

Holmgren, K., Lee-Thorp, J.A., Cooper, G.R.J., Lundblad, K., Partridge, T.C., Scott, L., Sithaldeen, R., Talma, A.S., Tyson, P.D. (2003) ‘Persistent millennial-scale climatic variability over the past 25,000 years in Southern Africa’, *Quaternary Science Reviews,* 22, pp. 2311-2326.

Hong, D-G. (1998) *Luminescence stimulated from quartz by green light: developments relevant to dating.* Unpublished PhD Thesis, University of Edinburgh.

Humphries, M.S., Benitez-Nelson, C.R., Bizimis, M., Finch, J.M. (2017) 'An Aeolian sediment reconstruction of regional wind intensity and links to larger scale climate variability since the last deglaciation from the east coast of southern Africa', *Global and Planetary Change,* 156, pp. 59-67.

Humphries, M.S., Green, A.N., Finch, J.M. (2016a) 'Evidence of El Niño driven desiccation cycles in a shallow estuarine lake: The evolution and fate of Africa's largest estuarine system, Lake St Lucia', *Global and Planetary Change,* 147, pp. 97-105.

Huntley, D.J., Godfrey-Smith, D.I., Haskell, E.H. (1991) 'Light-induced emission spectra from some quartz and feldspars', *International Journal of Radiation Applications and Instrumentation. Part D. Nuclear Tracks and Radiation Measurements,* 18(1-2), pp. 127-131.

Huntley, D.J., Godfrey-Smith, D.I., Thewalt, M.L.W. (1985) 'Optical dating of sediments', *Nature,* 313, pp. 105-107.

Huntley, D.J., Lian, O.B. (2006) 'Some observations on tunnelling of trapped electrons in feldspars and their implications for optical dating', *Quaternary Science Reviews,* 25(19-20), pp. 2503-2512.

IPCC (2014) *Climate Change 2014: Synthesis Report. Contribution of Working Groups I, II and III to the Fifth Assessment Report of the Intergovernmental Panel on Climate Change.* Geneva: IPCC. Available at: https://www.ipcc.ch/pdf/assessment-report/ar5/syr/SYR_AR5_FINAL_full_wcover.pdf (Accessed: 17 January 2017).

Jackson, M.L., Sayin, M., Clayton, R.N. (1976) 'Hexafluorosilicic Acid Reagent Modification for Quartz Isolation', *Soil Science Society of America,* 40(6), pp. 958-960.

Jacobs, Z., Duller, G.A.T., Wintle, A.G. (2006) 'Interpretation of single grain $D_e$ distributions and calculation of $D_e$', *Radiation Measurements,* 41, pp. 264-277.

Jacobs, Z., Wintle, A.G., Roberts, R.G., Duller, G.A.T. (2008) 'Equivalent dose distributions from single grains of quartz at Sibudu, South Africa: context, causes and consequences for optical dating of archaeological deposits', *Journal of Archaeological Science,* 35(7), pp. 1808-1820.

Jain, M., Murray, A.S., Bøtter-Jensen, L. (2004) 'Optically stimulated luminescence dating: How significant is incomplete light exposure in fluvial environments?', *Quaternaire,* 15(1-2), pp. 143-157.

Jankowski, N.R., Jacobs, Z. (2018) 'Beta dose variability and its spatial contextualisation in samples used for optical dating: An empirical approach to examining beta microdosimetry', *Quaternary Geochronology,* 44, pp. 23-37.

Jia, J., Yang, Y., Cai, T., Gao, J., Xia, X., Li, Y., Gao, S. (2018) 'On the sediment age estimated by $^{210}$Pb dating: probably misleading "prolonging" and multiple-factor-caused "loss"', *Acta Oceanologica Sinica,* 37(6), pp. 30-39.

Jones, P.D., Salmon, M. (2005) 'Preliminary reconstructions of the North Atlantic Oscillation and the Southern Oscillation Index from measures of wind strength and direction taken during the CLIWOC period', *Climatic Change,* 73, pp. 131-154.

Jongman, B., Winsemius, H.C., Aerts, J.C.J.H., de Perez, E.C., van Aalst, M.K., Kron, W., Ward, P.J. (2015) 'Declining vulnerability to river floods and the global benefits of adaptation', *Proceedings of the National Academy of Sciences,* 112(18), pp. 2271-2280.

Jury, M.R. (1996) 'Regional teleconnection patterns associated with summer rainfall over South Africa, Namibia and Zimbabwe', *International Journal of Climatology,* 16, pp. 135-153.

Jury, M.R. (2019) 'South Africa's Future Climate: Trends and Projections', in Knight, J., Rogerson, C. (eds.) *The Geography of South Africa.* Switzerland: Springer International Publishing, pp. 305-312.

Kovacs, Z.P. (1988) 'Preliminary hydrological assessment of the Natal flood', *Civil Engineering = Siviele Ingenieurswese,* 30(1), pp. 7-13.

Kovacs, Z.P., Du Plessis, D.B., Bracher, P.R., Dunn, P., Mallory, G.C.L. (1985) Documentation of the 1984 Domoina Floods. Republic of South Africa: Department of Water Affairs.

Kreutzer, S., Burow, C., Dietze, M., Fuchs, M.C., Schmidt, C., Fischer, M., Friedrich, J. (2018). Luminescence: Comprehensive Luminescence Dating Data Analysis. R package version 0.9.0. https://CRAN.R-project.org/package=Luminescence.

Kreutzer, S., Schmidt, C., Fuchs, M.C., Dietze, M., Fischer, M., Fuchs, M. (2012) 'Introducing an R package for luminescence dating analysis', *Ancient TL,* 30(1), pp. 1-8.

Kruger, A.C. (1999) 'The influence of the decadal-scale variability of summer rainfall on the impact of El Nino and La Nina events in South Africa', *International Journal of Climatology,* 19, pp. 59-68.

Kruger, A.C. (2006) 'Observed trends in daily precipitation indices in South Africa: 1910-2004', *International Journal of Climatology,* 26, pp. 2275-2285.

Lee-Thorp, J.A., Holmgren, K., Lauritzen, S.E., Linge, H., Moberg, A., Partridge, T.C., Stevenson, C., Tyson, P.D. (2001) 'Rapid climate shifts in the southern Arfican interior throughout the Mid to Late Holocene', *Geophysical Research Letters,* 28(23), pp. 4507-4510.

Lehmann, J., Coumou, D., Frieler, K. (2015) 'Increased record-breaking precipitation events under global warming', *Climatic Change,* 132, pp. 501-515.

Lepper, K., Larsen, N.A., McKeever, S.W.S. (2000) 'Equivalent dose distribution analysis of Holocene eolian and fluvial quartz sands from Central Oklahoma', *Radiation Measurements,* 32(5-6), pp. 603-608.

Lepper, K., McKeever, S.W.S. (2002) 'An objective methodology for dose distribution analysis', *Radiation Protection Dosimetry,* 101(1-4), pp. 349-352.

Li, B., Jacobs, Z., Roberts, R.G., Li, S-H. (2013) 'Extending the age limit of luminescence dating using the dose-dependent sensitivity of MET-pIRIR signals from K-feldspar', *Quaternary Geochronology,* 17, pp. 55-67.

Li, B., Li, S-H. (2011) ‘Luminescence dating of K-feldspar from sediments: A protocol without anomalous fading correction’, *Quaternary Geochronology,* 6(5), pp. 468-479.

Li, G., Dong, G., Wen, L., Chen, F. (2014) ‘Overbank flooding and human occupation of the Shlongka site in the Upper Yellow River Valley, northeast Tibet Plateau in relation to climate change since the last deglaciation’, *Quaternary Research,* 82(2), pp. 354-365.

Lindsay, P., Mason, T.R., Pillay, S., Wright, C.I. (1996) ‘Suspended particulate matter and dynamics of the Mfolozi estuary, KwaZulu-Natal: Implications for environmental management’, *Environmental Geology*, 28(1), pp. 40-51.

Liritzis, I., Stamoulis, K., Papachristodoulou, C., Ioannides, K. (2013) ‘A re-evaluation of radiation dose-rate conversion factors’, *Mediterranean Archaeology and Archaeometry,* 13(3), pp. 1-15.

Liu, Z., Zhu, J., Rosenthal, Y., Zhang, X., Otto-Bliesner, B.L., Timmerman, A., Smith, R.S., Lohmann, G., Zheng, W., Timm, O.E. (2014) ‘The Holocence temperature conundrum’, *Proceedings of the National Academy of Sciences,* 111(34), pp. E3501-E3505.

Lomax, J., Hilgers, A., Radtke, U. (2011) ‘Palaeoenvironmental change recorded in the palaeodunefields of the western Murray Basin, South Australia – New data from single-grain OSL-dating’, *Quaternary Science Reviews,* 30(5-6), pp. 723-736.

Lombard, M., Wadley, L., Jacobs, Z., Mohapi, M., Roberts, R.G. (2010) ‘Still Bay and serrated points from Umhlatuzana Rock Shelter, Kwazulu-Natal, South Africa’, *Journal of Archaeological Science,* 37(7), pp. 1773-1784.

Lyons, R., Tooth, S., Duller, G.A.T. (2013) ‘Chronology and controls of donga (gully) formation on the upper Blood River catchment, KwaZulu-Natal, South Africa: Evidence for a climatic driver of erosion’ *The Holocene,* 23(12), pp. 1875-1887.

MacKellar, N., New, M., Jack, C. (2014) ‘Observed and modelled trends in rainfall and temperature for South Africa: 1960-2010’, *South African Journal of Science,* 110(7/8), pp. 51-63.

Madsen, A.T., Duller, G.A.T., Donnelly, J.P., Roberts, H.M., Wintle, A.G. (2009) 'A chronology of hurricane landfalls at Little Sippewissett Marsh, Massachusetts, USA, using optical dating', *Geomorphology,* 109(1-2), pp. 36-45.

Madsen, A.T., Murray, A.S., Andersen, T.J. (2007) 'Optical Dating of Dune Ridges on Rømø, a Barrier Island in the Wadden Sea, Denmark, *Journal of Coastal Research,* 23(5), pp. 1259-1269.

Madsen, A.T., Murray, A.S., Andersen, T.J., Pejrup, M., Breuning-Madsen, H. (2005) 'Optically stimulated luminescence dating of young esturine sediments: a comparison with $^{210}$Pb and $^{137}$Cs dating', *Marine Geology,* 214(1-3), pp. 251-268.

Malherbe, J., Dieppois, B., Maluleke, P., Van Staden, M., Pillay, D.L. (2016) 'South African droughts and decadal variability', *Natural Hazards,* 80(1), pp. 657-681.

Marcott, S.A., Shakun, J.D. (2015) 'Holocene climate change and its context for the future', *Pages,* 23(1), p. 28.

Marcott, S.A., Shakun, J.D., Clark, P.U., Mix, A.C. (2013) 'A Reconstruction of Regional and Global Temperature for the Past 11,300 Years', *Science,* 339, pp. 1198-1201.

Markey, B.G., Bøtter-Jensen, L., Duller, G.A.T. (1997) 'A new flexible system for measuring thermally and optically stimulated luminescence', *Radiation Measurements,* 27(2), pp. 83-89.

Martin, L., Incerti, S., Mercier, N. (2015b) 'DosiVox: Implementing Geant 4-based software for dosimetry simulations relevant to luminescence and ESR dating techniques', *Ancient TL,* 33(1), pp. 1-10.

Martin, L., Mercier, N., Incerti, S., Lefrais, Y., Pecheyran, C., Guerin, G., Jarry, M., Bruxelles, L., Bon, F., Pallier, C. (2015a) 'Dosimetric study of sediments at the beta dose rate scale: Characterisation and modelization with the DosiVox software', *Radiation Measurements,* 81, pp. 134-141.

Mason, S.J., Waylen, P.R., Mimmack, G.M., Rajaratnam, B., Harrison, J.M. (1999) 'Changes in extreme rainfall events in South Africa', *Climatic Change,* 41, pp. 249-257.

Mauz, B., Bode, T., Mainz, E., Blanchard, H., Hilger, W., Dikau, R., Zöller, L. (2002) 'The luminescence dating laboratory at the University of Bonn: equipment and procedures', *Ancient TL,* 20(2), pp. 53-61.

Mavume, A.F., Rydberg, L., Rouault, M., Lutjeharms, J.R.E. (2009) 'Climatology and Landfall of Tropical Cyclones in the South-West Indian Ocean', *Western Indian Ocean Journal of Marine Science,* 8(1), pp. 15-36.

Mayewski, P.A., Rohling, E.E., Stager, J.C., Karlen, W., Maasch, K.A., Meeker, L.D., Meyerson, E.A., Gasse, F., van Kreveld, S., Holmgren, K., Lee-Thorp, J., Rosqvist, G., Rack, F., Staubwasser, M., Schneider, R.R., Steig, E.J. (2004) 'Holocene climate variability', *Quaternary Research,* 62, pp. 243-255.

Mayya, Y.S., Morthekai, P., Murari, M.K., Singhvi, A.K. (2006) 'Towards quantifying beta microdosimetric effects in single-grain quartz dose distribution', *Radiation Measurements,* 41(7-8), pp. 1032-1039.

McCloskey, T.A., Liu, K. (2012) 'A 7000 year record of paleohurricane activity from a coastal wetland in Belize', *The Holocene,* 23(2), pp. 278-291.

McGlue, M.M., Silva, A., Zani, H., Corradini, F.A. (2012) 'Lacustrine records of Holocene flood pulse dynamics in the Upper Paraguay River watershed (Pantanal wetlands, Brazil)', *Quaternary Research,* 78(2), pp. 285-294.

Mejdahl, V. (1979) 'Thermoluminescence dating: Beta-dose attenuation in quartz grains', *Archaeometry,* 21(1), pp. 61-72.

Mercier, N., Falguéres, C. (2007) 'Field gamma dose-rate measurement with a NaI(Tl) detector: re-evaluation of the "threshold" technique', *Ancient TL,* 25(1), pp. 1-4.

Millard, A.R. (2006) 'Bayesian analysis of ESR dates, with application to Border Cave', *Quaternary Geochronology,* 1(2), pp. 159-166.

Mitsch, W.J., Bernal, B., Nahlik, A.M., Mander, Ü., Zhang, L., Anderson, C.J., Jørgensen, S.E., Brix, H. (2013) 'Wetlands, carbon and climate change', *Landscape Ecology,* 28, pp. 583-597.

Mousavi, M.E., Irish, J.L., Frey, A.E., Olivera, F., Edge, B.L. (2011) 'Global warming and hurricanes: the potential impact of hurricane intensification and sea level rise on coastal flooding', *Climatic Chance,* 104(3-4), pp. 575-597.

Munich Re (2017) *NatCatSERVICE Database.* Munich: Munich Re. Available at: http://natcatservice.munichre.com/events/1 (Accessed: 15 May 2017).

Murray, A., Marten, R., Johnston, A., Martin, P. (1987) 'Analysis for naturally occurring radionuclides at environmental concentrations by gamma spectrometry', *Journal of Radioanalytical and Nuclear Chemistry,* 115(2), pp. 263-288.

Murray, A.S., Olley, J.M. (2002) 'Precision and accuracy in the optically stimulated luminescence dating of sedimentary quartz: A status review', *Geochronometria,* 21, pp. 1-16.

Murray, A.S., Olley, J.M., Caitcheon, G.G. (1995) 'Measurement of equivalent doses in quartz from contemporary water-lain sediments using optically stimulated luminescence', *Quaternary Science Reviews,* 14(4), pp. 365-371.

Murray, A.S., Roberts, R.G. (1998) 'Measurement of the equivalent dose in quartz using a regenerative-dose single-aliquot protocol', *Radiation Measurements,* 29(5), pp. 503-515.

Murray, A.S., Svendsen, J.I., Mangerud, J., Astakhov, V.I. (2007) 'Testing the accuracy of quartz OSL dating using a known-age Eemian site on the river Sula, northern Russia', *Quaternary Geochronology,* 2(1-4), pp. 102-109.

Murray, A.S., Thomsen, K.J., Masuda, N., Buylaert, J.P., Jain, M. (2012) 'Identifying well-bleached quartz using the different rates of quartz and feldspar luminescence signals', *Radiation Measurements,* 47(9), pp. 688-695.

Murray, A.S., Wintle, A.G. (1999) 'Isothermal decay of optically stimulated luminescence in quartz', *Radiation Measurements,* 30(1), pp. 119-125.

Murray, A.S., Wintle, A.G. (2000) ‘Luminescence dating of quartz using an improved single-aliquot regenerative-dose protocol’, *Radiation Measurements,* 32, pp. 57-73.

Murray, A.S., Wintle, A.G. (2003) ‘The single aliquot regenerative dose protocol: potential for improvements in reliability’, *Radiation Measurements,* 37, pp. 377-381.

Murray, A.S., Wintle, A.G., (2000) ‘Luminescence dating of quartz using an improved single-aliquot regenerative-dose protocol’, *Radiation Measurements,* 32(1), pp. 57-73.

Nathan, R.P., Thomas, P.J., Jain, M., Murray, A.S., Rhodes, E.J. (2003) ‘Environment dose rate heterogeneity of beta radiation and its implications for luminescence dating: Monte Carlo modelling and experimental validation’, *Radiation Measurements,* 37(4-5), pp. 305-313.

Nel, W. (2009) ‘Rainfall trends in the KwaZulu-Natal Drakensberg region of South Africa during the twentieth century’, *International Journal of Climatology,* 29, pp. 1634-1641.

Neller, R.J., Salo, J.S., Räsänen, M.E. (1992) ‘On the formation of blocked valley lakes by channel avulsion in upper Amazon foreland basins’, *Z.Geomorph,* 36, pp. 401-411.

Nelson, M.S., Rittenour, T.M. (2015) ‘Using grain-size characteristics to model soil water content: Application to dose-rate calculation for luminescence dating’, *Radiation Measurements*, 81, pp. 142-149.

Neumann, F.H., Scott, L., Bousman, C.B., van As, L. (2010) ‘A Holocene sequence of vegetation change at Lake Eteza, coastal KwaZulu-Natal, South Africa’, *Review of Palaeobotany and Palynology,* 162, pp. 39-53.

Neumann, F.H., Stager, J.C., Scott, L., Venter, H.J.T., Weyhenmeyer, C. (2008) ‘Holocene vegetation and climate records from Lake Sibaya, KwaZulu-Natal (South Africa)’, *Review of Palaeobotany and Palynology,* 152, pp. 113-128.

Nicholson, S.E. (1997) ‘An analysis of the ENSO signal in the tropical Atlantic and western Indian Oceans’, *International Journal of Climatology,* 17, pp.345-375.

Nicholson, S.E. (2001) ‘Climatic and environmental change in Africa during the last two centuries’ *Climate Research,* 17, pp. 123-144.

Norström, E., Scott, L., Partridge, T.C., Risberg, J., Holmgren, K. (2009) ‘Reconstruction of environmental and climate changes at Braamhoek wetland, eastern escarpment South Africa, during the last 16,000 years with emphasis on the Pleistocene-Holocene transition’, *Palaeogeography, Palaeoclimatology, Palaeoecology,* 271, pp. 240-258.

Olley, J., Caitcheion, G., Murray, A. (1998) ‘The distribution of apparent dose a determined by optically stimulated luminescence in small aliquots of fluvial quartz: Implications for dating young sediments’, *Quaternary Science Reviews,* 17(11), pp. 1033-1040.

Olley, J., Roberts, R.G., Murray, A.S. (1997) ‘Disequilibria in the uranium decay series in sedimentary deposits at Allen’s Cave, Nullarbor Plain, Australia: Implications for dose rate determinations’, *Radiation Measurements,* 27(2), pp. 433-443.

Olley, J.M., Caitcheon, G.C., Roberts, R.G. (1999) ‘The origin of dose distributions in fluvial sediments, and the prospect of dating single grains from fluvial deposits using optically stimulated luminescence’, *Radiation Measurements,* 30(2), pp. 207-217.

Olley, J.M., De Deckker, P., Roberts, R.G., Fifield, L.K., Yoshida, H., Hancock, G. (2004) ‘Optical dating of deep-sea sediments using single grains of quartz: a comparison with radiocarbon’, *Sedimentary Geology,* 169(3-4), pp. 175-189.

Olley, J.M., Murray, A.S., Roberts, R.G. (1996) ‘The Effects of Disequilibria in the Uranium and Thorium Decay Chains on Burial Dose Rates in Fluvial Sediments’, *Quaternary Science Reviews,* 15, pp. 751-760.

Olley, J.M., Pietsch, T., Roberts, R.G. (2004) ‘Optical dating of Holocene sediments from a variety of geomorphic settings using single grains of quartz’, *Geomorphology,* 60(3-4), pp. 337-358.

Olley, J.M., Roberts, R.G., Murray, A.S. (1997) ‘Disequilibria in the uranium decay series in sedimentary deposits at Allen’s Cave, Nullarbor Plain, Australia: Implications for dose rate determinations’, *Radiation Measurements,* 27(2), pp. 433-443.

Olley, J.M., Roberts, R.G., Yoshida, H., Bowler, J.M. (2006) ‘Single-grain optical dating of grave-infill associated with human burials at Lake Mungo, Australia’, *Quaternary Science Reviews,* 25(19-20), pp. 2469-2474.

Ouyang, Z., Becker, R., Shaver, W., Chen, J. (2014) ‘Evaluating the sensitivity of wetlands to climate change with remote sensing techniques’, *Hydrological Processes,* 28, pp. 1703-1712.

Owen, L.A., Kamp, U., Spencer, J.Q., Haserodt. (2002) ‘Timing and style of the Late Quaternary glaciation in the eastern Hindu Kush, Chitral, northern Pakistan: a review and revision of the glacial chronology based on new optically stimulated luminescence dating’, *Quaternary International*, 97-98, pp. 41-55.

Parker, G., Muto, T., Akamatsu, Y., Dietrich, W.E., Lauer, J.W. (2008) ‘Unravelling the conundrum of river response to rising sea-level from laboratory to field. Part II. The Fly-Strickland River system, Papua New Guinea’, *Sedimentology,* 55(6), pp. 1657-1686.

Partridge, T.C., Scott, L., Hamilton, J.E. (1999) ‘Synthetic reconstructions of southern African environments during the Last Glacial Maximum (21-18 kyr) and the Holocene Altithermal (8-6 kyr)’, *Quaternary International,* 57/58, pp. 207-214.

Porat, N., Botham G. (2008) ‘The luminescence chronology of dune development of the Maputaland coastal plain, southeast Africa’, *Quaternary Science Reviews,* 27, pp. 1024-1046.

Porat, N., Faerstein, G., Medialdea, A., Murray, A.S. (2015) ‘Re-examination of common extraction and purification methods of quartz and feldspar for luminescence dating’, *Ancient TL*, 33(1), pp. 22-30.

Prescott, J.R., Hutton, J.T. (1988) ‘Cosmic Ray and Gamma Ray Dosimetry for TL and ESR’, *Nuclear Tracks and Radiation Measurements,* 14(1/2), pp. 223-227.

Prescott, J.R., Hutton, J.T. (1994) ‘Cosmic Ray Contributions to Dose Rates for Luminescence and ESR Dating: Large Depths and Long-Term Time Variations, *Radiation Measurements,* 23(2/3), pp. 497-500.

Preusser, F., Chithambo, M.L., Götte, T., Martini, M., Ramseyer, K., Sendezera, E.J., Susino, G.J., Wintle, A.G. (2009) ‘Quartz as a natural luminescence dosimeter’, *Earth Science Reviews,* 97, pp. 196-226.

Ramsay, P.J. (1995) ‘9000 years of sea-level change along the southern African coastline’, *Quaternary International,* 31, pp. 71-75.

Ramsay, P.J., Cooper, J.A.G. (2002) ‘Late Quaternary Sea-Level change in South Africa’, *Quaternary Research,* 57, pp. 82-90.

Reason, C.J.C., Mulenga, H. (1999) ‘Relationships between South African rainfall and SST anomalies in the southwest Indian Ocean’, *International Journal of Climatology,* 19, pp. 1651-1673.

Rees-Jones, J. (1995) ‘Optical Dating Of Young Sediments Using Fine-Grain Quartz’, *Ancient TL,* 13(2), pp. 9-14.

Repinski, P., Holmgren, K., Lauritzen, S.E., Lee-Thorp, J.A. (1999) ‘A later Holocene climate record from a stalagmite, Cold Air Cave, Northern Province, South Africa’, *Palaeogeography, Palaeoclimatology, Palaeoecology,* 150, pp. 269-277.

Rhodes, E.J. (2011) ‘Optically stimulated luminescence dating of sediments over the past 200,000 years’, *Annual Review of Earth and Planetary Sciences,* 39, pp. 461-488.

Rhodes, E.J., Bronk Ramsey, C., Outram, Z., Batt, C., Willis, L., Dockrill, S., Bond, J. (2003) ‘Bayesian methods applied to the interpretation of multiple OSL dates: high precision sediment ages from Old Scatness Broch excavations, Shetland Isles’, *Quaternary Science Reviews,* 22(10-13), 1231-1244.

Rhodes, E.J., Fanning, P.C., Holdaway, S.J. (2010) 'Developments in optically stimulated luminescence age control for geoarchaeological sediments and hearths in western New South Wales, Australia', *Quaternary Geochronology,* 5(2-3), pp. 348-352.

Rittenour, T.M. (2008) 'Luminescence dating of fluvial deposits: applications to geomorphic, palaeoseismic and archaeological research', *Boreas,* 37, pp. 613-635.

Roberts, H.M. (2007) 'Assessing the effectiveness of the double-SAR protocol in isolating a luminescence signal dominated by quartz', *Radiation Measurements*, 42, pp. 1627-1636.

Roberts, R.G., Galbraith, R.F., Yoshida, H., Laslett, G.M., Olley, J.M. (2000) 'Distinguishing dose populations in sediment mixtures: a test of single-grain optical dating procedures using mixtures of laboratory dosed-quartz', *Radiation Measurements,* 32(5-6), pp. 459-465.

Roberts, R.G., Jacobs, Z., Li, B., Jankowski, N.R., Cunningham, A.C., Rosenfeld, A.B. (2015) 'Optical dating in archaeology: thirty years in retrospect and grand challenges for the future', *Journal of Archaeological Science,* 56, pp. 41-60.

Rodnight, H. (2008) 'How many equivalent dose values are needed to obtain a reproducible distribution?', *Ancient TL,* 26(1), pp. 3-9.

Rodnight, H., Duller, G.A.T., Wintle, A.G., Tooth, S. (2006) 'Assessing the reproducibility and accuracy of optical dating fluvial deposits', *Quaternary Geochronology,* 1(2), pp. 109-120.

Rowland, J.C., Dietrich, W.E. (2006) 'The evolution of a tie channel', in Parker, G. and Garcia, M.H (eds.) *River, Coastal and Estuarine Morphodynamics,* London: Taylor Francis Group, pp. 725-736.

Rowland, J.C., Dietrich, W.E., Day, G., Parker, G. (2009) 'Formation and maintenance of single-thread tie channels entering floodplain lakes: Observations from three diverse river systems', *Journal of Geophysical Research,* 114(F2), F02013.

Rowland, J.C., Lepper, K., Dietrich, W.E., Wilson, C.J., Sheldon, R. (2005) 'Tie channel sedimentation rates, oxbow formation age and channel migration rate from optically stimulated luminescence analysis of floodplain deposits', *Earth Surface Processes and Landforms,* 30, pp. 1161-1179.

Santisteban, J.I., Mediavilla, R., de Frutos, L.G., Cilla, I.L. (2019) 'Holocene floods in a complex fluvial wetland in central Spain: Environmental variability, climate and time', *Global and Planetary Change,* 181, pp. 1-16.

Schneider, C.A., Rasband, W.S., Eliceiri, K.W. (2012) 'NIH Image to ImageJ: 25 years of image analysis', *Nature Methods,* 9, pp. 671-675.

Schneider, T., Bischoff, T., Haug, G. (2014) 'Migrations and dynamics of the intertropical convergence zone', *Nature,* 513, pp. 45-53.

Schulte E, Hopkins B. (1996) 'Estimation of soil organic matter by weight loss-on-ignition', in Magdoff F, Tabatabai M, Hanlon E (eds.) *Soil organic matter: Analysis and interpretation*. Madison: Soil Science Society of America, pp. 21-31.

Scott, L. (1982) 'Late Quaternary fossil pollen grains from the Transvaal, South Africa', *Review of Palaeobotany and Palynology,* 36(3-4), pp. 241-278.

Scott, L., Holmgren K., Talma, A.S., Woodborne, S., Vogel, J.C. (2003) 'Age interpretation of the Wonderkrater spring sediments and vegetation change in the Savanna biome, Limpopo province, South Africa', *South African Journal of Science,* 99, pp. 484-488.

Scott, L., Steenkamp, M., Beaumont, P.B. (1995) 'Palaeoenvironmental conditions in South Africa at the Pleistocene-Holocene transition', *Quaternary Science Reviews,* 14(9), pp. 937-947.

Scott, L., Thackeray, J.F. (1987) 'Multivariate analysis of late Pleistocene and Holocene pollen spectra from Wonderkrater, Transvaal, South Africa', *South African Journal of Science,* 83, pp. 93-98.

Singarayer, J.S., Bailey, R.M. (2003) 'Further investigations of the quartz optically stimulated luminescence components using linear modulation', *Radiation Measurements,* 37(4-5), pp. 451-458.

Singarayer, J.S., Bailey, R.M., Ward, S., Stokes, S. (2005) 'Assessing the completeness of optical resetting of quartz in the natural environment', *Radiation Measurements,* 40(1), pp. 13-25.

Singleton, A.T., Reason, C.J.C. (2007) 'Variability in the characteristic of cut-off low pressure systems over subtropical southern Africa', *International Journal of Climatology,* 27, pp. 295-310.

Spooner, N.A. (1994) 'The anomalous fading of infrared-stimulated luminescence from feldspars', *Radiation Measurements,* 23(2-3), pp. 625-632.

Srivastava, P., Juyal, N., Singhvi, A.K., Wasson, R.J., Bateman, M.D. (2001) 'Luminescence chronology of river adjustment and incision of Quaternary sediments in the alluvial plain of the Sabarmati River, north Gujarat, India', *Geomorphology*, 36(3-4), pp. 217-229.

Stager, J.C., Ryves, D.B., King, C., Madson, J., Hazzard, M., Neumann, F.H., Maud, R. (2013) 'Late Holocene precipitation variability in the summer rainfall region of South Africa', *Quaternary Science Reviews,* 67, pp. 105-120.

Steig, E.J., Morse, D.L., Waddington, E.D., Stuiver, M., Grootes, P.M., Mayewski, P.A., Twickler, M.S., Whitlow, S.I. (2000) 'Wisconsinan and Holocene climate history from an ice core at Taylor Dome, Western Ross Embayment, Antarctica', *Geografiska Annaler,* 82(2-3), pp. 213-235.

Stockmann, U., Minasny, B., Pietsch, T.J., McBratney, A.B. (2013) 'Quantifying processes of pedogenesis using optically stimulated luminescence', *European Journal of Soil Science,* 64, pp. 145-160.

Stokes, S., Bray, H.E., Blum, M.D. (2001) 'Optical resetting in large drainage basins: tests of zeroing assumptions using single-aliquot procedures', *Quaternary Science Reviews,* 20(5-9), pp. 879-885.

Strack, M. (2008) 'Executive Summary for Policymakers "Peatlands in Global Change"', in Stack, M. (ed.) *Peatlands and Climate Change.* Jyväskylä: International Peat Society, pp. 9-12.

Swales, S., Storey, A.W., Roderick, I.D., Figa, B.S. (1999) 'Fishes of floodplain habitats of the Fly River system, Papua New Guinea, and changes associated with El Niño droughts and algal blooms', *Environmental Biology of Fishes,* 54, pp. 389-404.

Talma, A.S., Vogel, J.C. (1992) 'Late Quaternary paleotemperatures derived from a speleothem from Cango Caves, Cape Province, South Africa', *Quaternary Research,* 37, pp. 203-213.

Tanoue, M., Hirabayashi, Y., Ikeuchi, H. (2016) 'Global-scale river flood vulnerability in the last 50 years', *Scientific Reports,* 6, 36021.

Taylor, A.R.D., Howard, G.W., Begg, G.W. (1995) 'Developing wetland inventories in Southern Africa: A review', *Vegetatio,* 118(1/2), pp. 57-79.

The Weather Company (2015) *Tropical Storm Domoina.* USA. Available at: https://www.wunderground.com/hurricane/southern-indian/1984/Tropical-Storm-Domoina (Accessed: 09th January 2017).

Thompson, J.A., Chen, J., Yang, H., Li, T., Bookhagen, B., Burbank, D. (2018) 'Coarse- versus fine-grain quartz OSL and cosmogenic $^{10}$Be dating of deformed fluvial terraces on the northweast Pamir margin, northwest China', *Quaternary Geochronology,* 46, pp. 1-15.

Thomsen, K.J., Murray, A.S., Bøtter-Jensen, L. (2005) 'Sources of variability in OSL dose measurements using single grains of quartz', *Radiation Measurements,* 39(1), pp. 47-61.

Thomsen, K.J., Murray, A.S., Bøtter-Jensen, L., Kinahan, J. (2007) 'Determination of burial dose in incompletely bleached fluvial samples using single grains of quartz', *Radiation Measurements,* 42(3), pp. 370-379.

Thomsen, K.J., Murray, A.S., Buylaert, J.P., Jain, M., Hansen, J.H., Aubry, T. (2016) 'Testing single-grain quartz OSL method using sediment samples with independent age control from the Bordes-Fitte rockshelter (Roches d'Abilly site, Central France)', *Quaternary Geochronology,* 31, pp. 77-96.

Thomsen, K.J., Murray, A.S., Jain, M. (2012) 'The dose dependency of the over-dispersion of quartz OSL single grain dose distributions', *Radiation Measurements,* 47(9), pp. 732-739.

Thomsen, K.J., Murray, A.S., Jain, M., Bøtter-Jensen, L. (2008) 'Laboratory fading rates of various luminescence signals form feldspar-rich sediment extracts', *Radiation Measurements,* 43(9-10), pp. 1474-1486.

Truscott, A.J., Duller, G.A.T., Bøtter-Jensen, L., Murray, A.S., Wintle, A.G. (2000) 'Reproducibility of optiallcay stimulated luminescence measurements from single grains of $Al_2O_3$:C and annealed quartz', *Radiation Measurements,* 32(5-6), pp. 447-451.

Turner, S., Plater, A. (2004) 'Palynological evidence for the origin and development of late Holocene wetland sediments: Mdlanzi Swamp, KwaZulu-Natal, South Africa', *South African Journal of Science,* 100, pp. 220-229.

Tyson, P.D., Dyer, T.G.J., Mametse, M.N. (1975) 'Secular changes in South African rainfall: 1880 to 1972', *Quarterly Journal of the Royal Meteorological Society,* 101(430), pp. 817-833.

Tyson, P.D., Karlen, W., Holmgren, K., Heiss, G.A. (2000) 'The Little Ice Age and medieval warming in South Africa', *South African Journal of Science,* 96, pp. 121-126.

Tyson, P.D., Preston-Whyte, R.A. (2000) *The Weather and Climate of Southern Africa.* 2nd ed. Cape Town: Oxford University Press.

U.S. Geological Society (1978) 'LM31790801978201AAA04', Available at: http://earthexplorer.usgs.gov/ (Accessed: 03 September 2015).

U.S. Geological Society (1984) 'LT51670801984153XXX01, Available at: http://earthexplorer.usgs.gov/ (Accessed: 03 September 2015).

U.S. Geological Society (2015) 'LC81670802015174LGN00', Available at: http://earthexplorer.usgs.gov/ (Accessed: 03 September 2015).

Umfolozi Sugar Mill (2015) *Umfolozi Sugar Mill History.* South Africa. Available at: http://www.umfolozisugarmill.co.za/page.aspx?ID=5855 (Accessed: 21st December 2015).

Vogel, J.C., Fuls, A., Visser, E. (2001) ‘Radiocarbon adjustments to the dendrochronology of a yellowwood tree’, *South African Journal of Science,* 97, pp. 164-166.

Wallinga, J. (2002) ‘Optically stimulated luminescence dating of fluvial deposits: a review’, *Boreas,* 31, pp. 302-322.

Webster, P.J., Holland, G.J., Curry, J.A., Chang, H.-R. (2005) ‘Changes in Tropical Cyclone Number, Duration, and Intensity in a Warming Environment’, *Science,* 309, pp. 1844-1846.

Wintle, A.G. (1973) ‘Anomalous Fading of Thermo-luminescence in Mineral Samples’, *Nature,* 245, pp. 143-144.

Wintle, A.G. (1975) ‘Thermal quenching of thermoluminescence in quartz’, *Geophysical Journal of the Royal Astronomical Society,* 41(1), pp. 107-113.

Wintle, A.G., Murray, A.S. (1997) ‘The relationship between quartz thermoluminescence, photo-transferred thermoluminescence and optically stimulated luminescence’, *Radiation Measurements,* 27(4), pp. 611-624.

Wintle, A.G., Murray, A.S. (1998) ‘Factors controlling the shape of the OSL decay curve in quartz’, *Radiation Measurements,* 29(1), pp. 65-79.

Wintle, A.G., Murray, A.S. (1998) ‘Towards the development of a preheat procedure for OSL dating of quartz’, *Radiation Measurements,* 29(1), pp. 81-94.

Wintle, A.G., Murray, A.S. (2000) ‘Quartz OSL: Effects of thermal treatment and their relevance to laboratory dating procedures’, *Radiation Measurements,* 32(5-6), pp. 387-400.

Wintle, A.G., Murray, A.S. (2006) ‘A review of quartz optically stimulated luminescence characteristics and their relevance in single-aliquot regeneration dating protocols’, *Radiation Measurements,* 41(4), pp. 369-391.

Woda, C., Fuchs, M. (2008) ‘On the applicability of the leading edge method to obtain equivalent doses in OSL dating and dosimetry’, *Radiation Measurements,* 43(1), pp. 26-37.

Wood, J.C. (2015) ‘Section 1.2.3: Determination of Moisture Content and Total Organic Carbon within Basin Environments: Loss-on-Ignition’, in Cook, S.J., Clarke, L.E., Nield, J.M (eds.) *Geomorphological Techniques (Online Edition).* London: British Society for Geomorphology, pp. 1-7.

Zedler, J.B., Kercher, S. (2005) ‘Wetland Resources: Status, Trends, Ecosystem Services, and Restorability’, *Annual Review of Environment and Resources,* 30, pp. 39-74.

Zhang, J.F., Zhou, L.P., Yue, S.Y. (2003) ‘Dating fluvial sediments by optically stimulated luminescence: selection of equivalent doses for age calculation’, *Quaternary Science Reviews,* 22(10-13), pp. 1123-1129.

Zimmerman, D.W. (1971) ‘Thermoluminescent dating using fine grains from pottery’, *Archaeometry,* 13(1), pp. 29-52.

Zöller, L., Pernicka, E. (1989) ‘A note on overcounting in alpha-counters and its elimination’, *Ancient TL,* 7(1), pp. 11-14.

# Appendix A: Risø TL/OSL Reader Reproducibility Assessment

The machine reproducibility estimates generated in Chapter 3.1.5 for the Risø reader used in this research, are derived from the data provided within the following tables.

**Table A.1:** Machine reproducibility data for six 8 mm multi-grain aliquots of 180-250 µm sensitised quartz (Hansen *et al.,* 2015).

| Aliquot | Average $L_x/T_x$ | Standard Deviation | Errors arising from Counting Statistics | Machine Reproducibility |
|---|---|---|---|---|
| 1 | 1.92 ±0.10 | 0.024 | 0.003 | 0.012 |
| 2 | 1.87±0.09 | 0.017 | 0.003 | 0.009 |
| 3 | 1.95±0.10 | 0.012 | 0.003 | 0.006 |
| 4 | 1.95±0.10 | 0.018 | 0.004 | 0.009 |
| 5 | 1.94±0.10 | 0.017 | 0.004 | 0.008 |
| 6 | 1.91±0.10 | 0.025 | 0.004 | 0.013 |
| | | | **$L_x/T_x$ Average =** | 0.010 (1%) |
| | | | **Per Measurement =** | 0.007 (0.7%) |

**Table A.2:** Machine reproducibility data for 29 single-grains of 180-250 µm sensitised quartz (Hansen *et al.*, 2015).

| Grain Position | Average $L_x/T_x$ | Standard Deviation | Errors arising from Counting Statistics | Machine Reproducibility |
|---|---|---|---|---|
| 1 | 1.99±0.11 | 0.039 | 0.017 | 0.018 |
| 2 | 1.91±0.12 | 0.074 | 0.022 | 0.037 |
| 3 | 1.99±0.14 | 0.109 | 0.027 | 0.053 |
| 6 | 2.32±0.13 | 0.103 | 0.012 | 0.044 |
| 8 | 1.89±0.13 | 0.088 | 0.026 | 0.044 |
| 10 | 1.97±0.11 | 0.062 | 0.016 | 0.031 |
| 12 | 2.18±0.13 | 0.119 | 0.017 | 0.054 |
| 13 | 2.13±0.13 | 0.093 | 0.019 | 0.043 |
| 18 | 2.06±0.13 | 0.058 | 0.021 | 0.026 |
| 23 | 2.20±0.14 | 0.131 | 0.022 | 0.059 |
| 42 | 1.90±0.15 | 0.118 | 0.035 | 0.059 |
| 45 | 2.23±0.17 | 0.144 | 0.031 | 0.063 |
| 49 | 1.94±0.10 | 0.051 | 0.011 | 0.026 |
| 51 | 2.02±0.11 | 0.043 | 0.015 | 0.020 |
| 52 | 1.96±0.14 | 0.103 | 0.031 | 0.050 |
| 59 | 1.88±0.13 | 0.074 | 0.029 | 0.036 |
| 60 | 2.06±0.14 | 0.137 | 0.025 | 0.065 |
| 64 | 2.05±0.11 | 0.028 | 0.008 | 0.013 |

**Table A.2 (continued):** Machine reproducibility data for 29 single-grains of 180-250 µm sensitised quartz (Hansen *et al.,* 2015).

| Grain Position | Average $L_x/T_x$ | Standard Deviation | Errors arising from Counting Statistics | Machine Reproducibility |
|---|---|---|---|---|
| 65 | 2.04±0.11 | 0.046 | 0.009 | 0.022 |
| 66 | 2.07±0.12 | 0.069 | 0.016 | 0.032 |
| 67 | 2.02±0.11 | 0.058 | 0.013 | 0.028 |
| 68 | 2.00±0.12 | 0.093 | 0.019 | 0.045 |
| 69 | 2.02±0.10 | 0.036 | 0.008 | 0.017 |
| 76 | 1.98±0.11 | 0.045 | 0.015 | 0.021 |
| 78 | 2.04±0.13 | 0.059 | 0.022 | 0.027 |
| 79 | 2.05±0.15 | 0.069 | 0.031 | 0.030 |
| 81 | 1.98±0.22 | 0.148 | 0.056 | 0.069 |
| 91 | 2.09±0.11 | 0.030 | 0.011 | 0.013 |
| 97 | 2.01±0.12 | 0.085 | 0.016 | 0.042 |
| | | | **$L_x/T_x$ Average =** | 0.038 (3.8%) |
| | | | **Per Measurement =** | 0.027 (2.7%) |

# Appendix B: Supplementary Data for Hydrofluoric Acid Treatment Investigations

### B1. Variation in Sample Mass Treated – Impact upon $D_e$

The Shapiro-Wilk normality tests conducted upon $D_e$ estimates (not transformed) obtained from the sample mass scenarios highlighted in in Chapter 4.4.3.2 are accompanied by the Q-Q plots presented in Figure B1.1 and B1.2

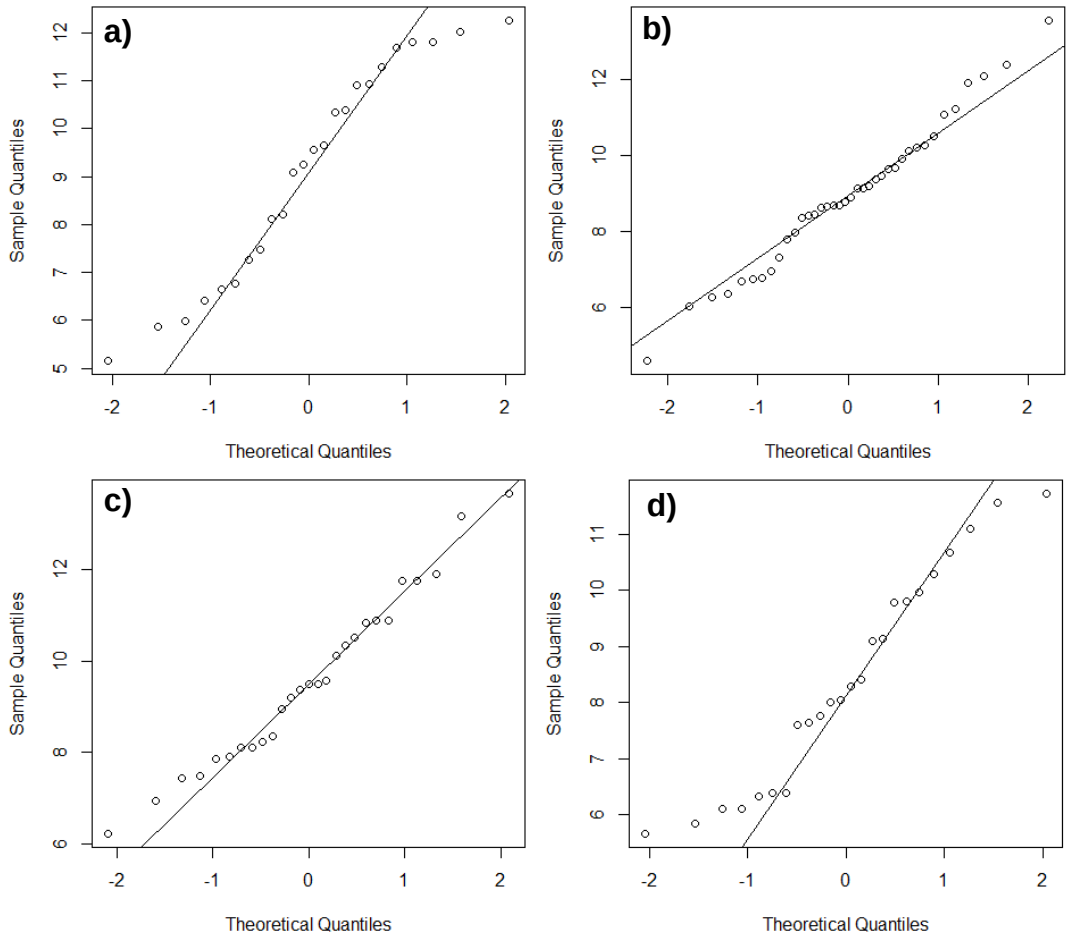


**Figure B1.1:** Q-Q plots for $D_e$ values obtained using 'strict' rejection criteria for variable masses (a: No HF, b: 2.46, c: 4.92 and d: 9.84 g) of GL14023 treated with 100 ml of HF.

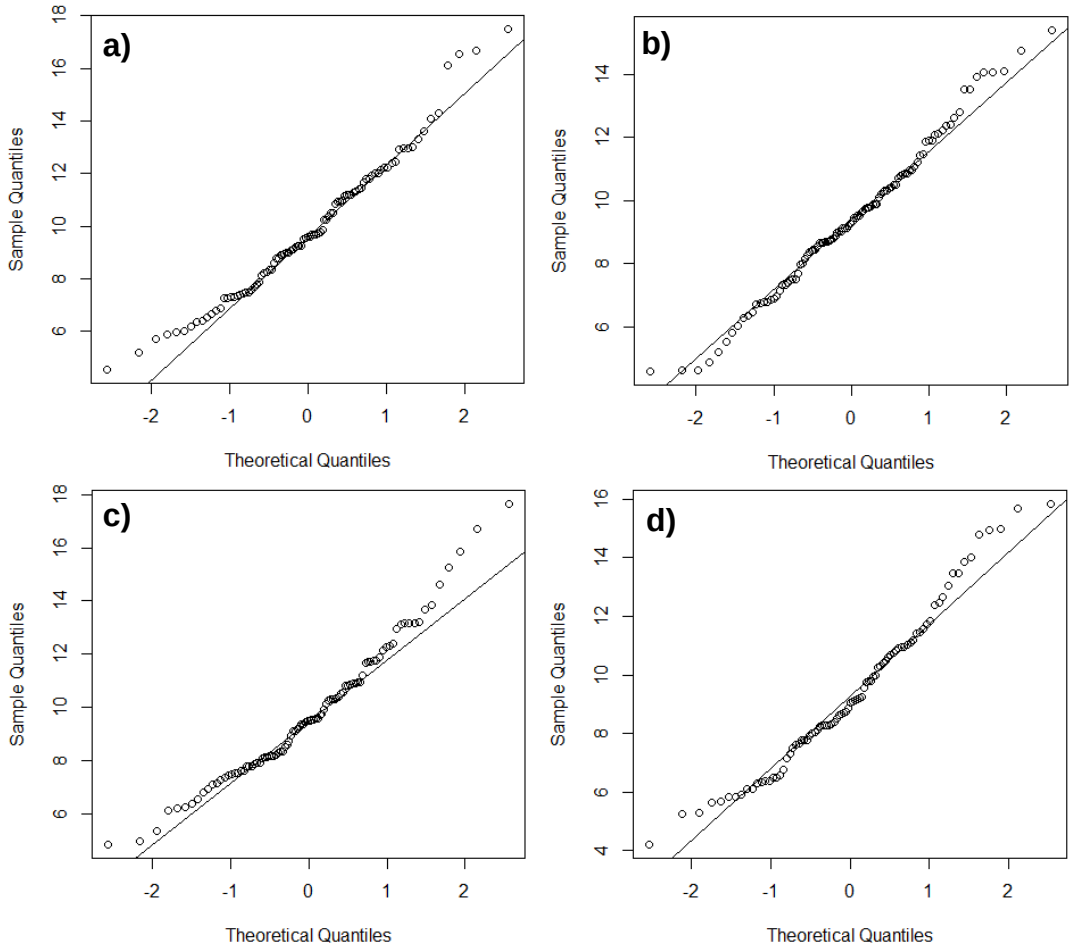


**Figure B1.2:** Q-Q plots for $D_e$ values obtained using 'relaxed' rejection criteria for variable masses (a: No HF, b: 2.46, c: 4.92 and d: 9.84 g) of GL14023 treated with 100 ml of HF.

Of the statistical parameters explored in Chapter 4.4.3 for variations in mass treated with HF, kurtosis of $D_e$ populations appeared to display a linear trend when strict adoption criteria were applied. A trend line is fitted in Figure B1.3 which indicates that an increase in mass treated with 100 ml of HF results in a decrease in kurtosis.

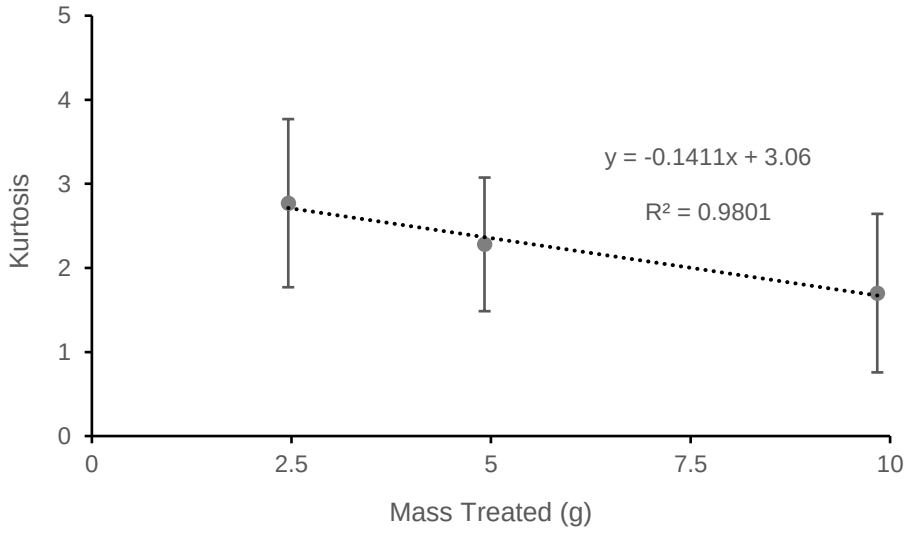


**Figure B1.3:** Kurtosis of $D_e$ estimates obtained using 'strict' rejection criteria for various masses of GL14023 treated with 100 ml of HF.

## B2. Variation in HF Treatment Time – Impact upon $D_e$

Abanico plots obtained using relaxed rejection criteria for each HF time scenario investigated in Chapter 4.4.4 are provided in Figures B2.1-3. All appear to produce unimodal distributions with less distinctive changes relative to those observed using strict rejection criteria.

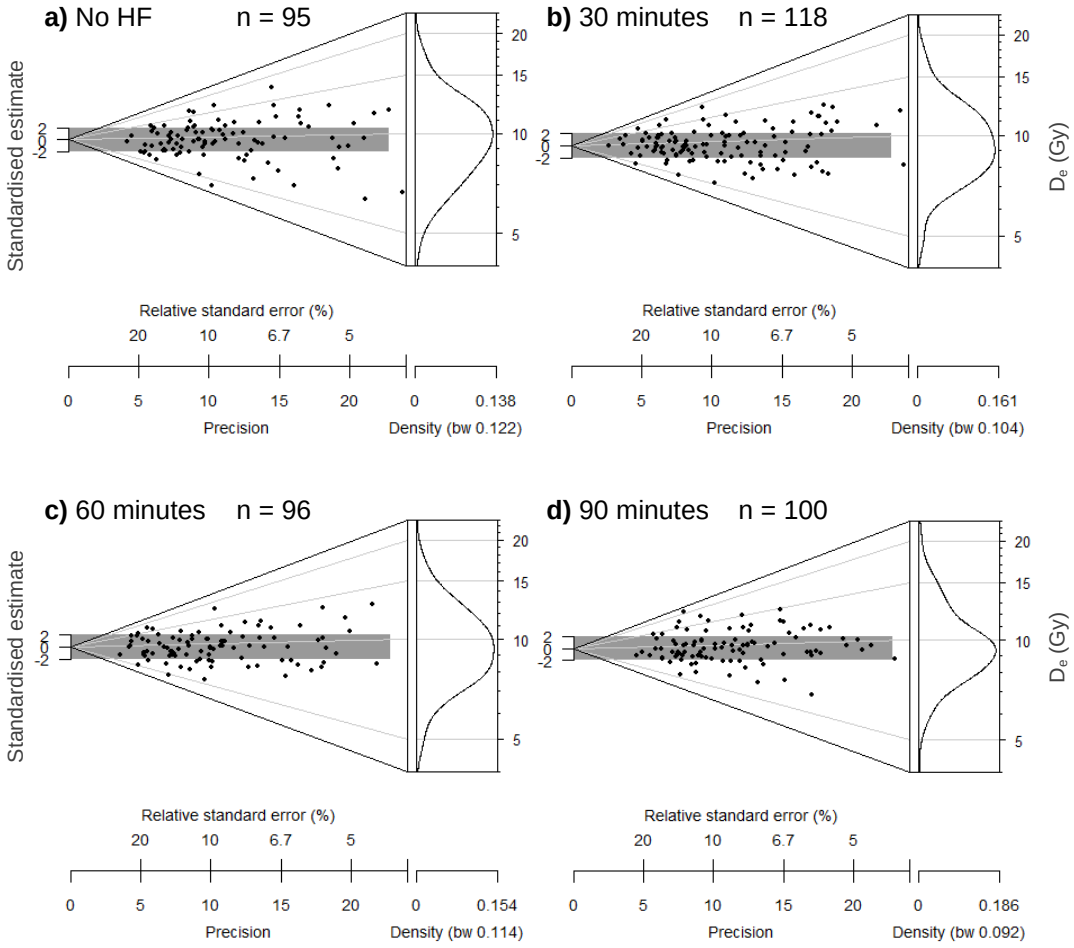


**Figure B2.1:** Abanico plots of single-grain $D_e$ values for 180-250 µm quartz from GL14023 treated with 100 ml of HF for; a) 0, b) 30, c) 60 and d) 90 minutes. Relaxed rejection criteria adopted.

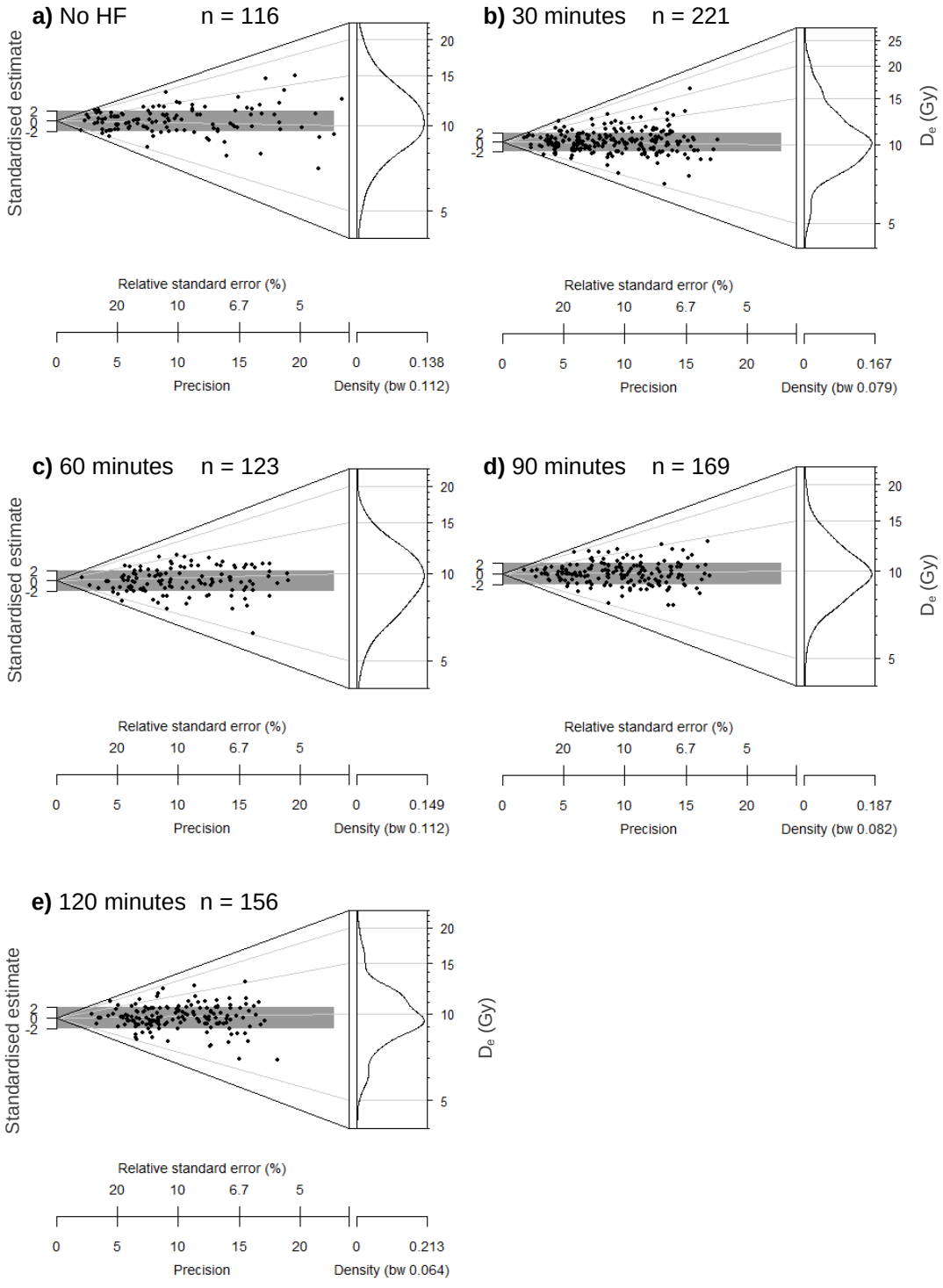


**Figure B2.2:** Abanico plots of single-grain $D_e$ values for 180-250 µm quartz from GL15025 treated with 100 ml of HF for; a) 0, b) 30, c) 60, d) 90 and e) 120 minutes. Relaxed rejection criteria adopted.

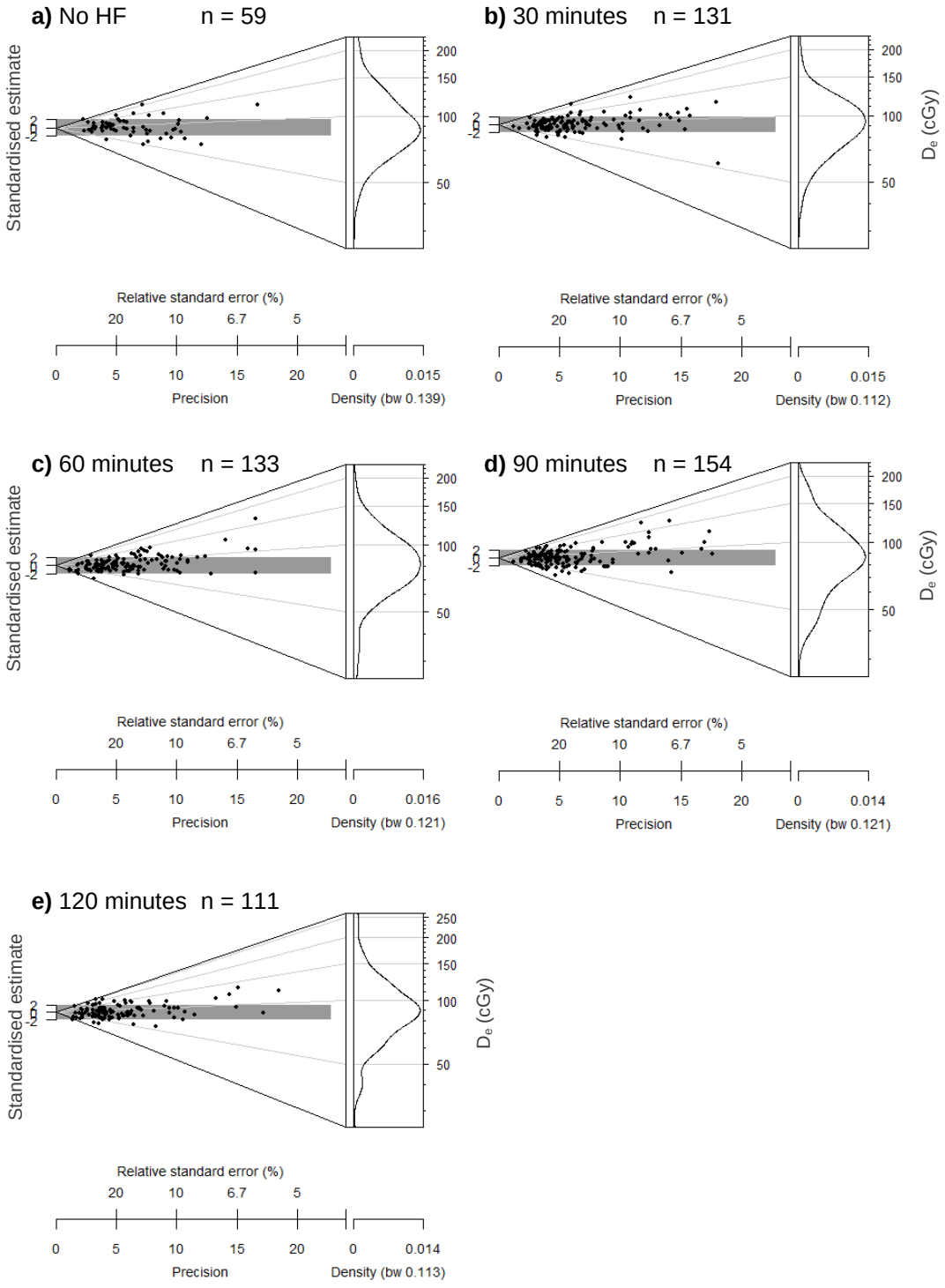


**Figure B2.3:** Abanico plots of single-grain $D_e$ values for 180-250 µm quartz from GL16180 treated with 100 ml of HF for; a) 0, b) 30, c) 60, d) 90 and e) 120 minutes. Relaxed rejection criteria adopted (Note: Change in scale to cGy (i.e. 0.01 Gy)).

The Shapiro-Wilk normality tests conducted upon $D_e$ estimates (not transformed) obtained from the HF time scenarios highlighted in in Chapter 4.4.3.4 are accompanied by the Q-Q plots presented in Figures: B2.4 to B2.9.

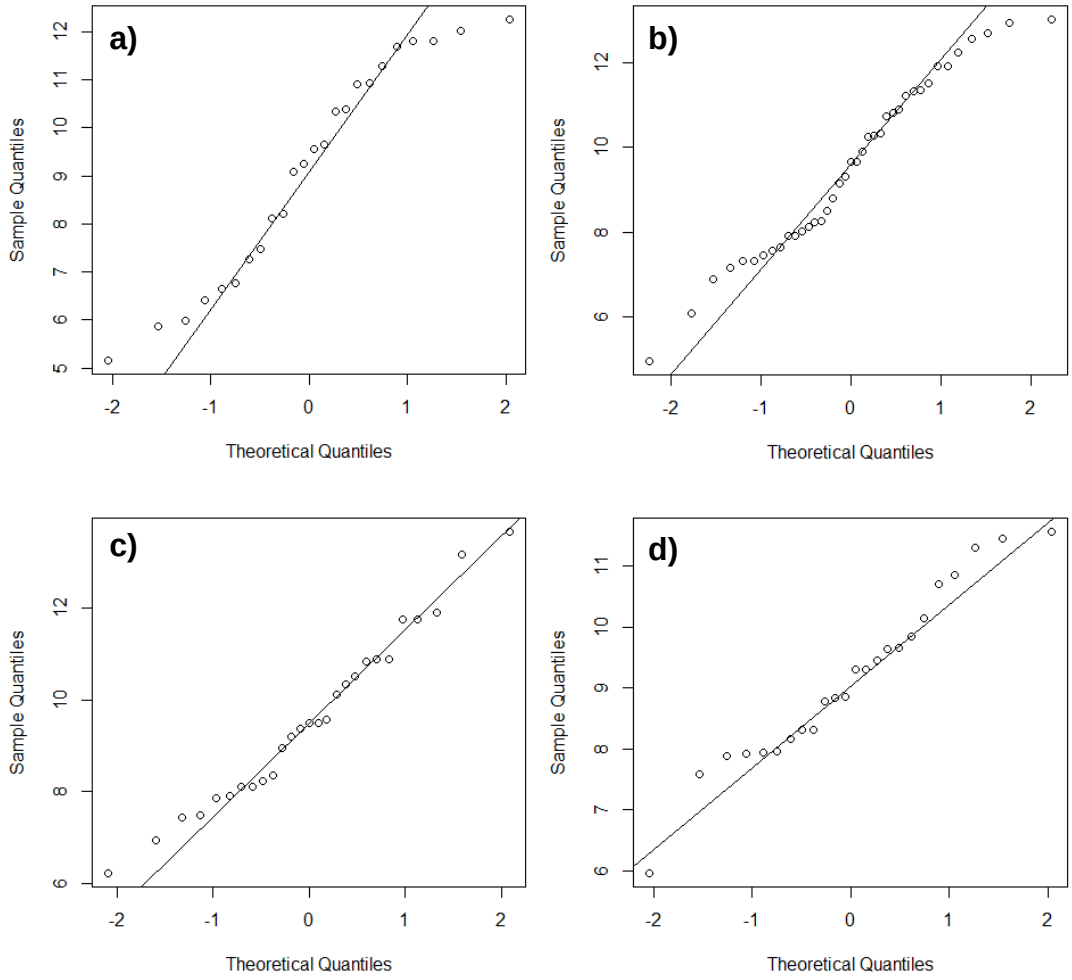


**Figure B2.4:** Q-Q plots for $D_e$ values obtained using 'strict' rejection criteria for 4.92 g fractions of GL14023 treated with various 100 ml HF durations (a: No HF, b: 30, c: 60 and d: 90 minutes).

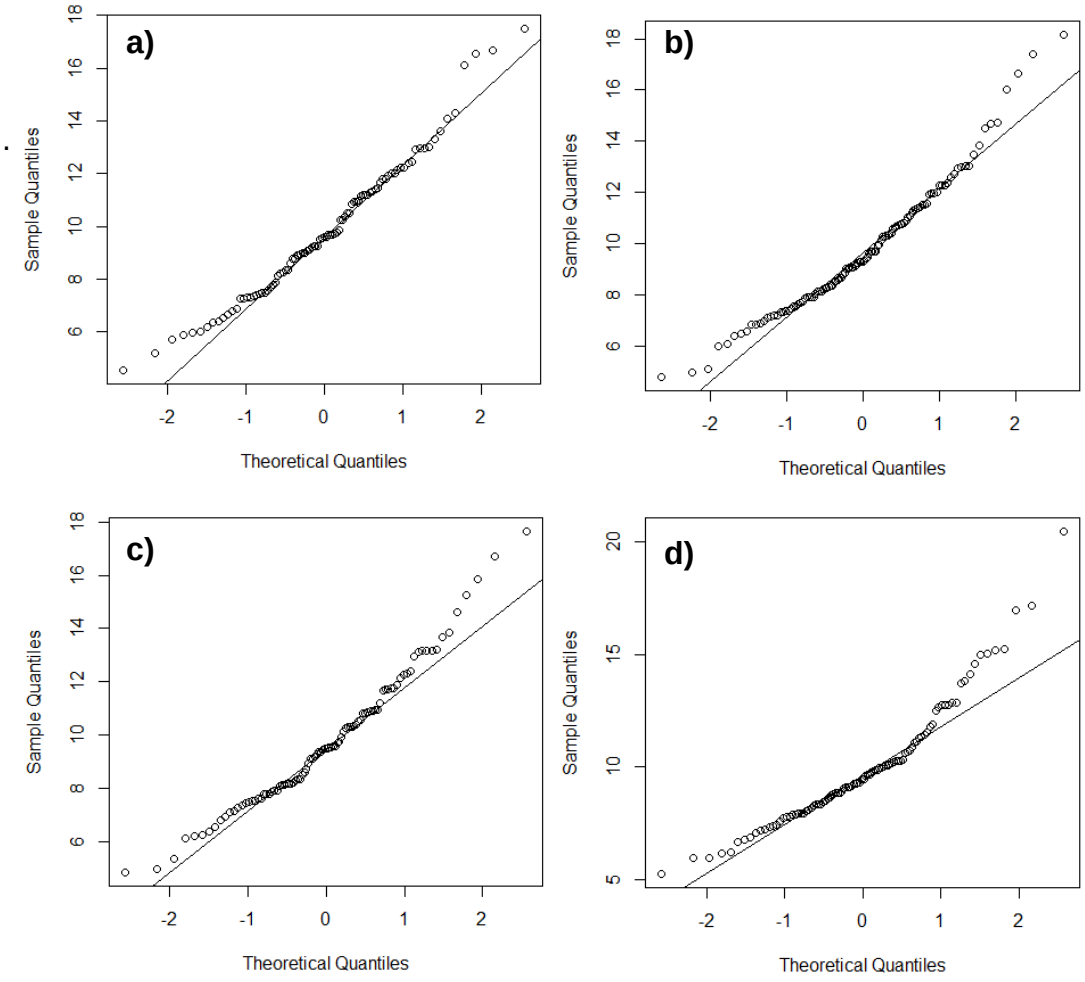


**Figure B2.5:** Q-Q plots for $D_e$ values obtained using 'relaxed' rejection criteria for 4.92 g fractions of GL14023 treated with various 100 ml HF durations (a: No HF, b: 30, c: 60 and d: 90 minutes).

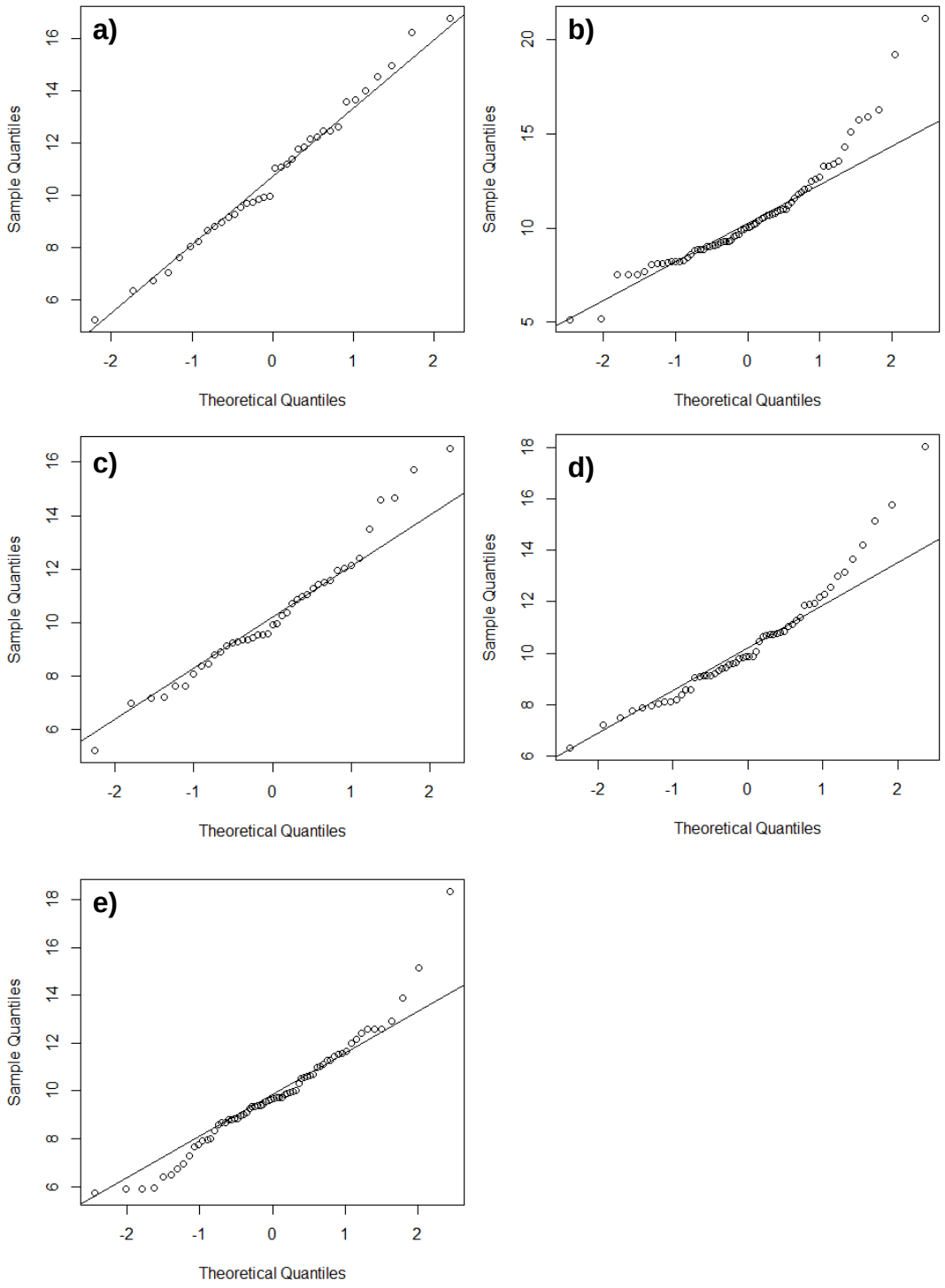


**Figure B2.6:** Q-Q plots for $D_e$ values obtained using 'strict' rejection criteria for 5 g fractions of GL15025 treated with various 100 ml HF durations (a: No HF, b: 30, c: 60, d: 90 and e: 120 minutes).

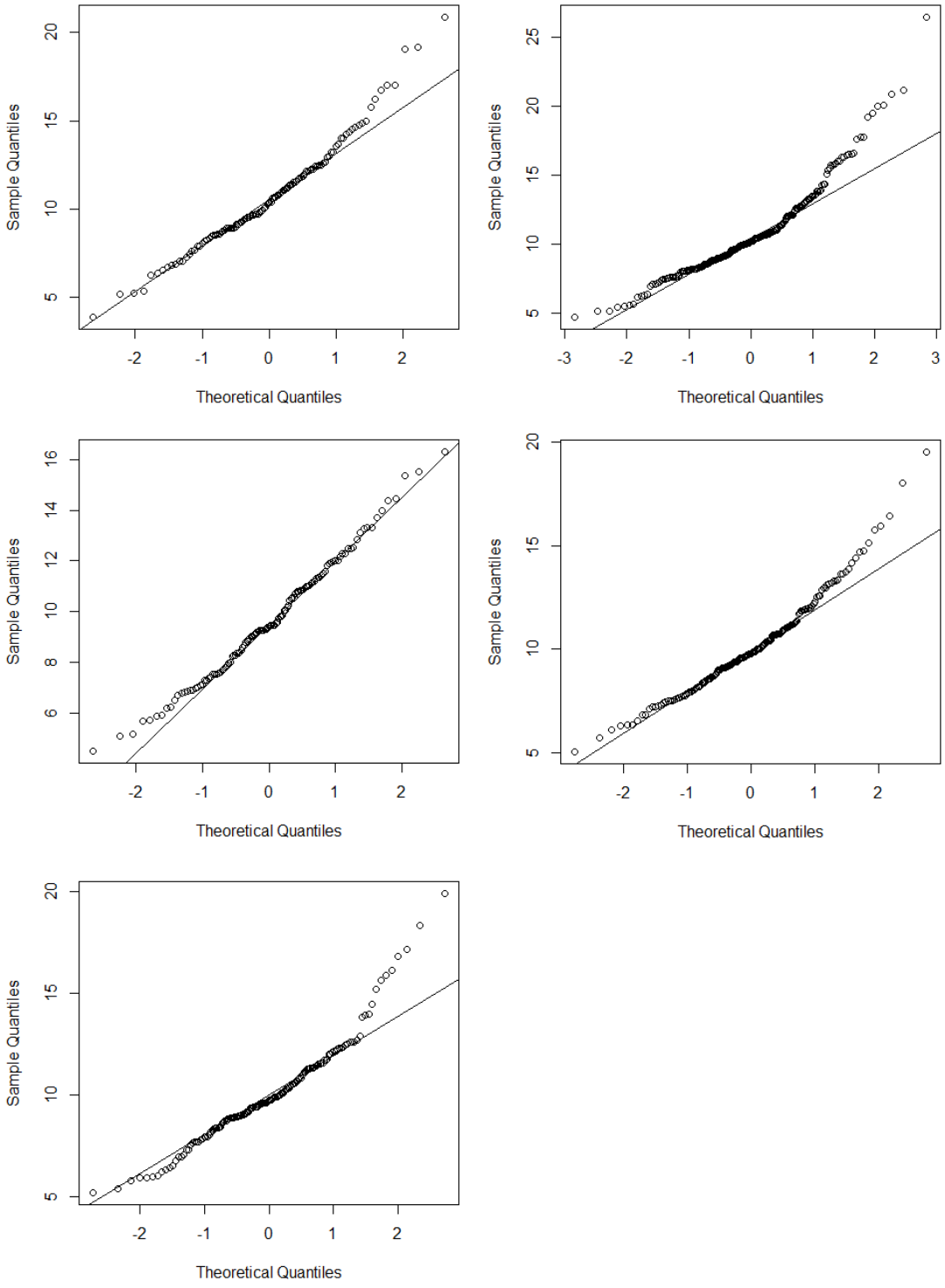


**Figure B2.7:** Q-Q plots for $D_e$ values obtained using 'relaxed' rejection criteria for 5 g fractions of GL15025 treated with various 100 ml HF durations (a: No HF, b: 30, c: 60, d: 90 and e: 120 minutes).

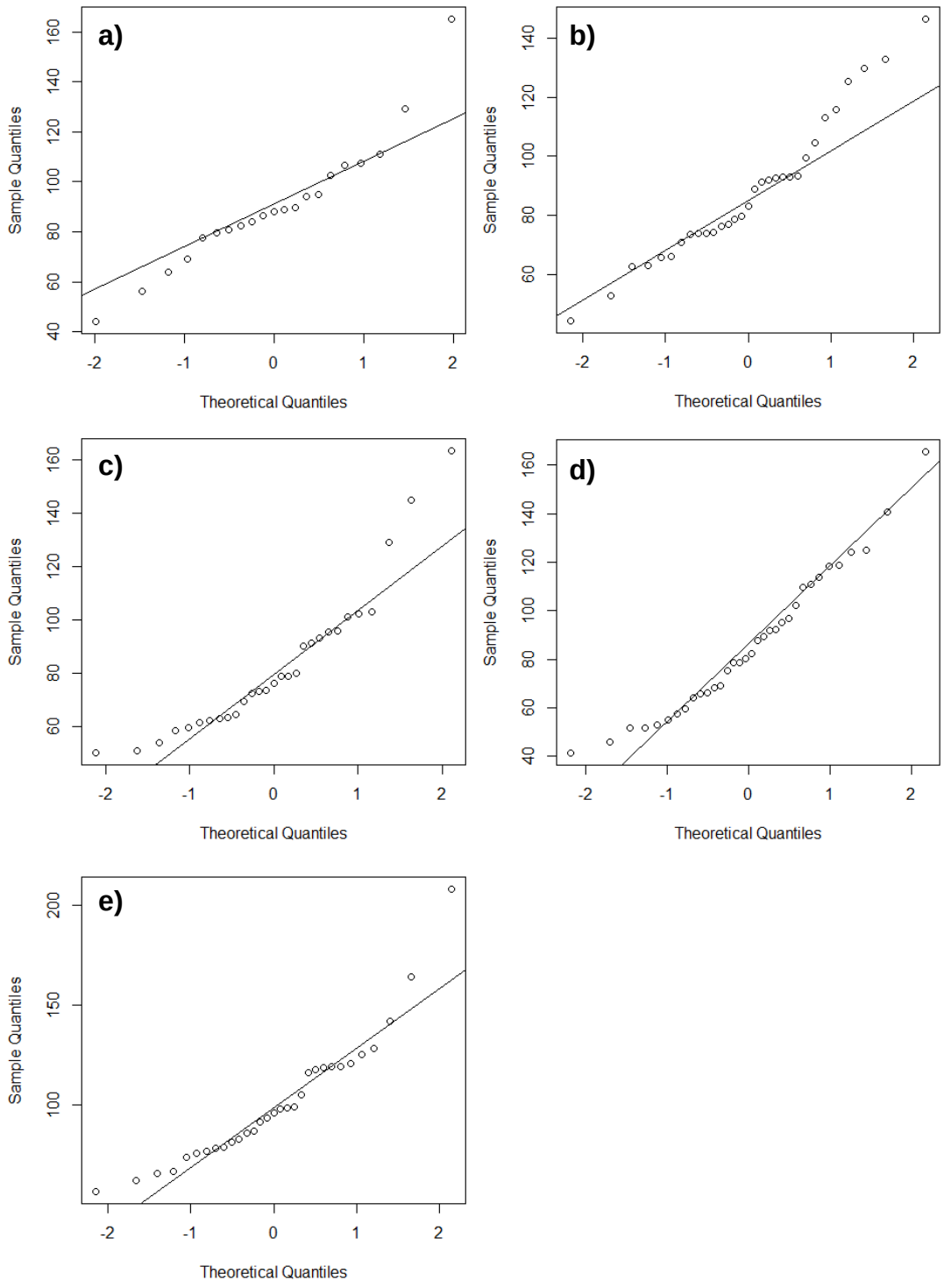


**Figure B2.8:** Q-Q plots for $D_e$ values obtained using 'strict' rejection criteria for 5 g fractions of GL16180 treated with various 100 ml HF durations (a: No HF, b: 30, c: 60, d: 90 and e: 120 minutes).

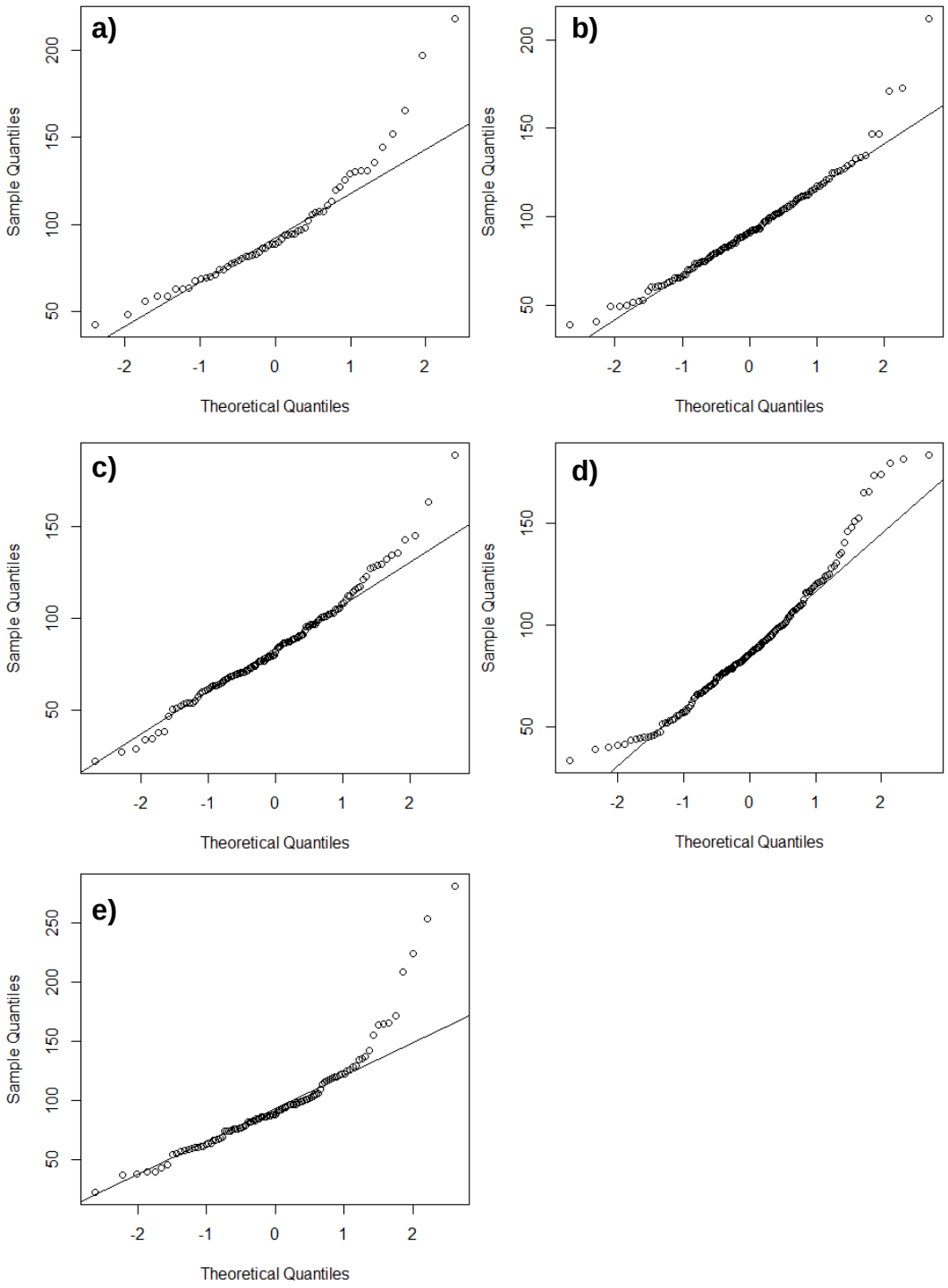


**Figure B2.9:** Q-Q plots for $D_e$ values obtained using 'relaxed' rejection criteria for 5 g fractions of GL16180 treated with various 100 ml HF durations (a: No HF, b: 30, c: 60, d: 90 and e: 120 minutes).

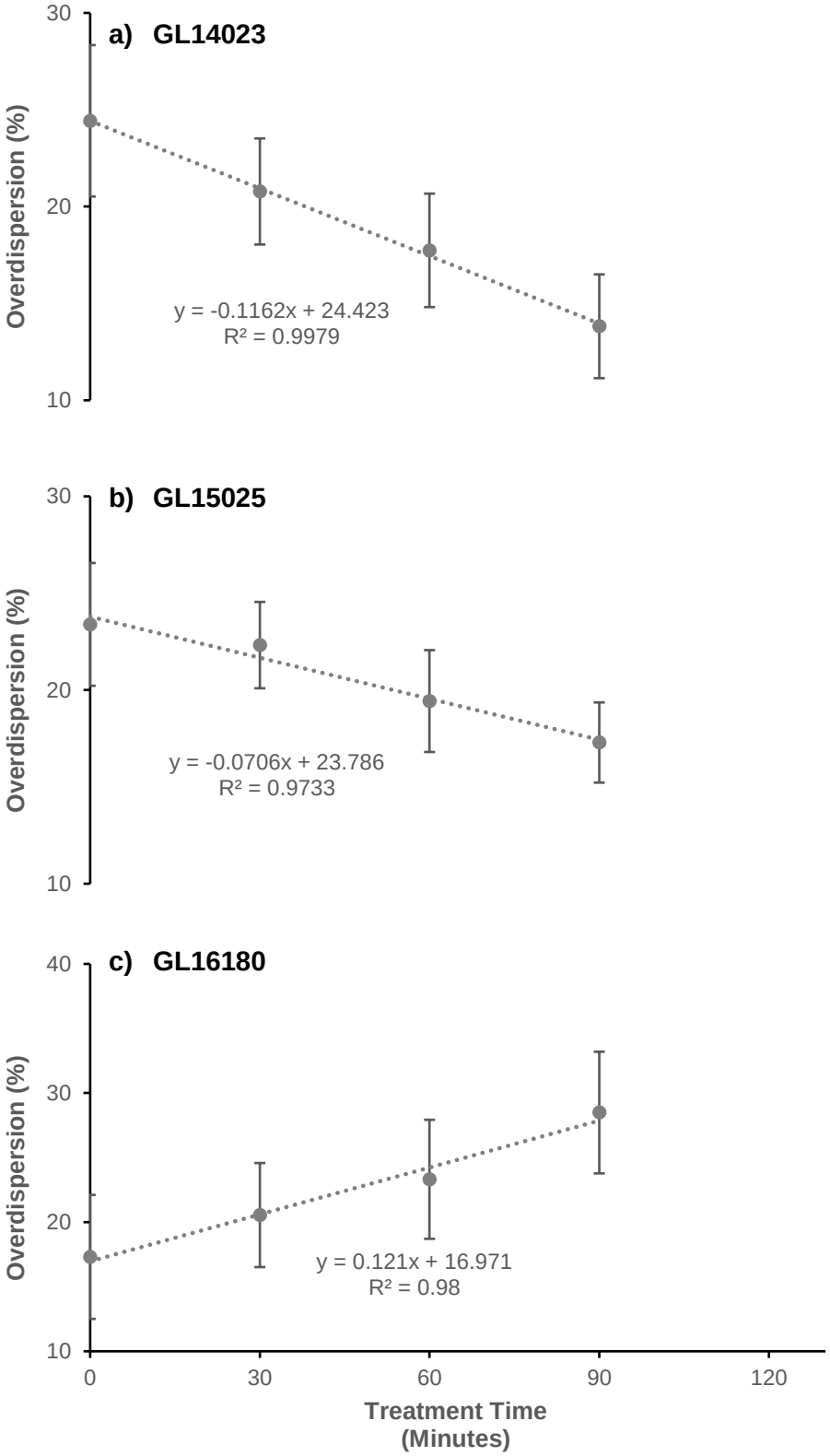


**Figure B2.10:** Linear regression of overdispersion for $D_e$ estimates obtained from a) GL14023, b) GL15025 and c) GL16180 using 'strict' rejection criteria for various HF treatment durations (120 minute treatment omitted for sample GL15025 and GL16180).

## B3. Variation in HF Treatment Time – Removal of Feldspars

All SAR measurement sequences for the HF investigation included an IR stimulation so that feldspar inclusions could be identified through the calculation of post-IR/OSL depletion ratios. Example IRSL signals for the untreated and 30 minute HF treatments are presented in Figure B3.1.

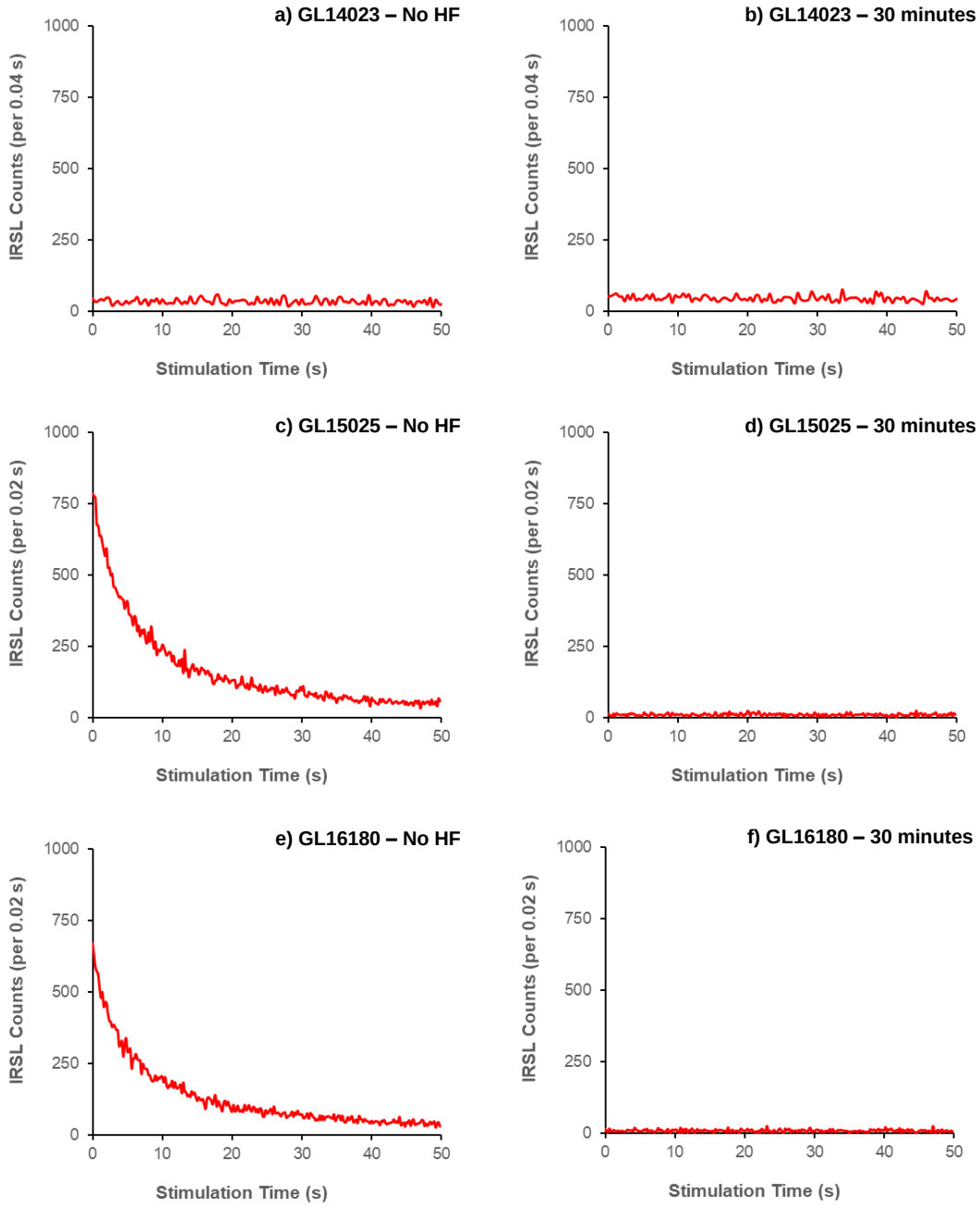


**Figure B3.1:** IRSL signals for GL14023, GL15025 and GL16180 180-250 µm quartz following a 4 Gy β-dose. Data for 0 and 30 minute HF treatments.

# Appendix C: Supplementary Data for Optical Dating of Mfolozi Sediments

## C1. South Lake Dose-Recovery Tests

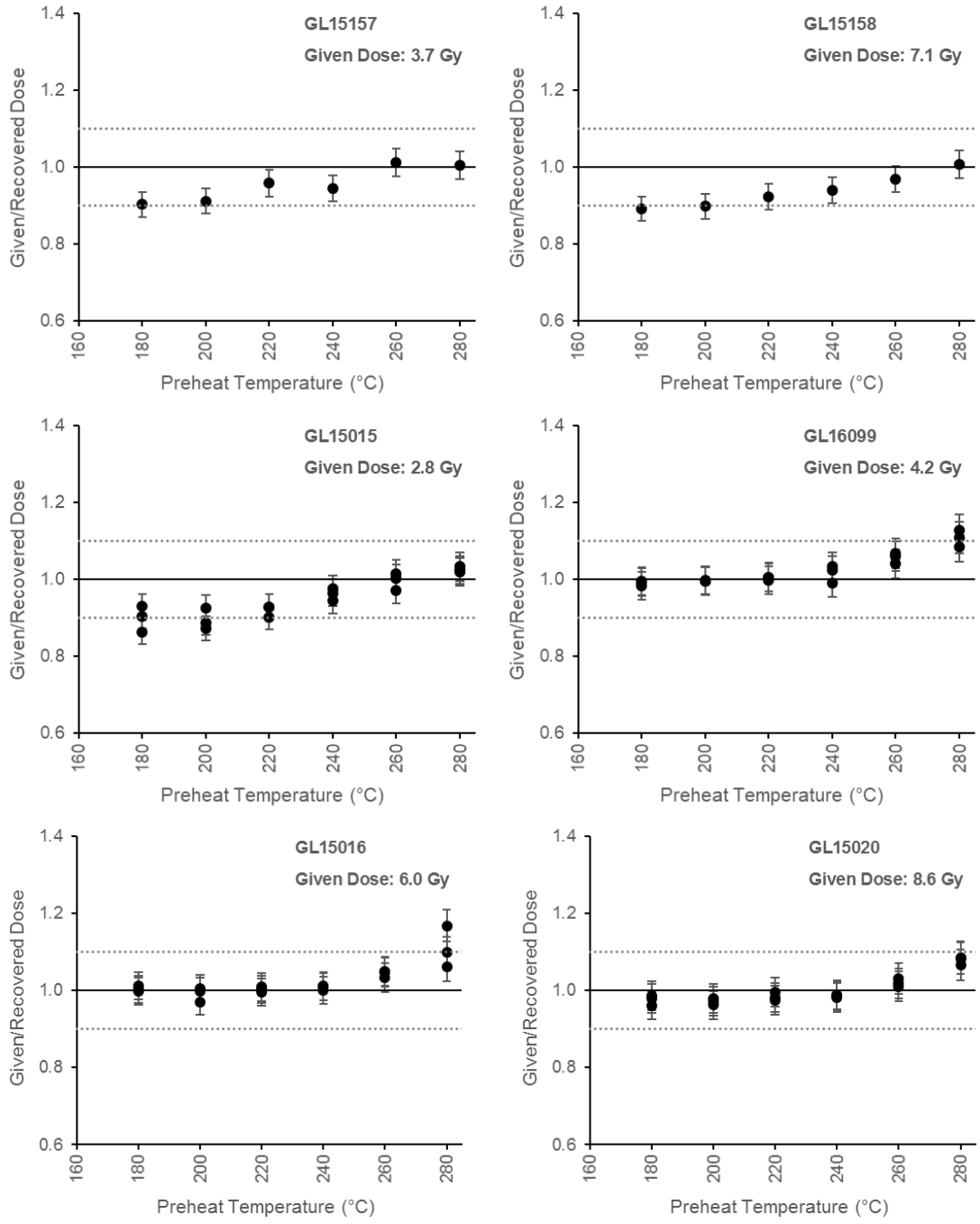


**Figure C1.1:** South Lake Dose-Recovery plots (depth order)

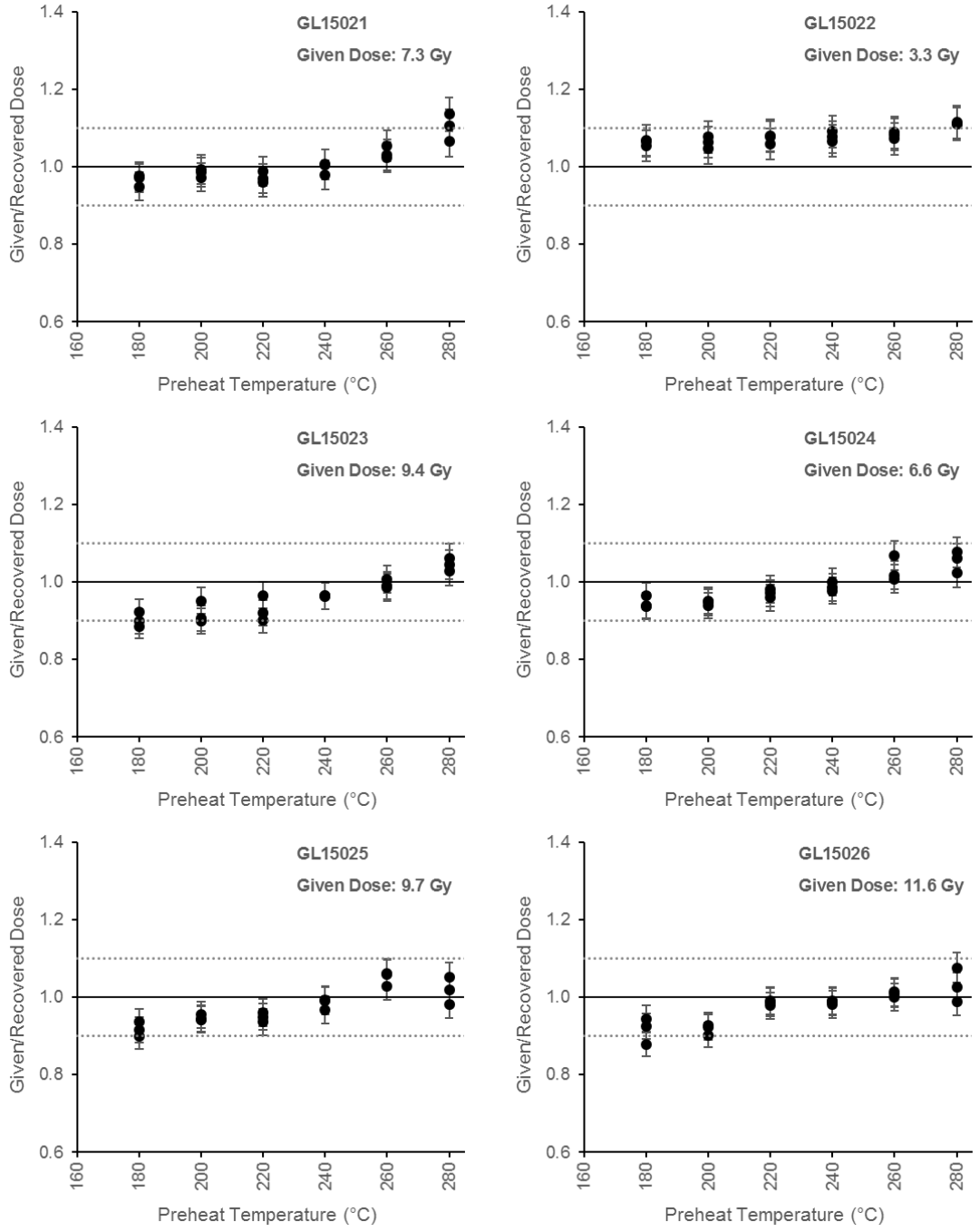


**Figure C1.2:** South Lake Dose-Recovery plots - continued

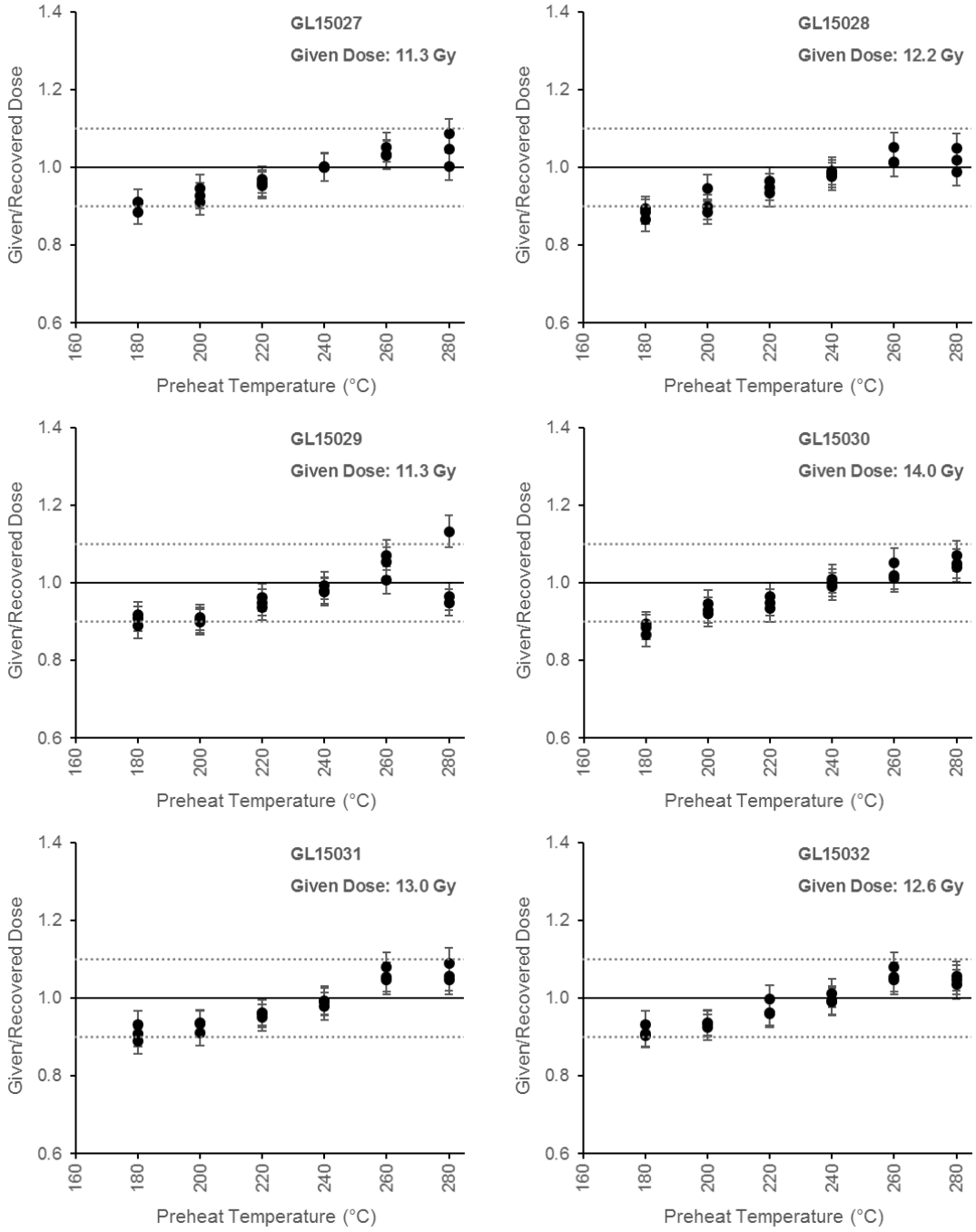


**Figure C1.3:** South Lake Dose-Recovery plots - continued

## C.2: Differences in South Lake fine-grain sensitivity change

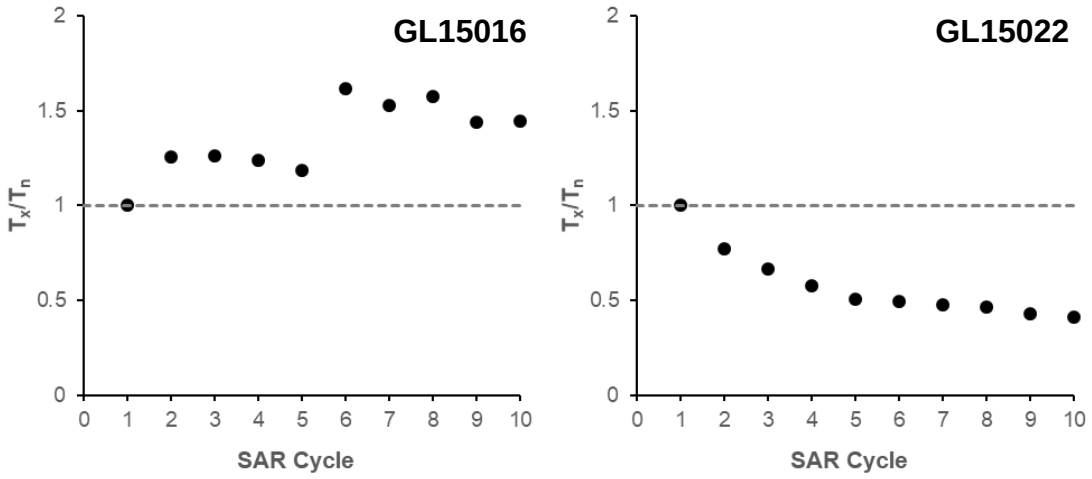


**Figure C2.1:** Typical increase in sensitivity ($T_x/T_n$) for South Lake 5-15 µm quartz as displayed by GL15016 compared to the decrease in sensitivity displayed by GL15022

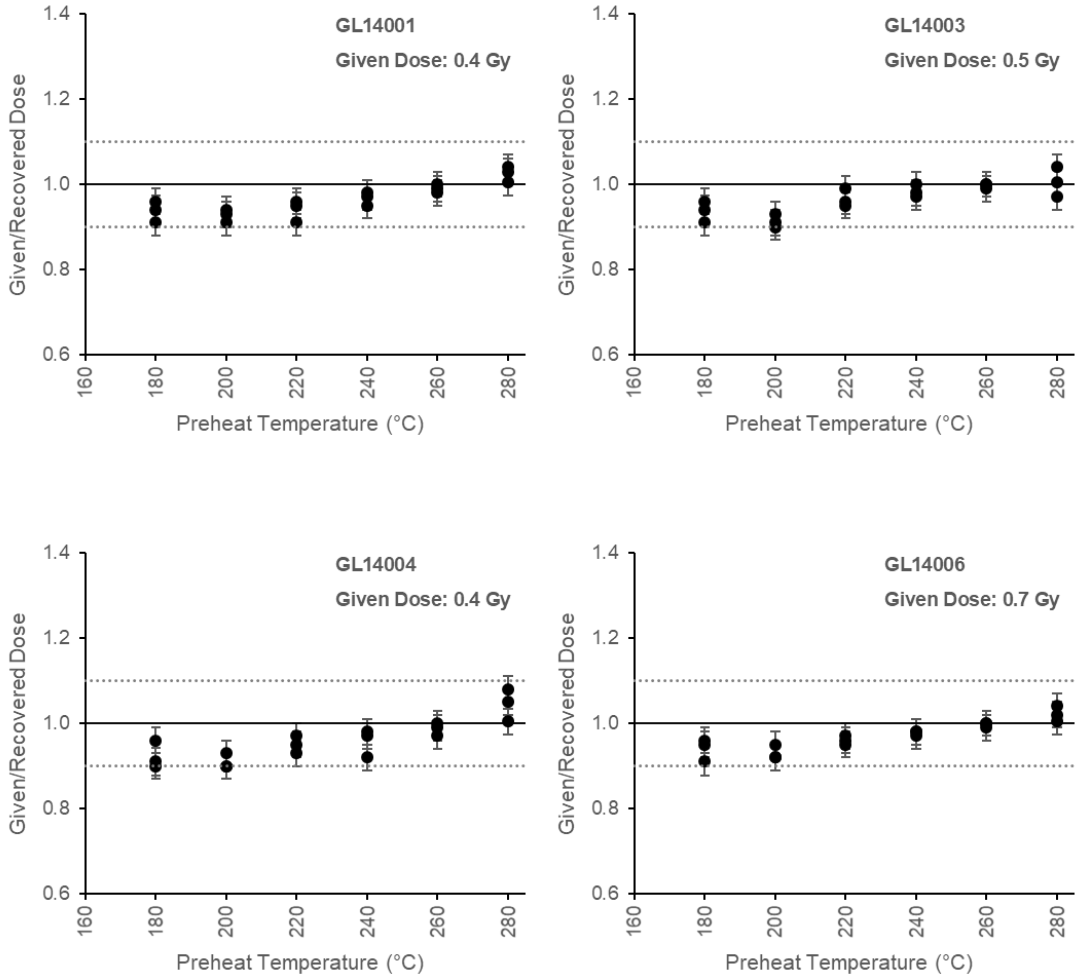


**Figure C3.1:** UCOSP face Dose-Recovery plots

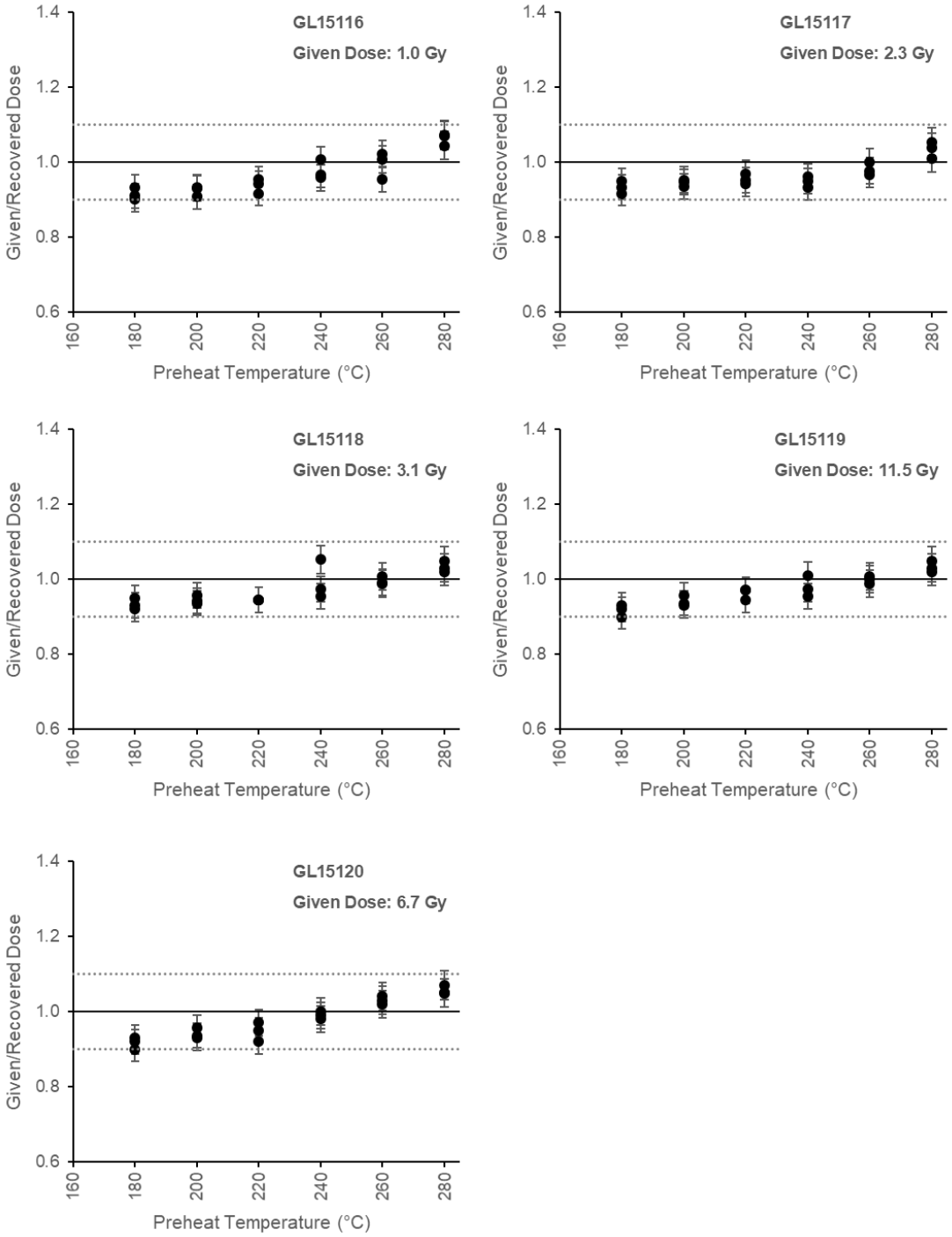


**Figure C3.2:** UCOSP core Dose-Recovery plots

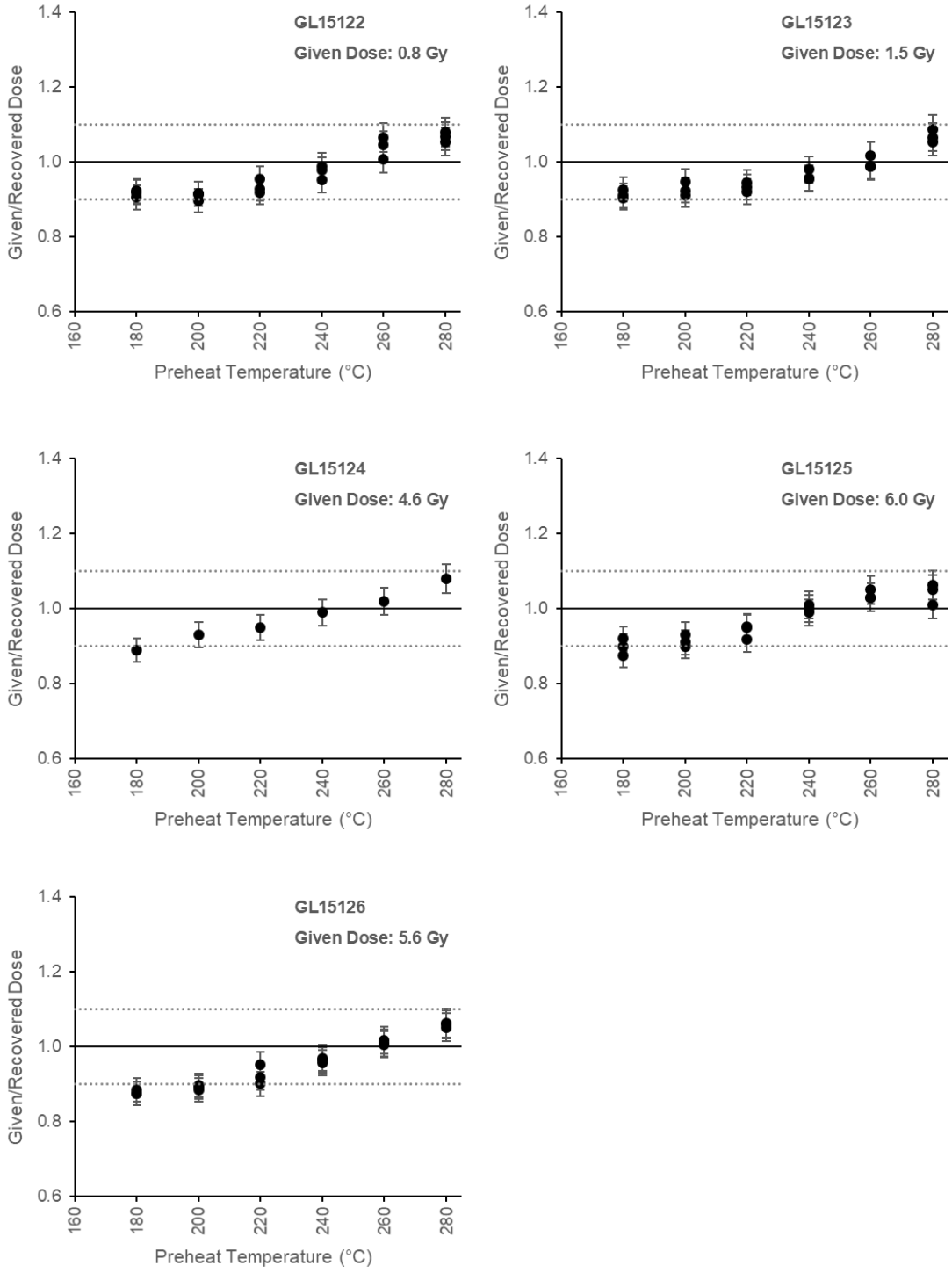


**Figure C4.1:** Futululu Dose-Recovery plots

# Appendix D: OxCal Bayesian Deposition Model Code

The OxCal P_Sequence deposition models in Chapter 6 were produced using the code presented here.

***South Lake P_Sequence deposition model including all age estimates (Figure 6.2.1):***

```
Plot()
 {
  P_Sequence("SL Outlier Final",100,20,U(-2,2))
  {
   timescale="OSL";
   Boundary();
   Date("GL15032",N(calBP(6590),941))
   {
    z=4.62;
   };
   Date("GL15031",N(calBP(7149),1023))
   {
    z=4.33;
   };
   Date("GL15030",N(calBP(7146),1025))
   {
    z=4.1;
   };
   Date("GL15029",N(calBP(6389),913))
   {
    z=3.87;
```

```
};
Date("GL15028",N(calBP(5741),813))
{
 z=3.74;
};
Date("GL15027",N(calBP(5773),812))
{
 z=3.27;
};
Date("GL15026",N(calBP(5824),827))
{
 z=3.13;
};
Date("GL15025",N(calBP(5244),728))
{
 z=2.88;
};
Date("SL_AMS_5",N(calBP(4725),135))
{
 z=2.71;
};
Date("GL15024",N(calBP(3525),481))
{
 z=2.58;
};
Date("GL15023",N(calBP(3780),570))
{
 z=2.09;
};
Date("GL15022",N(calBP(1847),230))
{
 z=1.81;
};
Date("SL_AMS_3A",N(calBP(1392),22.5))
{
 z=1.72;
};
Date("GL15021",N(calBP(3466),430))
```

```
  {
   z=1.68;
  };
  Date("GL15020",N(calBP(3671),467))
  {
   z=1.58;
  };
  Date("SL_AMS_1",N(calBP(1182),55))
  {
   z=1.2;
  };
  Date("SL_AMS_2",N(calBP(1291),46))
  {
   z=0.9;
  };
  Date("GL15016",N(calBP(2805),358))
  {
   z=0.85;
  };
  Date("GL16099",N(calBP(1543),192))
  {
   z=0.72;
  };
  Date("GL15015",N(calBP(270),40))
  {
   z=0.48;
  };
  Date("GL15158",N(calBP(54),8))
  {
   z=0.32;
  };
  Date("GL15157",N(calBP(55),8))
  {
   z=0.17;
  };
  Boundary();
 };
};
```

***South Lake P_Sequence deposition model with outlying age estimates removed (Figure 6.2.2):***

```
Plot()
 {
  P_Sequence("SL Omitted Final Dec",100,20,U(-2,2))
  {
   timescale="OSL";
   Boundary();
   Date("GL15032",N(calBP(6590),941))
   {
    z=4.62;
   };
   Date("GL15031",N(calBP(7149),1023))
   {
    z=4.33;
   };
   Date("GL15030",N(calBP(7146),1025))
   {
    z=4.1;
   };
   Date("GL15029",N(calBP(6389),913))
   {
    z=3.87;
   };
   Date("GL15028",N(calBP(5741),813))
   {
    z=3.74;
   };
   Date("GL15027",N(calBP(5773),812))
   {
    z=3.27;
   };
   Date("GL15026",N(calBP(5824),827))
   {
    z=3.13;
   };
```

```
Date("GL15025",N(calBP(5244),728))
{
 z=2.88;
};
Date("SL_AMS_5",N(calBP(4725),135))
{
 z=2.71;
};
Date("GL15024",N(calBP(3525),481))
{
 z=2.58;
};
Date("GL15023",N(calBP(3780),570))
{
 z=2.09;
};
Date("GL15022",N(calBP(1847),230))
{
 z=1.81;
};
Date("SL_AMS_3A",N(calBP(1392),22.5))
{
 z=1.72;
};
Date("SL_AMS_1",N(calBP(1182),55))
{
 z=1.2;
};
Date("SL_AMS_2",N(calBP(1291),46))
{
 z=0.9;
};
Date("GL16099",N(calBP(1543),192))
{
 z=0.72;
};
Date("GL15015",N(calBP(270),40))
{
```

```
  z=0.48;
 };
 Date("GL15158",N(calBP(54),8))
 {
  z=0.32;
 };
 Date("GL15157",N(calBP(55),8))
 {
  z=0.17;
 };
 Boundary();
};
};
```

### *UCOSP P_Sequence deposition model (Figure 6.3.1):*

```
Plot()
 {
  P_Sequence("UCOSP Dec Final",100,20,U(-2,2))
  {
   timescale="OSL";
   Boundary();
   Date("GL15120",N(calBP(1583),242))
   {
    z=7.35;
   };
   Date("GL15119",N(calBP(1042),169))
   {
    z=6.75;
   };
   Date("GL15118",N(calBP(1087),166))
   {
    z=6.35;
   };
   Date("GL15117",N(calBP(807),118))
   {
    z=6.15;
   };
   Date("GL15116",N(calBP(184),27))
   {
    z=5.15;
   };
   Date("GL14006",N(calBP(99),15))
   {
    z=3;
   };
   Date("GL14004",N(calBP(80),12))
   {
    z=1.95;
   };
   Date("GL14003",N(calBP(50),8))
```

```
  {
   z=1.55;
  };
  Date("GL14001",N(calBP(31),7))
  {
   z=0.69;
  };
  Boundary();
 };
};
```

### *Futululu P_Sequence deposition model (Figure 6.4.1):*

```
Plot()
 {
  P_Sequence("Fut Dec 2",100,30,U(-2,2))
  {
   timescale="OSL";
   Boundary();
   Date("GL15126",N(calBP(2102),306))
   {
    z=3.82;
   };
   Date("GL15125",N(calBP(2083),301))
   {
    z=2.9;
   };
   Date("GL15124",N(calBP(1891),296))
   {
    z=2.77;
   };
   Date("GL15123",N(calBP(218),32))
   {
    z=1.67;
   };
   Date("GL15122",N(calBP(214),30))
   {
    z=0.75;
   };
   Boundary();
  };
 };
```